The Build-Up of Galactic Stellar Nuclei

Katja Fahrion

München 2021

The Build-Up of Galactic Stellar Nuclei

Dissertation
an der Fakultät für Physik
der Ludwig–Maximilians–Universität
München

vorgelegt von
Katja Fahrion
geboren in Neu-Ulm

München, den 11. Mai 2021

Erstgutachter: PD Dr. Klaus Dolag
Zweitgutachter: Prof. Dr. Joseph Mohr
ESO Betreuerin: Dr. Mariya Lyubenova
Tag der mündlichen Prüfung: 12. Juli 2021

Abstract

Nuclear star clusters are the densest stellar systems in the Universe and are found in the centres of all types of galaxies. At least 70 per cent of all galaxies – and at masses of $M_{\rm gal} \sim 10^9 M_\odot$ even more than 90 per cent – are nucleated. As nuclear star clusters retain information regarding their evolutionary history imprinted in their stellar populations, they provide unique windows into the various physical processes that shape the nuclei of galaxies.

The goal of this thesis is to explore the formation mechanisms of nuclear star clusters. They might form directly at the galaxy centre out of gas, explaining the presence of young stars or extended star formation histories. Additionally, the formation out of pre-enriched gas can lead to high metallicities in the formed star cluster. Alternatively, nuclear star clusters might be produced through the mergers of globular clusters. As globular clusters contain old, often metal-poor stars, this formation channel can produce old, metal-poor nuclear star clusters.

There is evidence that both paths occur and also hybrid scenarios have been proposed. However, the relative contribution of either channel and their correlation with galaxy properties are not yet established because constraining the dominant formation channel with observations requires a panoramic view of all the involved stellar components. In this thesis, I employ integral-field spectroscopy of different galaxies with the MUSE instrument. I extract and analyse the spectra of the nuclear star clusters, the globular cluster population, and the underlying stellar body to obtain their kinematics and stellar population properties.

Studying the elliptical galaxy FCC 47, I find evidence that its massive, metal-rich, and kinematically decoupled nuclear star cluster has formed from efficient in-situ star formation. The study of two nearby nucleated dwarf galaxies gives a different result: their nuclear star clusters are significantly less enriched than the host galaxies and were likely formed out of the merger of metal-poor globular clusters. To explore how these case studies compare with the general galaxy population, I analyse the ages, metallicities, and star formation histories of nuclear star clusters in comparison to globular clusters and their hosts in 25 galaxies, mainly in the Fornax galaxy cluster. This study finds a clear transition of the dominant nuclear star cluster formation channel with both galaxy and nuclear star cluster mass. While globular cluster accretion forms the nuclear star clusters of low-mass galaxies, central star formation is responsible for the efficient mass build-up in the most massive nuclear star clusters. At intermediate masses both channels can contribute. The transition between these formation channels seems to occur at galaxy masses of $M_{\rm gal} \sim 10^9 M_\odot$ and nuclear star cluster masses of $M_{\rm NSC} \sim 10^7 M_\odot$.

To understand this trend from a theoretical viewpoint, I employ a semi-analytical model that describes nuclear star cluster formation from the dynamical evolution of an initial star cluster population. The mass of the so-formed nuclear star cluster depends on the available mass in star clusters and this model finds a similar trend: low-mass nuclear star clusters can be built efficiently out of globular clusters, but forming high-mass nuclear star clusters requires significant amounts of additional star formation to let them grow beyond $M_{\rm NSC} > 10^7 M_\odot$.

In summary, I explore nuclear star cluster formation in individual galaxies, finding solid observational evidence for a transition in the dominant nuclear star cluster formation scenario with galaxy properties. These results are fundamental for understanding nuclear star clusters as unique probes of the evolutionary history of galaxies and they lay the basis for future studies exploring nuclear star cluster formation in different environments or galaxy types.

Zusammenfassung

Kernsternhaufen sind die dichtesten Sternhaufen im Universum und können in den Zentren aller Galaxientypen gefunden werden. Mindestens 70 Prozent aller Galaxien – und bei Galaxien mit Massen $M_{\rm gal} \sim 10^9 M_\odot$ sogar über 90 Prozent – haben einen Kernsternhaufen. Die Sterne in Kernsternhaufen tragen Informationen über die Entwicklung des Sternhaufens in sich und erlauben somit einen Einblick in die physikalischen Prozesse, die eine Rolle bei der Entstehung von Galaxienzentren spielen.

Das Ziel dieser Dissertation ist es, die Entstehungsmechanismen von Kernsternhaufen zu untersuchen. Zum Beispiel können sich Kernsternhaufen aus Gas im Galaxienzentrum bilden, was junge Sterne oder komplexe Sternentstehungsgeschichten erklären kann. Zusätzlich kann die Entstehung aus angereichertem Gas zu hohen Metallizitäten führen. Alternativ können sie durch das Verschmelzen von Kugelsternhaufen entstehen. Da Kugelsternhaufen alte Sterne mit oft geringen Metallizitäten enthalten, kann so ein alter, metallarmer Kernsternhaufen entstehen.

Die Datenlage zeigt, dass beide Wege vorkommen und auch Mischszenarien wurden postuliert. Allerdings ist weder die relative Gewichtung dieser verschiedenen Mechanismen, noch deren Zusammenhänge mit Galaxieneigenschaften bekannt, denn um die Entstehungsszenarien mit Beobachtungen einzuschränken, müssen alle involvierten Komponenten untersucht werden. Ich benutze integrale Feldspektroskopie mit dem MUSE Instrument um Spektren und schließlich die kinematischen und chemischen Eigenschaften von Kernsternhaufen, Kugelsternhaufen und den Galaxien zu extrahieren und analysieren.

Die Untersuchung der elliptischen Galaxie FCC 47 zeigt, dass deren massereicher, angereicherter und kinematisch entkoppelter Kernsternhaufen aus effizienter Sternentstehung gebildet wurde. Die Untersuchung zweier Zwerggalaxien ergibt ein anderes Resultat: ihre Kernsternhaufen sind deutlich metallärmer als die Galaxien selbst und sind wahrscheinlich durch die Verschmelzung metallarmer Kugelsternhaufen entstanden. Um die Ergebnisse dieser Fallstudien in das Gesamtbild der Galaxienpopulation einzuordnen, analysiere ich die Alter, Metallizitäten und Sternentstehungsgeschichten von Kernsternhaufen im Vergleich zu Kugelsternhaufen und den zentralen Regionen in 25 Galaxien, hauptsächlich im Fornax Galaxienhaufen. Dies zeigt einen klaren Wandel des dominanten Kernsternhaufenentstehungswegs abhängig von der Galaxien- und Kernsternhaufenmasse. Während die Verschmelzung von Kugelsternhaufen die massearmen Kernsternhaufen in Zwerggalaxien hervorbringt, entstehen massereiche Kernsternhaufen in massereichen Galaxien durch Sternentstehung und beide Wege können bei mittleren Massen beitragen. Der Übergang liegt bei Galaxienmassen von $M_{\rm gal} \sim 10^9 M_\odot$ und Kernsternhaufenmassen von $M_{\rm NSC} \sim 10^7 M_\odot$.

Um diesen Trend besser zu verstehen, benutze ich ein semianalytisches Modell, das die Entstehung von Kernsternhaufen durch die dynamische Entwicklung einer Kugelsternhaufenpopulation beschreibt. In diesem Modell hängt die Kernsternhaufenmasse von der verfügbaren Masse in Sternhaufen ab und es zeigt sich ein ähnlicher Trend: massearme Kernsternhaufen können aus Kugelsternhaufen entstehen, aber um massereiche Kernsternhaufen zu bilden, muss zusätzliche Sternentstehung stattfinden, da sonst Massen von $M_{\rm NSC} > 10^7 M_\odot$ nicht erreicht werden können.

Zusammenfassend gesagt, untersuche ich die Entstehung von Kernsternhaufen in einzelnen Galaxien und finde klare Anzeichen für einen Wandel des Entstehungswegs abhängig von Galaxieneigenschaften. Diese Resultate sind elementar um Kernsternhaufen als einzigartige Zeitzeugen der Galaxienentwicklung zu verstehen und können als Ausgangspunkt für zukünftige Studien in anderen Galaxientypen und Umgebungen genutzt werden.

Contents

Acronyms

M/L	mass-to-light ratio.
ΛCDM	Λ Cold Dark Matter.
GMM	Gaussian mixture modelling.
pPXF	penalised pixel-fitting.
ACS	Advanced Camera for Surveys.
ACSFCS	ACS Fornax Cluster Survey.
ACSVCS	ACS Virgo Cluster Survey.
AO	adaptive optics.
BCDs	blue compact dwarf galaxies.
CCDs	charge-coupled devices.
CMB	cosmic microwave background.
CMDs	colour-magnitude diagrams.
CZR	colour-metallicity relation.
dEs	dwarf ellipticals.
dIrrs	dwarf irregulars.
DM	dark matter.
dSphs	dwarf spheroidal galaxies.
ELT	Extremely Large Telescope.
ESO	European Southern Observatory.
ETGs	early-type galaxies.
F3D	Fornax 3D Survey.
FDS	Fornax Deep Survey.
FOV	field-of-view.
FWHM	full width at half maximum.
GALACSI	Ground Atmospheric Layer Adaptive Corrector for Spectroscopic Imaging.
GCS	globular cluster system.
GCs	Globular clusters.
HST	*Hubble Space Telescope*.
IFS	integral-field spectroscopy.
IMBHs	intermediate mass black holes.
IMF	initial mass function.

JWST	*James Webb Space Telescope*.
KDC	kinematically decoupled component.
LISA	Laser Interferometer Space Antenna.
LOS	line-of-sight.
LOSVD	line-of-sight velocity distribution.
LSST	Legacy Survey of Space and Time.
LTGs	late-type galaxies.
MC	Monte Carlo.
MCMC	Markov-Chain Monte Carlo.
MDF	metallicity distribution function.
MGE	Multi Gaussian Expansion.
MUSE	Multi Unit Spectroscopic Explorer.
MW	Milky Way.
MZR	mass-metallicity relation.
NFW	Navarro-Frenk-White.
NGFS	Next Generation Fornax Survey.
NGVS	Next Generation Virgo Survey.
NSCs	Nuclear star clusters.
PSF	point spread function.
S/N	signal-to-noise ratio.
SFHs	star formation histories.
SINFONI	Spectrograph for INtegral Field Observations in the Near Infrared.
SMBHs	supermassive black holes.
SSPs	single stellar populations.
UCDs	ultra compact dwarf galaxies.
UDGs	ultra diffuse galaxies.
VLT	Very Large Telescope.
VST	VLT Survey Telescope.
YMCs	young massive star clusters.
ZAP	Zurich Atmosphere Purge.

List of Figures

List of Tables

In the beginning there was nothing,
which exploded.

Terry Pratchett, Lords and Ladies

1 | Introduction

From the beginning of humankind, we have looked into the night sky in the hope of understanding the Universe and our place within it. Astronomy is one of the oldest of the natural sciences, with the earliest records dating back thousands of years. For centuries, astronomy was closely intertwined with mythology and religion, but the development of the telescope in the 17th century and the following paradigm shift in the Copernican Revolution has changed our worldview drastically and has paved the way for modern astronomy. The next major leaps in observational astronomy then came with the development of photography and spectroscopy in the 19th century, but it took until the early 20th century before the existence of other galaxies outside our own Galaxy was established. Now, a century later, our understanding of the nature and properties of galaxies has much improved thanks to the emergence of ever better telescopes and instruments.

Today, we understand galaxies as the fundamental building blocks that constitute the large-scale structure of the Universe. In the simplest terms, galaxies are a collection of stars, gas, dust, and dark matter held together by gravity. A closer look, however, unveils a multitude of different shapes, colours, and morphologies in the galaxy population and individual galaxies show a diverse range of substructure and stellar components.

A look into the night sky already reveals several of these components of our own Galaxy to the naked eye. The morphology of the Milky Way (MW) is dominated by its disk spanning the whole sky like a bright band of stars (or spilled milk). Apart from the disk, individual stars are visible as well as star clusters – spherical collections of gravitationally bound stars. One of the most prominent star cluster observable from the Northern Hemisphere is M 54, the Pleiades, an open star cluster containing a few thousands of stars. Globular clusters (GCs) such as ωCentauri or 47 Tucanae, which are both visible from the Southern Hemisphere, are much more extreme star clusters with hundreds of thousands to millions of member stars tightly packed together. However, the most massive star cluster in our Galaxy is found right at the Galactic Centre: the nuclear star cluster.

Nuclear star clusters (NSCs) are the densest stellar systems in the Universe and are found at the centres of most galaxies. Sitting at the bottom of the galactic gravitational potential well, NSCs experience a variety of different astrophysical processes that shape the nuclei of galaxies, from central star bursts to interactions with black holes. Hence, their formation and evolution is closely linked to the evolution of their host galaxy. Because NSCs retain the information of their evolutionary history imprinted in their stellar populations, they provide an unique window into the formation and growth of galactic nuclei.

In this thesis, I present a study of galaxies and their massive star clusters with the aim of

Figure 1.1.: Illustration of different galaxy types. *Left*: the early-type galaxy M 87, the central galaxy of the Virgo galaxy cluster (c: NASA/ESA). *Middle*: The late-type galaxy M 101 (c: NASA/ESA). *Right*: Fornax dwarf spheroidal, a nearby dwarf galaxy (c: ESO/Digitized Sky Survey 2).

constraining the formation and growth of NSCs. Using integral-field spectroscopy (IFS) with the Multi Unit Spectroscopic Explorer (MUSE) instrument at the Very Large Telescope (VLT) of the European Southern Observatory (ESO), I explore the processes that form and shape galactic stellar nuclei and investigate the connection to GCs and the host galaxies.

1.1 Galaxies

Galaxies can be loosely described as gravitationally bound systems of stars, gas, and dust that reside in the centres of dark matter (DM) haloes. Galaxies range in size from dwarf galaxies containing only a few thousand stars (e.g. Segue 1, Belokurov et al. 2007) to giants consisting of trillions of stars and they surely are some of the most spectacular objects in our Universe (Fig. 1.1). In 1926, Edwin Hubble established the first galaxy classification scheme that divides the galaxy population into broad categories based on their apparent morphology (Hubble 1926): elliptical galaxies, lenticulars, and spiral galaxies. Ellipticals are galaxies that have ceased star formation globally (see left panel in Fig. 1.1). Together with lenticular galaxies (S0 - galaxies), they are classified as early-type galaxies (ETGs) and are characterised by red colours and old stellar ages. Spiral galaxies (middle panel in Fig. 1.1) like our MW have disk-like morphologies, spiral arms, and on-going star formation and are often referred to as late-type galaxies (LTGs). Outside of this classification scheme are low-mass dwarf galaxies (right panel in Fig. 1.1), that often have irregular morphologies.

1.1.1 Measuring galaxy properties

Our knowledge of galaxies has evolved together with the technological advances made in the instrumentation that is used to study them. The earliest studies of galaxies and their morphologies were made with photographic plates and have focused on measuring global structural properties by describing galaxy light distributions. For many years, the light profiles of ETGs were thought to be best described with a brightness profile $I(R)$ that decreases $\propto R^{1/4}$ (de Vaucouleurs 1948). Later, a more generalised parametrisation was

introduced in form of the Sérsic profile (Sérsic 1968):

$$I(R) = I_{\rm eff} \exp\left\{-b(n)\left[\left(\frac{R}{R_{\rm eff}}\right)^{1/n} - 1\right]\right\}, \tag{1.1}$$

where $b(n) \approx 2n - 0.327$. $R_{\rm eff}$ is the effective radius that describes the radius of a circle enclosing half of the total galaxy luminosity and $I_{\rm eff}$ is the surface brightness at this radius. The Sérsic index n describes the galaxy concentration and increases with galaxy luminosity or mass (e.g. Kormendy et al. 2009). Setting $n = 4$ gives the de Vaucouleurs profile and $n = 1$ is equal to an exponential profile that gives a good approximation of the light profile of LTGs. Therefore, the Sérsic index can be used as a proxy for the galaxy type and such parametric fitting has long proved to be a powerful technique to quantify galaxies and their structure (Freeman 1970; Kormendy 1977).

With the advent of charge-coupled devices (CCDs), it became possible to go beyond the analysis of one-dimensional surface brightness profiles. Instead, the two-dimensional light distribution could be studied, often by analysing the isophotal shapes to detect deviations from elliptical shapes[1] (e.g. Franx et al. 1989; Peletier et al. 1990). Later, parametric image fitting tools were developed that enabled an accurate decomposition of the 2D light distribution into physical components (e.g. GALFIT; Peng et al. 2002, 2010, IMFIT; Erwin 2015). Such techniques now allow us to dissect galaxies into their sub-components and are commonly used to, for example, study the abundance and properties of galaxy bulges in LTGs (Gao & Ho 2017).

The advances in our understanding of galaxies did not only come from the development of more sensitive cameras, but was always accompanied by spectroscopy. In the 1950s, spectroscopic observations of ionised gas in external LTGs yielded the first measurements of rotation curves (rotational velocity versus galactocentric distance, e.g. Burbidge et al. 1959). The subsequent discovery of flat rotation curves at large radii brought up the need for a dark component in addition to the visible component to explain the motion of stars in the gravitational potential of a galaxy (Rubin & Ford 1970; Rubin et al. 1980), and today DM is one of the fundamental pillars in the paradigm of how galaxies form and evolve (White & Rees 1978; Blumenthal et al. 1984).

In the 1970s, spectrographs became sensitive enough to not only detect bright ionised gas lines, but also stellar absorption spectra. Long-slit spectroscopy was used, for example, to measure stellar rotation in gas-free ETGs. This revealed that less massive ETGs and galaxy bulges - central spheroidal components of LTGs - rotate faster than massive ETGs (Binney 1978; Kormendy & Illingworth 1982; Davies & Illingworth 1983).

Around the same time, the first large surveys were introduced that obtained photometric or spectroscopic measurements of a large number of galaxies, for example the CfA Redshift Survey, that collected radial velocities for 2400 galaxies (Huchra et al. 1983). Such projects and their contemporary counterparts like the Great Observatories Origins Deep Survey (GOODS, Giavalisco et al. 2004) or the Sloan Digital Sky Survey (SDSS) give the opportunity to trace the galaxy population and its evolution back in time by studying galaxies at different

[1] Isophotes are lines of equal surface brightness.

redshifts[2] (see the review by Conselice 2014).

The most recent major technological advancement in how we can study galaxies was made with the development of IFS. IFS combines photometry with spectroscopy by providing a low to mid-resolution spectrum for each spatial pixel and hence allows to build maps of kinematics and stellar population properties by fitting the stellar absorption lines (see e.g. Sect. 2.4 or Bittner et al. 2019). IFS has revolutionised our understanding of the complexity that can be found in galaxies and has shown that galaxy classification solely based on morphology is incomplete. Today, more and more effort is put into quantifying galaxies based on their kinematic and stellar population structure (e.g. Cappellari 2016), but the categorisation of galaxies into ETGs, LTGs, and dwarf galaxies is still widely used.

1.1.2 Early-type galaxies

ETGs have approximately spheroidal shapes, a smooth distribution of stars, and lack spiral arms. In optical colours, ETGs appear usually red as a consequence of their old stellar populations that are dominated by low-mass stars with low surface temperatures. In the 1970s, the first long-slit spectroscopic studies of ETGs have shown that ETGs can rotate and since then IFS has greatly advanced our understanding of their kinematic structure. With respect to previous IFS prototypes, the SAURON IFS instrument (Bacon et al. 2001) dramatically improved the data quality and hence the applicability of IFS for galaxy studies. The SAURON survey (de Zeeuw et al. 2002) was the first project that provided two-dimensional maps of kinematics, ionised gas, and stellar populations of 48 ETGs. In combination with later surveys such as the ATLAS3D project (Cappellari et al. 2011) or CALIFA (Husemann et al. 2013), it was soon established that ETGs can show a plethora of internal kinematic structures including rotating disks, decoupled components, misaligned disks, and counter-rotating populations (McDermid et al. 2006; Krajnović et al. 2011; Cappellari 2016; Zhu et al. 2018a).

At the same time, IFS has shown that ETGs can show various features in their stellar populations. ETGs exhibit radial age and metallicity gradients and typically the mean stellar ages and metallicities increase towards the centres of galaxies (Koleva et al. 2011; Zhuang et al. 2019; Santucci et al. 2020). Often, kinematic and morphological substructures are reflected in components with different stellar populations, for example in the form of metallicity-enhanced disks (McDermid et al. 2015). Besides population differences within individual galaxies, stellar population analysis of large galaxy samples has revealed the mass-metallicity relation (MZR), a relation that connects the stellar mass of a galaxy to its mean metallicity (Gallazzi et al. 2005; Bellstedt et al. 2021): more massive galaxies are more metal-rich due to more efficient self-enrichment (Gallazzi et al. 2005; Kirby et al. 2013). Additionally, massive ETGs appear to have shorter durations of star formation and are older than low-mass objects (Gallazzi et al. 2005; McDermid et al. 2015).

[2]The redshift z is defined as: $z = \frac{\lambda_{\rm obs} - \lambda_0}{\lambda_0}$, where $\lambda_{\rm obs}$ is the observed wavelength of a spectral line and λ_0 is the rest-frame wavelength of the same line as measured in a laboratory on Earth. In an expanding Universe with a finite speed of light the redshift gives an estimate of distance and look-back time.

1.1.3 Late-type galaxies

LTGs are classified based on their morphologies that show stellar disks and often spiral arms. The middle panel in Fig. 1.1 shows M 101, a prominent spiral galaxy at 6.4 Mpc distance (Shappee & Stanek 2011). This image already illustrates that LTGs generally show much more substructure than ETGs, even beyond the presence of spiral arms: LTGs can have bars and various types of bulges in their centre, dust lanes tracing the star formation in the spiral arms, or multiple disks with varying thickness.

The presence of ongoing star formation shapes the structure of LTGs, as is evident from clumpy spiral arms, knots of star formation, and bright central star bursts. Often, the structure in young stellar populations and star forming associations is traced by molecular gas out of which new stars form (e.g. Lee et al. 2021) as well as by dust which is created as a byproduct of massive star formation (e.g. Leśniewska & Michałowski 2019).

From a dynamical viewpoint, LTGs are more rotation-supported than ETGs. Disks are dynamically cold systems[3], but their inner regions can be pressure-supported (Zhu et al. 2018b). The different kinematics are also reflected in different stellar populations. The disks of LTGs are typically characterised by young stellar populations whose light is dominated by hot massive stars giving rise to blue colours, while the central regions can be significantly older (e.g. Parikh et al. 2021).

Surely the most commonly known LTG is our own Galaxy, the MW. The MW has a stellar mass of $M_{\rm gal} \sim 6 \times 10^{10} M_{\odot}$ and a total mass of $M_{\rm dyn} \sim 10^{12} M_{\odot}$ (see the review by Bland-Hawthorn & Gerhard 2016 and references therein). It is a spiral galaxy with a bar, a central boxy/peanut shaped bulge[4], a spheroidal stellar halo, and a stellar disk composed of a young thin and an older thick disk (Bland-Hawthorn & Gerhard 2016). Our Galaxy hosts around 150 GCs (Harris 1996) in with masses between $10^4 - 10^6 M_{\odot}$, but the most massive star cluster, the MW NSC, sits at at the Galactic Centre with a mass of $\sim 3 \times 10^7 M_{\odot}$ (Schödel et al. 2014; Feldmeier et al. 2014; Feldmeier-Krause et al. 2017b).

1.1.4 Dwarf galaxies

Dwarf galaxies are the most abundant galaxy type in the Universe. They are loosely categorised as galaxies with a luminosity much lower than that of the MW, but the exact luminosity or mass threshold is not uniformly defined. Typically, dwarf galaxies have masses $M_{\rm gal} < 10^9 M_{\odot}$ and the faintest known galaxies reach masses down to $M_{\rm gal} < 10^5 M_{\odot}$ (Simon 2019). Different classification criteria exist and the earliest distinctions between dwarf and massive galaxies have been made based on their morphology and surface brightness (Sandage & Binggeli 1984). More recent distinctions are based on their internal kinematics and classify them as low-dispersion objects without strong rotational support (Lelli et al. 2014; Ivkovich & McCall 2019).

Typically, dwarf galaxies are categorised based on their gas content: gas-rich dwarfs can be dwarf irregulars (dIrrs) or blue compact dwarf galaxies (BCDs). Both galaxy types exhibit

[3]So-called dynamically cold systems are rotation-supported, whereas hot systems are supported by random motions rather than circular rotation.

[4]The peanut-shaped bulge might be actually part of the bar, e.g. Fragkoudi et al. (2017).

ongoing star formation, but while BCDs show strong, short-lived star bursts (Thornley et al. 2000), dIrrs exhibit prolonged star formation at low rates (McQuinn et al. 2010). Gas-poor dwarf galaxies fall into two groups as well: dwarf spheroidal galaxies (dSphs) and dwarf ellipticals (dEs). dSphs comprise the lowest-mass galaxies in the Universe, and due to their low luminosities, they were originally only identified in the Local Group. The right panel in Fig. 1.1 shows the Fornax dSph, one of the earliest discovered dwarf galaxies (Shapley 1938). dEs were first found in galaxy clusters and were thought to be a class of more massive dwarf galaxies substantially different from the local dwarfs due to selection effects (Sandage & Binggeli 1984; Grebel 2001). However, more recent studies suggest a continuous transition between dSphs and dEs (Forbes et al. 2011; Lieder et al. 2012), but the established nomenclature remains and commonly dSphs refer to dwarfs in the Local Group and low-density environments and dEs to dwarfs in cluster environments (Ivkovich & McCall 2019).

In the 2000s, another possible type of dwarf galaxies was discovered in galaxy clusters: ultra compact dwarf galaxies (UCDs), compact objects that exceed the sizes and masses of typical GCs (Minniti et al. 1998; Hilker et al. 1999b; Drinkwater et al. 2000). It was speculated that those might be dwarf galaxies, but as discussed in Sect. 1.4.4, UCDs are likely star clusters - either the high-mass end of the GC population or remnant NSCs of disrupted galaxies. On the other end of the density spectrum, ultra diffuse galaxies (UDGs) are found. These galaxies have sizes similar to massive galaxies, but very low masses ($M_{\rm gal} \sim 10^7 M_\odot$, van Dokkum et al. 2015) and are thus difficult to detect. They have recently captured the attention of cosmologists and astronomers alike because some UDGs appear to be lacking DM (van Dokkum et al. 2018, 2019), which is challenging expectations from the standard cosmological model.

1.1.5 Galaxy clusters

Most galaxies are not isolated but are part of larger associations of galaxies and DM bound by gravity. Our MW is part of the Local Group that also contains the Andromeda galaxy (M 31), the Triangulum Galaxy (M 33) as well as at least 80 dwarf galaxies (McConnachie 2012). The Local Group has a diameter of around 3 Mpc and a total mass (including DM) of $M_{\rm dyn} \sim 2 \times 10^{12} M_\odot$ (Karachentsev & Kashibadze 2006; Peñarrubia et al. 2014). While galaxy groups contain from only a few up to a few hundred massive galaxies, galaxy clusters are the largest structures in the Universe and can have thousands of member galaxies – but the distinction between groups and clusters is ill-defined (Tully 2015). The total mass of galaxy groups and clusters ranges from 10^{11} to $10^{15} M_\odot$ for the most massive clusters like the Coma galaxy cluster (Kubo et al. 2007).

The two closest galaxy clusters are the Virgo ($D \sim 16.5$ Mpc, Mei et al. 2007) and Fornax galaxy clusters ($D \sim 20$ Mpc, Blakeslee et al. 2009, shown in Fig. 1.2). Virgo contains ~ 1300 confirmed massive members (Kim et al. 2013) and has a total mass of $\sim 1 \times 10^{15} M_\odot$ (Fouqué et al. 2001). In contrast, the main cluster of Fornax consists of a few hundred galaxies (Ferguson 1989), has a total mass of $\sim 7 \times 10^{14} M_\odot$ (Nasonova et al. 2011), and a

virial radius[5] of 2.2° (∼ 0.7 Mpc, Drinkwater et al. 2001). Besides the main cluster that is located around the central galaxy NGC 1399 (FCC 213), Fornax also contains the NGC 1316 group that is infalling into the main cluster (Drinkwater et al. 2001).

Both the Virgo and Fornax galaxy clusters are well-studied environments with many projects and surveys analysing individual galaxies or the clusters as a whole. In the context of this thesis, studies with the *Hubble Space Telescope* (HST) Advanced Camera for Surveys (ACS) in the framework of the ACS Virgo Cluster Survey (ACSVCS) and the ACS Fornax Cluster Survey (ACSFCS), are among the most influential (Côté et al. 2004; Jordán et al. 2007). Those surveys targeted the massive ETGs in these two galaxy clusters, studied their overall structures, and established a distance scale (Blakeslee et al. 2009). Furthermore, extensive photometric GC catalogues were assembled with accurate photometry in the HST ACS F475W filters (∼ g band) and F850LP filters (∼ z band) as presented in Jordán et al. (2009) and Jordán et al. (2015). The nucleated ETGs in Virgo and Fornax have been studied in the ACSVCS (Côté et al. 2006) and ACSFCS (Turner et al. 2012), respectively. These works provide photometry of the NSCs including their magnitudes in the g and z band as well as their effective radii.

Figure 1.2.: Image of the central region of the Fornax galaxy cluster (c: ESO). The central galaxy NGC 1399 is on the left-hand side.

Virgo and Fornax have also been studied photometrically with the Next Generation Virgo Survey (NGVS) and Next Generation Fornax Survey (NGFS), respectively, using multi-band photometry from the Canada French Hawaii Telescope (for Virgo) and the Dark Energy Camera at the Cerro Tololo Interamerican Observatory (for Fornax). These two projects explored the dwarf galaxy population in these galaxy clusters (see Ferrarese et al. 2012 for Virgo, Muñoz et al. 2015; Eigenthaler et al. 2018 for Fornax) and the nucleated galaxies in Virgo were analysed by Sánchez-Janssen et al. (2019) and by Ordenes-Briceño et al. (2018) in Fornax.

Another influential photometric survey of the Fornax cluster is the Fornax Deep Survey (FDS), a multi-band survey with the VLT Survey Telescope (VST) that maps most of the area inside the virial radius (Iodice et al. 2016). Fig. 1.2 shows a colour image of the Fornax cluster from the FDS. Venhola et al. (2020) presented an analysis of the dwarf galaxies and a large catalogue of GC candidates was collected by Cantiello et al. (2020). As will be described in more detail in Chapt. 4 and 5, many galaxies analysed in this work were observed with the MUSE instrument (Bacon et al. 2010) as part of the Fornax 3D Survey

[5]The virial radius is the radius of a gravitationally bound system within which the virial theorem applies. The virial theorem relates the time average of the kinetic energy with that of the potential energy of the system. A virialised galaxy cluster has reached equilibrium between expansion and gravitational collapse.

(F3D), a magnitude-limited survey of 32 galaxies inside the virial radius of Fornax that was created to complement the FDS project with IFS (Sarzi et al. 2018).

1.1.6 Formation and evolution of galaxies

In the standard cosmological model - the spatially flat Λ Cold Dark Matter (ΛCDM) model with cosmological constant Λ - the Universe started with the Big Bang and expanded afterwards. In the beginning, the Universe was a hot, dense plasma of photons and matter that expanded and slowly cooled. Eventually the Universe reached densities and temperatures that allowed electrons and baryons to stably combine for the first time to build atoms, mostly in the form of neutral hydrogen. At this time (ca. 350'000 years after the Big Bang), photons decoupled from the baryons and since then freely propagate as the cosmic microwave background (CMB) that has the density fluctuations of this last scattering surface imprinted. Tight constraints on the parameters of the ΛCDM model have been placed by measurements of the anisotropies, temperature fluctuations, and angular correlations in the CMB, most recently by the Planck satellite (Planck Collaboration et al. 2014). According to these measurements, the Universe is ~ 13.8 Gyr old, and it is composed of dark energy ($\Omega_\Lambda \sim 0.7$), DM ($\Omega_{\rm DM} \sim 0.25$), and baryons ($\Omega_b \sim 0.05$). Here, $\Omega_{\rm X}$ refers to the present day density parameter of the different species.

In the ΛCDM framework, the first structures assembled from the gravitational collapse of primordial overdensities. At a redshift of $z \sim 10 - 30$, the first DM haloes formed in which baryons settled and ultimately formed stars in the first galaxies (e.g. Glover 2005; Greif 2015; Schauer et al. 2020). Ultra-violet radiation from these stars re-ionised the Universe at a redshift $z \sim 6 - 10$, marking the epoch of reionisation (see the review by Wise 2019). Meanwhile, structures continued to grow and merged under the influence of gravity to form the large-scale structure of the Universe, often called the cosmic web (left panel in Fig. 1.3): filaments of galaxies and DM connect nodes consisting of the most massive galaxy clusters. These filaments are separated by large voids in which the density of galaxies is very low (Lindner et al. 1995). Extensive surveys of large fractions of the sky were able to map this cosmic web (Colless et al. 2003; Abazajian et al. 2003) and found that its properties are in agreement with the results of cosmological DM-only simulations like the Millenium simulation (Fig. 1.3, Springel et al. 2005), marking one of the big successes of the ΛCDM model.

Embedded in the ΛCDM cosmological model is the hierarchical scheme of galaxy formation and evolution. Based on results from cosmological simulations that incorporate gas dissipation and baryonic physics in addition to DM, a two-phase formation scheme has been established (e.g. Oser et al. 2010; Pillepich et al. 2014): in the first phase, stars form in-situ in the parent galaxy from gas that has settled in a DM halo. Then, in the second phase, the galaxy grows its mass through mergers and accretion of satellite galaxies. Simulations indicate that the fraction of stars born outside of the original progenitor, the ex-situ fraction, is a strong function of galaxy mass and formation history. At $M_{\rm gal} \sim 10^9 M_\odot$, ex-situ mass fractions are low, whereas 90 % of the stellar mass in the most massive galaxies ($M_{\rm gal} > 10^{11} M_\odot$, i.e. central galaxies of galaxy clusters) is expected to have originated in accreted galaxies (Oser et al. 2010; Pillepich et al. 2018; Davison et al. 2020).

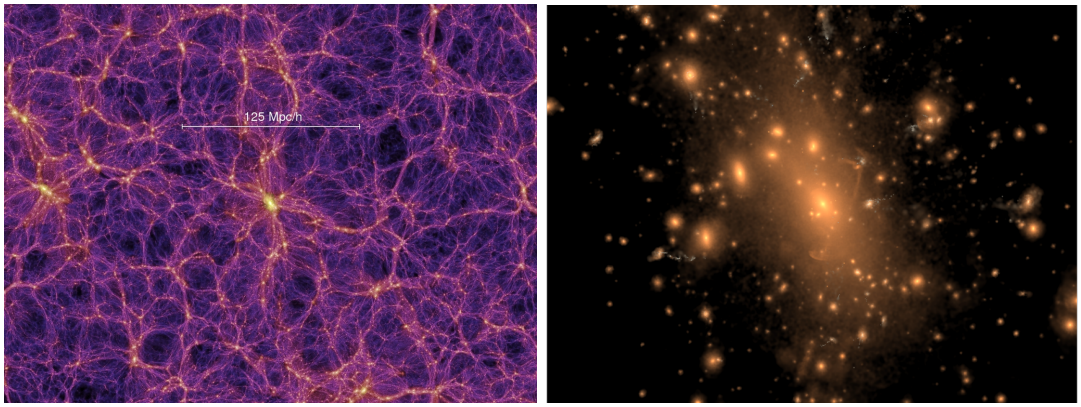

Figure 1.3.: Cosmological simulations. *Left*: Large scale DM distribution (cosmic web) from the Millenium simulation (Springel et al. 2005). *Right*: Stellar light distribution of a simulated galaxy cluster from the Illustris simulation (Vogelsberger et al. 2014).

Observations of our own Galaxy support the growth of galaxies via accretion and mergers. For example, the Sagittarius dSph is currently being disrupted by the MW as evident from the long stellar stream that traces its past orbit around our Galaxy (Ibata et al. 1997; Law & Majewski 2010). Growing number of streams were discovered in the last years due to Gaia astrometry and many could be connected to one or several GCs as independent tracers of accretion (Ibata et al. 2019). In distant galaxies, the identification of streams is challenging due to their low surface brightness. However, in some external galaxies shell-like structures were identified with deep photometry that are evidence of recent merger activity (Malin & Carter 1983; Sikkema et al. 2007).

Nonetheless, for external galaxies, the most convincing evidence for mergers shaping galaxies comes from the observations of currently interacting systems that often show disturbed morphologies and kinematics. One example of such a system are the Antennae galaxies, a pair of interacting galaxies with strong star formation. Interacting galaxies are rare in the local Universe, but it is assumed that they represent a significant portion of the galaxy population at high redshift (e.g. Schreiber et al. 2015). Due to their strong star formation, interacting galaxies are particular relevant to study the formation of star clusters as they harbour young massive star clusters which might resemble the progenitors of the ancient GCs (e.g. Adamo et al. 2020 and see Sect. 1.2.3).

1.2 Globular clusters

Star clusters are gravitationally bound systems of stars that are ubiquitous in galaxies. They come in various shapes and can range from low-mass, sparse open clusters that contain a few thousand young stars to massive star clusters that populate the full radial extent of galaxies from the very centre (nuclear star clusters) out into the far halo regions (globular clusters).

1.2.1 Globular cluster properties

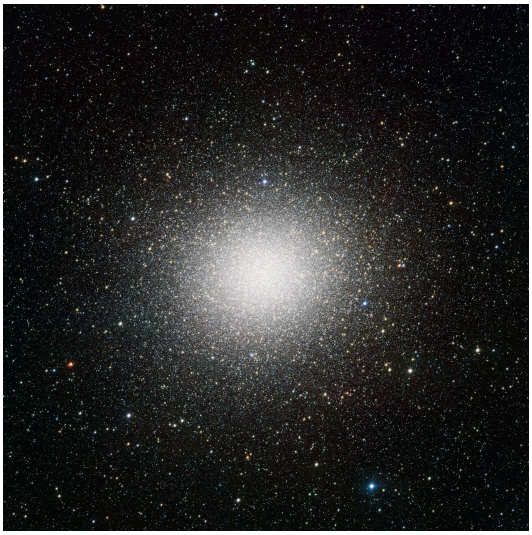

Figure 1.4.: VST image of ωCentauri, the most massive GC of the MW (c: ESO/INAF).

Globular clusters are massive star clusters with masses between 10^4 and $10^7\,M_\odot$ and effective radii of a few parsecs (e.g. Jordán et al. 2007; Masters et al. 2010), and hence GCs are extremely dense stellar systems that can be observed in distant galaxies (see reviews by Brodie & Strader 2006; Forbes et al. 2018). While most dwarf galaxies only have a handful of GCs (Forbes et al. 2018), the MW has around $\sim$ 150 GCs (Harris 1996), and the most massive galaxies in the Universe can have more than 10000 GCs (Côté et al. 2006; Peng et al. 2008).

In the MW, deep photometry of GCs with high spatial resolution can be used to analyse individual stars, as seen in Fig. 1.4 that shows an image of ωCentauri, the most massive GC in our Galaxy. Such resolved studies are currently only possible in the MW and its satellites. Here, deep colour-magnitude diagrams (CMDs) that plot the colour[6] versus magnitude (or luminosity) of individual stars are used to accurately infer the ages and metallicities of stars in a GC via isochrone fitting. This technique is based on the fact that a population of stars freshly born out of a gas cloud will initially follow a narrow sequence in the CMD where more massive stars are hotter (hence bluer) and brighter. As time passes, the position of stars on the CMD changes since massive stars evolve quickly to more advanced phases of their evolution as predicted by stellar evolution models.

This is illustrated in Fig. 1.5 which displays CMDs of three star clusters of different ages using Gaia photometry[7] together with theoretical isochrone tracks of stellar populations that are characterised by different stellar ages and metallicities[8]. In the Pleiades open cluster (age $\sim$ 100 Myr), almost all stars are still on the so-called main sequence and are burning hydrogen in their core. These stars fall on a narrow line in the CMD, in which more massive stars are brighter and bluer. In contrast, the open cluster M 67 with an age of $\sim$ 3 Gyr, contains evolved stars that have moved from the main sequence towards redder colours as a consequence of their evolution from hydrogen core burning to helium burning. This creates a turn-off point in the CMD. As more massive stars exhaust their central hydrogen more quickly, they evolve faster and hence this turn-off moves to fainter stars as time passes. This can be seen in the CMD of 47 Tuc, an ancient GC. In this GC, only dwarf stars are still burning hydrogen in their core. However, not only the age of a stellar population determines

[6]The colour of an astronomical source is defined as the flux difference in two different photometric bands, for example $V - I$ or $g - z$.
[7]obtained from the Gaia archive (`https://gea.esac.esa.int/archive/`).
[8]PARSEC tracks from Bressan et al. (2012) (`http://stev.oapd.inaf.it/cgi-bin/cmd`).

the position of stars on a CMD, but also the metallicity as the bottom right panel in Fig. 1.5 shows. The metals in the atmospheres of more enriched stars absorb light at blue wavelengths and thus metal-rich stellar populations appear redder than metal-poor ones at the same age. In addition, the details of stellar evolution change with metallicity (e.g. Mapelli & Bressan 2013; Ramachandran et al. 2019).

In early studies, GCs have been regarded as prototypical single stellar populations (SSPs). Their CMDs match well with the expectations of a population of stars that all share the same age and metallicity. Deep photometric observations of MW GCs with HST and spectroscopy of individual stars have changed this picture and have shown that many GCs show multiple populations of stars that differ in their chemical composition (see the review by Bastian & Lardo 2018). However, with regard to the extragalactic systems that are considered in this thesis, the assumption that GCs can be described by a single age and metallicity is still valid because the typical spreads in ages and metallicities are much smaller (< 1 Gyr and < 0.05 dex, respectively, Tailo et al. 2016; Bastian & Lardo 2018) than what can be currently recovered with integrated-light spectroscopy of extragalactic GCs (e.g. Usher et al. 2019; Asa'd & Goudfrooij 2020; Asa'd et al. 2021).

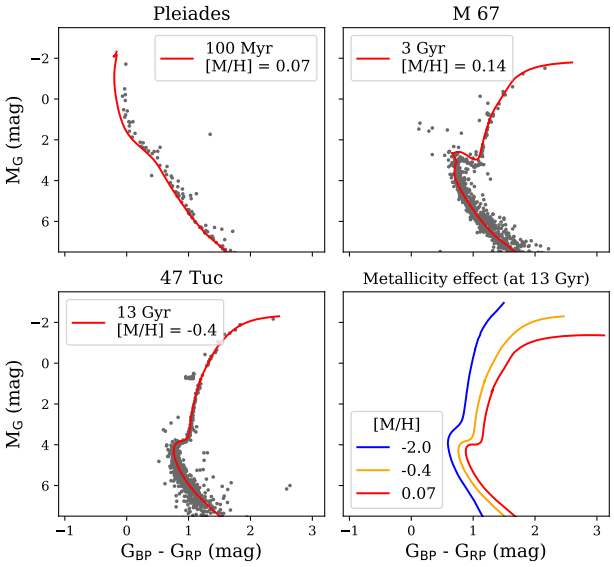

Figure 1.5.: CMDs of three star clusters (the young open clusters Pleiades and M67 as well as the GC 47 Tuc) with theoretical PARSEC isochrones (Bressan et al. 2012) using Gaia photometry. The data was obtained from the Gaia archive.

One of the main characteristics of GCs that has been established with studies of MW GCs are their extremely old stellar ages > 12 Gyr (Marín-Franch et al. 2009; Forbes & Bridges 2010; VandenBerg et al. 2013; Leaman et al. 2013). GCs are among the oldest structures in the Universe, formed at redshifts $z \gtrsim 2$. For extragalactic systems, age uncertainties are significantly larger, but also extragalactic GCs have been found to be extremely old with ages above 10 Gyr (e.g. Puzia et al. 2005; Strader et al. 2006; Usher et al. 2019). Their old ages make GCs potentially powerful fossil records of galaxy evolution because we can assume that they still retain information of their birthplace encapsulated in the stars observed today.

1.2.2 Globular clusters as tracers of galaxy evolution

In the hierarchical scheme of galaxy formation, galaxies grow from mergers and interactions. To understand galaxy evolution observationally, it is crucial to reconstruct mass assembly history of individual galaxies. In the MW, individual merger events were recently discovered thanks to Gaia. The Gaia mission (Gaia Collaboration et al. 2016) provides six-dimensional information (3D positions and velocities) for a billion MW stars and enables identification of

coherent structures in the orbital distribution that can be traced back to past mergers (Helmi et al. 2018; Kruijssen et al. 2019a, 2020). Similar studies are unfortunately not possible beyond the Local Group with current telescopes as only line-of-sight (LOS) velocities and global distance measurements can be accessed. However, in distant galaxies, bright point-source tracers like GCs are regarded as tracers of galaxy assembly because they preserve the chemical composition of their birthplace in their stellar populations (e.g. Peng et al. 2008; Forbes & Bridges 2010; Forbes et al. 2011; Brodie et al. 2014; Harris et al. 2016; Harris et al. 2017). Additionally, their orbital properties, measured from the LOS velocities of individual GCs in a large globular cluster system (GCS), provide hints as to the assembly history and dynamical evolution of their parent galaxy (Forbes et al. 2017; Watkins et al. 2019).

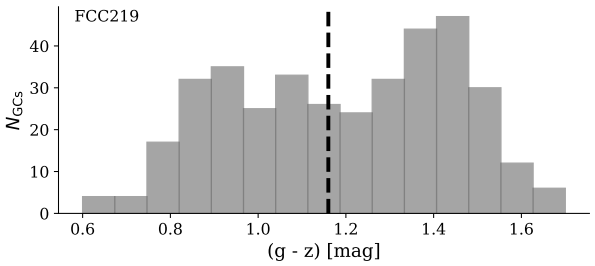

Figure 1.6.: Bimodal GC colour distribution for FCC 219, a massive ETG in the Fornax cluster. The colours refer to the HST ACS F475W (g) and F850LP (z) bands. Data from Jordán et al. (2015). The dashed line shows the traditional division between red and blue GCs at $g - z = 1.16$ mag (e.g. Peng et al. 2008; Liu et al. 2019).

In the last decades, large photometric surveys, for example the ACSVCS and ACSFCS in the Virgo or Fornax galaxy clusters (e.g. Côté et al. 2004; Jordán et al. 2007), have collected extensive photometric catalogues of GC candidates (Peng et al. 2006; Jordán et al. 2009, 2015). Aside from their mass and size (effective radius), GCs are typically classified by their photometric colour (e.g. in the ACS g and z bands) and it has been found that many galaxies have a bimodal GC colour distribution with a red and blue population (e.g. Kundu & Whitmore 2001; Larsen et al. 2001; Peng et al. 2006; Sinnott et al. 2010). Figure 1.6 illustrates this for one galaxy in the Fornax cluster. Under the assumption that these GCs are as old as the ones in the MW, this colour bimodality has been translated into a metallicity bimodality, where the blue GCs are blue not because of younger ages but because they contain less enriched stars than the red GCs (Ashman & Zepf 1992; Côté et al. 1998; Beasley et al. 2002). This colour and metallicity bimodality has been interpreted in the scheme of the two-phase formation of massive galaxies where the metal-rich GCs are assumed to form in-situ in massive haloes or during major mergers in which rapid enrichment leads to their high metallicities. In contrast, the metal-poor GCs are thought to have their origin in metal-poor dwarf galaxies that were later accreted (Kravtsov & Gnedin 2005; Tonini 2013; Li & Gnedin 2014; Katz & Ricotti 2014; Forbes & Remus 2018). Therefore, the metallicity difference between in-situ born and accreted GCs is a direct consequence of the MZR of the galaxies the GCs were born in.

In the MW, several GCs are likely accreted from low-mass dwarf galaxies. There is evidence that at least five GCs were brought in as part of the Sagittarius dSph (Bellazzini et al. 2003; Law & Majewski 2010; Massari et al. 2017), and this number might be as high as $\sim$ 20 accreted GCs (Minniti et al. 2021). Using orbital parameters revealed by Gaia in combination with GC ages and metallicities, several other GCs have now been linked to likely accretion events in the MW's assembly history (Kruijssen et al. 2019b, 2020). These studies are based on results from targeted cosmological simulations that incorporate GC

formation in a self-consistent way and allow to trace back the assembly of simulated MW-like galaxies (Kruijssen et al. 2019a; Pfeffer et al. 2020).

Unveiling the origin of GCs outside the MW is more challenging, but in general photometric and spectroscopic observations of GCSs support the idea of two subpopulations with different origins. Spectroscopic studies of large samples of GCs in individual galaxies have found diverse kinematics for red and blue GC subpopulations. Often, the red GCs seem to follow the kinematics of the stellar spheroid of a galaxy (e.g. Schuberth et al. 2010; Strader et al. 2011; Pota et al. 2013), which is expected for a common formation history of host and red GCS (Shapiro et al. 2010). The blue GC population often has a higher velocity dispersion in agreement with a population that was accreted from galaxies on different orbits (e.g. Lee et al. 2008), but rotation signatures have been found for both the red and blue populations (e.g. Arnold et al. 2011; Foster et al. 2011; Pota et al. 2013).

In context of galaxy assembly, the metallicity distribution function (MDF) of GCs is of particular importance. If GCs trace the metallicity of their birthplace, the diverse merger histories of major galaxies as predicted from cosmological simulations (e.g. Kruijssen et al. 2019a) translate into diverse shapes of the MDF. Consequently, inferring its shape from observations can put constraints on the merger history. In accordance with expectations from bimodal colour distributions, the GC MDF was found to have a bimodal shape with a metal-poor ([Fe/H] ~ -1.5 dex) and a metal-rich component ([Fe/H] ~ -0.5 dex) in many galaxies, for example in the MW (e.g. Harris & Canterna 1979; Zinn 1985), Centaurus A (NGC 5128, Beasley et al. 2008), and the Sombrero galaxy (M104, Alves-Brito et al. 2011). However, in some galaxies such as M31, the bimodality of the GC MDF is debated (e.g. Barmby et al. 2000; Galleti et al. 2009), with recent studies indicating even a trimodal distribution (Caldwell & Romanowsky 2016).

Because a detailed study of extragalactic GC MDFs requires time-expensive spectroscopy of individual GCs, often optical photometric studies of GC systems are used to infer the MDF from bimodal colour distributions. However, this conversion crucially depends on the shape of colour-metallicity relation (CZR) which connects photometric colours to the more physical quantity of metallicity. If it is linear, bimodal colour distributions translate into bimodal MDFs, but both Richtler (2006) and Yoon et al. (2006) suggested that a strongly non-linear CZR can produce bimodal colour distributions from broad unimodal metallicity distributions. Such highly non-linear CZRs can challenge the view of a simple two-phase galaxy formation, but due to the lack of large homogeneous samples of spectroscopic GC metallicities, there is no consensus on the shape of the CZR. Using the few spectroscopic GC metallicities available at that time, Peng et al. (2006) presented a piecewise linear CZR with a breakpoint at $(g - z) \sim 1.0$ mag. A similar description was found by Usher et al. (2012), while Sinnott et al. (2010) and Harris et al. (2017) proposed a CZR described by a quadratic function. More recently, Villaume et al. (2019) presented a linear CZR based on metallicities of 177 GCs of M 87. The different results on the shape of the CZR might be connected to different measurement techniques but could also indicate that the CZR is not universal and depends on the host galaxy or the environment (Usher et al. 2015; Villaume et al. 2019). In Sect. 4.4.4 the derivation of the CZR from the F3D GCs is presented.

1.2.3 Globular cluster formation

The potential of GCs as tracers of galaxy evolution hinges drastically on their formation sites, times, and conditions. The typical accuracy achieved to measure stellar ages is not yet sufficient to establish when exactly GCs formed (Forbes et al. 2018). Due to observational uncertainties, it is unclear whether they formed at redshifts $z \sim 6$ and could have contributed to the epoch of reionisation (e.g. see the cosmological simulation by Ma et al. 2021), or whether they formed later at a redshift $z \sim 2$ coinciding with the peak of the cosmic star formation rate (Madau & Dickinson 2014). Future observations with the *James Webb Space Telescope* (JWST) or ESO's Extremely Large Telescope (ELT) can complement optical studies of MW GCs by covering the infrared wavelength range. This will reduce uncertainties in the age measurements (Forbes et al. 2018), but for now it is debated when GCs formed.

In addition, the formation sites and formation conditions of GCs are still unknown because direct observations of star cluster formation in high redshift galaxies are currently not possible due to the limited spatial resolution of today's telescopes. However, the star cluster population of interacting galaxies in the local Universe might give indications of the formation conditions of GCs. For example, Adamo et al. (2020) presented an HST study of several interacting galaxies and analysed their young massive star clusters (YMCs). YMCs overlap in sizes and masses with GCs and were proposed to be the progenitors of ancient GCs (Zepf et al. 1999). GCs and YMCs are described by different mass (or luminosity) functions. While GCs typically show a peaked mass function with a peak at $\sim 10^5 M_\odot$ (Jordán et al. 2007), YMCs have mass functions that are represented by a power-law with a cut-off mass of $\sim 10^6 - 10^7 M_\odot$ (Adamo et al. 2020). It is yet unclear whether the two mass functions can be reconciled by considering the disruption of low-mass clusters in the tidal field of galaxies (e.g. Renaud et al. 2017; Pfeffer et al. 2018; Adamo et al. 2020).

In modern simulations, GC formation is often considered as a byproduct of strong star formation at high redshift and high gas pressures (Elmegreen 2010; Kruijssen 2015). The required high gas pressures might be reached in interacting galaxies, highlighting the importance of galaxy mergers (Renaud et al. 2017), or in galaxy disks at high redshift (Pfeffer et al. 2018; Ma et al. 2020). An end-to-end description of GC formation is difficult in cosmological simulations due to the different scales and physical processes that are involved (see Ma et al. 2020). However, several cosmological zoom-in simulations have been successful in self-consistent modelling of the formation and evolution of GCs by coupling a theoretical model of GC formation and evolution to cosmological simulations (e.g. the E-MOSAICS project, Pfeffer et al. 2018; Kruijssen et al. 2019a).

1.3 Nuclear star clusters

Nuclear star clusters (NSCs) are massive star clusters and are even more extreme in their properties than GCs. They are the brightest, most massive, densest star clusters in the Universe. These properties allow us to detect them nowadays in galaxies well beyond the Local Group, but due to their compact sizes, studies of NSCs require high spatial resolution to identify them against the bright galaxy centres they live in. With the launch of the HST and the development of efficient CCDs, NSCs could be identified unambiguously as star clusters in both early- and late-type galaxies (e.g. Matthews & Gallagher 1997; Phillips et al. 1996; Carollo et al. 1997; Matthews et al. 1999; Böker et al. 2002). Today, extensive catalogues of NSC properties are available, mainly from photometric studies of nucleated galaxies with the HST, but a number of NSCs have also been studied with spectroscopy to unveil their kinematics and stellar population properties. In the following, their main properties are summarised (see Neumayer et al. 2020 for an extensive review on NSCs).

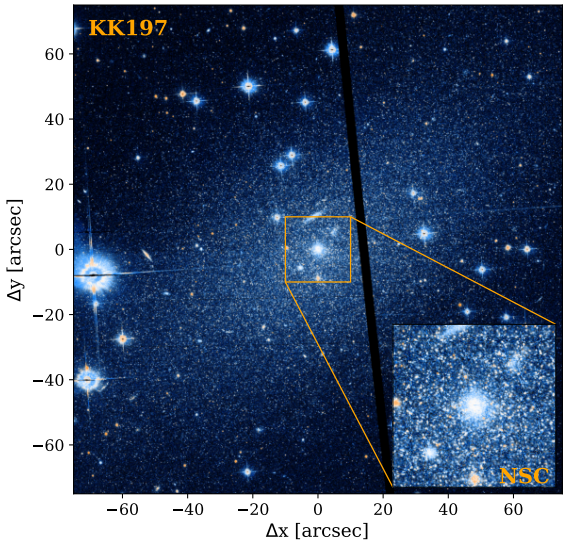

Figure 1.7.: HST colour image of the dwarf galaxy KK197 (see Chapt. 3) from the ACS F814W and F606W filters. The zoom shows the NSC of this galaxy as well as a GC in the lower left corner.

1.3.1 Nuclear star cluster masses and sizes

NSCs are usually identified as compact sources that stand out above the central surface brightness of their host galaxy. Figure 1.7 shows a HST colour image of the dwarf galaxy KK197 at a distance of 4 Mpc. A thorough analysis of this galaxy is presented in Chapt. 3. The inset in the corner of this figure shows a zoom to the central region which is dominated by the NSC. Additionally, a GC is visible in the zoomed region. Both star clusters have similar sizes with $R_{\rm eff} \sim 3$ pc, but the NSC is ten times as massive.

This is but one example of the general trend, as Fig. 1.8 illustrates. This figure shows the masses, sizes, and surface mass densities for NSCs, GCs, and ETGs. NSCs have on average similar sizes as GCs with a median size of $R_{\rm eff} \sim 3$ pc, but the NSC size distribution has an extended tail to sizes > 50 pc (Neumayer et al. 2020). While GCs have masses between 10^4 and $10^6 M_\odot$ (e.g. Jordán et al. 2007; Masters et al. 2010), the NSC mass distribution extends from 10^5 to $10^8 M_\odot$, (Böker et al. 2004; Walcher et al. 2005; Côté et al. 2006; Turner et al. 2012; den Brok et al. 2014; Georgiev et al. 2016; Spengler et al. 2017). Consequently, NSCs can reach extreme surface mass densities of $\sim 10^6 M_\odot {\rm pc}^{-2}$ (or volume densities of $\sim 10^5 M_\odot {\rm pc}^{-3}$), making them the densest stellar systems in the Universe.

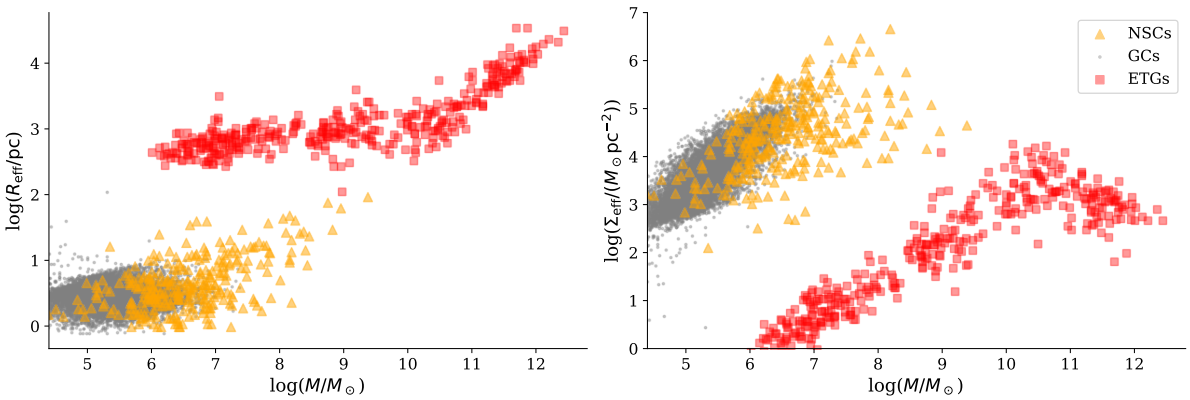

Figure 1.8.: Structural properties of NSCs in comparison to other stellar systems. *Left*: stellar mass versus effective radius, *right*: stellar mass versus surface mass density. NSCs (orange triangles, Côté et al. 2006; Turner et al. 2012; Georgiev et al. 2016), GCs (grey points) and ETGs (red squares) from the catalogue of Misgeld & Hilker (2011).

1.3.2 Internal kinematics

Measuring the internal kinematics of a star cluster is challenging and requires spatially resolved spectroscopy. With the advent of adaptive optics (AO) facilities on ground-based 8-m class telescopes such as ESO's VLT or Keck and the advancement in sensitivity of IFS instruments, such studies became possible for the NSCs of nearby galaxies.

Already the earliest IFS studies revealed that many NSCs show significant internal rotation, both in LTGs and ETGs (Seth et al. 2008a, 2010). Figure 1.9 shows the LOS velocity and velocity dispersion map of the NSC of the ETG FCC 47 as one example of a rotating NSC. The data were acquired with the Spectrograph for INtegral Field Observations in the Near Infrared (SINFONI) instrument (Eisenhauer et al. 2003), a now decommissioned IFS instrument at ESO's VLT and were originally presented in Lyubenova & Tsatsi (2019). This NSC shows strong rotation that reaches velocities of ± 70 km s^{-1} and has a pronounced peak in velocity dispersion at its centre. FCC 47 and its NSC are further studied with wide field MUSE IFS in Chapt. 2

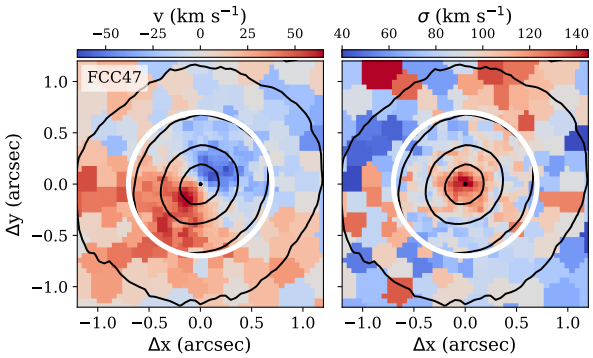

Figure 1.9.: Internal kinematics of the NSC of the ETG FCC 47, located in the Fornax galaxy cluster. The data were acquired with SINFONI and originally presented in Lyubenova & Tsatsi (2019). *Left*: LOS velocity map, showing the strong rotation of the NSC. *Right*: velocity dispersion, showing a strong peak at the centre of the NSC. The white circle refers to the effective radius ($R_{\rm eff} = 0.7'' \sim 67$ pc). The figure shows a $1.2'' \times 1.2''$ field-of-view, corresponding to ~ 110 pc $\times$ 110 pc.

Significant rotation velocities in NSCs are often accompanied by complex density distributions and flattened light profiles (Böker et al. 2002; Neumayer et al. 2020). Especially

massive NSCs can reach ellipticities[9] as high as $\epsilon = 0.6$, but elongated, disk-like structures have been found in NSCs of both LTG and ETG hosts and in most cases the elongation of the NSC is aligned with the disk of the host galaxy (Seth et al. 2006; Spengler et al. 2017).

Beyond rotation signatures that are directly visible from LOS velocity maps of IFS data (e.g. Fig. 1.9), detailed dynamical modelling can reveal the complex orbital structure of some NSCs. For example, Lyubenova et al. (2013) employed a dynamical Schwarzschild orbit-superposition model[10] of the ETG FCC 277 and identified significant amounts of counter-rotating orbits in addition to a dynamically cold disk structure in FCC 277's NSC. Counter-rotation was also found in the NSC of NGC 404 (Seth et al. 2010). The MW NSC is another example of a kinematically complex NSC that contains multiple populations with different kinematics (Feldmeier-Krause et al. 2020). Globally, the MW NSC shows a maximum LOS rotation velocity of $\sim \pm$ 50 km s^{-1} and a velocity dispersion of $\sim$ 60 km s^{-1}. The rotation axis of the MW NSC appears to be misaligned with respect to the disk by 9° (Feldmeier et al. 2014).

1.3.3 Stellar population properties

Deriving stellar population properties such as ages and metallicities of star clusters is even more challenging than measuring the internal kinematics as it depends on many assumptions. For nearby GCs, ages and metallicities can be determined fairly straightforwardly from isochrone fitting (see Sect. 1.2) or stellar spectroscopy, but for star clusters in external galaxies, only integrated properties are available as individual stars are no longer resolved. For these systems, ages and metallicities can be estimated from photometry, for example by employing optical colours, but this approach is often limited by the age-metallicity degeneracy (Worthey 1994). As shown in the CMDs in Fig. 1.5, red colours can be produced by either old or metal-rich populations. Using multiple photometric bands that cover the infra-red, optical, and ultraviolet parts of the electromagnetic spectrum can help to break this degeneracy because stars of different ages and metallicities can produce features at these other wavelength ranges that are not visible in the optical regime (Worthey 1994; Chies-Santos et al. 2011; Spengler et al. 2017; Adamo et al. 2020).

Alternatively, integrated-light spectroscopy can be used (see the review by Conroy 2013), either using index measurements of individual spectral absorption lines, or full spectrum fitting. In the latter, the spectra of star clusters (or any stellar component) are fitted to model spectra from stellar population synthesis models. These models use a similar approach as theoretical isochrones (Fig. 1.5), but they are coupled to either theoretical or empirical spectral stellar libraries and hence produce a combined spectrum of a stellar population of a given age and metallicity. An additional input of these models is the initial mass function (IMF) that describes how many stars of a certain mass are born and consequently how the isochrones are populated. The shape of the IMF are debated and it is unclear whether it is a universal function or differs with environment (see the review Bastian et al. 2010).

[9] $\epsilon = 1 - a/b$, where a is the major axis and b the minor axis.

[10] Schwarzschild modelling is described in Sect. 2.5.2 as well as in van den Bosch et al. (2008), van de Ven et al. (2008), and Zhu et al. (2018b).

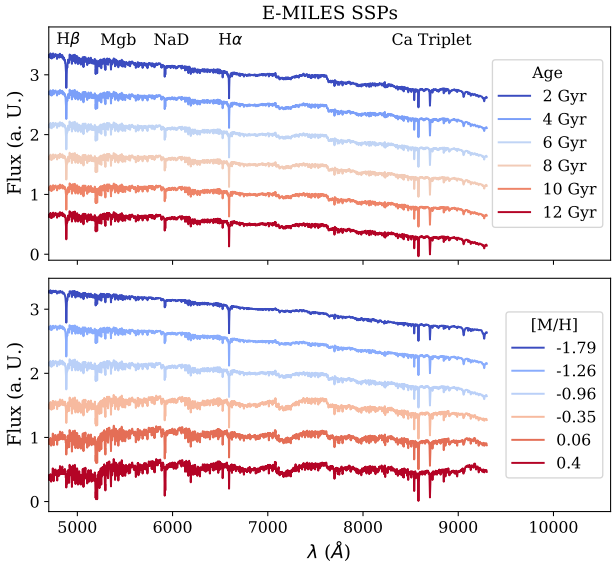

Figure 1.10.: E-MILES SSP models of different ages and metallicities. *Top*: SSPs with [M/H] = −0.96 dex and varying age. *Bottom*: SSPs with Age = 12 Gyr and varying metallicity. The spectra are normalised and shifted for visualisation.

Figure 1.10 shows E-MILES SSP models[11] of different ages and metallicities in the optical wavelength range from 4700 to 9300 Å. These models are based on the Medium resolution INT Library of Empirical Spectra (MILES), an empirical stellar library. The models shown in the figure were constructed using the BaSTI isochrones (Pietrinferni et al. 2004, 2006) and a MW-like double power law (bimodal) IMF with a high-mass slope of 1.30 (Vazdekis et al. 1996).

In addition to age and metallicity, the light element abundance ratio [α/Fe] is often an important parameter in stellar population studies. It gives the relative abundance of so-called α-elements like oxygen, neon, magnesium, or calcium. Core-collapse supernova that mark the end of massive, short-lived stars produce these elements, while Type Ia supernova release mainly iron-peak elements (such as iron, nickel, and cobalt). The latter involve white dwarfs – the end stages of low mass stars - and hence occur with a temporal delay to core-collapse supernova. As a consequence, [α/Fe] decreases with time in a population that is continuously evolving and it can be used to study the star formation timescales of local galaxies (Conroy et al. 2014). It is often found that massive galaxies as well as GCs reach high values of [α/Fe]. This is interpreted as a sign of short formation timescales because their populations are mainly enriched by massive stars on short timescales (e.g. Segers et al. 2016). Different SSP models use different prescriptions for the α-enrichment (see also Sect. 2.4), and the E-MILES SSPs shown in Fig. 1.10 have the α-enrichment behaviour of the solar neighbourhood imprinted because they are constructed from an empirical stellar library of nearby stars.

IFS is generally able to derive accurate metallicities and young ages, but the recovery of old ages from integrated-light spectroscopy is challenging because the spectral absorption features in the optical wavelength range barely change between a population at 8 and 12 Gyr (Fig. 1.10) and stellar population models in the infrared are not well calibrated (Conroy 2013; Usher et al. 2019; Asa'd & Goudfrooij 2020; Asa'd et al. 2021). Despite the limitations in stellar population analysis from integrated light, it is now established that NSCs can have complex stellar population properties, as the MW NSC already shows. It is dominated by an old population (> 5 Gyr, Blum et al. 2003; Genzel et al. 2010; Feldmeier-Krause et al. 2017a), but also contains very young stars (< 10 Myr, Lu et al. 2013). The stars in the NSC span a wide range of metallicities (Feldmeier-Krause et al. 2017a; Do et al. 2018), and recently a minor old, metal-poor population was discovered (Feldmeier-Krause et al. 2020). This is in agreement with studies of other LTGs that often find multiple populations

[11] http://research.iac.es/proyecto/miles/

in the NSCs (Walcher et al. 2005; Rossa et al. 2006; Carson et al. 2015; Kacharov et al. 2018). While the mass is typically dominated by old stellar populations, young stars are present in almost all LTG NSCs studied so far (Rossa et al. 2006; Kacharov et al. 2018). The star formation histories (SFHs) of LTG NSCs, meaning the age distributions of stars that allows us to determine what fraction of stars have formed at a given time, is often a complex function with multiple episodes of star formation or continuous star formation (Kacharov et al. 2018).

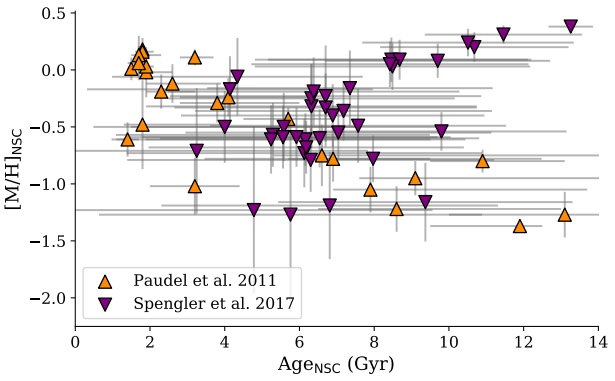

Figure 1.11.: NSC ages and metallicities from the samples of Paudel et al. (2011) and Spengler et al. (2017).

NSC SFHs enable us to reconstruct the mass assembly of NSCs, but are only available for a restricted sample of nearby bulgeless LTGs in which the NSC clearly dominates the central light. In other galaxies, contamination from the main stellar body makes detailed stellar population analysis challenging, and thus these studies focus more on establishing the mean NSC ages and metallicities. Studying nucleated galaxies in the Virgo galaxy cluster, both Paudel et al. (2011) and Spengler et al. (2017) found young NSCs in otherwise old ETGs and dEs, but most NSCs in ETGs show no evidence of recent (< 1 Gyr) or ongoing star formation. The NSCs in these systems were found to cover a broad range of metallicities. They are often more metal-rich than their host galaxy (Spengler et al. 2017; Neumayer et al. 2020). However, at lower galaxy masses, metal-poor NSCs were found that are less enriched than their host galaxy (see Chapt. 3 & 5 and Alfaro-Cuello et al. 2019; Johnston et al. 2020). Figure 1.11 shows NSC ages and metallicities from Paudel et al. (2011) and Spengler et al. (2017) to illustrate the large range of stellar populations found in NSCs. While Paudel et al. (2011) used spectroscopy, Spengler et al. (2017) used broad band photometry to infer the stellar population properties and as Fig. 1.11 shows, the associated uncertainties are large, especially for the recovered ages.

1.4 Nuclear star clusters and their host galaxies

The existence of supermassive black holes (SMBHs) at the centres of galaxies has been suggested already in the 1960s (Salpeter 1964; Wolfe & Burbidge 1970; Lynden-Bell & Rees 1971) and is now established through the observations of stars orbiting at the centre of the MW (Gravity Collaboration et al. 2018) and the SMBH shadow in M 87 with the Event Horizon Telescope (Event Horizon Telescope Collaboration et al. 2019).

Since the beginning of the century, it has been known that the mass of the central SMBH of a galaxy correlates with with the bulge velocity dispersion (Ferrarese & Merritt 2000). Similar relations were found for the bulge mass and luminosity, and stellar mass of the host galaxy and generally more massive galaxies host more massive SMBHs (Kormendy & Ho

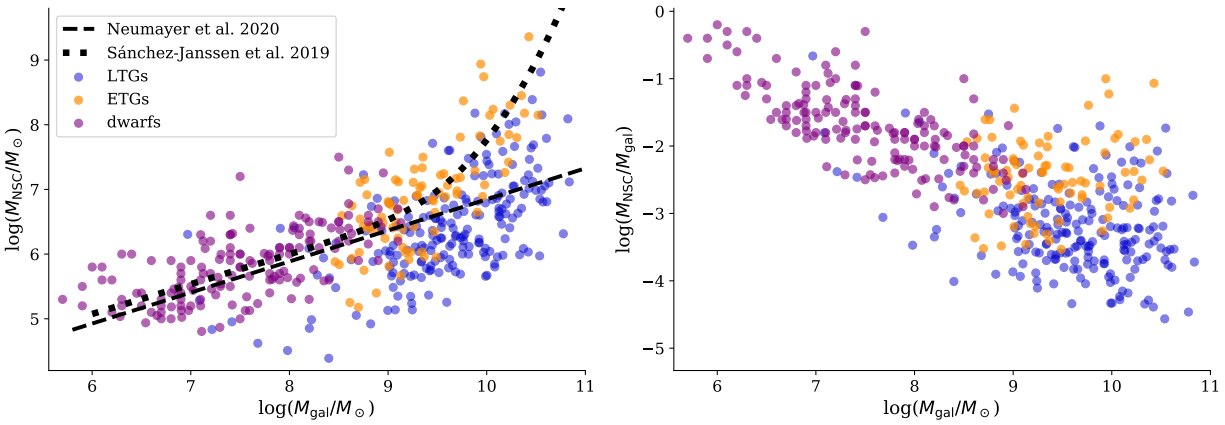

Figure 1.12.: Correlation between NSC and galaxy masses. Left: Galaxy and NSC masses, divided into LTGs (blue, Georgiev et al. 2016), ETGs (orange, NSC masses from Côté et al. 2006; Turner et al. 2012, galaxy masses from Peng et al. 2008; Liu et al. 2019), and dwarf galaxies (purple Ordenes-Briceño et al. 2018; Sánchez-Janssen et al. 2019). The dashed black line shows the $M_{\rm NSC} - M_{\rm gal}$ relation from Neumayer et al. (2020) with a slope of ~ 0.48, the dotted line shows the non-linear relation from Sánchez-Janssen et al. (2019). *Right*: NSC-to-galaxy mass ratio.

2013; McConnell & Ma 2013). This is an intriguing finding because these relations connect galaxies that extend over several tens of kpc to the sub-parsec scales of the SMBH in their centres and the low scatter around the relations imply a co-evolution of galaxies and their central BHs.

1.4.1 Scaling relations

Interestingly, similar relations were also found between NSCs and their host galaxies (Balcells et al. 2003; Graham & Guzmán 2003), and effort was put into establishing relations between the NSC mass and galaxy properties such as bulge luminosity, velocity dispersion, and total stellar mass (Ferrarese et al. 2006; Wehner & Harris 2006; Rossa et al. 2006). It was suggested that NSCs and BHs follow the same scaling relations (Ferrarese et al. 2006), but larger sample sizes found different relations for NSCs and SMBHs (Erwin & Gadotti 2012; Georgiev et al. 2016; Ordenes-Briceño et al. 2018; Sánchez-Janssen et al. 2019).

Figure 1.12 shows the NSC mass - galaxy mass relation for NSCs hosted by ETGs, LTGs, and dwarf galaxies (Côté et al. 2006; Turner et al. 2012; Georgiev et al. 2016; Ordenes-Briceño et al. 2018; Sánchez-Janssen et al. 2019). The dashed black line in this figure refers to the $M_{\rm NSC} - M_{\rm gal}$ relation from Neumayer et al. (2020) as the most recent example. This relation was derived from a sample containing both ETG and LTG hosts and has a slope of 0.48, in agreement with other studies (Balcells et al. 2003; Scott & Graham 2013; den Brok et al. 2014). Georgiev et al. (2016) found steeper slopes of 1 and 1.3 for massive LTGs and ETGs, similar to the slope of the SMBH-bulge mass relation (McConnell & Ma 2013; Saglia et al. 2016). Additionally including nucleated dwarf galaxies, both Sánchez-Janssen et al. (2019) and Ordenes-Briceño et al. (2018) proposed that the NSC mass - galaxy mass relation is best represented by a non-linear function with a steeper slope for galaxies $> 5 \times 10^9 M_\odot$ (shown as the dotted line in Fig. 1.12). Therefore, the NSC mass - galaxy mass relation

is still debated and it likely differs from the galaxy mass-SMBH mass relation, at least for low galaxy masses. Also the $M - \sigma$ relation that connects the stellar velocity dispersion of a galaxy to the mass of the central massive objects appears to differ between NSCs and SMBHs. While the $M_{\rm BH} - \sigma$ relation has a slope between 4 and 5 (Kormendy & Ho 2013; Saglia et al. 2016; Capuzzo-Dolcetta & Tosta e Melo 2017), the $M_{\rm NSC} - \sigma$ relation appears to be shallower, with a slope of ~ 2 (Scott & Graham 2013; Capuzzo-Dolcetta & Tosta e Melo 2017; Nguyen et al. 2018).

The right panel in Fig. 1.12 shows the mass ratio between NSC and host galaxy as a function of galaxy mass for the same sample. It shows that the NSC-to-galaxy mass ratio decreases with galaxy mass. While NSCs in dwarf galaxies can contain significant fractions of the total galaxy mass (> 10 %), this fraction reduces to $\lesssim 0.1\%$ for massive galaxies ($> 10^9 M_\odot$). In these massive galaxies, the mass in NSCs becomes negligible.

1.4.2 Co-existence of nuclear star clusters and supermassive black holes

There are several cases where NSCs and central SMBHs are found to co-exist in the same galaxy (e.g. Graham & Spitler 2009). The MW is the most prominent example, where a SMBH with a mass of $4 \times 10^6 M_\odot$ sits at the centre of the NSC (Genzel et al. 2010; Schödel et al. 2014; Gravity Collaboration et al. 2018). Fig. 1.13 shows the BH-to-NSC mass ratio as a function of galaxy mass for a very restricted sample of galaxies in which both the NSC and BH masses are constrained (Neumayer et al. 2020). This mass fraction increases with galaxy mass and thus the BHs begin to dominate the central mass budget for galaxies more massive than $\gtrsim 3 \times 10^{10} M_\odot$. Those might be systems where the SMBH begins to affect the further growth of the NSC due to BH binary mergers and dynamical interactions with the stars of the NSC (Antonini et al. 2015). At lower galaxy masses, the NSC mass dominates. In UCDs, which might be remnant NSCs (see Sect. 1.4.4 and 2.7), SMBHs were found that constitute up to 15% of the UCD mass (Seth et al. 2014; Ahn et al. 2017, 2018; Afanasiev et al. 2018).

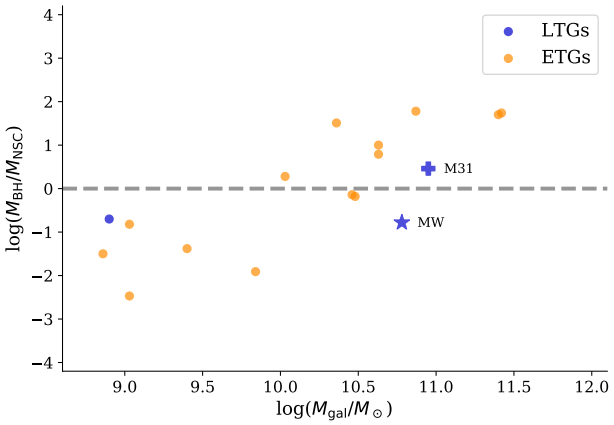

Figure 1.13.: BH-to-NSC mass ratio as function of galaxy mass. Data taken from Neumayer et al. (2020). LTGs are shown in blue, ETGs in orange.

Signatures of gas accretion onto a BH (so-called active BHs) have been found in several NSCs based on X-ray features or analysis of ionised gas emission lines (Filippenko & Ho 2003; Seth et al. 2008b; Miller et al. 2015). However, NSCs are also prime targets to hunt for inactive (non-accreting) BHs because they provide the high stellar densities and luminosities to enable a study of the internal kinematics in which the BH can leave a detectable imprint.

This is often seen as a steep rise in velocity dispersion at the centre. Nonetheless, dynamical modelling is required to infer the dynamical NSC and SMBH masses (Nguyen et al. 2017, 2018, 2019) and often only upper limits are available (Voggel et al. 2018; Neumayer et al. 2020).

1.4.3 Nucleation fraction of galaxies

The fraction of galaxies that host a NSC, the nucleation fraction, is high. It was found that NSCs reside in the centres of > 70 % of all galaxies (Böker 2010) and in recent years, the picture has become more detailed due to increasingly large sample sizes that also cover low-mass dwarf galaxies.

Sánchez-Janssen et al. (2019) analysed NSCs in the dwarf galaxies of the NGVS and combined the results with the ACSVCS NSCs (Côté et al. 2006) to derive the nucleation fraction of galaxies in the Virgo galaxy cluster as a function of galaxy mass. They concluded that the nucleation fraction reaches its peak at > 90 % for galaxies with masses $M_{\rm gal} \sim 10^9 M_\odot$ and drops steadily to < 10% for the highest and lowest galaxy masses ($M_{\rm gal} < 10^6 M_\odot$ and $M_{\rm gal} > 10^{11} M_\odot$, respectively). Using a more diverse sample of galaxies, Neumayer et al. (2020) found a similar functional form of the nucleation fraction that does not differ significantly for LTGs and ETGs and recently Zanatta et al. (2021) found a high fraction (~ 50 %) of dwarfs with NSCs in the Coma galaxy cluster.

For the least massive dwarf galaxies ($M_{\rm gal} < 10^6 M_\odot$), the nucleation fraction is close to zero (Ordenes-Briceño et al. 2018), but also GCs are scarce in these galaxies (Forbes et al. 2018), so these objects might not be able to form massive star clusters. At the other end of the mass spectrum, it has been suggested that interactions between NSCs and the central SMBHs might disrupt existing NSCs or directly inhibit NSC formation (Côté et al. 2006; Neumayer & Walcher 2012; Antonini et al. 2015; Arca-Sedda et al. 2016).

1.4.4 Stripped nuclear star clusters

During the accretion of low-mass galaxies, the main stellar body of the satellite gets disrupted, but massive star clusters like NSCs can survive such interactions relatively unscathed. Examples from our MW directly illustrate that stripped NSCs are hiding in the GC population of massive galaxies. It has been proposed that ωCentauri (NGC 5139, Fig. 1.4), the most massive GC in the MW, is the stripped NSC of an accreted galaxy due to the presence of multiple stellar populations (e.g. King et al. 2012) and its retrograde orbit (Majewski et al. 2000). The case for M 54, the second most massive MW GC, appears to be even more convincing as it is still located in the centre of the Sagittarius dwarf galaxy (e.g. Ibata et al. 1997; Bellazzini et al. 2008) and thus is likely a NSC in the process of being stripped by the MW (Alfaro-Cuello et al. 2019). A NSC origin has also been proposed for several other GCs based on their chemodynamical properties (e.g. Pfeffer et al. 2021).

Stripped NSCs are also proposed as an origin for ultra-compact dwarf galaxies (UCDs). UCDs were discovered about two decades ago in studies of galaxy clusters as isolated, compact stellar objects (Minniti et al. 1998; Hilker et al. 1999b; Drinkwater et al. 2000). With masses of $10^6 < M < 10^8\,M_\odot$, effective radii between 7 and 100 pc, and old ages > 10

Gyr (Drinkwater et al. 2003; Haşegan et al. 2005; Mieske et al. 2006; Evstigneeva et al. 2007; Mieske et al. 2013), UCDs have properties comparable to those of GCs and NSCs, but can be more extended (e.g. Misgeld & Hilker 2011; Brodie et al. 2011; Norris et al. 2014; Janz et al. 2016). On the mass-size plane they occupy the region between star clusters and compact elliptical galaxies (e.g. Misgeld & Hilker 2011; Brodie et al. 2011; Norris et al. 2014; Janz et al. 2016).

Their intermediate nature reflects in the proposed formation scenarios for UCDs. It was suggested that they could be remnant NSCs of (dwarf) galaxies that were disrupted and stripped of their stellar body in an interaction with a more massive galaxy (Phillipps et al. 2001; Bekki et al. 2003; Drinkwater et al. 2003; Pfeffer & Baumgardt 2013; Strader et al. 2013). Alternatively, UCDs could constitute the high-mass end of the GC mass function observed in the rich GC populations of massive galaxies (e.g. Mieske et al. 2002, 2004; Kissler-Patig et al. 2006; Mieske et al. 2012; Mahani et al. 2021). To explain their extended sizes, it was further suggested that UCDs might form from the mergers of multiple GCs in star cluster complexes (Fellhauer & Kroupa 2002; Maraston et al. 2004; Fellhauer & Kroupa 2005; Brüns et al. 2011; Mahani et al. 2021).

There is evidence that UCDs are a mix of stellar systems from different formation pathways (Brodie et al. 2011; Da Rocha et al. 2011; Janz et al. 2016). For example, simulations of the stripping scenario produce too low numbers of UCDs to match the observed populations in galaxy clusters (Pfeffer et al. 2014, 2016). Nonetheless, there are several UCDs where the stripped NSC scenario is established due to the presence of a SMBH - similar to what is found in NSCs (Sect. 1.4.2). Studies of massive UCDs in the Virgo and Fornax cluster have detected signatures of a SMBH that can constitute up to 15% of the UCD's mass (Seth et al. 2014; Ahn et al. 2017, 2018; Afanasiev et al. 2018).

As of now, the sample of identified NSC-type UCDs is biased to high stellar masses, where SMBHs can be found with high angular resolution IFS observations or the brightness of the UCD enables a detailed study of its SFH (Norris et al. 2015). These high-mass UCDs typically were once the nuclei of stripped massive galaxies with initial masses $> 10^9 M_\odot$ (Norris & Kannappan 2011; Seth et al. 2014; Ahn et al. 2018; Afanasiev et al. 2018). But also the remnant nuclei of stripped dwarf galaxies ($M_* \sim 10^8 M_\odot$) should be found among the low-mass UCDs ($< 10^7 M_\odot$), as for example N-body simulations show (Pfeffer & Baumgardt 2013).

1.5 Formation scenarios of nuclear star clusters

The existence of NSCs as dense star clusters in the centre of galaxies has been known for decades and as discussed above, NSCs are very common objects that are found in a majority of galaxies from low-mass dwarf galaxies to high mass ETGs and LTGs. Nonetheless, the formation of NSCs is still debated and in general, two different mechanisms are discussed in the literature: the infall and subsequent merger of (gas-free) GCs and the in-situ formation from gas directly at the galaxy centre (see Fig. 1.14 or Neumayer et al. 2020).

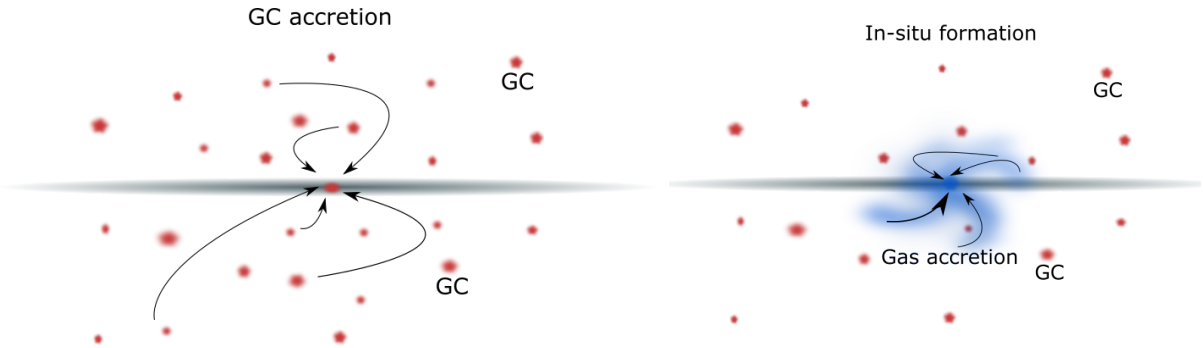

Figure 1.14.: Schematic illustration of NSC formation pathways. *Left*: NSC formation from the infall of GCs (GC accretion or GC inspiral scenario). *Right*: NSC formation from in-situ star formation.

1.5.1 In-spiral of globular clusters

After the discovery of the first NSCs in external galaxies, Tremaine et al. (1975) suggested that NSCs are a natural consequence of GCs orbiting in a galaxy because as massive compact objects, GCs experience dynamical friction that decelerates their motion (Chandrasekhar 1943). Consequently, they will spiral towards the centre and build the NSC via the subsequent mergers of GCs. Since the dynamical friction deceleration is proportional to the mass of the GCs, more massive GCs fall first into the centre.

The first supportive evidence for this formation scenario was found when several ETGs were observed to show a lack of GCs in their central regions (McLaughlin 1995; Capuzzo-Dolcetta & Tesseri 1999; Lotz et al. 2004; Capuzzo-Dolcetta & Mastrobuono-Battisti 2009). Later, detailed N-body simulations have been successful in reproducing properties of NSCs with the GC infall scenario. The first N-body simulations of a few star clusters evolving in the tidal field of a galaxy found that they build a super-star cluster with similar density and velocity dispersion profiles as found in NSCs (Capuzzo-Dolcetta & Miocchi 2008b,a). Antonini et al. (2012) used an N-body simulation of a MW-like galaxy with 12 evolving GCs and a central SMBH and found that the resulting NSC has properties consistent with the global structural properties of the MW NSC. By further considering the merger of GCs of different ages and metallicities, Perets & Mastrobuono-Battisti (2014) concluded that GC mergers can introduce different components in the NSC that are still separated by their stellar populations even a few billion years after the infall. In a similar spirit, Tsatsi et al. (2017) was able to also reproduce the kinematics of the MW NSC from a pure GC accretion simulation and showed that NSCs formed from infalling GCs can have flattened shapes and non-zero angular momenta (see also Lyubenova & Tsatsi 2019).

There are also targeted N-body simulations to analyse the evolution of star clusters that are observed close to galaxy centres. For example, Arca-Sedda & Capuzzo-Dolcetta (2016) presented an N-body model of the dwarf starburst galaxy Henize 2-10 and found that the central star clusters of this galaxy will build an NSC within ~ 10 Myr. A similar N-body simulation approach was used by Schiavi et al. (2021) to study the evolution of two star clusters found near the centre of the LTG NGC 4654. The authors concluded that these star clusters will merge to a NSC within 100 Myr.

Semi-analytical models of GC accretion that follow the statistical evolution of GC systems in a tidal field to build NSCs were successful in reproducing properties of the NSC population such as the radius-mass relation (Antonini et al. 2012; Antonini 2013) or the NSC-to-galaxy mass relation (Gnedin et al. 2014), although with a different normalisation. Recently, Leaman & van de Ven (2021, subm.) presented a semi-analytical model based on the dynamical evolution of a GC population under dynamical friction and mass loss that is successful in predicting the shape of the nucleation fraction (see also Chapt. 6). However, the intrinsic scatter in established NSC-host relations has been difficult to address given the number of physical processes and scales at play.

In the simplest assumptions, the infall of GCs is a gas-free and dissipationless process in which ancient, often metal-poor GCs merge to form the NSC. For this reason, the NSC should reflect the stellar populations of the accreted GCs and hence this scenario can naturally explain the low metallicities and old ages found in some NSCs of dwarf galaxies (Alfaro-Cuello et al. 2019; Johnston et al. 2020) if they were formed out of metal-poor GCs that are ubiquitously found in the halo regions of galaxies (see Sect. 1.2 or Peng et al. 2006). The recently discovered minor, old populations of metal-poor stars in the MW NSC (Feldmeier-Krause et al. 2020) can also be explained by the accretion of a metal-poor GC (or by the accretion of metal-poor stars from a dwarf galaxy, Arca Sedda et al. 2020).

Despite its success in explaining metal-poor populations, general NSC properties, and average scaling relations, the GC inspiral scenario of NSC formation is not sufficient to explain the large diversity in NSC properties. Using N-body simulations of evolving GCs similar to those of Capuzzo-Dolcetta & Miocchi (2008b,a), Hartmann et al. (2011) were able to reproduce the structural properties – in particular densities and shapes – of two NSCs, but found that the internal kinematics are not sufficiently reproduced and require additional gas-accretion. Similarly, while the angular momentum of most of the NSCs studied by Lyubenova & Tsatsi (2019) can be explained from inspiralling GCs (Tsatsi et al. 2017), the high angular momentum of the NSC of the ETG FCC 47 (see Chapt. 2) is inconsistent with GC infall from random directions and would require GC accretion from a preferred direction. In addition, the properties of the MW NSC are likely not consistent with having formed solely from the accretion of GCs. While the density profile, flattening, and rotation signature can be reproduced from GC infall simulations (Antonini et al. 2012; Tsatsi et al. 2017), the presence of very young stars (< 1 Gyr) indicates additional in-situ star formation.

Although the GC infall formation channel is generally focused on GCs, it has to be noted that infalling clusters can also be younger massive clusters (Agarwal & Milosavljević 2011). Using numerical simulations, Guillard et al. (2016) proposed a composite 'wet migration' scenario where a massive cluster forms in the early stages of galaxy evolution in a gas-rich disk and then migrates to the centre while keeping its initial gas reservoir, possibly followed by mergers with other gas-rich clusters. Paudel & Yoon (2020) identified off-center young star clusters in dwarf elliptical galaxies and suggested that those could be examples of seed NSCs in such a wet-merger scenario. As these young massive clusters with ages < 10 Myr can form close to the centres of their hosts from pre-enriched material (e.g. Kornei & McCrady 2009; Nguyen et al. 2014; Georgiev & Böker 2014), they can also lead to young, metal-rich populations in the NSCs (Arca-Sedda & Capuzzo-Dolcetta 2014, 2016; Schiavi et al. 2021).

1.5.2 In-situ star formation

In the in-situ formation scenario (right panel in Fig. 1.14), NSCs form directly at the galactic centre from infalling gas that undergoes star formation (Mihos & Hernquist 1994; Milosavljević 2004; Bekki et al. 2006; Bekki 2007). This can happen repeatedly in several strong star formation episodes or as continuous nuclear star formation, as the bursty or extended SFHs of some NSCs indicate (Kacharov et al. 2018).

The in-situ formation channel depends on internal feedback mechanisms and the available gas content. Many different mechanisms for funnelling gas to the centre have been studied, with a focus on LTGs. Mihos & Hernquist (1994) proposed that gas-rich mergers of galaxies will lead to a build-up of gas in the merger remnant and the subsequent star formation can form compact objects similar to NSCs. Later, simulations by Hopkins & Quataert (2010) showed that gas infall to the centre can happen as a result of gravitational torques during gas-rich mergers that trigger gas clouds to undergo gravitational collapse.

There are also in-situ NSC formation mechanisms that do not require gas-rich mergers. Milosavljević (2004) suggested that magneto-rotational instabilities in gas disks can funnel gas towards the nucleus with rates sufficiently for continuous star formation. Additionally, the non-axisymmetric potential of galactic bars can result in bar-driven gas infall into the centre (Shlosman et al. 1989, 1990). This might happen in a continuous flow of gas in a nuclear spiral (e.g. Kim & Elmegreen 2017) or nuclear rings (Hunt et al. 2008). Emsellem et al. (2015) presented a targeted simulation of this process by studying the gas fuelling towards a central SMBH in a barred MW-like galaxy. In their simulation, gas-infall is triggered by dynamical resonances in the bar and brought to the inner few parsecs via nuclear spirals. They found that a central star cluster can form around an existing BH from gas that piles up and decouples from the large-scale disk. Interestingly, observations of the barred galaxy NGC 6946 have reported $\sim 10^7 M_\odot$ of molecular gas in the centre out of which a NSC might form (Schinnerer et al. 2006, 2007). Therefore, this gas-driven fueling mechanism could be a pathway through which NSCs still form today.

Bekki et al. (2006) and Bekki (2007) suggested a similar process occurring in gaseous disks embedded in stellar spheroids at higher redshifts. Using numerical simulations, they found that star clusters can form from the infall and merger of stellar and gaseous clumps that arise in nuclear spirals as a result of gravitational instability and propose that such a process at high redshift could explain NSCs in now gas-free ETGs. They found the resulting NSCs to be younger and more metal-rich than their hosts, similar to what was observed for some dwarf galaxies in the Virgo galaxy cluster (Paudel et al. 2011; Spengler et al. 2017). Additionally, Emsellem & van de Ven (2008) proposed a tidal compression mechanism: in galaxies with rather flat density profiles (Sérsic indices $n \lesssim 3.5$), the tidal field becomes compressive and thus gas can collapse in the centre on spatial scales similar to the radii of NSCs found in LTGs and ETGs. This mechanism can also explain the scaling relation between the NSC and host mass as a consequence of the compressive force being able to accumulate more central mass in more massive galaxies, but fails to explain low-mass NSCs in dwarf galaxies.

Using numerical simulations to study NSC formation (or star cluster formation in general) from in-situ star formation in a galactic or even cosmological context is challenging due to

the various physical processes that are involved (e.g. Li & Gnedin 2019; Ma et al. 2020). The details of the gravitational potential and resonances in individual galaxies are key in driving gas flows to the central regions (Sormani et al. 2018), and the complex radiation field in galactic nuclei prevents a simple understanding of how efficiently star formation proceeds (Longmore & Kruijssen 2018). Therefore, semi-analytical approaches are often taken to explore the in-situ formation mechanism (e.g. Antonini et al. 2015). To date, Brown et al. (2018) presents the only study of NSCs in a cosmological simulation, although with focus on NSCs in dwarf galaxies and only considering the evolution to $z \sim 1.5$. They find extended SFHs and significant metallicity spreads as a result of pollution by supernovae ejections. In their simulations, NSCs are more metal-rich than their host galaxies due to formation from pre-enriched gas.

Although the details of the in-situ formation channel have not yet been explored theoretically, there is plenty of observational evidence of this channel acting in the growth of NSCs. As mentioned above, the presence of young stars in the NSCs of many LTGs (Kacharov et al. 2018; Nguyen et al. 2019) suggests in-situ formation. These younger populations are often rotating and have flattened density distributions, as expected if they formed initially in a gas-rich disk-like structure and lost part of their angular momentum due to vertical dynamical heating (Seth et al. 2006). The presence of emission lines from ionised gas found in some NSCs further is direct evidence of ongoing in-situ star formation (Walcher et al. 2006; Seth et al. 2008a).

While recent or ongoing star formation is certainly a sign-post of the in-situ NSC formation channel, this process could have been also responsible for the formation of old, metal-rich NSCs found in massive ETGs. As Turner et al. (2012) suggest, the red colours of some of the most massive NSCs in their sample indicate formation from metal-rich gas to explain the associated high metallicities. Further, they argue that NSCs can be created with dissipative processes before or during mergers and interactions that transform previously gas-rich galaxies to ETGs. The significantly flattened NSCs found in the highest mass ETGs are also indicating a formation from dissipative processes when gas falls to the galaxy centre and forms a star forming disk (Spengler et al. 2017).

In the last years, there is mounting evidence that neither of the two presented NSC formation channels alone is able to explain the large diversity in NSC properties, scaling relations, and stellar populations. This is true for the total NSC population as well as for individual NSCs as the NSC of the MW shows. As another example, Lyubenova et al. (2013) used a dynamical Schwarzschild model of the NSC of the ETG FCC 277 and found that its dynamically cold disk is indicating formation from in-situ star formation, but additional GC mergers are required to explain the presence of counter-rotating populations. Similarly focusing on individual galaxies, Hartmann et al. (2011) and Antonini et al. (2012) proposed that GC inspiral can contribute a large fraction ($\sim 50\%$) to the total NSC mass, but additional gas dissipation and in-situ star formation are required to explain all of the observed properties. Therefore, a mixture of both processes might have been involved in the formation of some NSCs.

1.5.3 Different formation mechanisms in different galaxies

There is evidence that both NSC formation processes are realised in nature, and the relative strength of them might be a function of galaxy properties. Based on dynamical friction arguments, Turner et al. (2012) suggested that GC infall is a suitable scenario to explain the growth of NSCs in low to intermediate mass galaxies. In contrast, dynamical friction timescales exceed the Hubble time for high-mass galaxies and thus Turner et al. (2012) concluded that in-situ star formation from accreted gas becomes the dominant NSC formation mechanism in massive galaxies. This was further supported by the red colours that indicated high metallicities of the NSCs in the most massive galaxies.

Antonini et al. (2015) came to a similar conclusion based on a semi-analytical galaxy formation model that follows both in-situ NSC formation and GC inspiral. They found GC inspiral can only form NSCs less massive than a few $10^7 M_\odot$ and that around 50% of the total mass in NSCs is formed from in-situ star formation, but this fraction increases for the highest-mass ETGs ($M_{\rm gal} \sim 10^{11} M_\odot$). However, their model failed to reproduce the drop in the nucleation fraction at low galaxy masses and their NSC-to-host mass relation predicts less massive NSCs as observed (Ordenes-Briceño et al. 2018).

Recently, Neumayer et al. (2020) collected evidence for a transition of the NSC formation channel with galaxy mass. They found that NSCs in galaxies less massive than $10^9 M_\odot$ can be more metal-poor than their host galaxy, while more massive galaxies have NSCs that are more metal-rich than their host and often show flattened density distributions as expected from dissipative processes. In addition, they pointed out that the NSC-to-host mass scaling relation matches expectations from GC inspiral only for low-mass galaxies (Gnedin et al. 2014; Sánchez-Janssen et al. 2019) and there appears to be a break in the NSC size-mass relation that shows a different behaviour for massive NSCs ($M_{\rm NSC} > 3 \times 10^6 M_\odot$). Based on the shape of the nucleation fraction curve that peaks for galaxies with masses of $M_{\rm gal} \sim 10^9 M_\odot$ and the metallicity contrast, Neumayer et al. (2020) suggested a transition between GC inspiral and in-situ formation happening at masses of $M_{\rm gal} \sim 10^9 M_\odot$.

The argumentation presented in Neumayer et al. (2020) hints towards a trend in the dominant NSC formation channel changing with galaxy mass, but the evidence is tentative. For example, the presented metallicity contrast is based in part on comparisons between measured NSC metallicities and the host metallicity as expected from the MZR of galaxies that can have a substantial scatter (Gallazzi et al. 2005; Kirby et al. 2013). In addition, many studies compare NSC and host using different data sets or are using approaches that do not account for the contribution of the galaxy light at the NSC position. Consequently, a detailed analysis of NSC formation in different galaxies that incorporates an extensive view of all the involved components is still missing. Establishing the processes involved in the formation of NSCs is the main goal of this thesis.

1.6 This thesis

How do nuclear star clusters form? As detailed in the previous section, NSCs are complex stellar systems that show a variety of different structural, kinematic, and stellar popula-

tion properties. The different proposed formation scenarios illustrate that NSCs cannot be regarded as isolated star clusters, but in order to constrain their formation, a panoramic view of all of the involved components is essential. It is crucial to treat NSCs as parts and products of the complex interplay between galaxies and their star clusters.

The IFS instrument MUSE, mounted at ESO's VLT on Cerro Paranal in Chile is the ideal instrument to study NSC formation. It provides a wide field-of-view (FOV), high spatial resolution, and spectral coverage in the optical wavelength range. These properties allow us to explore the kinematic and stellar population properties of NSCs, their host galaxies, and the GC population. In this thesis, I present studies of NSC formation based on MUSE data of individual galaxies and discuss how the observational results compare with expectations from a semi-analytical model. The remainder of this thesis is structured as follows:

Chapter 2

This chapter presents a MUSE study of the ETG FCC 47 in the Fornax cluster. The MUSE instrument is described in this chapter, as well as the techniques and methods for the extraction and analysis of star clusters (NSC and GCs). The analysis of FCC 47 and its massive NSC was originally published in Fahrion et al. (2019b). In addition, Fahrion et al. (2019a) presented the discovery and subsequent analysis of a UCD in close projection to the centre of FCC 47.

Chapter 3

While Chapt. 2 presents the analysis of a massive galaxy, this chapter focuses on two nucleated dwarf galaxies (KKs 58 and KK 197) that are satellites of Centaurus A. Using similar techniques as presented before, their NSCs and GCs are analysed with MUSE data. This chapter was originally published in Fahrion et al. (2020c).

Chapter 4

NSCs and GCs are closely intertwined: NSCs might form through mergers of GCs and stripped NSCs can hide in large GC populations. Therefore, it is pivotal to also establish the properties of GCs. Therefore, this chapter presents a thorough analysis of spectroscopic GCs and explores their capabilities as tracers of galaxy properties and galaxy evolution. It describes the spectroscopic GC catalogue that I derived from the F3D MUSE data and explores how the kinematics and metallicities of the GCs compare to the underlying galaxy light, as originally published in Fahrion et al. (2020c). Further, this chapter presents the non-linear relation between photometric GC colours and spectroscopic metallicities that was derived from the F3D GC catalogue (published in Fahrion et al. 2020b).

Chapter 5

In this chapter, I present a detailed analysis of the NSC stellar populations and star formation histories in comparison to the underlying host galaxies in 25 nucleated galaxies in order to

derive the dominant NSC formation channel. This chapter is published in Fahrion et al. (2021).

Chapter 6

Chapt. 6 describes a semi-analytical model of NSC formation based on the dynamical evolution of a GC population in the tidal field of a galaxy. This model explores how the dominant NSC formation channel depends on galaxy properties like galaxy mass or NSC mass. This chapter will be published as Fahrion et al. (2021, subm.), a paper submitted to the Astronomy & Astrophysics journal that is currently under review.

Chapter 7

Here I summarise the results of this thesis, compare them to literature studies and discuss them in the context of ongoing research in extragalactic astronomy. Additionally, an outlook for future research questions with upcoming telescopes is presented.

In a dark place we find ourselves, and a little more knowledge lights our way.

Yoda, Star Wars

2 | Analysing nuclear star clusters with MUSE: FCC 47

Constraining NSC formation requires a panoramic view of all the involved components. This is nowadays possible with modern day IFU instruments such as MUSE. To illustrate how MUSE can be used to study these different components, this chapter focuses on one galaxy in particular that is a treasure trove for this kind of study due to its large NSC, rich GC population, and presence of an UCD: the ETG FCC 47. This chapter is based on Fahrion et al. (2019a) and Fahrion et al. (2019b)[1].

2.1 The early-type galaxy FCC 47

FCC 47 is a low-mass ETG with a stellar mass of $M_{\rm gal} \sim 10^10 M_\odot$ (Saulder et al. 2016; Liu et al. 2019) and an effective radius in the B band of 30 arcsec ($\sim$ 3 kpc, Ferguson 1989). FCC 47 is located in the outskirts of the Fornax cluster ($D = 18.3 \pm 0.6$ Mpc, Blakeslee et al. 2009), outside of the virial radius, with a projected distance of $\sim$ 780 kpc to the central galaxy NGC 1399. Due to this remote location, FCC 47 was not targeted by the F3D survey. As described in the following, MUSE data was acquired following a science verification proposal.

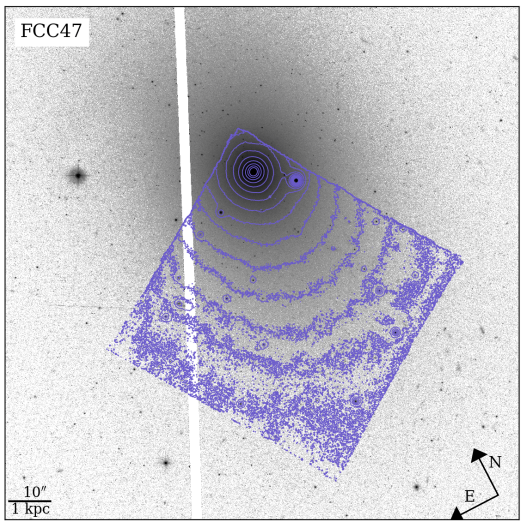

Figure 2.1.: HST ACS data of FCC 47 with surface brightness contours from the collapsed MUSE cube (white light image) superimposed in purple.

FCC 47 offers an ideal laboratory to explore NSC formation. Using HST data from the ACSFCS (Jordán et al. 2007), Turner et al. (2012) determined that FCC 47 has a particularly large NSC with an effective radius of $r_{\rm eff} = 0.750 \pm 0.125'' = 66.5 \pm 11.1$ pc in

[1] I started the work on FCC 47 already during my Master's project at the University of Heidelberg that was a precursor to this thesis. Some of the results are included in the Master's thesis in a preliminary form, but I significantly improved my methods and repeated the analysis during the first months of my PhD. I restructured this chapter with respect to the papers to focus on the parts relevant for the remainder of this thesis and on the improvements made during the PhD.

the F475W filter ($\sim g$ band). Using the same ACS data, Jordán et al. (2015) identified more than 300 GC candidates associated with FCC 47 and in the ACSFCS study of GC specific frequencies of Liu et al. (2019), FCC 47 appears as an outlier with a specific frequency[2] $S_{N,z} = 4.61 \pm 0.21$ that is much higher than the typical specific frequency of ETGs with similar mass of $S_{N,z} \sim 1$.

The NSC of FCC 47 was also studied with AO-supported high angular resolution IFS observations with SINFONI by Lyubenova & Tsatsi (2019) among five other NSCs of ETGs in the Fornax cluster (see also Lyubenova et al. 2013). The NSC of FCC 47 stands out from this sample due to its large size, strong rotation, and pronounced velocity dispersion peak (see Fig. 1.9). In this chapter, we aim to constrain the formation of FCC 47's massive NSC. We use observations with the MUSE instrument that enables a simultaneous study of the kinematic and chemical properties of FCC 47's stellar body, its NSC, and the GC system. We further report on the discovery of a UCD in the MUSE FOV.

2.2 The Multi Unit Spectroscopic Explorer (MUSE) instrument

MUSE (Bacon et al. 2010) is an integral-field spectrograph mounted at the Nasmyth platform B of the Unit Telescope 4 on ESO's VLT in Paranal, Chile (see Fig. 2.2). It consists of 24 individual integral-field units that together provide a near continuous FOV of $1' \times 1'$ on the sky in the wide field mode with a spatial sampling of $0.2''$, resulting in $\sim 90\,000$ individual spaxels. Along the wavelength direction, MUSE covers the optical wavelength range between 4700 and 9300 Å sampled at 1.25 Å. The mean full width at half maximum (FWHM) of the line-spread function is 2.5 Å ,but the FWHM is a function of wavelength (Guérou et al. 2016). The mean velocity resolution ranges from $\sigma \sim 35$ to 80 km s^{-1} depending on the wavelength range, which limits the determination of low velocity dispersions from integrated light spectroscopy (e.g. Emsellem et al. 2019). However, the peak positions of absorption and emission lines can be determined with much higher accuracy $\delta v < 5$ km s^{-1} (Valenti et al. 2018).

MUSE is a second generation instrument at the VLT. In 2014, the instrument saw first light and in 2017, its AO facility - the Ground Atmospheric Layer Adaptive Corrector for Spectroscopic Imaging (GALACSI) AO system - was commissioned. GALACSI uses four sodium laser guide stars to correct for atmospheric turbulence in real time and hence increases the spatial resolution of MUSE (see Fig. 2.2). Our study of FCC 47 is based on AO-assisted MUSE data acquired during the science verification phase directly after the commissioning of the GALACSI system (programme 60.A-9192, P.I. Fahrion). The data were acquired on the 17th of September 2017. We placed the NSC in a corner of the MUSE FOV (see Fig. 2.1). This off-centre positioning was chosen such that a simultaneous observation of the NSC as well as a large number of GCs was possible.

Following the observing strategies of the F3D project, the exposures of FCC 47 were dithered by $0.2''$and rotated by 90° to reduce the signature of MUSE's 24 integral-field units

[2] $S_{N,z} = N_{\rm GC} \times 10^{0.4(M_z+15)}$ with the total z-band magnitude M_z and the number of GCs $N_{\rm GC}$.

Figure 2.2.: Unit Telescope 4, the host of the MUSE instrument. *Left*: Two of the four sodium lasers mounted around the primary mirror of UT4. *Right*: View from the platform at the VLT of the laser guide stars pointing in the sky, shortly after twilight. Both images: taken by K. Fahrion, Sept. 2019.

on the final image. The data consist of ten exposures with 360 seconds exposure time each. Dedicated sky exposures of three minutes were taken in between the science exposures to perform sky modelling and reduce the contamination from sky emission lines. Our MUSE + AO data were taken in the nominal mode, meaning a wavelength coverage from 4750 to 9300 Å. In addition, the regime from 5800 to 6000 Å is filtered out because the sodium lasers of the AO system would otherwise saturate the detector in the sodium D line (see Fig. 2.5).

Due to unfortunate weather conditions, the seeing during the observation was $\sim 1.6''$, however, the AO system was able to reduce this to a final FWHM of the point spread function (PSF) of $\sim 0.7''$. The data are not ideal to study the effect of the AO system on the MUSE PSF as there is only one bright foreground star in the FOV that is located close to the centre of the galaxy. Its light profile therefore suffers from strong contamination from the bright galaxy background. Nonetheless, we fitted both a Gaussian and Moffat profile using IMFIT (Erwin 2015) and achieved equally good results. We therefore assumed a Gaussian PSF profile with a FWHM of $0.7''$ needed for the extraction of GC spectra although the precise shape of the PSF is not crucial for our study. The PSF FWHM corresponds to the effective radius of the NSC in FCC 47 (also $0.7''$), meaning that the especially large NSC allowed us to formally resolve it, while usually NSCs at this distance cannot be resolved with MUSE in the wide field mode.

We processed the raw data following the standard reduction pipeline version 2.2 (Weilbacher et al. 2014) incorporated in a ESO reflex environment (Freudling et al. 2013) that is able to handle the AO data. The data reduction includes bias and overscan subtraction, flat-field correction, wavelength calibration, determination of the line-spread function, and illumination correction. To further reduce the sky residual lines, we applied the Zurich Atmosphere Purge (ZAP) principal component analysis algorithm (Soto et al. 2016)[3].

[3] https://zap.readthedocs.io/en/latest/

2.3 Extraction of spectra

In the following, we describe how MUSE spectra from the different stellar components in FCC 47 were extracted. We differentiate between the integrated galaxy light, the GCs, and the NSC. The methods described here are similar to those that are used in the following chapters, but were further improved throughout this thesis.

2.3.1 Galaxy stellar light

The extraction of stellar light kinematics and especially stellar population properties requires a minimum spectral signal-to-noise ratio (S/N). To get a continuous view of these properties from the integrated stellar light, we binned the MUSE data with the Python version of the Voronoi binning routine described in Cappellari & Copin (2003a). This method enables an adaptive binning to provide a constant spectral S/N per bin.

For FCC 47, we chose a target S/N of 100 to ensure an accurate extraction of the line-of-sight velocity distribution (LOSVD) parameters as well as the metallicity, stellar age, and α-element abundance. For the purpose of creating a reliable dynamical Schwarzschild orbit-superposition model, S/N = 100 is necessary (Krajnović et al. 2015). To avoid accreting large bins in the outer regions, where errors are strongly non-Poissonian, we excluded all spaxels with S/N < 1. The Voronoi-binned MUSE cube contains 435 bins (see Fig. 2.6).

2.3.2 Globular clusters

To extract the spectra of GCs from the MUSE cube, we performed the following steps: First, their spatial location in the unbinned MUSE data was determined. This is difficult in the collapsed MUSE image as the majority of GCs (among other point sources) are hidden in the high surface brightness area of the galaxy. For this reason, we determined the individual GC positions after subtracting a model of the galaxy creating a residual image in which the point sources can be identified with standard peak-finding methods. While this has been commonly done in photometric studies, here we have the extra fidelity and luxury of being able to identify the residual signatures of GCs in each single wavelength slice of the MUSE data cube. To ensure a sufficient spatial S/N for the detection of GCs, we created residual images of different slabs from the blue to the red end of the data cube, each containing 50 combined wavelength slices.

A variety of different approaches were tested to create residual images including a simple unsharp mask approach using a median filter, Multi Gaussian Expansion (MGE) modelling (Bendinelli 1991; Monnet et al. 1992; Emsellem et al. 1994; Cappellari 2002), and a multi-component IMFIT model (Erwin 2015). The unsharp mask approach has to be used carefully to avoid losing the faintest GCs and sources in the bright central region. Using MGE or IMFIT yielded consistent results, but for reasons of time efficiency, we used a simple MGE model using the code described in Cappellari (2002) in the following. The MGE technique models the two-dimensional surface brightness distribution of a galaxy as a arbitrary number of two-dimensional Gaussian functions. These do not represent physical components in galaxies, but this technique is a computationally fast method to model

galaxy light distributions. For galaxies that have a more complex morphology (e.g. disks with bulges), MGE modelling might be insufficient for removing the galaxy light and IMFIT should be used in these cases.

After the MGE model is subtracted from the white-light image of FCC 47, point sources can be extracted using DAOSTARFINDER, a Python module that implements the DAOPHOT algorithm (Stetson 1987) into a Python class. This code is usually used to find real point sources like stars, but also detects slightly extended sources very well. DAOSTARFINDER returns a list of image coordinates of point sources, but these are not exclusively GCs. A contamination from unresolved background galaxies and foreground stars has to be considered. We used the ancillary catalogue of GC candidates from the ACSFCS (Jordán et al. 2015) for cross-reference and to build the initial sample of GC candidates. The candidates in this catalogue were selected based on their photometric and morphological characteristics, following the approach described in Jordán et al. (2007).

We detected 42 GC candidates from the HST catalogue of FCC 47 out of 93 in the MUSE pointing and used the associated positional information to extract their spectra from the MUSE cube. We used a PSF-weighted circular aperture extraction assuming a Gaussian PSF with FWHM = 0.7″ (3.5 pixels) on the original data cube. Because many of the GC candidates are in high surface brightness areas, we also extracted and subtracted a background spectrum from an annulus aperture around each GC candidate to characterise the local galaxy contribution. The annulus had a width of 5 pixel and the inner radius was placed 8 pixels from the GC centre. The background spectrum was averaged over the used pixels to normalise for the area and no further scaling is applied. For GCs closer than 10″ from the galaxy centre we chose an aperture width of 3 pixels and a distance of 6 pixels because of the more strongly varying background. For GCs with distances larger than 30″, we use annuli with a width of 9 pixels to ensure a high S/N background spectrum. However, for these outer GCs, the background level is low. The annulus size was chosen to optimise the S/N of the final background-subtracted GC spectrum. Choosing a size that differs by only a few pixels does not affect the recovered radial velocities and mean metallicities considerably, but can increase the uncertainties by a few percent.

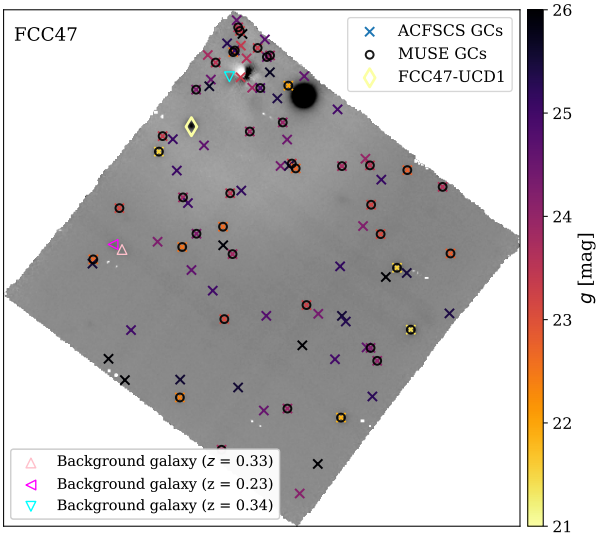

Figure 2.3.: Residual image of FCC 47 after subtracting a MGE model of the galaxy. The coloured crosses show the position of GC candidates in the HST catalogue of Jordán et al. (2015), colour-coded by their *g*-band magnitude. The black circles show the position of 42 GC candidates that are found with the DAOSTARFINDER routine in the MUSE data by cross referencing with the catalogue. The diamond indicates the position of FCC 47-UCD1 with a *g*-band magnitude of ∼ 21 mag. The triangles indicate the positions of emission-line background galaxies we found in the MUSE cube.

Inspecting the GC spectra, we found one GC candidate close in projection to the NSC that is not a GC, but rather a star-forming background galaxy at redshift $z \sim 0.34$ with visible emission lines of hydrogen, nitrogen and oxygen. In addition to this object, we found two other background galaxies with strong emission lines in the MUSE cube as shown in Fig. 2.3.

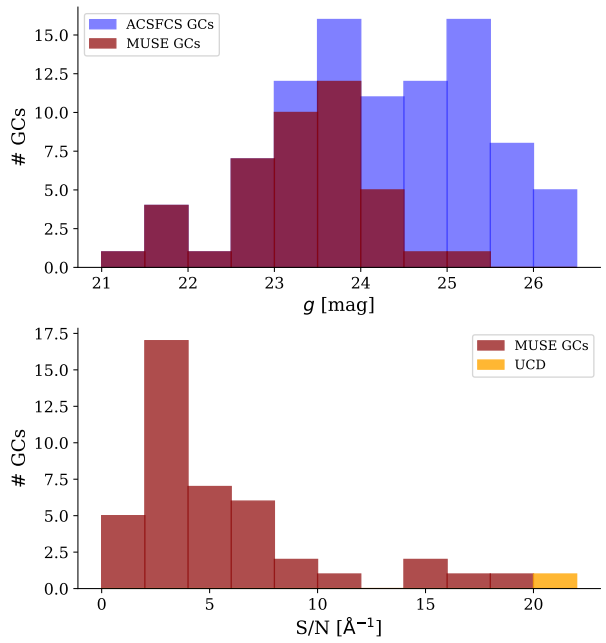

Figure 2.4.: Distributions of magnitudes and S/N of the extracted GCs. Top: Distribution of g-band magnitudes of the GC candidates in the MUSE FOV from Jordán et al. (2015) (blue). The red distribution highlights the GC candidates found in the MUSE data with our method. Bottom: Histogram of spectral S/N of the GC candidates and FCC 47-UCD1.

The top panel in Fig. 2.4 shows a histogram of all GC g-band magnitudes from ACSFCS in comparison to the ones that were found in the MUSE data. It reveals that our sample is complete down to a g-band magnitude of 23 mag. We are missing five GCs with a magnitude of < 24 mag because they all lie within $10''$ in projection from the galaxy centre. In this central region, the extraction of GCs is difficult due to the strongly varying galaxy background that is not completely removed by our MGE model, as the residuals show (Fig. 2.3). The bottom panel of Fig. 2.4 shows the histogram of spectral S/N of the extracted GCs, determined in a continuum region around 6500 Å. We found 25 GCs with S/N > 3, out of those 17 have S/N > 5 and 5 GCs even reach S/N > 10. A S/N > 3 is required to measure a reliable line-of-sight (LOS) velocity and to confirm membership to the FCC 47 systems. The remaining candidates cannot be confirmed as GCs due to their low S/N. With our approach we found 42 of 93 (45 %) GC candidates from the ACSFCS catalogue in the MUSE FOV. The detection of GCs with MUSE strongly depends on the PSF FWHM.

In addition to the GC candidates that were already in the catalogue, it is possible to add sources manually by inspecting their spectra. We reported the discovery of a UCD with a spectral S/N ~ 20 in an accompanying paper (Fahrion et al. 2019a, see Sect. 2.7). We included FCC 47-UCD1 in the analysis of the GCs presented below, but highlight it as a distinct object in the associated figures.

2.3.3 Spectrum of the nuclear star cluster

The exceptionally large size of the NSC in FCC 47 and its brightness allowed us to extract a MUSE spectrum of the NSC. The analysis from Turner et al. (2012) showed that the NSC dominates the inner $\sim 0.5''$ by more than 2 magnitudes. This implies that the inner few spaxels are completely dominated by the light of the NSC, however, there still is a

non-negligible contribution from the underlying galaxy. To extract a clean NSC spectrum we used a similar approach as for the GC spectra and used a PSF-weighted circular aperture in combination with a annulus-extracted background spectrum. This approach treats the NSC as another point-source, although it is formally resolved within our MUSE data. Nonetheless, we chose the PSF-weighted extraction to maximise the flux from the NSC. The galaxy background was determined in an annulus aperture that is placed at 5 pixels separation from the central pixel and has a width of 3 pixels. This way, we determined the galaxy contribution directly outside of the NSC, which is crucial to estimate the flux level of the background that shows a strong gradient in the central region. We subtracted the background spectrum from PSF-weighted NSC spectrum both normalised to the same area without additional weighting, such that we assume that the background flux level is flat between the centre and the position where we extract the annulus spectrum. This is a justified assumption for FCC 47 as for example the double Sérsic decomposition as presented in Turner et al. (2012) shows. From the position where we take the annulus spectrum to the centre, the galaxy component's surface brightness varies by < 1 mag arcsec^{-2}, but this depends on the two component Sérsic fit to the galaxy light profile. For reference, we show the local galaxy spectrum together with the background subtracted NSC spectrum in Fig. 2.5. The galaxy background is clearly bluer than the NSC and thus applying an additional weight to it in the subtraction would result in a even redder NSC spectrum. The background-subtracted NSC spectrum has a spectral S/N ~ 125. To be applicable to other galaxies, this method of extracting the NSC spectrum was refined as described in Chapt. 5.

2.4 Extracting kinematics and stellar population properties

The following sections describe how we extracted kinematics and stellar population properties from the extracted MUSE spectra. Again, we differentiated between galaxy light, NSC, and GCs.

2.4.1 Full spectrum fitting with PPXF

For external galaxies, extraction of integrated stellar kinematics is done with broadened stellar templates. For example, the established IRAF routine FXCOR determines radial velocity and velocity dispersion of a spectrum by cross-correlating in Fourier space with a template spectrum (Fitzpatrick 1993). Nowadays this comparison is often done in pixel space rather than Fourier space to enable simultaneous extraction of stellar populations and gas kinematics while also allowing for masking of bad pixels and other observational effects.

In this thesis, I used Python implementation of the penalised pixel-fitting (PPXF) method[4] (Cappellari & Emsellem 2004; Cappellari 2017) to extract the stellar kinematics and population properties, such as mass-weighted mean ages and metallicities, from the MUSE spectra. PPXF is a full spectrum fitting method that uses a penalised maximum

[4] https://www-astro.physics.ox.ac.uk/~mxc/software/

likelihood approach to fit a combination of user-provided template spectra to the target spectrum. The main ingredients of PPXF are described in the following and a more detailed description can be found in Cappellari (2017).

The model galaxy spectrum $G_{\rm mod}$(x) as a function of $x = \ln\lambda$, the natural logarithm of the wavelength λ, can be described as a convolution of the template spectrum $T(x)$ with the LOSVD L as the latter determines the line positions and their broadening:

$$G_{\rm mod}(x) = T(x) * L(cx), \tag{2.1}$$

where c is the speed of light. If the template was not obtained with the same instrument as the galaxy spectrum, it further has to be broadened to match the instrumental resolution, introducing another convolution.

In PPXF, the galaxy spectrum is modelled via:

$$G_{\rm mod}(x) = \sum_{n=1}^{N} w_n \left\{ [T_n(x) * L_n(cx)] \sum_{k=1}^{K} a_k P_k(x) \right\} + \sum_{m=0}^{M} b_m P_m(x) + \sum_{j=0}^{J} c_j S_j(x), \tag{2.2}$$

where T_n are the N templates used in the fit that can have different LOSVDs L_n and w_n are their weights. P_k and P_m are multiplicative and additive polynomials of degree k and m. Additive polynomials can minimise template mismatch but because they affect the strength of individual absorption lines, they should only be used to derive the LOSVD parameters. Multiplicative polynomials correct the spectrum for inaccuracies in the spectral calibration. S_j are spectra of the sky that can be included in the fit if a sky subtraction is lacking.

In PPXF, the LOSVDs $L_n(v)$ as a function of velocity v are described with a Gauss-Hermite parametrisation (van der Marel & Franx 1993; Gerhard 1993):

$$L(y) = \frac{\exp(-y^2/2)}{\sigma\sqrt{2\pi}} \left[1 + \sum_{i=3}^{I} h_i H_i(y) \right], \tag{2.3}$$

where $y = (v - V)/\sigma$, with the radial velocity V and velocity dispersion σ. Additional moments of the LOSVD are parametrized with Hermite polynomials H_i (with coefficients h_3, h_4, etc) that describe deviation from the Gaussian form.

In the fitting process, PPXF minimises the mismatch between model spectrum (quantified, e.g. by the LOSVD and the polynomials as in Eq. 2.2) and observed spectrum by solving for the weights w_n. By construction, PPXF penalises against non-Gaussian solutions of the LOSVD when the data quality is insufficient to obtain its full shape. As output, PPXF returns both the best-fitting values of the LOSVD and the weights w_n of the used model spectra. As the model spectra are typically characterised by varying stellar population parameters, for example by a Cartesian grid of age and metallicity, the weights enable a reconstruction of the best-fitting mean age and metallicity.

2.4.2 Choice of SSP models

Throughout this thesis, I used MILES SSP models[5] (Vazdekis et al. 2010). These SSP synthesis models give the spectral energy distributions for stellar populations of a single age

[5] http://research.iac.es/proyecto/miles/

and single metallicity. The original MILES spectra have a coverage between 3525 and 7500 Å. The extended library, called E-MILES, covers a broader wavelength range from 1680 to 50000 Å including the spectral lines of the Calcium Triplet around 8500 Å. The template spectra in both libraries have a spectral resolution of 2.5 Å (Falcón-Barroso et al. 2011), the mean instrumental resolution of MUSE. Throughout this work, I used the description of the line-spread function from Guérou et al. (2016), BaSTI isochrones (Pietrinferni et al. 2004, 2006) and a Milky Way-like, double power law (bimodal), IMF with a high mass slope of 1.30 (Vazdekis et al. 1996).

Although the E-MILES templates allow us to fully exploit the broad wavelength coverage of the MUSE instrument, only 'baseFe' models are available. These reproduce the metallicity and light-element abundance pattern of the Milky Way and assume [M/H] = [Fe/H] for high metallicities. For lower metallicities, α-enhanced input spectra are used, such that [M/H] is higher than [Fe/H] (Vazdekis et al. 2010). On the other hand, the MILES models have a restricted wavelength range, but additionally offer scaled solar models ([α/Fe] = 0) and alpha enhanced models ([α/Fe] = 0.4 dex). These α-variable MILES models allow to study the distribution of α-abundances from high S/N spectra. Because the original MILES library only offers two different [α/Fe] values, using a regularised fit with pPXF seems unphysical. To create a better sampled grid of SSP models for the fits, we linearly interpolated between the available SSPs to create a grid from [α/Fe] = 0 to [α/Fe] = 0.4 dex with a spacing of 0.1 dex. These models were created under the assumption that the [α/Fe] abundances behave linearly in this regime and only give the average [α/Fe], however, in reality the abundances of different α-elements might be decoupled. The low S/N of the GC spectra make an extraction of [α/Fe] abundances challenging. We therefore fitted the GCs with the E-MILES SSP templates to exploit the broad wavelength range of these models, but we noted a metallicity offset of 0.2 dex between E-MILES and scaled-solar MILES models. This is caused by the way the E-MILES templates are constructed to match the Milky Way abundance pattern: the input low-metallicity spectra are metal-enhanced (Vazdekis et al. 2016).

To summarise, we used the baseFe E-MILES templates for the GC spectra on the full MUSE wavelength range to determine estimates of the LOS velocity and metallicities. To extract ages, metallicities and [α/Fe] abundances from the high S/N spectra of the NSC and the integrated stellar light, we used the α-variable MILES spectra on a wavelength range from 4500 to 7100 Å.

We did not fit simultaneously for the kinematics and stellar population properties, but used a two-step approach (Sánchez-Blázquez et al. 2014). Each spectrum was first fitted for its LOSVD parameters using additive polynomials of order 25 and no multiplicative polynomials to ensure a well-behaved continuum that is necessary to get an accurate measurement of the LOSVD parameters. In the second step, the LOSVD parameters were fixed for the fit of the stellar population parameters and we used multiplicative polynomials of order eight instead of additive polynomials as the relative strength of absorption lines is crucial to determine the stellar population properties. In the end, the pPXF fit returned the LOSVD parameters and the weight coefficients of each input SSP template. In this way, the age and metallicity distributions can be recovered.

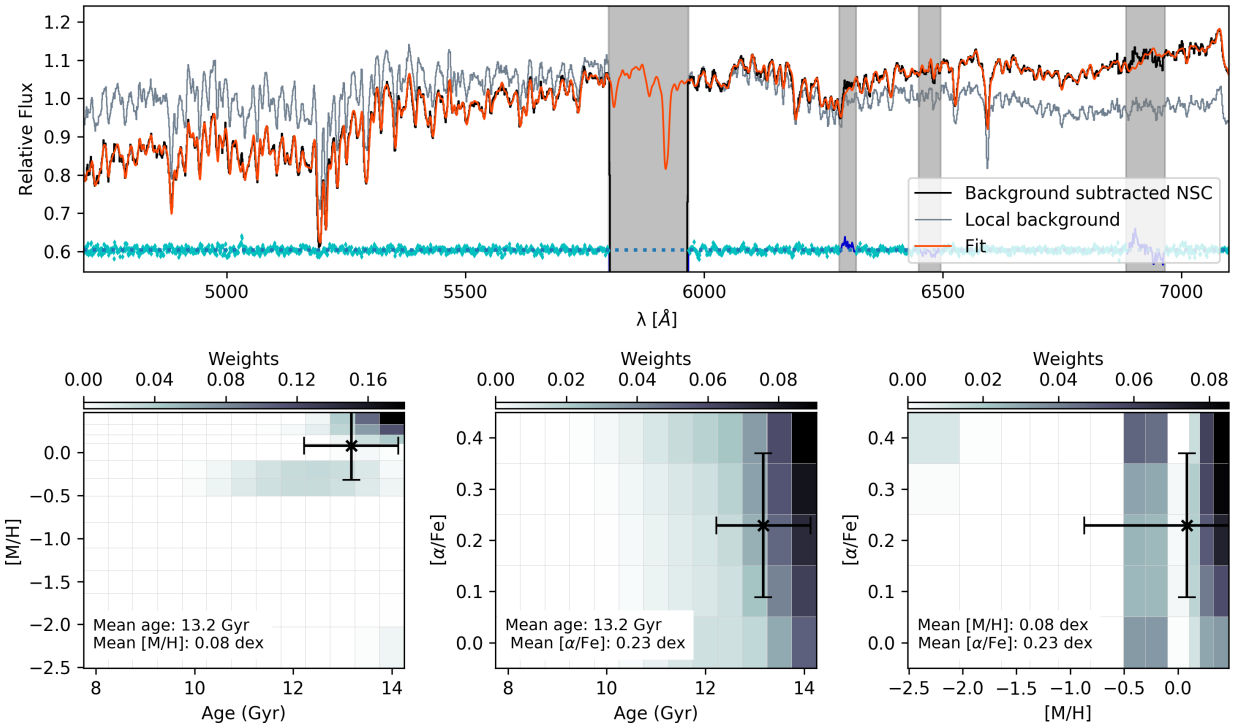

Figure 2.5.: PPXF fit to the background-subtracted NSC spectrum of FCC 47. *Top*: The original normalised spectrum is shown in black, the best-fit spectrum in red. For comparison, the spectrum of the local galaxy background is shown in grey. The residual is shown in blue, shifted to 0.6 for visualisation. Masked regions appear as grey shaded. We masked strong sky line residuals as well as the empty region around the sodium D line that is filtered out due to the AO lasers. *Bottom*: Weight maps illustrating the age - metallicity (*left*), age - [α/Fe] (*middle*) and [α/Fe] - metallicity (*right*) grids. The weight of each template used in the fit is given by the greyscale. The black cross shows the weighted mean age, metallicity, and α-element abundance with errorbars. The weight maps are normalised. A regularisation parameter of 30 was used in this fit.

2.4.3 Galaxy light and NSC spectrum

The high S/N of the binned stellar light and the NSC spectrum allowed us to accurately measure the LOSVD parameters and recover the distribution of ages and metallicities. We fitted for the LOS velocity, the velocity dispersion, and the higher order moments h_3 and h_4.

We estimated the typical uncertainties of the kinematic fit using a Monte Carlo (MC) approach (e.g. Cappellari & Emsellem 2004; Pinna et al. 2019a). After the first fit, we drew randomly from the PPXF residual in each wavelength bin and added this to the (noise-free) best-fit spectrum to create 300 realisations that were fitted to obtain a well-sampled distribution. The uncertainty is then given by the standard deviation (or 16th and 84th percentile) of this distribution. Testing uncertainties in five different bins, we found maximum uncertainties of 4 km s^{-1} and 6 km s^{-1} for the stellar LOS velocity and velocity dispersion, respectively. For the higher moments of the LOSVD, h_3 and h_4, we found typical uncertainties of 0.02 km s^{-1} for both.

By construction, using SSP templates discretises the stellar population distribution of a galaxy. Regularisation can be used to find a smooth solution by enforcing smooth variations from one weight to its neighbours. This is especially crucial for the recovery of SFHs from the data. Finding the right regularisation parameter is, however, non-trivial (see e.g, Böcker et al. 2020). Typically, the regularisation parameter is determined on a sub-sample of spectra and then kept fixed (as described in McDermid et al. 2015). We calibrated the regularisation on a few binned spectra taken from the central part of the galaxy following the recommendation by Cappellari (2017) and McDermid et al. (2015): Firstly, the noise spectrum is rescaled to obtain a unit χ^2 in an unregularised fit. Then, the regularisation parameter is given by the one that increases the χ^2 value of the fit by $\sqrt{2N_{\rm pix}}$, where $N_{\rm pix}$ is the number of fitted (unmasked) spectral pixels. This value gives the smoothest solution that is still consistent with the data. Based on this calibration, we used a regularisation parameter of 70 for the binned stellar light fits.

We treated the cleaned NSC spectrum similarly to the galaxy light spectra. It has a S/N of 125 that allows to extract age, metallicities and [α/Fe] distributions. Because of this high S/N, we calibrated the regularisation separately and used a regularisation parameter of 30 for the PPXF fit. Figure 2.5 shows the fit to the cleaned NSC spectrum. The bottom panels of this figure show the grid of age, metallicity, and [α/Fe] models. The best-fit model is the weighted sum of the SSPs with their weights colour-coded.

2.4.4 Globular clusters

In contrast to the stellar light, the GCs have a low S/N (< 20). This prevented us from detailed stellar population analysis as especially the age is ill-constrained at this spectral quality, and fitting α-element abundances is even more challenging. In addition, the intrinsic velocity dispersion of typical GCs is $\sigma_{\rm GC} \sim 10$ km s^{-1}, well below the MUSE instrumental resolution and therefore not accessible. Nonetheless, bright GCs allowed us to determine their radial velocity and estimate their mean metallicity. We tested the requirements for the S/N as described in Appendix A.1 and found that radial velocities can be recovered down to a S/N > 3, whereas the mean metallicity can be estimated for S/N > 10 under the

assumption that the GCs are single stellar population objects. In later projects of this thesis, we relaxed the latter S/N criterion to S/N $\geq$ 8, see Sect. 4.3.3. We used the E-MILES SSP models to fit the GCs, because their broad wavelength range helps to reduce uncertainties.

Since the S/N varies strongly among the GCs, we determined the radial velocity (and, if possible, the mean metallicity) with its uncertainty for each GC using 300 realisations in an MC-like fashion as described in Sect. 2.4.3. As we could not find indications of young ages ($<$ 10 Gyr) in unrestricted fits, we restricted the SSP library to ages $>$ 10 Gyr to speed up the MC runs for the velocity and metallicity measurements. In the best cases, the random uncertainties on the velocity and metallicity, determined from the width of the MC distribution, were $<$ 10 km s^{-1} and $\sim$ 0.10 dex, respectively. The afore mentioned regularisation approach can be used for high S/N spectra of the stellar light and the NSC. For the GCs, however, we assumed them to be SSP objects and do not use regularisation in the fit. The mean metallicity should be unaffected. As mentioned before, choosing the α-enhanced MILES models instead of the E-MILES causes a constant shift of $\sim$ 0.2 dex towards higher metallicities, while relative metallicities stay constant.

2.5 Kinematics of FCC 47

In the following, we describe our results of the extraction of kinematics from the MUSE spectra. We differentiate between the high S/N spectra of integrated galaxy light and the low S/N results from the GCs.

2.5.1 Galaxy light

The maps of stellar light LOS mean velocity v, velocity dispersion σ, and the higher order LOSVD parameters h_3 and h_4 for FCC 47 are shown in Figure 2.6. The velocity map revealed FCC 47's interesting velocity structure. While there is no net rotation visible at larger radii in the FOV, a small rotating disk with a diameter of roughly 20″ ($\sim$ 2 kpc) is found near the centre. This feature is rotating with a maximum velocity of $\lesssim$ 20 km s^{-1}, relative to the systemic galaxy velocity of 1444.4 $\pm$ 2.0 km s^{-1}. This disk structure is rotating along the main photometric axis, whereas the very centre of FCC 47 is rotating around a different axis offset by $\sim$ 115°. The NSC rotation is seen over an extent of $\sim$ 3″ (250 pc, 15 pixels).

The velocity dispersion map shows a strong peak in the centre, where it reaches values of $\sim$ 125 km s^{-1} and drops sharply to values of $\sim$ 80 km s^{-1} before showing a more gradual decrease to values $<$ 60 km s^{-1} in the outskirts. The h_3 and h_4 maps are rather featureless, but h_3 shows anti-correlation to the rotation of the disk structure.

The rotation in the centre matches the rotation of the NSC as studied by Lyubenova & Tsatsi (2019) using SINFONI+AO data (see Fig. 1.9). In the MUSE data, the NSC does not reach the same maximum velocity and velocity dispersion as in the SINFONI data. The maximum rotation velocity is reduced from $\sim$ 60 km s^{-1} observed with SINFONI down to $\sim$ 20 km s^{-1}. Additionally, the velocity dispersion is less peaked in the MUSE data and only reaches 125 km s^{-1} instead of 160 km s^{-1} in the SINFONI data. By convolving the SINFONI maps to match the MUSE PSF with a Gaussian kernel, we found that this difference is

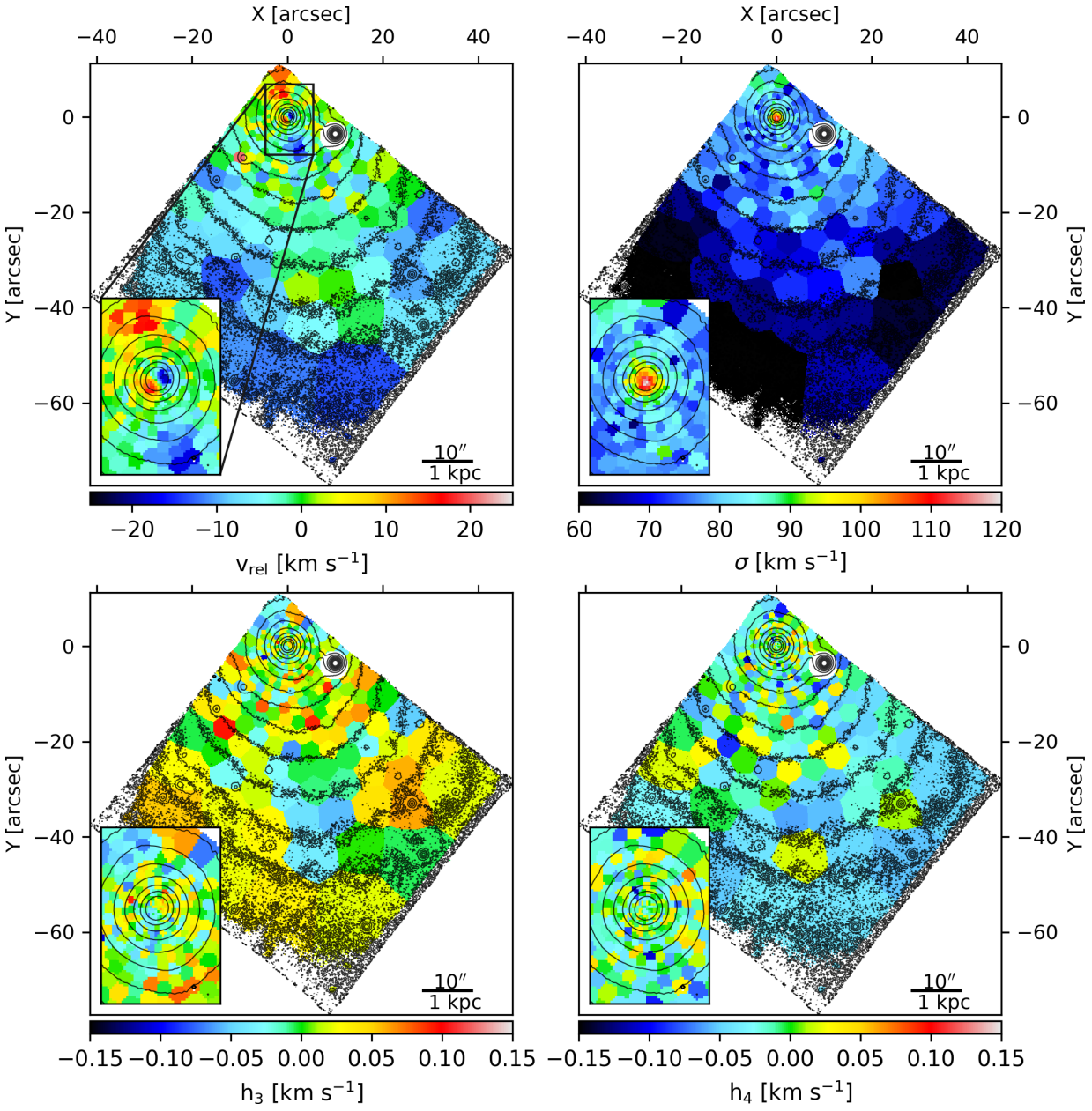

Figure 2.6.: Stellar light kinematic maps for FCC 47 acquired from the Voronoi-binned MUSE cube. *Top left*: Mean relative velocity of the integrated light with respect to a systemic velocity of 1444 km s^{-1}. *Top right*: Velocity dispersion σ. *Bottom left*: h_3 and *bottom right*: h_4. The inset shows a zoom to the central region to highlight the inner structure. We show the same isophotes as used in Fig. 2.1. The effective radius of the NSC (0.7″) corresponds to the radius of the innermost isophotal contour.

caused by the larger MUSE PSF that smears out the NSC's contribution to the velocity structure. This clear link between the SINFONI and MUSE structures shows, however, that the rotating central structure is indeed the NSC of FCC 47.

Both the rotating disk structure and the NSC classify as a kinematically decoupled component (KDC) because they are decoupled from the non-rotating main body of FCC 47. KDCs were discovered decades ago with long-slit spectroscopy (Efstathiou et al. 1982; Franx & Illingworth 1988). Large IFS surveys such as SAURON (Bacon et al. 2001) or ATLAS3D (Cappellari et al. 2011) have revealed that a significant fraction of ETGs have a KDC, especially slow-rotators (Emsellem et al. 2007). Simulations suggest that the formation of KDCs is triggered by major mergers (Jesseit et al. 2007; Bois et al. 2011; Tsatsi et al. 2015), but once formed, a KDC can be stable over a long time in a triaxial galaxy (van den Bosch et al. 2008; Rantala et al. 2019). KDCs are not rare in slow-rotating galaxies like FCC 47, however two decoupled components certainly are. To explore the nature and origin of FCC 47's dynamical structure, we constructed an orbit-based dynamical Schwarzschild model based on the MUSE kinematic data (Sect. 2.5.2).

Using the Wide Field Spectrograph (WiFeS, Dopita et al. 2010) on the Australian National University 2.3-m telescope, Scott et al. (2014) presented LOS velocity and velocity dispersion maps of FCC 47 among nine other ETGs in the Fornax clusters and classified FCC 47 as a fast rotator based on their data. However, we find that our MUSE maps do not resemble the WiFeS data at all. The reason for this is unknown.

2.5.2 Orbit-based dynamical model of FCC 47

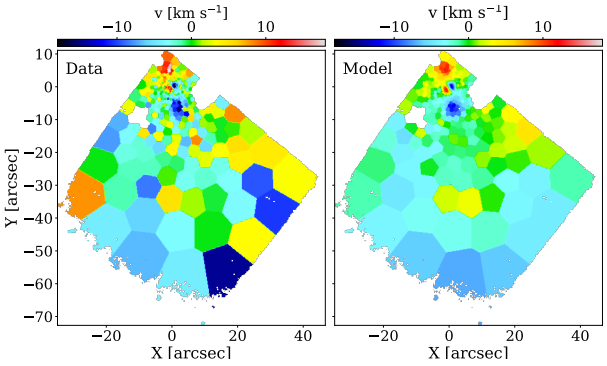

Figure 2.7.: LOS velocity map of FCC 47 (*left*) and velocity map of the best-fitting Schwarzschild model (*right*). The white patches indicate masked bins.

In this section we briefly summarise the results from the orbit-based dynamical Schwarzschild model that was used to infer the orbital structure of FCC 47 from the MUSE data. The full description can be found in Sect. 7 of Fahrion et al. (2019b). A detailed description of the concept of Schwarzschild modelling can be found in van den Bosch et al. (2008); van de Ven et al. (2008), and Zhu et al. (2018b).

Schwarzschild modelling directly infers the distribution function that describes the positions and velocities of all stars in a galaxy, as the weights of orbits in the galaxy's gravitational potential. In this way, not only mass and density profiles can be determined, but it is also possible to explore the orbital structure of a galaxy. To create a Schwarzschild model, first a suitable model of the gravitational potential has to be constructed. Then, a representative orbital library for this potential is calculated, and finally, a combination of orbits that reproduce the observed light distribution and kinematic maps is found.

The Schwarzschild model of FCC 47 reproduced the rotational structures of the NSC and

the disk component as shown in Fig. 2.7. Our model finds a total stellar mass of FCC 47 of $M_{\rm gal} = 1.5 \pm 0.1 \times 10^{10} M_{\odot}$, and, extrapolated outside of our data coverage, a total mass of the dark halo $M_{\rm vir} = 1.1 \pm 1.0 \times 10^{12} M_{\odot}$. The uncertainty is large due the lack of data at larger radii.

The Schwarzschild model reveals the orbital structure of FCC 47, which is shown in Fig. 2.8. This figure shows the distribution of circularity λ (a measure of angular momentum, where $\lambda = 0$ indicates hot orbits and $\lambda = \pm 1$ refers to cold, disk-like orbits) versus radius. We found that the orbital distribution around the short axis is complex (λ_z). In the inner region, the orbital structure is dominated by hot and warm orbits. Over all radii, the fraction of counter-rotating orbits is high, which explains the negligible rotation in the outskirts of the galaxy as the two counter-rotating populations with warm orbits cancel each others rotation signatures while still showing a high velocity dispersion. This kinematic feature has been routinely observed in galaxies hosting extended counter-rotating stellar components (see Corsini 2014 for a review).

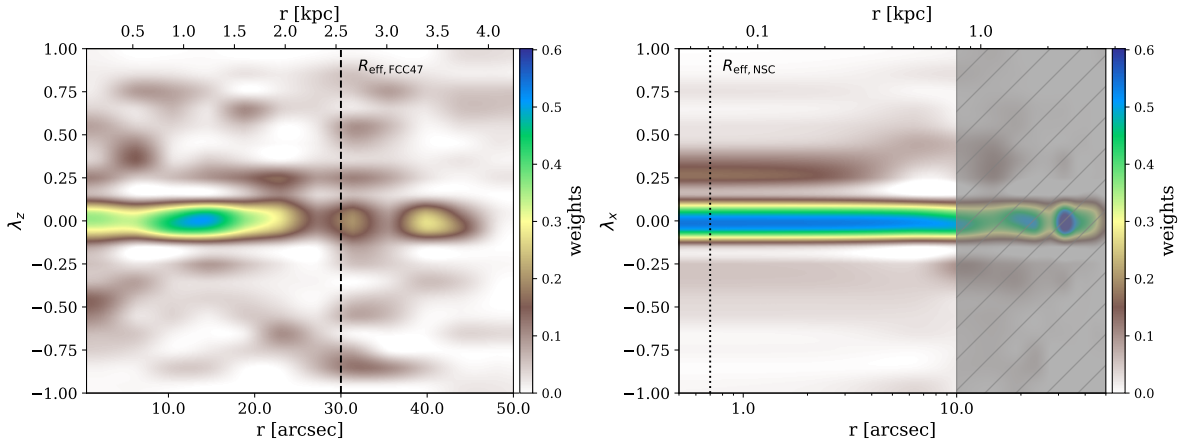

Figure 2.8.: Distribution of orbital weights of the Schwarzschild model of FCC 47. *Left*: Circularity λ_z of the used orbits along the long axis versus radius. *Right*: Distribution along short axis. The shaded area shows the region where we lack coverage with the MUSE data along the short axis.

The orbit distribution for the circularity around the long axis (λ_x) shows less structure. It is completely dominated by hot orbits over all radii, but we can identify the signature of the NSC as kinematically colder orbits that create the rotation feature of the NSC.

The orbital distributions shown in Fig. 2.8 reveal the nature of the two kinematically decoupled components in FCC 47. The rotation of the disk seen on a ~ 2 kpc scale (see Fig. 2.6) is not a decoupled component as such, instead the high fraction of counter-rotating orbits indicate that this apparent rotating disk is the result of two much more extended counter-rotating populations that show an imbalance on the scale of the disk. The small rotation amplitude of the apparent disk rotation can be explained by this small difference in mass fractions. On the other hand, the NSC appears to be a separate component with a distinct kinematic signature. Besides the NSC, there is no evidence for other populations that show disk-like prolate rotation. The limited spatial resolution of the MUSE data does not allow to estimate a contribution from a central SMBH to this mass.

2.5.3 Globular clusters

For the 25 GCs with S/N > 3 we determined their radial velocities with pPXF. We could not find any signs of rotation in the GC system due to our small sample size. Figure 2.9 shows the relative GC velocities with respect to the systemic velocity of FCC 47 as function of their projected distance from the galactic centre, colour-coded by their $(g - z)$ colour from the ACSFCS catalogue (Jordán et al. 2015).

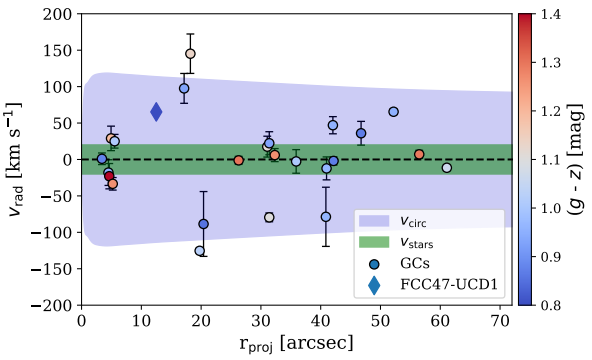

Figure 2.9.: Radial profile of GC LOS velocities in comparison to the observed scatter in stellar light velocities (green) and the circular velocity profile (blue).

The blue shaded area gives the circular velocity amplitude for FCC 47 based on the results from our dynamical model (Sect. 2.5.2). FCC 47-UCD1 is shown as the diamond symbol. The green shaded area indicates the maximum visible rotation amplitude seen in the stellar light map and reveals that the radial velocities for many GCs do not exceed the circular velocity amplitude, meaning that they are bound to FCC 47. This is particularly true for the red GC population ($g - z > 1.16$ mag) as they show less scatter around the systemic velocity of FCC 47, having a velocity dispersion of 23.0 $\pm$ 3.8 km s^{-1}. The blue GCs, however, span a wider range of velocities and have a velocity dispersion of 42.0 $\pm$ 6.8 km s^{-1}. The uncertainties refer to the uncertainties from fitting a Gaussian distribution to the histogram of LOS velocities.

2.6 Stellar population properties of FCC 47

Besides kinematics, we also extracted stellar population properties from the MUSE spectra of the galaxy, the NSC, and the GCs. In the following we describe our results of the stellar population analysis.

2.6.1 Galaxy light

From the weights given by the regularised pPXF fit of the α-variable MILES SSP template spectra to the Voronoi binned data, we constructed maps of mean age, metallicity, and α-element abundance ratios ([α/Fe]) as shown in Fig. 2.10. The centre of FCC 47 reaches super-solar metallicities and shows a strong gradient towards lower metallicities within 10″ from the centre. The outskirts reach a metallicity of ~ -0.4 dex. The extent of the metal-rich central region is the same as the rotating NSC seen in Figure 2.6. As the comparison to SINFONI data showed, this region is completely dominated by the light from the NSC, smeared out by the MUSE PSF. The NSC appears to be significantly more metal-rich than the surrounding galaxy. The shown maps were extracted using the α-variable MILES

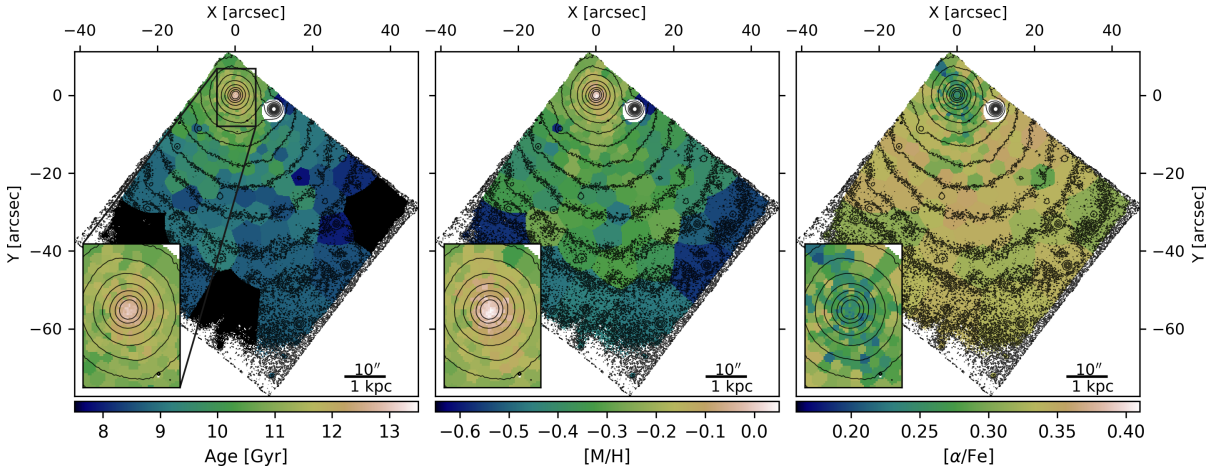

Figure 2.10.: Stellar population maps of FCC 47. Mean ages (*left*), metallicities [M/H] (*middle*) and [α/Fe] abundance ratios (*right*) as determined from a full spectrum fit with pPXF using the α-variable MILES template spectra. The maps are mass-weighted. We show the same isophotes as in Fig. 2.1. The inset shows a zoom to the central region and the innermost isophote contour corresponds to the size of the NSC ($R_{\rm eff}$ = 0.7″).

models, but we found a very similar metallicity distribution when using the baseFe E-MILES models, however, shifted to lower metallicities by 0.2 dex (see the metallicity gradient shown in Fig. 2.11). This is most likely caused by the rather smooth distribution of α-abundances in the outskirts, as the right panel in Fig. 2.10 illustrates. This is in contrast to the MW-like behaviour, encapsulated in the baseFe E-MILES models. The main body of FCC 47 is α-enhanced and shows lower values on the extent of the rotating disk structure. The NSC cannot be seen as a separate component in the [α/Fe] map, but shows similar values as the disk of [α/Fe] $\sim$ 0.25 dex.

FCC 47 is overall old ($>$ 8 Gyr) with a gradient towards older ages in the centre and the NSC ($\sim$ 13 Gyr). The outer galaxy seems to have formed last with the youngest ages found here. Using the recovered mass weights from the pPXF fit (see Fig. 2.4), we can explore how the mass fraction of different components change in different regions of FCC 47.

The mass fraction of the old stellar population ($>$ 11 Gyr) decreases from 93% in the background-subtracted NSC to 79% in the centre to 48% in the disk region (defined as the region where disk-like rotation is observed) to 20% in the rest of the galaxy. Using the same spatial decomposition, we found that the NSC is dominated by a metal-rich population ([M/H] $>$ 0 dex) that constitutes 67% of the mass in both the cleaned NSC spectrum and the central region. This mass fraction reduces to 47% in the disk and to 29% in the outskirts. Comparing the different maps, we find that the metallicity shows a strong gradient of $\sim$ 0.5 dex between NSC and the effective radius of the galaxy (30″) and the mean age decreases from 13 Gyr to 9 Gyr over the same extent, while the [α/Fe] abundances show a much milder gradient and increase by $\sim$ 0.1 dex.

2.6.2 The nuclear star cluster

We fitted the background-subtracted NSC spectrum separately to the binned stellar light (see Fig. 2.5), allowing a detailed study of the NSC's stellar populations. For comparison, we also show the spectrum of the local background that was used for the subtraction. This background spectrum is clearly bluer than the cleaned NSC spectrum and applying no subtraction would therefore bias the stellar population analysis towards younger ages or more metal-poor populations. From the weight maps shown in Fig. 2.5, we again found that the NSC shows little substructure in ages and thus must have formed very early on without any later episodes of star formation. However, we found indications of two separate populations that differ in metallicity: There seems to be a dominating metal-rich population and a secondary population with lower metallicities. The dominant metal-rich component constitutes 67% of the NSC mass. The two populations seem to have similar [α/Fe] values. We note, because our models only included [α/Fe] values from 0.0 to 0.4 dex, boundary effects from the model grid can introduce uncertainties, but the presence of two populations with different metallicities should be real.

The stellar population analysis allowed us to estimate the stellar mass of the NSC. As we did not have predictions for the mass-to-light ratio (M/L) from the α-variable MILES models, we fitted the NSC again with the E-MILES SSP models and use their predictions for the stellar M/L for each age and metallicity in the HST/ACS F475W filter. The inferred age and metallicity weights were then translated into M/L weights. The weighted mean M/L of the NSC is 5.3 $M_\odot/L_\odot$. Varying [α/Fe] will have a small effect on the M/L, however, the uncertainty of the derived mass is governed by the uncertainty on the magnitude. Turner et al. (2012) found an apparent magnitude of the NSC of 16.09 $\pm$ 0.19 mag in the ACS F475W filter (g band), translating to a luminosity of $L = (1.37 \pm 0.23) \times 10^8 L_\odot$, assuming a distance modulus of 31.31 mag (Blakeslee et al. 2009). For the photometric mass, we found $M_{\mathrm{NSC,\,phot}} = (7.3 \pm 1.2) \times 10^8 M_\odot$, corresponding to $\sim$5 % of the total stellar mass of FCC 47. The uncertainty was inferred from 1000 draws assuming a Gaussian distribution of the magnitude. With this mass, the NSC of FCC 47 is among the more massive known NSCs as was already expected from its large size. The mass agrees with the enclosed mass profile from the dynamical model within the inner 2.7″, the extent of the NSC in the MUSE data.

2.6.3 Globular clusters

Measuring the metallicities of the GCs is challenging due to the low S/N. The MUSE data enabled us to estimate spectroscopic metallicities for a sub-sample of 5 GCs and FCC 47-UCD1. For this measurement, we used the E-MILES SSP templates because they give the smallest uncertainty due to the broad wavelength range.

The metallicities of the five GCs and FCC 47-UCD1 are shown in a radial profile presented in Fig. 2.11. Four of those GCs have a blue colour and are metal-poor, while the fifth GC is red and metal-rich. Its metallicity is comparable to that of the NSC. Due to the low number of GCs with metallicity estimate, our view on FCC 47's GC system is biased.

We used the photometric colours to determine the total mass of the GC system in a similar

fashion to the mass of the NSC, however, mostly based on photometric SSP predictions that show an age-metallicity degeneracy. Under the assumption that all GCs have an age of 13 Gyr, we used the E-MILES SSP predictions for the HST/ACS filters to convert $(g-z)$ colours to metallicities and subsequently to M/Ls. With the g-band magnitudes from the HST catalogue, these are then converted to photometric masses. This way, we estimate the total mass of the GC system (including FCC 47-UCD1 and all GCs with pGC > 0.5 in the ACSFCS catalogue) to be $\sim 1.2 \times 10^8 M_\odot$. A mass fraction of 77 % is in the blue GC population ($g-z < 1.15$ mag), 23 % in the red. This estimate is not precise, but shows that the entire GC system only constitutes $\sim 17\%$ of the mass found in the NSC ($7 \times 10^8 M_\odot$), even though FCC 47 has a large GC system for its mass.

2.6.4 Metallicity distribution from the centre to the outskirts

Figure 2.11 shows the radial profiles of metallicity for the GCs, the UCD (Sect. 2.7), and the NSC in FCC 47. For this comparison, we exclusively used the metallicites obtained with the baseFe E-MILES SSP templates. The stellar light profile was extracted from the binned map using ellipses with constant position angle of 69° and ellipticity of 0.28.

This figure shows the variety of different stellar systems that were found within FCC 47 and their chemical composition. The highest metallicities are found at the centre of the galaxy, more precisely in the NSC that is even more metal-rich than an extrapolation of the galaxy metallicity gradient would imply. This is another indication that the NSC of FCC 47 is not just the continuation of the stellar light, but instead is a separate component. Most of the GCs and FCC 47-UCD1, on the other hand, have generally lower metallicities than the underlying stellar body of FCC 47 and are much more metal-poor than the NSC. However, we found one GC that has a higher metallicity than its local galaxy background, also indicated by its red colour. This GC is only slightly more metal-poor than the NSC and has a projected distance to the centre of $\sim 56''$(~ 50 kpc).

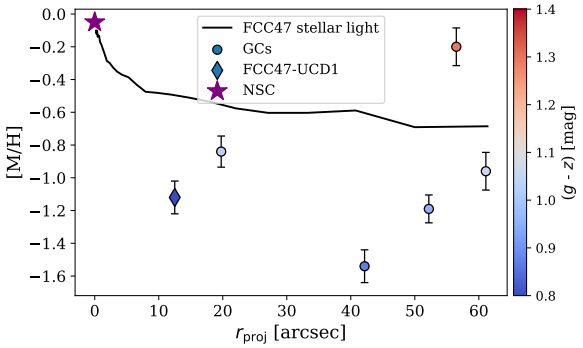

Figure 2.11.: Radial profile of GC metallicities in comparison to their photometric colours, the NSC, and the integrated galaxy light.

2.7 FCC 47-UCD1: a metal-poor UCD

In Fahrion et al. (2019a), we presented the discovery of FCC 47-UCD1, a UCD at 1 kpc projected distance from the centre of FCC 47 based on the MUSE AO data and archival HST ACS data. In this section, we summarise the main results of this paper.

2.7.1 Photometry of FCC 47-UCD1

We discovered FCC 47-UCD1 as a bright point-source in the MUSE data with similar radial velocity as FCC 47, but that was not listed as a GC in the catalogues of Jordán et al. (2015). In addition to the MUSE data, we used archival HST ACS data in the F475W (g) and F850LP (z) filters to study the structural properties of FCC 47-UCD1. As the UCD is close in projection ($13''= 1.1$ kpc) to the centre of FCC 47, the galaxy background has to be removed. This is achieved by creating an IRAF ELLIPSE model of the host galaxy in each filter and subtracting it from the data. The structural parameters of the UCD are then determined using IMFIT (Erwin 2015), a modular procedure to fit 2D surface brightness distributions.

We used IMFIT to fit FCC 47-UCD1 with two single component models (King and Sérsic, respectively) and two two-component models (King + Exponential and King + Sérsic). We use generalized King models[6] that are parametrized by a core radius R_c, a concentration $C = \mathrm{R}_t/\mathrm{R}_c$ as ratio between tidal and core radius and a variable exponent α. We use 10× oversampled PSFs in the two filters to ensure accurate representation of the smallest scales.

The 2D surface brightness images of the UCD and the residuals after subtracting the different IMFIT models are shown in Fig. 2.12. The single component fits perform well with no obvious difference between King and Sérsic models. In contrast, the two component models tend to overestimate the UCD flux at the centre. We conclude that FCC 47-UCD1 is best described by a single generalized King profile with an absolute magnitude in the g band of -10.55 mag and a colour of $(g - z) = 1.46$, similar to the colours of the blue GC population of FCC 47. Its absolute magnitude is consistent with FCC 47-UCD1 being the most massive GC of FCC 47's rich GC system as given by FCC 47's GC luminosity function Villegas et al. (2010). However, we found an effective radius of ~ 24 pc. With this size, the UCD is more than twice as large as any GC in FCC 47.

2.7.2 MUSE spectroscopy of FCC 47-UCD1

Similar to the GCs in FCC 47, we extracted the spectrum of FCC 47-UCD1 using a PSF-weighted circular aperture and subtracted the galaxy background as determined from an annulus spectrum around the UCD. The resulting MUSE spectrum has a S/N ~ 20, which is sufficient to derive kinematics and stellar population properties. We fitted its spectrum with PPXF.

We found a relative velocity of ~ 65 km s^{-1} with respect to the systemic velocity of FCC 47, confirming membership to the FCC 47 system. However, for such a low-mass system as the UCD, the velocity dispersion is close to or below the MUSE instrumental resolution, and thus we can only give an upper limit of the velocity dispersion of $\sigma < 17$ km s^{-1}. This was inferred from fitting the spectral region around 8600 Å, where MUSE reaches the highest spectral resolution.

From full spectral fitting, we found a spectroscopic metallicity of [M/H] $= -1.12 \pm 0.10$ dex

[6]The generalized King profile is given by $I(R) = I_0 \left[\frac{1}{(1+(R/R_c)^2)^{\frac{1}{\alpha}}} - \frac{1}{(1+(R_t/R_c)^2)^{\frac{1}{\alpha}}} \right]^{\alpha}$

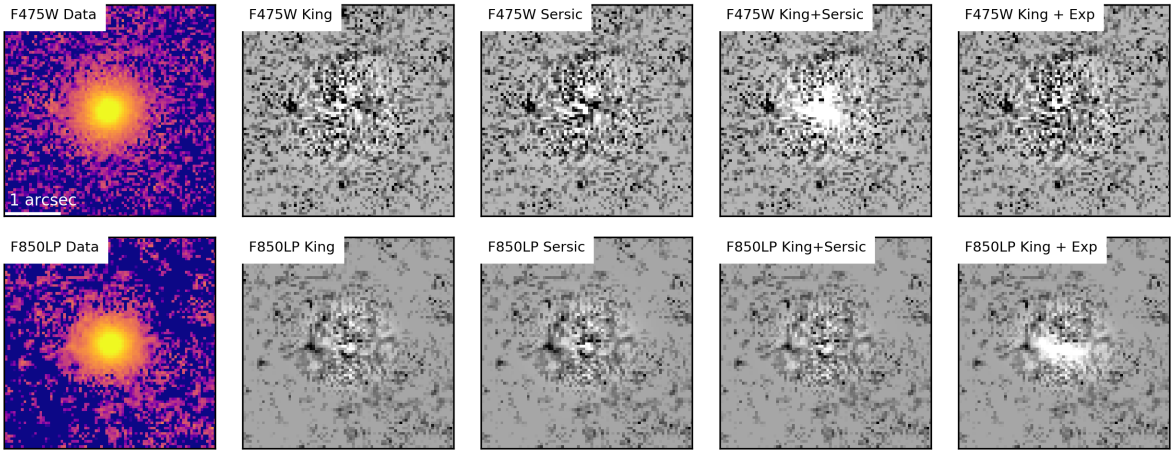

Figure 2.12.: 2D structural analysis. *First column*: HST UCD images in the F475W filter (g band, *first row*) and F850LP (z band, *second row*) after an ELLIPSE model of the galaxy background is subtracted. The second and third columns show residual images after subtracting a single generalised King model or a Sérsic model, respectively. The third and forth columns show residuals after subtracting two component models with a King and Sérsic and a King and exponential model, respectively. Each panel shows a $3'' \times 3''$ (266×266 pc) cut out. Black and white colours show positive and negative residuals.

and a generally old age (> 8 Gyr). Our data does not give any indication of multiple or young populations. We can exclude a significant contribution to the spectrum from a young stellar population.

2.7.3 Mass estimation of FCC 47-UCD1

We used the mass modelling procedure described in Hilker et al. (2007) to derive an upper limit on the dynamical mass of FCC 47-UCD1 from the upper limit of the velocity dispersion. This approach uses the structural parameters as determined by the photometric fit of the generalised King profile and translates the 2D luminosity profile into a 3D density profile (see also Sect. 3.4.5). The modelling gives an upper limit of the dynamical mass of $M_{\rm dyn} < 1.3^{+1.6} \times 10^7 M_\odot$ using the King model parameters in the F475W filter. The lower limit on the dynamical mass can not be constrained with our spectrum; however, we can assume that it can not be less than the photometric mass. This upper limit is comparable to masses of other UCDs with similar effective radii (e.g. Mieske et al. 2008).

The stellar population analysis allows us to estimate the stellar mass of the UCD. We translated the metallicity into a photometric M/L using the E-MILES SSP predictions for the HST ACS F475W filter. Assuming an old age of 13 Gyr, we interpolated the given grid of SSP models to draw 5000 values of the M/L ratio using a Gaussian distribution of the metallicity with a mean of -1.12 dex and standard deviation of 0.10 dex. We found $M/L_{\rm SSP,\,g} = 2.42\,^{+0.08}_{-0.10}\,\frac{M_\odot}{L_\odot}$ and with a total luminosity of the UCD of $L_{\rm UCD} = 2.01 \times 10^6 L_\odot$ based on its g-band magnitude and a distance of 18.3 Mpc, this translates to a photometric stellar mass of $M_*^{\rm g} = 4.87\,^{+0.21}_{-0.16} \times 10^6\,M_\odot$. This is roughly half of the upper limit we derived for the dynamical mass.

2.7.4 Origin of FCC 47-UCD1

The blue colour and low metallicity of FCC 47-UCD1 in comparison with FCC 47's GC system and host metallicity indicate an ex-situ origin of this UCD, but the photometric, kinematic, and structural properties of FCC 47-UCD1 do not allow us to unambiguously pinpoint its nature. The magnitude, colour, metallicity, and the absence of an extended envelope are consistent with it being a very massive star cluster.

However, the stripped NSC of a dwarf galaxy can show similar properties (see Fig. 2.13 and Pfeffer & Baumgardt 2013). The very large effective radius of ~ 24 pc makes it a complete outlier from the rest of FCC 47's GCs. This is perhaps the most convincing argument that this object is different from typical GCs, making FCC 47-UCD1 a candidate of the stripped nucleus of a metal-poor dwarf galaxy, similar to the ones we find in the MW (e.g. ωCen and M54). In the case the UCD is the remnant NSC of a stripped dwarf galaxy, known scaling relations between NSC mass and host galaxy mass (Georgiev et al. 2016) and the mass-metallicity relation of dwarf galaxies (Kirby et al. 2013) allow us to estimate that its hypothetical progenitor could have been a dwarf galaxy with a mass of a few $10^8 M_\odot$. This would imply that the progenitor has lost at least 95% of its initial mass in an minor merger event with a mass ratio of $\sim$ 1:100.

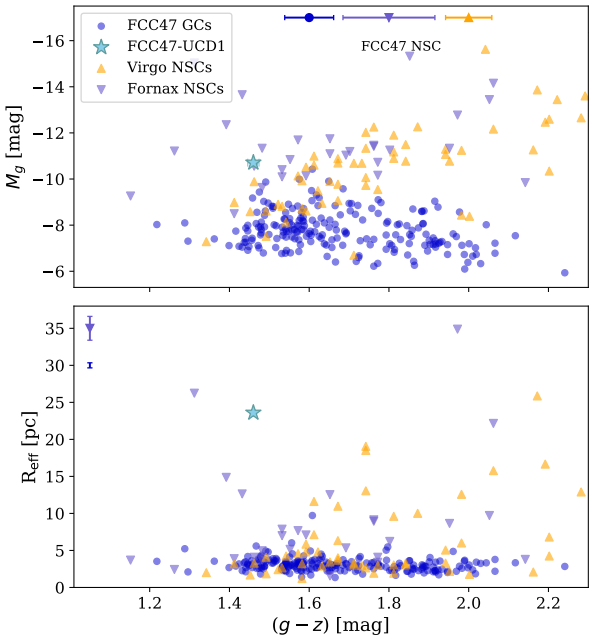

Figure 2.13.: *Top*: Colour-magnitude diagram for the UCD (light blue), the GCs in FCC 47 (blue circles, Jordán et al. 2015), NSCs in the Virgo cluster (orange triangles, Côté et al. 2006) and in the Fornax cluster (purple triangles, Turner et al. 2012). Typical colour errors are shown with the symbols on the top. *Bottom*: Effective radii for GCs, NSCs, and the UCD.

2.8 Discussion

FCC 47 is a ETG with $M_{\rm gal} \sim 10^{10} M_\odot$ in the outskirts of the Fornax cluster with a particularly large NSC and rich GC system. Our MUSE study has revealed several peculiarities that distinguish this galaxy from others, for example the presence of two visible KDCs. In the following we use our comprehensive collection of information to put constraints on the formation history of FCC 47's massive NSC.

2.8.1 The star clusters in FCC 47

We first want to discuss our findings for the star clusters in FCC 47. Comparing the NSC with FCC 47's GC system and the galaxy itself allows us to put constraints on the NSC

formation.

The nuclear star cluster

FCC 47 was targeted because of its particularly large NSC with an effective radius of 66 pc (Turner et al. 2012). Using a large sample of NSCs in ETGs and LTGs, Georgiev et al. (2016) studied various scaling relations between mass and size of the NSC and host mass properties. The observed relation between NSC size and host mass would predict a NSC with an effective radius of ~ 20 pc for a galaxy with the stellar mass of FCC 47. However, the observed radius of 66 pc is still within the scatter and there are several other ETGs with NSCs of similar sizes in this mass range. In addition to the size, our data allowed to estimate the stellar mass of the NSC to be $\sim 7 \times 10^8 M_\odot$ using stellar population models. This is a massive NSC and is slightly more massive than NSCs of a similar size, but again it lies within the scatter of the NSC size-mass relation (Georgiev et al. 2016). Nonetheless, this high mass places the NSC among the most massive known NSCs (e.g. Sánchez-Janssen et al. 2019).

The NSC constitutes the peak of metallicity and stellar age in FCC 47 and is clearly more metal-rich than the immediate surrounding galaxy, in fact it is possible that a large fraction of the strong central metallicity gradient can be explained by the metal-rich NSC being smeared out by the MUSE PSF. While many NSCs were found to also contain young stellar populations (Rossa et al. 2006; Paudel et al. 2011), the NSC in FCC 47 shows no contribution from young stars (< 10 Gyr). It contains the oldest stellar ages, indicating a quick metal-enrichment and early quenching of star formation. We could identify two subpopulations in the NSC, a dominant population with super-solar metallicities and intermediate [α/Fe], and a secondary component that has a lower metallicity (~ -0.4 dex) and a higher α-abundance ratio. These two populations could be explained by continuous and efficient self-enrichment of an initially metal-poor and α-enhanced stellar population that increased metallicity and decreased [α/Fe] due to the pollution from supernovae Ia ejecta. These supernovae release iron into the interstellar medium within ~ 1 Gyr (Thomas et al. 2005), in agreement with the exclusively old ages we found in the NSC. As we could not find different SFHs for the metal-poor and metal-rich subpopulations, the self-enrichment must have stopped early in this picture. Alternatively, the more metal-poor component could indicate NSC mass growth through the accretion of GCs of this chemical composition.

In the study of Lyubenova & Tsatsi (2019) that used high angular resolution IFU SINFONI data of five NSCs of galaxies in the Fornax cluster, the NSC of FCC 47 stood out with having the strongest rotation and consequently having the highest angular momentum of the observed sample. The MUSE data confirmed the rotation of the NSC, but allowed us to set it into context with the rest of the galaxy and we found that the NSC rotates as a KDC around an axis offset by 115° from the main photometric (and rotation) axis of the galaxy. While the NSC in the MW shows evidence for a small misalignment between the rotation of the NSC and the galactic plane (Feldmeier et al. 2014), the gas-rich LTGs studied by Seth et al. (2008b) have NSCs that rotate in the plane of their host. Due to lower intrinsic rotation and a more spherical geometry, kinematically misaligned NSCs could be easier to spot in ETGs.

The NSC in FCC 47 was originally identified as an excess of light at the centre of the galaxy (Turner et al. 2012). Our analysis showed that the NSC is indeed a distinct component of FCC 47, both in its kinematic and stellar population properties.

The globular clusters

The ETG FCC 47 has a rich GC system with more than 300 candidates identified in the ACSFCS (Jordán et al. 2015). We could identify 42 GCs in our MUSE data, with 25 having a spectral S/N high enough to extract their LOS velocity. With this small number GC sample, we could not identify rotating substructures, but we found that the GCs show a large velocity dispersion. This is in agreement with other studies that have established that GCs usually are a dynamical hot system (e.g. Kissler-Patig & Gebhardt 1998; Dabringhausen et al. 2008), supported by velocity dispersion. However, there have been detections of rotating subsystems in other galaxies (e.g. Foster et al. 2016; Forbes et al. 2017). We noted that the blue GC subpopulation shows a larger velocity dispersion than the red GCs, as in most other galaxies (e.g. Schuberth et al. 2010). In addition, the ACSFCS study shows that red GCs are more centrally concentrated and as a consequence the distribution of GC colours shows a radial gradient from red to blue in the outskirts.

From the five GCs that are bright enough to estimate their metallicity and FCC 47-UCD1, we found four blue GCs that are significantly more metal-poor than the galaxy at their projected distance. The fifth GC is red and has a higher metallicity, similar to the NSC. Combined with the fact that we could not find indications of young ages in the GCs or the stellar light, the bimodality of GC colours in FCC 47 might be truly an effect of a metallicity bimodality, however, we only have five GCs to support this. Using the photometric colours from the ACSFCS and assuming an old age (13 Gyr) for all ACSFCS GC candidates, we estimated that the GC system has a total mass of $\sim 1 \times 10^8 M_\odot$. This is only $\sim 17\%$ the mass found in the NSC.

The larger velocity dispersion, the low metallicities of the blue GCs, and the GC colour gradient indicate an ex-situ origin of the blue GC system. Generally, the bimodal colour distribution of GCs as observed in many galaxies is interpreted in this scheme, with the red (metal-rich) GC population having formed in-situ while the blue GCs were accreted through minor mergers with metal-poorer dwarf galaxies (Côté et al. 1998; Hilker et al. 1999a; Lotz et al. 2004; Peng et al. 2006; Côté et al. 2006; Georgiev et al. 2008). The red, metal-rich GC population might have formed together with the NSC and the metal-rich galaxy population, that has a smaller mass fraction and thus is hidden within the metal-poor population of FCC 47, that is particularly dominant at larger radii.

2.8.2 Constraints on the formation of FCC 47's nuclear star cluster

Having collected information on the kinematic and stellar population structure of FCC 47 itself, its NSC, and the GCs, we want to explore if we can put constraints on the formation of FCC 47's massive NSC. We explore the implications of the two most commonly discussed scenarios, accretion of GCs and in-situ formation of the NSC.

Globular cluster accretion scenario

In the GC accretion scenario, the NSC forms from the (dry) accretion of in-spiralling GCs that make their way to the centre due to dynamical friction. Although the in-fall of GCs with random orbits can result in a low net angular momentum of the NSC, simulations have shown that some NSCs can have significant rotation. In the case of the NSC of FCC 47, a comparison to N-body simulations (Antonini et al. 2012; Perets & Mastrobuono-Battisti 2014; Tsatsi et al. 2017) has shown that this high angular momentum can still be explained by gas-free accretion of GCs, but requires a preferred in-fall orbital direction as discussed by Lyubenova & Tsatsi (2019). However, we could not find any indication for rotation substructure in the GC population, possible due to the low numbers of available GC LOS velocities and an incomplete spatial coverage.

The old age and the absence of young populations in the NSC are consistent with the accretion of gas-free GCs. We found that the NSC constitutes the metal-rich peak of FCC 47 and is significantly more metal-rich than the blue (metal-poor) GC population, however, we found at least one red GC that has a similar metallicity. Our current sample of GCs with metallicity measurements is very limited, but the comparison of GC colours shows that there probably still are GCs in FCC 47 with metallicities similar to the NSC. These red GCs are also more centrally concentrated and thus it is possible that the NSC has formed or grown by accreting such GCs, similar to the GCs found in the bulge of the MW (e.g. Côté 1999; Muñoz et al. 2017, 2018). The presence of a minor more metal-poor population in the NSC, might indicate some accretion of old, metal-poor and α-enhanced stars, possibly also accreted in an in-spiral of a few metal-poor GCs. However, it is unclear if the steep central metallicity gradient can be explained by GC in-spiral because the disk region already shows significantly lower metallicities or whether (and how much) additional gas accretion would be needed.

Similarly, the composite formation scenario proposed by Guillard et al. (2016) could give a viable explanation for the formation of the NSC in FCC 47. In their scenario, a massive gas-rich GC forms close to the centre and spirals inwards within a few Gyr, possibly followed by a merger with a second gas-rich GC. Depending on whether a second GC falls to the centre, this model predicts significant rotation in the formed NSC and a fast quenching of star formation in the centre because of gas being expelled, in agreement with the old age and high metallicity we find for the NSC in FCC 47. However, it is unclear if this scenario can explain the KDC with the offset rotation axis and the described accretion of only two massive GCs is not viable for FCC 47. To explain its mass, a large number of star clusters must have merged within the first Gyr of the galaxy.

Independent of the kinematic and chemical structure of the NSC and the GCs, the high mass of the NSC makes formation solely by GC accretion unlikely. As our estimate shows, the NSC is much more massive than the total GC system as observed today. To explain its mass of $\sim 7 \times 10^8 M_\odot$, it must have accreted early-on hundreds of GCs that must have been quite massive ($> 10^6 M_\odot$) to explain the high (and homogeneous) metallicity. Modelling the effects of dynamical friction, evolution including mass loss and tidal stripping on the GC system of the MW and M 87, Gnedin et al. (2014) found that GC accretion can contribute a large fraction of mass to NSCs in galaxies with $M_{\rm gal} < 10^{11} M_\odot$. However, following their

predicted scaling between NSC and galaxy stellar mass, FCC 47's NSC should have a mass of $\sim 1 \times 10^8 M_\odot$ assuming growth through GC accretion. This estimate would increase if FCC 47 had been extremely efficient in forming massive metal-rich star clusters early on, but it is questionable how such a large population of metal-rich GCs could have formed.

We therefore conclude that the formation of the NSC in FCC47 is unlikely to have been dominated by the gas-free accretion of old GCs. However, from simple dynamical arguments, it follows that there must have been some GC accretion in such a rich GC system and the accretion of young metal-rich star clusters early-on is still possible. Detailed modelling that accounts for the properties of FCC 47's GC system would be needed to get a handle on the relative fraction of mass build-up via dry GC accretion.

In-situ formation

The formation of the NSC through in-situ formation from infalling gas can explain the high mass and high metallicity better, but requires that a large supply of gas has been funnelled originally into the centre of FCC 47. This supply must have been quickly exhausted after a short period of efficient star formation and self-enrichment. With our data, we cannot constrain the mechanisms that have stopped the star formation in the NSC and the rest of the galaxy. We do not know if the gas was simply exhausted or it was removed, possibly due to interactions in the Fornax cluster environment, stellar feedback, or feedback from an accreting BH.

In the in-situ formation scenario, the infalling gas would inherit the angular momentum from its origin. However, there is no indication of other stellar populations rotating around the same axis as the NSC, neither in the galaxy main body nor within the GC population, but a larger sample of (red) GC velocities is needed to confirm this. Instead, the rotation axis of the NSC is offset with respect to the photometric axis and main rotation axis of the galaxy. The origin of the kinematically decoupled rotation of the NSC might not be connected to intrinsic formation scenarios as discussed, but could be evidence for a major merger that has altered FCC 47 kinematic structure significantly. Such a merger and the corresponding merger of the NSCs of the progenitor galaxies could also explain the high mass of FCC 47's NSC.

Evidence for merger history of FCC 47

KDCs are not a rare phenomenon, especially in massive ETGs ($M_{\rm gal} > 10^{10.8} M_\odot$, Krajnović et al. 2013). Classical KDCs have kpc sizes, similar to the rotating disk structure in FCC 47, and the more compact KDCs are often younger than the NSC of FCC 47 (McDermid et al. 2006, 2007).

Simulations of galaxy mergers have been able to explain the formation of KDCs, but they always require a major merger between massive galaxies. The central kinematic decoupling arises if, for example, gas dissipation, retrograde merger orbits, or the merger of gas-rich disks are incorporated in the simulations (Balcells & Quinn 1990; Barnes & Hernquist 1992; Jesseit et al. 2007; Bois et al. 2011). Tsatsi et al. (2015) showed that kpc-sized KDCs can

also form in a prograde merger of two disk galaxies during which reactive forces create short-lived reversal of the orbital spin.

Rantala et al. (2019) shows that KDCs may also arise from orbit reversals of the central SMBH caused by gravitational torques from expelled material in the dissipationless merger of two massive ETGs. For binary mergers of massive ETGs (each $M_{\rm gal} > 8 \times 10^{10} M_{\odot}$) with very massive SMBHs (each $> 10^{9} M_{\odot}$), they even find multiple KDCs, similar to what we found in FCC 47, however, the simulated KDCs still both rotate around the minor axis of the galaxy. In case the described scenario scales down to lower-mass galaxies such as FCC 47, the simulations predict a very massive SMBH as well as a tangential velocity anisotropy in the centre, which could be tested with future models that are also incorporating high resolution kinematic data of FCC 47's NSC.

In comparison to other galaxies of the Virgo and Fornax cluster, FCC 47 not only has a large and massive NSC (Turner et al. 2012), but also has a higher specific frequency of GCs within one effective radius than other galaxies of similar mass (Liu et al. 2019). This might imply that the formation of the NSC and the red, centrally concentrated GC system is connected. Thus, a scenario in which the NSC is an original part of the galaxy might be favoured. In such a scenario, the NSC, the metal-rich part of galaxy, and the red, metal-rich GCs could have formed together in clumpy, bursty star formation at high redshift (see also Beasley et al. 2018a). The galaxy then later underwent at least one major merger that created the counter-rotating populations and younger, more metal-poor outskirts. Specialised simulations would be required to test whether the decoupled rotation of the NSC could have survived the subsequent evolution of the galaxy or whether the kinematic decoupling itself could be a result of second major merger.

Independent of the exact formation scenario that has caused the peculiar kinematic structure of FCC 47, the presence of KDCs indicate the importance of mergers in the formation of both galaxy and NSC. Thus, studying other massive NSCs and their hosts is required to determine if the commonly discussed NSC formation scenarios are sufficient to explain the formation of the most massive NSCs in general.

2.9 Conclusions

In this chapter, we presented the comprehensive studies of the kinematic and stellar population structure of the ETG FCC 47 and an associated UCD using MUSE AO science verification data that were originally published in Fahrion et al. (2019a) and Fahrion et al. (2019b). We analysed both the integrated stellar light and GCs as discrete tracers of the kinematic and chemical structure, connecting the results to the kinematic and chemical study of the NSC. We summarise the results from the papers and this chapter as follows:

- We found that FCC 47 shows a complex velocity structure with two KDCs on different scales. While there is no significant rotation on large scales, a rotating disk structure with a rotation amplitude of $\sim$ 20 km s^{-1} is found with an extent of $\sim$ 2 kpc. The rotation axis of the NSC and of the inner disk are offset by $\sim$ 115°, constituting a second KDC.

- We constructed a Schwarzschild model to reveal FCC 47's orbital structure. According to this model, the main body of FCC 47 consists of two counter-rotating populations that cancel each others rotation signatures on large scales and show an imbalance near the centre. The NSC appears to be truly kinematically decoupled and we found no indication of other populations showing the same sense of rotation. The Schwarzschild model determined the total stellar mass of FCC 47 to be $M_{\rm gal} = 1.5 \times 10^{10} M_{\odot}$.

- FCC 47 is overall old (> 8 Gyr) and shows an age gradient from very old ages in the centre to younger ages in the outskirts. We did not find any evidence of young populations, gas, or dust. The galaxy shows a strong central metallicity gradient that flattens outwards. The region of high metallicity matches the extent of the NSC rotation structure. We therefore assumed that the high metallicity is associated to the NSC while the rest of the galaxy is significantly more metal-poor.

- Studying the galaxy-subtracted NSC spectrum finds two chemically distinct subpopulations: a dominating (67 %) metal-rich population with intermediate light element abundance ratio and a secondary population with lower metallicity and higher [α/Fe]. From the stellar population analysis, we found that the NSC is very massive ($M \sim 7 \times 10^8 M_{\odot}$).

- We extracted MUSE spectra of 42 GCs. 25 of these have a sufficient spectral S/N to determine their LOS velocity and a sub-sample of five GCs is bright enough for an estimate of their metallicities. The GC system does not appear to rotate, but the blue GC population shows a larger velocity dispersion than the red population. Four of the five GCs that allowed a measurement of their metallicity have blue colours and are found to be significantly metal-poorer than the galaxy. We estimated the total mass in GCs to be $\sim 1 \times 10^8 M_{\odot}$.

- We interpreted our results with respect to the formation channels of NSCs: the gas-free GC accretion and the in-situ formation scenario. With its high angular momentum, high mass, and high metallicity, the NSC of FCC47 is unlikely to have formed by accreting non-rotating, metal-poor GCs as observed in FCC 47 today. However, we could not rule out that the NSC has formed a fraction of its mass by accreting more metal-rich GCs or gas-rich massive star clusters early on. Possibly, the decoupled kinematics of the NSC are not an effect of the formation pathway, but rather are the result of a major merger that has altered FCC 47's kinematic structure.

FCC 47 was targeted as MUSE AO science verification target because of its large, strongly-rotating NSC, and rich GC system. The wealth of complexity in this galaxy has been surprising: we found two KDCs, a sharp central metallicity peak, and FCC 47-UCD1. As we argue in Fahrion et al. (2019a) and Sect. 2.7, the UCD could be the stripped nucleus of a disrupted dwarf galaxy and would therefore indicate a minor merger in FCC 47's past. In addition, the KDCs most likely are evidence of at least one major merger event that has altered the kinematic structure of the galaxy significantly.

I have learned all kinds of things from my many mistakes. The one thing I never learn is to stop making them.

Joe Abercrombie, Last Argument of Kings.

3 | Two nucleated dwarf galaxies near Centaurus A

In the last chapter, I illustrated how MUSE data of a single ETG in the Fornax cluster was used to constrain the formation of its very massive NSC. In this chapter, I investigate two galaxies at the other end of the galaxy mass range and study two nucleated dwarf galaxies near Centaurus A. This chapter is adapted from Fahrion et al. (2020c) and is part of a larger collaborative effort to characterise the properties of dwarfs (Müller et al. 2021a) and to study the dynamical configuration of the satellite system of Cen A (Müller et al. 2021b).

3.1 Introducing KKs58 and KK197

Nucleated dwarf galaxies have been studied in various environments, from dense galaxy clusters such as Virgo, Coma, or Fornax to less populated groups (e.g. Georgiev et al. 2009c; Georgiev & Böker 2014; den Brok et al. 2014; Ordenes-Briceño et al. 2018). In this work, we report on two nucleated dwarf elliptical galaxies that are confirmed members of the Centaurus group (Müller et al. 2019). The two major galaxies in the Centaurus group are Cen A (NGC 5128) at a distance of $\sim$ 3.8 Mpc (Rejkuba 2004), and M 83 (NGC 5236) at $D \approx$ 4.8 Mpc (Herrmann et al. 2008; Radburn-Smith et al. 2011). In the first survey of dEs in the Centaurus group, Jerjen et al. (2000b) identified 13 potential members and established group membership for five dEs through surface brightness fluctuation and velocity measurements. Jerjen et al. (2000a) pointed out potential nuclei in the two dEs ESO 219-010 and ESO 269-066, although a chance projection of a (nearby) star on the galaxy centre could not be excluded. Using observations with HST, Georgiev et al. (2009a) studied the properties of NSC and GC candidates in nearby dwarf galaxies, including 24 dwarfs in the Centaurus group complex, suggesting that four of them have NSCs (ESO 059-01, ESO 223-09, ESO 269-66 and KK197, Georgiev et al. 2009c). Recently, several surveys have targeted the Centaurus group providing a more complete census of the dwarf galaxy system (Crnojević et al. 2014, 2016, 2019; Müller et al. 2015, 2017, 2018c, 2019; Taylor et al. 2016, 2018) that as of now includes $\sim$70 dwarf galaxy candidates.

In this chapter, we present the analysis of the two nucleated dwarf galaxies KKs58 and KK197 in the Centaurus group, based on MUSE data. As mentioned, KK197 was among the dwarf galaxies previously analysed with HST data by Georgiev et al. (2009c), and photometric properties of its NSC and two GC candidates were presented in Georgiev et al. (2009a). We report the discovery of a new NSC in KKs58 (also known as Centaurus A-dE3, Jerjen

Table 3.1.: Basic information about KKs58 (Müller et al. 2019) and KK197 (Sharina et al. 2008; Georgiev et al. 2009c).

Property	KKs58	KK197
RA (J2000)	13:46:00.8	13:22:01.8
DEC (J2000)	−36:19:44	−42:32:08
D (Mpc)	$3.36\ ^{+0.18}_{-0.02}$	3.98
$d_{3D,\ Cen\ A}$ (kpc)	574	55
M_V (mag)	$-11.93^{+0.12}_{-0.01}$	−13.04

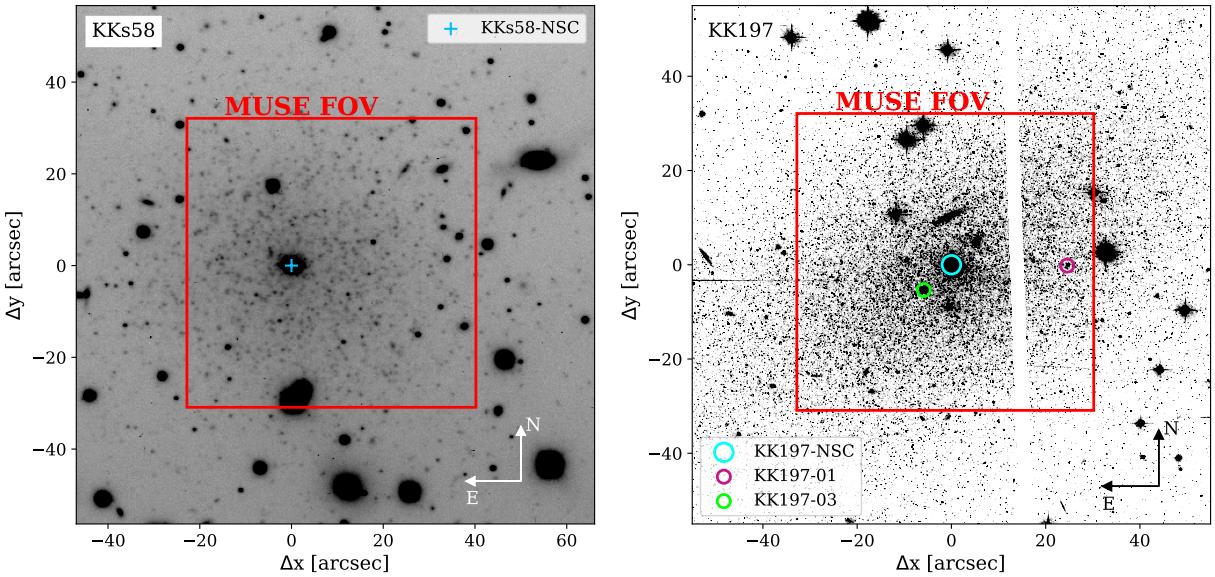

Figure 3.1.: Cutout of the FORS2 *I* band image of KKs58 (*left*, 10″≈ 160 pc) and of the HST F606W image of KK197 (*right*, 10″≈ 190 pc). The pointings of the MUSE FOV (1×1 arcmin ≈ 1×1 kpc) are indicated by the red squares. North is up and East to the left, the *xy* coordinates are relative to the NSCs. We indicate the positions of KKs58-NSC and the star cluster candidates of KK197 (Georgiev et al. 2009c).

et al. 2000a), which is the brightest dwarf galaxy in the sample of nine dwarf galaxies that were recently confirmed Cen A group members using ESO VLT FORS2 data (Müller et al. 2019). In a spectroscopic follow-up with MUSE, under observing program 0101.A-0193(B), we aimed to measure radial velocities of a selection of these galaxies to investigate the velocity distribution of the dwarf satellites arranged in a plane around Centaurus A (Tully et al. 2015; Müller et al. 2016, 2018b). Upon inspection of MUSE data we discovered that the bright compact source located in the centre of KKs58 has a velocity in agreement with the host galaxy, and thus it constitutes the newly discovered NSC of KKs58. Additionally, we could confirm the star cluster candidate KK197-02 from Georgiev et al. (2009c) to be the NSC of KK197.

3.2 MUSE data of KKs58 and KK197

Observations of KKs58 were acquired on 9 May 2018 under below-average sky conditions for Paranal (thin clouds and about 1.2″ seeing). The total exposure time on target was 2000 seconds. The observing strategy included four science exposures, each 500 seconds long, interleaved with two offset sky exposures of 250 seconds, in a sequence *OSOOSO*, where *'O'* is object and *'S'* is sky exposure. The offset sky location was selected 72″ East and 70″ North of the central pointing. We implemented small dithering offsets of 1–2″, and 90 degree rotation between subsequent exposures in order to minimise the noise residuals due to slicers and different channels.

The MUSE observations of KK197 were carried out within two observation blocks (OBs), each with a single *'OSO'* sequence of 2×1160 sec science exposures on target bracketing a single 580 sec long exposure of an adjacent empty sky region. The first OB was taken on 16 April 2018 under mostly clear sky. The atmospheric conditions during the night of 8-9 May were worse, with initially some thick clouds affecting the observation, later improving to thin clouds. Therefore, to compensate for loss of sensitivity due to clouds, part of the observing sequence was repeated resulting in 3 on-target exposures *'O'* of 1160 sec each interleaved with 580 sec long offset sky exposures *'O'* in a *'OSOOS'* sequence. Hence, the total exposure time for KK197 amounts to 5800 seconds. As for KKs58, small dithers and 90 degree rotation were implemented between science exposures. The fifth, repeated, science exposure had the same offset and rotator position (PA = 180°) as the first science exposure taken on 16 April.

We downloaded the MUSE Internal Data Products from the ESO Science Archive that included data reduction based on the MUSE pipeline version 2.2 (Weilbacher et al. 2012). The data have been pre-processed, bias and flat-field corrected, astrometrically calibrated, sky-subtracted, wavelength calibrated, and flux calibrated (Hanuschik et al. 2017)[1]. The sky subtraction used the offset sky exposures and to further reduce the sky residual lines, we applied the ZAP principal component analysis algorithm (Soto et al. 2016). Figure 3.1 shows portions of the deep I-band stacked FORS2 image of KKs58 (Müller et al. 2019) and the HST ACS image of KK197 (Georgiev et al. 2009c) with the MUSE FOVs indicated in red. These images were used to guide the selection of 'empty sky' regions with no evident stars or galaxies to be used by ZAP. The optimal sky mask turned out to be a selection of the faintest 9 - 12% pixels on the white light image created from the MUSE cube. With the dedicated sky observations and ZAP, bright sky emission lines could be reduced sufficiently, but in low S/N spectra, telluric lines above $\sim$ 7500 Å remain. As described in Sect. 3.4.1, we did not use the spectra above 7100 Å. Using DAOPHOT (Stetson 1987), we measured the FWHM of PSF in the collapsed MUSE images, as described in Müller et al. (2018c). Both MUSE cubes have an image quality of 1.0″.

[1]See also http://www.eso.org/observing/dfo/quality/PHOENIX/MUSE/processing.html

3.3 Photometry

In the following, we describe the photometric properties of KK197, KKs58, and their star clusters. KK197 was previously studied by Georgiev et al. (2009c) using HST data and for KKs58, we use Müller et al. (2015) DECam data.

3.3.1 KKs58 DECam photometry

KKs58 was observed with FORS2 and photometry of the individual bright red giant branch stars was used to measure the distance to the galaxy using the tip magnitude of the red giant branch (Müller et al. 2019). The bright source located approximately in the centre of the galaxy (at coordinates $(\Delta y, \Delta x) = (0, 0)$ in Fig. 3.1) was saturated on individual FORS2 images. To study the photometric structure of KKs58 and its NSC in more detail, we used the g and r-band DECam images from Müller et al. (2015). The data have an exposure time of 120 seconds in both filters. Using DAOPHOT aperture photometry (Stetson 1987), we obtained extinction-corrected magnitudes of the NSC of $g_{\rm NSC} = 18.44 \pm 0.05$ mag and $r_{\rm NSC} = 17.90 \pm 0.06$ mag, respectively, using galactic extinction values in the g and r-band of 0.200 and 0.134 mag (Schlafly & Finkbeiner 2011). The uncertainties are dominated by the zero-point uncertainties (~ 0.05 mag). The resulting colour of $(g-r)_0 = 0.54 \pm 0.08$ mag is typical for old stellar populations dominated by RGB stars such as in early-type dwarf galaxies (e.g. Müller et al. 2018a). To compare the NSC to a larger sample of literature sources, we converted these magnitudes into Johnson V-band using the relation from Lupton 2005[2].

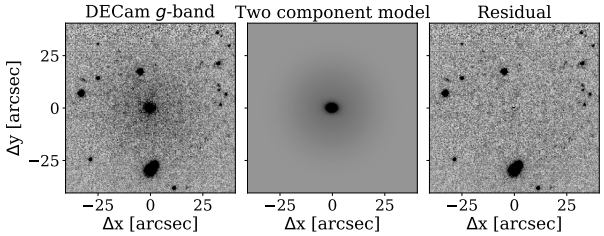

Figure 3.2.: Illustration of the two component IMFIT model. *Left*: Original DECam g-band image of KKs58. *Middle*: double Sérsic model. *Right*: residual after subtracting the model from the image. North is up, east is to the left.

We used the 2D image fitting routine IMFIT (Erwin 2015) to determine the structural parameters of the NSC. Our best-fit model, shown in Fig. 3.2, consists of two Sérsic models, one representing the NSC and the second corresponding to the underlying galaxy. This model considers a model of the PSF that we built with the effective PSF functionality of the Python package PHOTUTILS (Bradley et al. 2019) using ~ 10 stars in the FOV, following the prescription of Anderson & King (2000). We found effective radii of the NSC and the host of $R_{\rm eff} = 6.6 \pm 0.5$ pc ($0.40 \pm 0.02''$) and $R_{\rm eff} = 244.7 \pm 8.3$ pc ($15.0 \pm 0.5''$), respectively. The uncertainties were inferred with Markov-Chain Monte Carlo (MCMC) sampling. The effective radius of the host galaxy is lower than earlier measurements of 430 pc from Jerjen et al. (2000a), which could be due to better image quality and depth of the DECam images.

[2] https://www.sdss3.org/dr10/algorithms/sdssUBVRITransform.php
Using $M_V = g - 0.5784(g-r) - 0.0038$ and a distance modulus of 27.63 mag (Müller et al. 2019), we obtained an absolute magnitude of $M_V = -9.51 \pm 0.07$ mag.

According to our model, the NSC is elongated with an ellipticity of $\epsilon = 0.30 \pm 0.04$ at a position angle of 86 ± 2 ° clockwise from North, while the galaxy Sérsic model is completely spherical.

3.3.2 KK197 HST ACS photometry

KK197 was originally studied by Georgiev et al. (2009c) using the F606W and F814W filters of the HST ACS instrument with the aim of identifying GC candidates in nearby dwarf galaxies. The observations were obtained in HST cycles 12 and 13 (PI: I. Karachentsev) and are described in Georgiev et al. (2008) and Georgiev et al. (2009c). The identification of GC candidates was based on colour constraints and their (resolved) morphologies. For KK197, Georgiev et al. (2009a) reported three GC candidates and we list their properties in Tab. 3.2. The largest, dubbed KK197-02, is located at the photometric centre of KK197 and in the following we refer to this source as KK197-NSC. KK197-NSC has a similar brightness than KKs58-NSC, but is slightly smaller. KK197-01 and KK197-03 turned out to be indeed GCs, as our MUSE analysis confirmed (Sect. 3.4.4).

3.4 MUSE spectroscopic analysis

In the following we present our analysis of the MUSE data of KKs58 and KK197. In particular, we distinguish between the star clusters and the host galaxies. The same method of full spectral fitting, described in the next section, is applied to both.

3.4.1 Full spectral fitting of MUSE spectra

We fitted the MUSE spectra using pPXF (Cappellari & Emsellem 2004; Cappellari 2017). To fit the MUSE data of KKs58 and KK197, we used the MILES SSPs with BaSTI isochrones (Pietrinferni et al. 2004, 2006) and a MW-like, double power law (bimodal) IMF with a high-mass slope of 1.30 (Vazdekis et al. 1996). For comparisons to photometric measurements, we used the scaled-solar MILES models that do not include α-enhancement and thus have [M/H] = [Fe/H]. For a more thorough description of pPXF and the models, see Sect. 2.4.

Throughout this chapter, we fitted LOS velocities using additive polynomials of degree twelve and no multiplicative polynomials. When fitting for stellar population properties, we keep the LOS velocity fixed and used multiplicative polynomials of degree eight without any additive polynomials. In all cases, the velocity dispersions of the star clusters and host galaxies are close or below the MUSE resolution and are not accessible. To obtain realistic uncertainties on the LOS velocity, the mean metallicity and age, we used a MC approach with 100 realisations (e.g. Cappellari & Emsellem 2004; Pinna et al. 2019a; or Sect. 2.4).

In general, we distinguish the spectra by their spectral S/N, obtained in a continuum region around 6000 Å. In the worst cases, for S/N < 3, no reliable information can be drawn from the spectrum. For S/N > 3, at least the LOS velocity is measurable to confirm membership of a star cluster to its host. Fitting spectra with S/N ≥ 10 further gives reliable estimates of the mean metallicity. In the following, we give the ages as obtained from MC

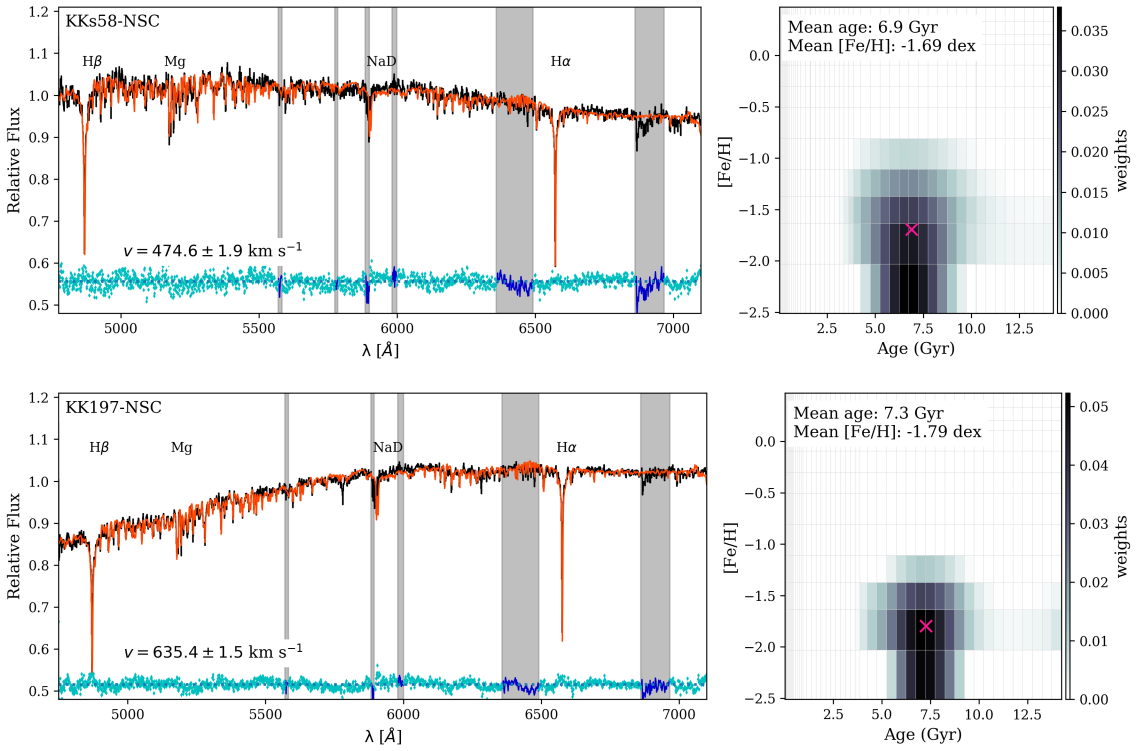

Figure 3.3.: Normalised spectrum of KKs58-NSC (*top*) and KK 197-NSC (*bottom*) fitted with pPXF and the scaled-solar MILES models. The input spectrum of the NSC is shown in black and the best-fitting combination of MILES SSP models is shown in red. The blue points indicate the residual, shifted to 0.5 for visibility. Masked regions with strong sky residual lines appear as grey-shaded. The right panels show the available grid of MILES SSP models in age and metallicity, colour-coded by their weight in the best-fit. The pink crosses mark the position of the weighted mean ages and metallicities. These are not corresponding to our final measurements from MC fitting listed in Tab. 3.2.

fitting with pPXF with their formal errors that are typically on the order of 1 Gyr, but these uncertainties might underestimate the true uncertainties due to the lack of strong age-sensitive features in the MUSE spectrum (see Appendix A.1). In addition, even when provided with a prior from photometry, measuring accurate ages of old stellar populations with integrated spectra is challenging and the resulting ages can deviate from the true ages by up to 5 Gyr (Usher et al. 2019). Age estimates of young populations < 5 Gyr, however, have a higher accuracy. For spectra with S/N > 50, such as the spectra of the NSCs, full spectral fitting with regularisation allows studying star formation histories and possible multiple populations. The regularisation ensures a smooth distribution of weights, that is needed, for example, to extract star formation histories (Böcker et al. 2020). Because the MILES models are normalised to 1 $M_{\odot}$, our stellar population properties are mass-weighted.

Due to non-photometric observing conditions, the flux calibration of our MUSE spectra has substantial systematic errors visible as different continuum shapes in KKs58 and KK197 (see Fig. 3.3). However, this should not affect our results because of the polynomials that are used by pPXF to account for the continuum variation that are not taken into account as constraint for stellar population determination.

3.4.2 KKs58's nuclear star cluster

The NSC of KKs58 is clearly visible in the MUSE FOV (Fig. 3.4). The NSC appears to be slightly elongated, similar to what we found in the FORS2 and DECam data. However, to extract its spectrum, we treated the NSC as a point source and used a circular aperture weighted by the PSF assuming a Gaussian profile with FWHM $= 1.0''$. This weighting helps to boost the signal of the NSC compared to the faint underlying galaxy background.

The NSC spectrum has S/N ~ 85. From 100 MC fits to the spectrum, we found a heliocentric LOS velocity of KKs58's NSC of $v_{\text{KKs58-NSC}} = 474.6 \pm 1.9\,\text{km s}^{-1}$. The top panel of Fig. 3.3 shows the original NSC spectrum and the regularised pPXF fit with a regularisation parameter of 70. We found a mass-weighted mean metallicity of [Fe/H] $= -1.69$ dex and a weighted mean age of ~ 7 Gyr. Testing with other stellar libraries highlights how challenging the determination of old ages is, because if we used the extended MILES library for the fitting, we found a mean age of ~ 9 Gyr. Nevertheless, the pPXF fit to the NSC spectrum can exclude recent star formation (< 2 Gyr) in the NSC. The regularised fit does not show multiple populations of different ages and metallicities. However, with the used SSP template grid and spectral quality, we are unable to detect the small metallicity variations of ~ 0.1 dex that can be found in massive MW GCs such as ωCen and M54 (Marino et al. 2015; Johnson et al. 2015). Therefore, we use 100 MC fits without regularisation to determine reliable measurements of mean age and metallicity. We derived an age of 6.9 ± 1.0 Gyr and [Fe/H] $= -1.75 \pm 0.06$ dex. The given uncertainties refer to random errors, but the systematic uncertainties can be larger. Both are consistent with the weighted means from the regularised fit.

We can use stellar population analysis of the NSC to estimate its stellar mass using the photometric predictions for the M/L for a given SSP of the scaled-solar MILES models. We used the predictions for the Johnson V band and determined the total luminosity using a randomly drawn V-band magnitude assuming a Gaussian distribution of the magnitude with

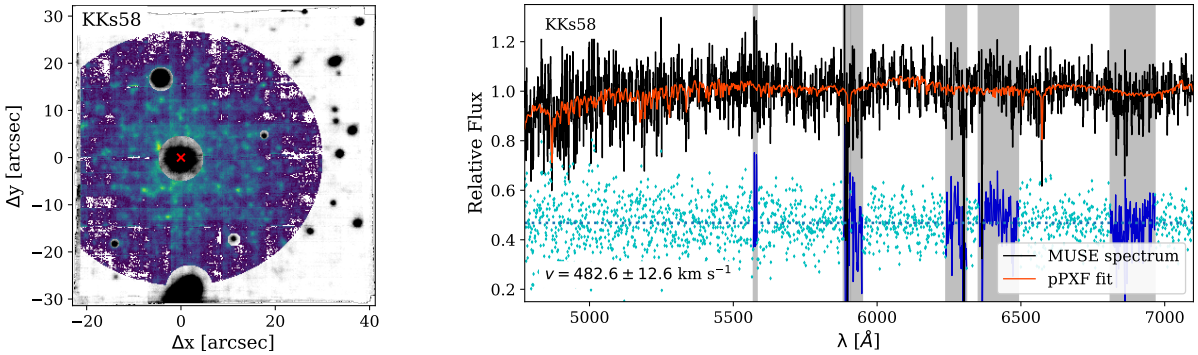

Figure 3.4.: Extraction of the KKs58 galaxy spectrum. *Left*: White-light image of KKs58, created by collapsing the MUSE cube along the spectral axis (10″≈ 160 pc). The position of the NSC is marked by the red cross. We show the mask that is used for the extraction of the integrated galaxy spectrum in green-blue colours while the masked pixels are shown with are in black and white. *Right*: pPXF fit to the normalised integrated spectrum of KKs58. The input spectrum is shown in black and the best-fitting combination of MILES SSP models is shown in red. The blue points indicate the residual, shifted to 0.5 for visibility. Masked regions with strong sky residual lines appear as grey-shaded. We only use the spectral range from 4500 to 7100 Å because the spectrum is heavily contaminated by sky residual and telluric lines at larger wavelengths.

$M_V = -9.51$ mag and $\sigma = 0.07$ mag. This was repeated 5000 times to accommodate for the magnitude uncertainties. We found a total luminosity of $L_{V,\,\mathrm{KKs58\text{-}NSC}} = 5.36 \pm 0.35 \times 10^5 L_\odot$ and $M/L_V = 1.37 \pm 0.15\ M_\odot/L_\odot$, corresponding to the expected M/L from our MC pPXF fit. This gives a stellar mass of $M_{*,\mathrm{KKs58\text{-}NSC}} = 7.34 \pm 0.87 \times 10^5 M_\odot$. KKs58-NSC is therefore less massive than the two most massive GCs in the MW, ω Cen and M 54 that have masses of $3.6 \times 10^6 M_\odot$ and $1.4 \times 10^6 M_\odot$, respectively (Baumgardt & Hilker 2018).

3.4.3 KKs58 galaxy spectrum

The galaxy KKs58 itself is very faint in the MUSE data as Fig. 3.4 illustrates. We attempted to bin the MUSE cube with the Voronoi binning scheme (Cappellari & Copin 2003a) to obtain a binned map of KKs58, but this was unsuccessful due to the low S/N. So we only extracted a single spectrum of the galaxy (right panel in Fig. 3.4) using a mask applied to the full cube (Fig. 3.4, left panel). Based on the galaxy shape in the DECam data and deep FORS2 image, this mask is circular with a radius of 120 pixels (24″≈ 390 pc), centred on the NSC, and excludes spaxels that have a negative mean flux, the NSC, and several foreground stars.

The final galaxy spectrum has a S/N of 11 and is heavily contaminated by sky residual and telluric lines above ∼ 7500 Å. The pPXF fit to the galaxy spectrum is shown in Fig. 3.4. Unfortunately, the S/N of the galaxy spectrum is not sufficient to explore the stellar population properties as we did it for KKs58-NSC. Nonetheless, we determined the LOS velocity, mean age and metallicity with 100 MC fits as described above. We measured a mean LOS velocity for KKs58 of $v_{\mathrm{KKs58}} = 482.6 \pm 12.6\,\mathrm{km\ s^{-1}}$, fully consistent with the LOS velocity of the NSC. We obtained a mean metallicity of [Fe/H] = −1.35 ± 0.23 dex and an age of ∼ 7 Gyr.

Müller et al. (2019) gave a photometric metallicity estimate taken from fitting the FORS2 colour magnitude diagram with old (10 Gyr) isochrones of [Fe/H] = −1.49 ± 0.80 dex, in agreement with our spectroscopic measurement.

We determined the stellar mass of KKs58 using the stellar population properties as obtained from the pPXF fit, deriving a M/L_V of 1.46 ± 0.15 $M_\odot/L_\odot$. With a total luminosity of $L_{V,\mathrm{KKs58}} = 5.02^{+0.55}_{-0.05} \times 10^6 L_\odot$ (Müller et al. 2019), this translates to a total stellar mass of $M_{*,\mathrm{KKs58}} = 7.33^{+1.10}_{-0.76} \times 10^6 M_\odot$. Therefore, the NSC-to-galaxy mass ratio is ∼ 10%, a typical value for a galaxy with such a mass (e.g. Sánchez-Janssen et al. 2019 or Fig. 1.12).

3.4.4 Star clusters in KK197

We extracted the spectra of KK197-NSC and the two GC candidates KK197-01 and 03 using a PSF-weighted circular aperture with a FWHM of 1.0″ and fitted these spectra with pPXF. The results of these fits can be found in Tab. 3.2. For the NSC of KK197, we found a LOS velocity of $v_{\mathrm{KK197\text{-}NSC}} = 635.4 \pm 1.5$ km s^{-1}.

KK197-NSC has a spectrum with a S/N of ∼ 100, sufficient to analyse the stellar populations properties such as age and metallicity distributions using a regularised fit (see bottom panel in Fig. 3.3). The weighted mean age and metallicity from the regularised fit are 7.3 Gyr and −1.79 dex, respectively, similar to the results for the NSC of KKs58. Again, the regularised fit gives no indication of multiple populations with the used SSP grid. Smaller scale variations such as small metallicity spreads as observed in some MW GCs cannot be ruled out. The 100 MC fits without regularisation give an age of 6.5 ± 1.0 Gyr and [Fe/H] = −1.84 ± 0.05 dex, in agreement with the weighted means of the regularised fit. The bright GC KK197-03 has a spectral S/N of 31, still sufficient to analyse the stellar populations. With 100 MC fits, we found [Fe/H] = −1.80 ± 0.11 dex and the LOS velocity of $v_{\mathrm{KK193\text{-}03}} = 642.6 \pm 3.8$ km s^{-1} clearly confirms membership to KK197. Our fit resulted in a mean age of ∼ 7 ± 1 Gyr in agreement with the NSC, but at this S/N the age is uncertain.

We determined the stellar masses of KK197-NSC and KK197-03 using the photometric predictions for the scaled-solar MILES models in the V band. For KK197-NSC, we found $L_{V,\mathrm{KK197\text{-}NSC}} = 7.60 \pm 0.42 \times 10^5 L_\odot$ and $M/L_V = 1.37 \pm 0.13\, M_\odot/L_\odot$. This results in a stellar mass of $M_{*,\mathrm{KK197\text{-}NSC}} = 1.04 \pm 0.11 \times 10^6 M_\odot$. The GC KK197-03 has a total luminosity of $L_{V,\mathrm{KK197\text{-}03}} = 7.12 \pm 0.39 \times 10^4 L_\odot$ and with a $M/L_V = 1.37 \pm 0.14\ M_\odot/L_\odot$, we obtained a mass of $M_{*,\mathrm{KK197\text{-}03}} = 9.76 \pm 1.13 \times 10^4\, M_\odot$. KK197-01, the faintest star cluster in KK197 identified by Georgiev et al. (2009c), has as S/N of 8, insufficient to obtain a reliable metallicity estimate. We can confirm its membership to KK197 based on its radial velocity of 636.4 ± 16.0 km s^{-1}.

By inspecting other point sources in the MUSE FOV, we identify two other potential faint star clusters (RA = 13:22:03.0, DEC = −42:32:07.5 and RA = 13:22:01.2, DEC = −42:32:18.3). Their MUSE spectra have low S/N of 6.2 and 4.5, respectively. Their measured LOS velocities are in agreement with KK197 of v= 652 ± 31 km s^{-1} and v= 663 ± 69 km s^{-1}, respectively. However, inspection of the HST image suggests that those are stars of KK197 blended along the line-of-sight.

3.4.5 Dynamical mass estimate of KK197-NSC

The NSC of KK197 was observed on 11 January 2010 with the UVES spectrograph on the VLT (Dekker et al. 2000) as part of the programme 084.D-0818 (PI: I. Georgiev). The instrumental setup included the red spectrograph arm with the standard setting centered on 580 nm, 2×2 CCD binning and a $1.2''$ slit width, which yielded a spectral resolution of R=34540, suitable for accurate velocity dispersion measurement. A single exposure of 3004 seconds resulted in a S/N ratio of 7 – 11 over the spectral range 4786 – 5761 Å covered with the lower CCD and S/N of 10–15 over 5835 – 6808 Å covered with the upper CCD. We downloaded the raw spectrum with the associated calibrations from the ESO Science Archive and reduced it using the ESO UVES pipeline (version 5.10.4) within the Reflex environment (Freudling et al. 2013). The velocity dispersion was measured by cross-correlating the spectrum of the KK197 NSC with a set of 18 UVES spectra of 13 different G and K-type giant stars having a range of metallicities ($-2.6 <$ [Fe/H] $< +0.3$ dex). These stars were observed as part of the UVES programme 069.D-0169 (PI: M. Rejkuba), which used the same red arm and 580 nm spectral setting, but had $1.0''$ slit width and no detector binning. We adopted the same procedure to measure the velocity dispersion as described in Rejkuba et al. (2007). First, given the difference in slit width and detector binning setup between the KK197-NSC and the giant star observations, we verified the dependency of velocity dispersion measurements on metallicity and instrumental broadening both with empirical templates and with synthetic spectra of K5 giants that were computed with different resolutions using the online spectrum synthesis tool developed and maintained at MPIA (Kovalev et al. 2018). The Fourier-filtered spectrum of the NSC was cross-correlated with all template spectra within the IRAF FXCOR task. The highest cross-correlation signal was measured for the stars with similar metallicity, and therefore for the final result we averaged the measurements for which the FXCOR *TDR* index was > 22 (see Tonry & Davis 1979). This resulted in the final velocity dispersion of $\sigma = 25.2 \pm 0.6$ km s^{-1} for the lower and $\sigma = 24.1 \pm 2.2$ km s^{-1} for the upper CCD. The median velocity of the NSC obtained from cross-correlation with template stars is $v = 636.68 \pm 0.77$ km s^{-1}, fully consistent with the velocity measured from the MUSE data.

To derive a dynamical mass for KK197-NSC, an aperture correction has to be applied to convert the observed velocity dispersion in the extracted slit area to a global and central velocity dispersion. We follow the same approach as described in Hilker et al. (2007). In short, we first constructed a 3D density profile from the structural parameters of a King profile fit (King 1962) to HST data (projected half-light radius $r_h = 3.03$ pc at a distance of 3.98 Mpc (this work) and concentration $c = 1.48$, Georgiev et al. 2009c). From that the cumulative mass distribution $M(< r)$, the potential energy $\phi(r)$, and the energy distribution function $f(E)$ are calculated. The corresponding 6D phase space density distribution is then sampled by an N–body representation of the NSC with 10^5 particles. x, y, z positions and vx, vy, and vz velocities are assigned to each particle, assuming spherical symmetry and an isotropic velocity dispersion. The influence of seeing is modelled by assuming that, in a projected version of the N–body model, the light from each particle is distributed as a 2D Gaussian with a FWHM that matches the observed seeing. For each particle, the fraction of the light that falls within the spectroscopic extraction aperture of $1.2'' \times 4.0''$ is calculated.

The fraction of light in that aperture is used as weighting factor for the velocities. The weighted velocity contributions are then used to calculate the expected velocity dispersion in the extracted slit area. Finally, the mass of the N-body model is iteratively adjusted such that the calculated velocity dispersion matches the observed one.

The model dynamical mass that matches the observed velocity dispersion of $\sigma = 25.2 \pm 0.6$ km s^{-1} for the lower CCD is $M_{\mathrm{KK197\text{-}NSC,\,dyn}} = 4.3 \pm 0.3 \times 10^6 M_\odot$. The global velocity dispersion of the NSC is $\sigma_g = 24.8$ km s^{-1} and the central one $\sigma_c = 30.4$ km s^{-1}, according to the modelled parameters. Our derived dynamical mass is about four times higher than the stellar mass derived from stellar population models. This difference might be caused by systematic uncertainties in the stellar population properties of the NSC and the assumptions of our mass modelling. We further discuss this in Sect. 3.5.3.

3.4.6 Stellar association in KK197

North-east of the KK197-NSC is an association of stars (see Fig. 3.5) that has a higher number density than the surrounding galaxy body and has a diameter of $\sim$ 33 pc (1.75″) in the HST image. We refer to this stellar association as KK197-SA. We extracted the spectrum of this region by selecting the pixels belonging to it above a flux threshold. The spectrum has a S/N of 11.1 and fitting for the velocity and mean metallicity with 100 MC fits, we found $v_{\mathrm{KK197\text{-}SA}} = 619.3 \pm 10.3$ km s^{-1} and [Fe/H] $= -1.59 \pm 0.15$ dex. With the low S/N, we cannot determine the age robustly, but our fits give a mean age of $\sim$ 10 Gyr, similar to the host galaxy. We cannot see any emission lines in the spectrum. This association of stars is clearly connected with KK197 and although the associated random errors are quite large, it appears to be more metal-poor than the host galaxy (mean metallicity of -0.84 ± 0.12 dex, see Fig. 3.6). The morphology excludes a classical GC. This stellar association might resemble an open star cluster, or maybe a GC in the process of being disrupted in the central potential of KK197.

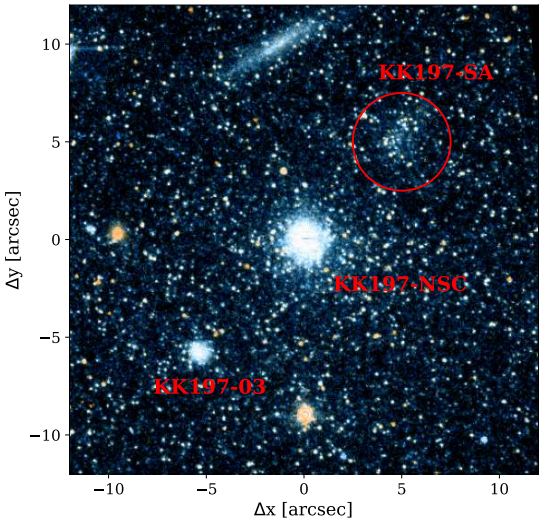

Figure 3.5.: HST colour image of the central part of KK197, using the F606W and F814W filters.

3.4.7 Galaxy KK197

The MUSE data of KK197 has a sufficient S/N to obtain a binned map of the integrated light after applying an ellipse cutout around the NSC. We masked bright stars, background galaxies, and the known star clusters in the FOV. The MUSE data of KK197 was binned to a continuous S/N of 25 using the Voronoi-binning scheme described in Cappellari & Copin (2003a). This map contains six bins. The binned spectra were fitted with PPXF with 100

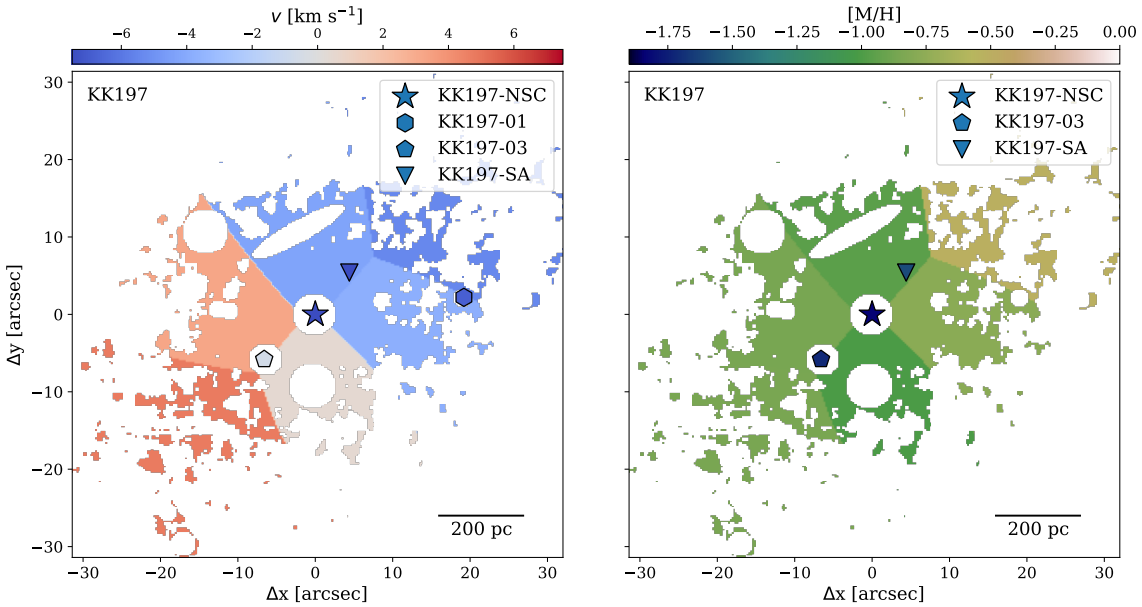

Figure 3.6.: Voronoi binned maps of KK197 in comparison to the star clusters. The maps were binned to S/N = 25. *Left*: LOS velocity map relative to the median velocity of 643.2 km s^{-1}. We added the LOS velocities of KK197-NSC, the two GCs and the loose stellar association of stars (KK197-SA) described in Sect. 3.4.6. *Right*: Mean metallicity map of KK197 obtained from an unregularised pPXF fit using the scaled-solar MILES SSP models.

MC runs each to acquire maps of the LOS velocities and the metallicities. Ages are uncertain at this S/N level, but we show the LOS velocity map and the mean metallicity map in Fig. 3.6. In these maps, we overplotted the properties of the NSCs and the GCs for comparison with the stellar light. In addition, Fig. 3.7 shows the position-velocity diagram for KK197. For this, we projected the bins onto the major axis and show their LOS velocity relative to the velocity obtained from the total galaxy spectrum of 643.2 km s^{-1}.

The LOS velocity field shows a rotation signal along the major axis of the galaxy with a maximum amplitude of $\sim \pm 5$ km s^{-1}. However, the Voronoi bins have typical LOS velocity uncertainties of ~ 4.5 km s^{-1}. We tested different binning schemes and obtained the same rotation signal robustly throughout these tests. The star clusters we identified in KK197 seem to be in agreement with the rotation signature, but deeper data is required to confirm it. Interestingly, the NSC might not be at rest with respect to the galaxy. Instead, from the total galaxy spectrum obtained from all six bins, we found a LOS velocity of $v_{KK197} = 643.2 \pm 3.5$ km s^{-1}, corresponding to a velocity difference between NSC and host of $\Delta v = 7.8 \pm 3.8$ km s^{-1}. A higher S/N in the galaxy spectrum would be required to confirm this offset.

KK197-NSC appears as a distinct component in the metallicity map shown in the right panel of Fig. 3.6. It is significantly more metal-poor than the galaxy field star population, for which we obtain a mean metallicity of [Fe/H] = -0.84 ± 0.12 dex. This is an intriguing result because in massive galaxies an opposite trend is found and the central region show higher metallicities due to efficient star formation fuelled by infalling, enriched gas (e.g. Spengler et al. 2017). Our metallicity estimate of the host galaxy is in agreement with the mean photometric metallicity of [Fe/H] = -1.05 dex determined by Crnojević et al. (2010) using the HST/ACS data. From the combined spectrum of KK197, we obtained a mean age of 10 ± 1 Gyr.

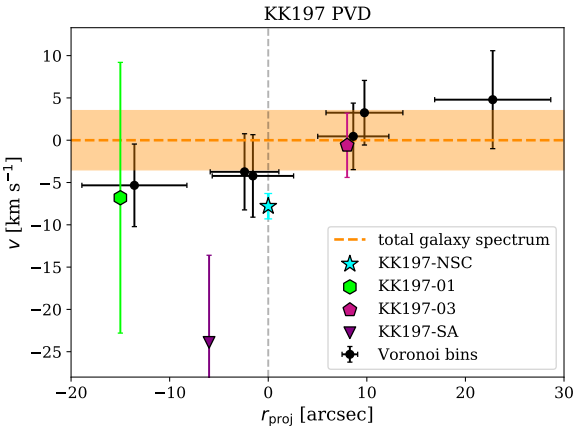

Figure 3.7.: Position-velocity diagram for KK197. The NSC, the GCs and the stellar association (KK197-SA) are marked by the coloured symbols. The x-axis is the distance projected on the major axis of the galaxy. The errorbars refer to the uncertainties from 100 MC fits. The orange coloured region shows host systemic the velocity.

Using the fit to the total spectrum of KK197 and its V-band magnitude of -13.04 mag (Georgiev et al. 2008), we derived a total stellar mass of $M_{*,\mathrm{KK197}} \sim 4 \times 10^7 M_\odot$. Based on this rough mass estimate, the ratio of NSC-to-host mass is $\sim$3 %, smaller than what is observed in KKs58.

3.5 Discussion

In the following, we place our measurements for KKs58 and KK197 into context with respect to other nucleated dwarf galaxies. We further discuss how the properties of the NSCs constrain their formation pathway and how the NSCs compare to UCDs.

3.5.1 Comparison to other nucleated galaxies

Both in KKs58 and KK197, we found metal-poor NSCs with metallicities comparable to metal-poor GCs. This is in agreement with a study of 61 NSCs of dwarf galaxies in the Fornax galaxy by Ordenes-Briceño et al. (2018) that found that most most dwarf nuclei have colours consistent with metal-poor GCs. They also report a bimodal mass distribution of dwarf galaxy NSCs with peaks at $\log(M_*/M_\odot) \approx 5.4$ and 6.3. With masses of $\log(M_*/M_\odot) = 5.9$ and 6.0, respectively, the NSCs of KKs58 and KK197 are located in between the two mass peaks.

We estimated the NSC-to-host stellar mass of KKs58 and KK197 to be $\sim$ 10% and $\sim$ 3%, respectively. These values use rough estimates of the host stellar mass, based on integrated magnitudes and a fixed mass-to-light ratio. These ratios are within the scatter for galaxies of similar mass (Ordenes-Briceño et al. 2018; Sánchez-Janssen et al. 2019). While the NSC-to-host mass relation appears to be independent of environment (Sánchez-Janssen et al. 2019),

Table 3.2.: Properties of KKs58, KK197, their NSCs and GCs. The quoted errors on v_{LOS}, [Fe/H], and age were derived with 100 fits to the respective spectra.

Object	RA (J2000)	DEC (J2000)	M_V (mag)	r_{eff} (pc)	S/N (Å^{-1})	v_{LOS} (km s^{-1})	[Fe/H] (dex)	M_* ($10^5 M_\odot$)
KKs58	13:46:00.8	−36:19:44	$-11.93^{+0.12}_{-0.01}$ [a]	244.7 ± 8.3	11.1	482.6 ± 12.6	−1.35 ± 0.23	$73.3^{+11}_{-7.6}$
KKs58-NSC	13:46:00.8	−36:19:44	−9.51 ± 0.07	6.6 ± 0.5	85.3	474.6 ± 1.9	−1.75 ± 0.06	7.34 ± 0.87
KK197	13:22:02.0	−42:32:08.1	−13.04 [b]	733 [c]	21.8	643.2 ± 3.5	−0.84 ± 0.12	∼ 400
KK197-NSC	13:22:02.0	−42:32:08.1	−9.89 ± 0.06 [b]	3.03 ± 0.13 [b]	99.8	635.4 ± 1.5	−1.84 ± 0.05	10.4 ± 1.1
KK197-01	13:21:59.8	−42:32:06.5	−5.75 ± 0.07 [b]	2.01 ± 0.17 [b]	8.1	636.4 ± 16.0	–	–
KK197-03	13:22:02.5	−42:32:13.8	−7.32 ± 0.06 [b]	2.63 ± 0.17 [b]	31.0	642.6 ± 3.8	−1.80 ± 0.11	0.98 ± 0.11
KK197-SA	13:22:01.6	−42:32:02.6	–	∼ 16	11.1	619.3 ±10.3	−1.59 ± 0.15	–

[a] from Müller et al. (2019).
[b] from Georgiev et al. (2009c), updated to a distance of $D = 3.87$ Mpc.
[c] from Sharina et al. (2008).

the mass ratio itself shows a trend with host stellar mass. The mass ratio seems to be higher in low-mass galaxies (see also Fig. 1.12), similar to what we find in the NSC-host system in the lower mass galaxy KKs58 compared to the more massive galaxy KK197. Nucleated late-type dwarf galaxies in low density environments can show a similar NSC-to-host mass fraction (Georgiev et al. 2016).

In our sample of 14 dwarf galaxies studied with MUSE, we found two nucleated dwarf galaxies. With a more complete sample, the effects of the Centaurus group environment on the nucleation fraction could be studied. Sánchez-Janssen et al. (2019) presented a study of the nucleation fraction of galaxies in different environments. They suggest that the nucleation fraction of dwarf galaxies appears to be lower in low density environments such as the Local Group when compared to the higher density environments of the Fornax, Virgo, or Coma clusters. The environment might also have an affect on the limiting galaxy mass threshold below which the nucleation fraction drops to zero. Studying dwarfs in the Fornax cluster, Ordenes-Briceño et al. (2018) determined a limiting mass of $\sim 2.5 \times 10^6 M_\odot$, while Sánchez-Janssen et al. (2019) identified a limiting mass of $\sim 5 \times 10^5 M_\odot$ in their study of the core region of the Virgo cluster. With a stellar mass of $7.3 \times 10^6 M_\odot$, KKs58 is already close to these thresholds. It is unclear if this limiting mass arises because low-mass galaxies become less efficient in forming NSCs or if there is a mechanism that can destroy them more easily. Due to its proximity, the Centaurus group provides an ideal laboratory to study the environmental effects on the nucleation fraction and the dwarf galaxies themselves.

3.5.2 Insights on nuclear star cluster formation

The formation of NSCs is still a heavily debated issue. As described in Sect. 1.5, typically two pathways are discussed: the in-situ formation directly at the galaxy's centre and formation from the inspiral and merging of GCs. With the collected data of KKs58 and KK197, we can put constraints on the formation of their NSCs.

The NSCs of both KKs58 and KK197 have a relatively simple star formation history with only one peak at $\sim$ 7 Gyr. We could not find any younger populations or emission lines that would indicate ongoing star formation. Nonetheless, our rough estimates of the ages of the host galaxies from their low S/N spectra (< 50) indicate that the NSC in KK197 could be younger than the main stellar body. However, measuring accurate ages of old (> 5 Gyr) stellar populations with integrated spectra is generally challenging (e.g. Spengler et al. 2017; Usher et al. 2019), and even more so in this case because the MUSE instrument lacks important age-sensitive features such as higher-order Balmer lines at bluer wavelengths. In addition, while the host galaxy spectra have only a low S/N, even the age measurements from the high S/N NSC spectra might be biased towards younger ages due to the presence of hot horizontal branch (HB) stars that most likely are present in massive star clusters (Schiavon et al. 2004; Ocvirk 2010; Georgiev et al. 2012). In the MW, almost all massive GCs have hot HB stars (Recio-Blanco et al. 2006; Lee et al. 2007) and their high effective temperatures ($T_{\rm eff} \sim 9000$ K) lead to a bias in spectroscopic metallicities towards younger ages especially in blue, metal-poor GCs of $\sim$ 4 Gyr compared to isochrone fitting (e.g. for NGC 3201 and NGC 5024; Dotter et al. 2010; Perina et al. 2011). Consequently, the age difference between NSC and host found in KK197 might be the result from uncertainty in the full spectral

fitting and an additional bias introduced by hot HB stars. Due to stellar crowding in the NSC, we cannot use isochrone fitting to the HST data to obtain a photometric age.

We observed a clear difference in metallicity between the two NSCs and their host galaxies. In KK197, we found a mean host galaxy metallicity of [Fe/H] = −0.84 dex, while the NSC and the bright GC (KK197-03) have a metallicity of [Fe/H] ∼ −1.8 dex. The NSC in KKs58 has a similarly low metallicity of [Fe/H] ∼ −1.75 dex and again, the host galaxy appears to be more metal-rich with a mean metallicity of ∼ −1.35 dex. For both galaxies, our spectroscopic metallicity estimates are in agreement with photometric estimates (Crnojević et al. 2010; Müller et al. 2019) and both galaxies follow the MZR of dwarf galaxies (Kirby et al. 2013).

That the NSCS are more metal-poor than their hosts is in contrast to the study by Paudel et al. (2011), who investigated nuclei of dwarf ellipticals in the Virgo cluster and established that a majority of them are more metal-rich then their host. However, these nuclei have absolute r-band magnitudes < -11 mag and are thus significantly more luminous than the NSCs of KKs58 and KK197. Since these NCSs are brighter and likely more massive than those studied here, a higher metallicity is fully expected (Spengler et al. 2017).

The simple star formation history and the NSCs being more metal-poor than their hosts disagrees with the in-situ formation of the NSCs in KKs58 and KK197. The in-situ scenario typically favours a more metal-rich NSC due to fast, repetitive gas accretion from the host's gas reservoir (e.g. Milosavljević 2004; Bekki 2007) and a prolonged star formation history at the centre of the potential well (Antonini et al. 2015). Because we find that the two NSCs have significantly lower metallicities than their hosts globally, it is unlikely that they have formed at the centres alongside with the metal-rich host galaxy, otherwise they should have experienced a complex star formation history and would be polluted by more metal-rich stars. When considering inflow of very metal-poor gas to the centre, for example from cold filaments (Cresci et al. 2010), we would expect to see an additional metal-rich population and an extended star formation history.

The GC accretion scenario, therefore, is more likely in the case of KKs58 and KK197. In this scenario, the NSC forms by accreting gas-free GCs that spiral into the galaxy's centre due to dynamical friction (e.g. Tremaine et al. 1975; Arca-Sedda & Capuzzo-Dolcetta 2014). Consequently, the formed NSC should reflect the properties of the accreted GCs that are typically more metal-poor than their hosts (e.g. Lamers et al. 2017). In KK197 this is further supported by the finding of the bright GC close in projection to the centre that shares the low metallicity of the NSC. In case the velocity offset between NSC and host in KK197 is confirmed, the NSC might not have settled at the centre yet and could still be in the process of spiralling in.

The presence of at least two other GCs in KK197 that have not sunk to the centre could be explained by larger initial formation distances (Angus & Diaferio 2009), but might also provide insight into the underlying DM distribution of the host galaxy. As has been discussed extensively for the case of the GC system of the Fornax dSph (e.g. Goerdt et al. 2006; Boldrini et al. 2019; Meadows et al. 2020), the orbits of inspiralling GCs are affected by the underlying DM distribution and could be used to differentiate between cuspy (centrally rising) or cored (centrally flat) DM profiles. GCs in dwarf galaxies are expected to quickly spiral towards the centre in cuspy DM halos (e.g. Tremaine et al. 1975), but might stall near

the core radius in cored DM halos (Goerdt et al. 2006). Constraining the inner DM slope observationally is challenging because of degeneracies with orbital anisotropy, mass-to-light ratios, halo shapes, and initial formation location of the GCs. With our limited data of KK197, we cannot study the underlying DM profile, but with precise ages and masses of the star clusters and the host galaxy, KK197 would provide an interesting testbed to study the cusp-core problem. The possible age difference between NSC and host we observed in KK197, if confirmed, could also resolve this so called timing problem, if the star clusters formed later at larger distances from metal-poor gas. A similar scenario has been recently discussed for the Fornax dSph (Leung et al. 2020).

We could not identify GCs in KKs58. All possible candidates turned out to be either foreground stars of the MW or background galaxies. Although we cannot exclude that there are undetected GCs outside the MUSE FOV, it is also possible that KKs58 only has one star cluster, the NSC. Under the assumption that the NSC was purely formed out of GCs, the NSC would then contain the entire original GC population of KKs58 with the exception of some that might have been stripped in tidal interactions with the group environment or are outside of the MUSE FOV. To test whether this is reasonable, we can compare the NSC-to-host mass ratio of $\sim 10\%$ to the GC system-to-host mass ratio typically found in such low-mass galaxies. Forbes et al. (2018) studied the GC system-to-host mass relation over a large range of host masses and found that the ratio can scatter between 0.1 and 10%. Consequently, KKs58 is already within this scatter without the presence of additional star clusters. The same conclusion can be drawn when comparing the GC specific frequency S_N of KKs58 to other dwarf galaxies. Assuming the NSC is of GC origin, KKs58 has $S_N \sim 16$ and KK197, with three confirmed star clusters, has $S_N \sim 18$. Both are in agreement with other dwarf galaxies of similar brightness that have $S_N \approx 10 - 20$ (Georgiev et al. 2010).

3.5.3 Possible UCD progenitors?

We compare the NSC of KKs58 and the star clusters of KK197 to other compact stellar systems in Fig. 3.8. This figure shows effective radii and absolute V-band magnitudes for a large sample of GCs, UCDs, and NSCs from literature compilations presented in Misgeld & Hilker (2011) and Fahrion et al. (2019a)[3]. We highlight the UCDs associated with Cen A (Rejkuba et al. 2007) to illustrate that those are generally on the fainter side of the UCD population and some even have a very similar size and magnitude as the NSCs of KKs58 and KK197. The NSCs are also placed among the fainter NSC population, especially the NSC of KK197. The two GCs in KK197 are well placed among other faint GCs known from studies of galaxy cluster environments.

In case KKs58 or KK197 would get destroyed in the group environment and the NSCs would be stripped without being destroyed or significantly altered, the remnant NSCs would fit within the UCD population, but might also be interpreted as a GC due to their magnitude and low mass. This highlights the ambiguity connected to the question of origin for UCDs. It has been suggested that UCDs could be the stripped nuclei of disrupted galaxies (Phillipps et al. 2001; Bekki et al. 2003; Drinkwater et al. 2003; Pfeffer & Baumgardt 2013; Strader

[3]Summarised in Sect. 2.7.

et al. 2013), the high-mass end of the star cluster population (Mieske et al. 2002, 2004; Kissler-Patig et al. 2006), or the result of merged star clusters (Fellhauer & Kroupa 2002; Maraston et al. 2004; Fellhauer & Kroupa 2005). So far, the only unambiguous confirmations of stripped NSC-type UCDs have been made for the most massive, metal-rich UCDs using either the presence of a SMBH detected with high-resolution IFU observations (Seth et al. 2014; Ahn et al. 2017, 2018; Afanasiev et al. 2018) or from the detection of a complex, extended star formation history (Norris et al. 2015). In contrast, objects like M 54 and ω Cen in the MW, as well as the comparison of the NSCs of KKs58 and KK197 to Cen A UCDs, show that the population of low-mass UCDs most likely also contains a significant population of stripped NSCs. Using simulations, Pfeffer et al. (2014) predicted the number of UCDs from stripped NSCs of a given stellar mass as a function of environment virial mass. For the Centaurus group, virial masses between 4.0 $\times 10^{12}$ and 1.4 $\times 10^{13} M_{\odot}$ are discussed (Karachentsev et al. 2007; Woodley 2006; Woodley et al. 2007, 2010a) and due to this large scatter, the number of predicted UCDs from stripped NSCs with masses $> 10^5 M_{\odot}$ ranges between $\sim 4 - 13$, following the prescription of Pfeffer et al. (2014). Because these predictions strongly depend on the nucleation fraction of galaxies, assessing the number and masses of dwarf galaxy NSCs can help to improve such models.

Confirming the NSC origin of a low-mass, metal-poor UCD is particularly challenging because its properties are mostly indistinguishable from a high-mass GC (see also Sect. 2.7). In the case of KKs58, the extended size and the ellipticity could give an indication, if it were to survive unaltered the disruption of its host. On the other hand, in case KK197 would be stripped of its NSC, it would be very difficult to distinguish it from the general intra-group population of low-mass GCs. However, simulations by Pfeffer & Baumgardt (2013) have shown that while the original NSCs do not expand during the stripping process, they can retain an remnant envelope from the galaxy body causing the resulting UCD to appear extended. Therefore, extended sizes of GCs at these low masses and metallicities could give further evidence of NSC-origin. Examples of faint envelopes around compact GC-like objects have been found in the Virgo (Liu et al. 2015) as well as in the Fornax cluster (Voggel et al. 2016).

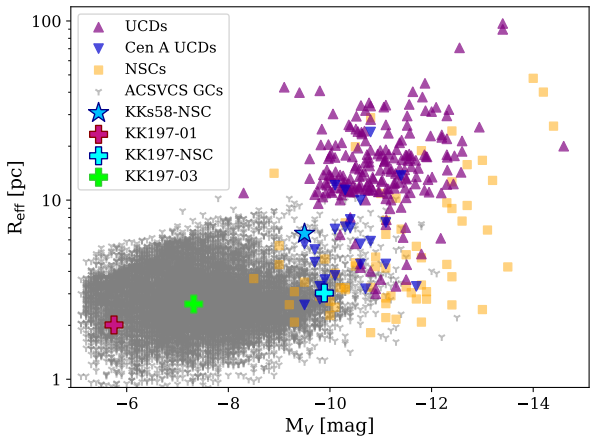

Figure 3.8.: V-band magnitudes versus effective radius for different compact stellar systems. NSCs and star clusters compilations are taken from Misgeld & Hilker (2011), the UCDs from Fahrion et al. (2019a). We highlight the UCDs of Cen A with blue triangles. The NSC of KKs58 is shown with the blue star. The star clusters of KK197 are shown by the crosses.

The elevated dynamical mass compared to our stellar population estimate of KK197-NSC is another observable that this NSC shares with many UCDs and some GCs (Haşegan et al. 2005; Rejkuba et al. 2007; Mieske et al. 2008; Taylor et al. 2010). Mieske et al. (2013) found a mean fraction of dynamical-to-stellar mass-to-light ratios of 1.7 for massive UCDs, which

is lower than our result for KK197-NSC, but still consistent within the scatter. As discussed before, our stellar population properties of the NSCs might be biased to lower ages due to the presence of hot horizontal branch stars. This also affects the M/L we use for the mass determination. For example, assuming an age of 13 Gyr instead of the best-fit age of 7 Gyr at the metallicity of KK197-NSC, increases the M/L_V from 1.4 to 2.1. In addition, our mass modelling assumes spherical symmetry and isotropy, and does not account for internal rotation of the NSC. However, simulations and observations have shown that NSCs can have complex density profiles (Böker et al. 2002) and kinematics (e.g. Lyubenova et al. 2013; Perets & Mastrobuono-Battisti 2014; Lyubenova & Tsatsi 2019; Fahrion et al. 2019b).

The elevated dynamical M/L can also have physical origin. Variations of the IMF in the clusters can result in this difference, both when considering top-heavy (Murray 2009; Dabringhausen et al. 2009) and bottom-heavy IMFs (Mieske & Kroupa 2008), and a central SMBH can also increase the dynamical M/L (Mieske et al. 2013).

3.6 Conclusions

This chapter is adapted from Fahrion et al. (2020c) and reports the discovery of a NSC in KKs58, a dwarf galaxy member of the Centaurus group, and analyse its properties based on new MUSE data and ancillary photometric data from FORS2 and DECam. Furthermore, we analyse the NSC and two GCs in KK197, another dwarf galaxy in the Centaurus group that was previously studied photometrically with HST ACS data (Georgiev et al. 2009a). We summarise our results as follows:

- We fitted KKs58's DECam g-band surface brightness image using a double Sérsic profile. We determined the NSC to be elliptical with an effective radius of 6.6 ± 0.5 pc at an absolute magnitude of $M_g = -9.19$ mag ($M_V = -9.51 \pm 0.07$ mag).

- We extracted a high S/N MUSE spectrum of KKs58-NSC and measured its LOS velocity (v = 474.6 ± 1.9 km s^{-1}) and stellar population properties with full spectral fitting. The NSC is at least ~ 7 Gyr old and metal-poor ([Fe/H] = −1.75 dex). Using the stellar population analysis, we obtain a stellar mass of $M_{*,\mathrm{KKs58-NSC}} = 7.3 \times 10^5 M_\odot$.

- The low surface brightness of KKs58 itself does not allow to obtain a map of its kinematic or stellar population properties. Instead, we extracted a single, low S/N spectrum and measured the LOS velocity of v = 482.6 ± 12.6 km s^{-1}. The low S/N gives only rough estimates of the age of ~ 7 Gyr and metallicity of [Fe/H] ~ -1.35 dex. The photometric metallicity estimate (Müller et al. 2019) is consistent with the NSC metallicity. For the host galaxy, we estimated the stellar mass of $M_{*,\mathrm{KKs58}} \approx 7 \times 10^6 M_\odot$.

- We confirmed the membership of three star clusters in KK197 based on their radial velocities. The stellar density is high enough to obtain a Voronoi binned map of the radial velocities and metallicity distribution. The galaxy shows a rotation signature with a projected maximum amplitude of ~ 5 km s^{-1}.

- The NSC of KK197 might show an offset velocity to the host galaxy of $\Delta v = 7.8 \pm 3.8$ km s^{-1}. Furthermore, its metallicity of [Fe/H] $= -1.84$ dex is significantly lower than the surrounding galaxy field stellar population ([Fe/H] ~ -0.84 dex). Using a high-resolution VLT UVES spectrum of KK197-NSC, we determined the dynamical mass of this star cluster to be $M_{\mathrm{dyn,\ KK197\text{-}NSC}} \approx 4 \times 10^6 M_\odot$, while we find a stellar mass of $\sim 1 \times 10^6 M_\odot$.

- We found for both dwarf galaxies that the NSCs are more metal-poor than the host galaxies. Comparing this to basic expectations from different NSC formation scenarios, the lower metallicity in the NSC makes a strong case for the GC accretion scenario, where the NSC forms out of inspiraling GCs that were formed farther out in the galaxy. The metal-poor GC found in KK197 further supports this scenario.

- We estimated NSC mass-to-host mass ratios of $\sim 3 - 10\%$ in the two dwarf galaxies, typical values for low-mass dwarf galaxies. The masses of the NSCs are also typical for NSCs of a dwarf galaxy as the comparison to larger samples of nucleated dwarfs shows. However, the stellar mass of KKs58 places it in a mass range where typically a very low nucleation fraction is observed.

- The mass, size, and metallicity places the NSCs of KKs58 and KK197 within the range of other NSCs, but also among known low-mass UCDs of the Centaurus group. This suggests that some of these UCDs might have originated from stripped NSCs of disrupted dwarf galaxies like KKs58 or KK197, although their observed properties today make them indistinguishable from the high-mass GC population.

Out of a sample of 14 dwarf galaxies observed with MUSE, we were able to identify two nucleated dwarfs. Although there have been successful attempts in searching for NSCs in dwarf galaxies of the Centaurus group (e.g. Georgiev et al. 2009c), the nucleation fraction of this environment is still unknown. Identifying potential NSCs in low-mass dwarf galaxies is generally challenging and requires either a spectroscopic measurement to confirm the membership to a galaxy via radial velocities or high-resolution photometry. At the same time, extracting even a single spectrum from an MUSE observation of faint host galaxies to measure radial velocities or stellar population properties is also difficult. In these cases, GCs or even NSCs provide excellent tracers of otherwise inaccessible properties of the host galaxies.

> Isn't it enough to see that a garden is beautiful without having to believe that there are fairies at the bottom of it too?
>
> Douglas Adams, The Hitchhiker's Guide to the Galaxy

4 | Globular clusters as tracers of galaxy properties and mass assembly

The previous chapters have shown how the properties of star clusters can be extracted and analysed from MUSE data. We have seen that in order to constrain NSC formation, a panoramic view of NSCs, GCs, and the host galaxies has to be collected. In this chapter, I focus now on a specific component: the GCs. I present an analysis of GCs from MUSE data of 32 galaxies in the Fornax cluster based on the F3D project (Sarzi et al. 2018).

This chapter is adapted from Fahrion et al. (2020a) and Fahrion et al. (2020b) to highlight the aspects that are most relevant to this thesis. While Fahrion et al. (2020a) presents the catalogue of spectroscopic GCs from the F3D survey, Fahrion et al. (2020b) focuses on the colour-metallicity relation inferred from this GC catalogue and its implication for GCs as tracers of galaxy assembly.

4.1 The need for spectroscopic globular cluster catalogues

Cosmological simulations provide a framework of galaxy formation and evolution via the hierarchical mergers of smaller galaxies, but the assembly of individual galaxies is challenging to constrain observationally. GCs are often used to study galaxy assembly due to their ubiquitous occurrence in all massive galaxies ($M_{\rm gal} > 10^9 M_\odot$, see Brodie & Strader 2006). Their potential as tracers of galaxy evolution is based on their old ages ($\gtrsim 10$ Gyr, Puzia et al. 2005; Strader et al. 2005), which sets their formation at a redshift of $z \gtrsim 2$. The survival of GCs until today allows us to view them as fossil records that have the chemodynamical properties of their origin encapsulated in their stellar population properties as well as in their orbital parameters which change only slowly over time (e.g. Brodie & Strader 2006; Beasley et al. 2008; Harris et al. 2016).

As described in Sect. 1.2, large photometric surveys such as the ACSVCS or ACSFCS have collected photometric catalogues of GC candidates (Peng et al. 2006; Jordán et al. 2015). These catalogues describe the sizes, luminosities, and colours of hundreds of GCs per galaxy, but to efficiently use GCs as tracers of galaxy, spectroscopy is required to study their kinematics and accurate stellar population properties. Nowadays, also large spectroscopic samples of extragalactic GCs exist, for example in the core of the Fornax cluster (Pota et al. 2018) or within the SAGES Legacy Unifying Globulars and Galaxies Survey (SLUGGS,

Brodie et al. 2014). These studies have shown that spectroscopic GC studies provide a powerful tool to trace the kinematics and metallicity of the host galaxy in the halo regions that are inaccessible with integrated light approaches due to the low surface brightness. However, with multi-object spectrographs, the inner regions of galaxies are usually avoided due to crowding of GCs in central regions and the difficulty of modelling the underlying bright galaxy light.

This chapter presents the a large catalogue of GCs obtained with MUSE from the central parts of galaxies that facilitates a direct comparison between GC properties and the underlying galaxy light and enables us to test how well GCs perform as tracers of galaxy properties. These galaxies were observed with MUSE as part of the F3D project. Additional, we present a non-linear CZR that was obtained using a sample of 187 GCs of 23 galaxies. Because F3D covers both ETGs and late-type galaxies (LTGs) with masses ranging between 10^8 and $10^{11} M_\odot$, we can explore a sample of GCs over a variety of galaxy masses. While most previous works have focused on rather massive galaxies with $M_{\rm gal} > 10^{10} M_\odot$, we can explore the effect of the host galaxy on the CZR because of the broad mass range of F3D galaxies.

4.2 Fornax3D MUSE data

F3D is a magnitude-limited survey ($M_V \lesssim -17$ mag) that targets all massive galaxies within the virial radius of the Fornax cluster. Of these galaxies, 22 are ETGs and 10 are LTGs, having stellar masses between 10^8 and 10^{11} $M_\odot$. The data acquisition of F3D was carried out between July 2016 and December 2017 using MUSE (Bacon et al. 2010) in the wide field mode configuration that provides a 1×1 arcmin^2 FOV per pointing, sampled at $0.2'' \times 0.2''$. The nominal wavelength range covers the optical from 4750 Å to 9300 Å with a sampling of 1.25 Å at a mean resolution of ~ 2.5 Å (see Sect. 2.2).

Depending on individual galaxies, between one and three pointings with MUSE were acquired. The total integration times for central and middle pointings are ~ 1 hour and halo pointings have a typical integration time of 1.5 hours, which was chosen to result in a limiting surface brightness of $\mu_B \approx 25$ mag arcsec^{-2}. The observations were carried out with a mean FWHM of the PSF of $\sim 0.8''$. This PSF in combination with the deep surface brightness level in the outer regions allow us to extract the spectra of a large number of point sources.

The data reduction of the F3D data is described in detail in Sarzi et al. (2018) and Iodice et al. (2019a), and was performed with the MUSE pipeline 2.2 (Weilbacher et al. 2012, 2016). It includes bias and flat-field correction, astrometric calibration, sky subtraction using dedicated sky observations, wavelength and flux calibration. To further reduce the contamination from sky lines, the ZAP algorithm (Soto et al. 2016) was applied.

Maps of the LOS velocities were presented in Iodice et al. (2019a) and in this work, we further used metallicity maps that were derived from the line-strength measurements presented in Iodice et al. (2019a) for a comparison to the GCs. More detailed maps of the stellar population properties will be subject of future work. We also included FCC 213 (NGC 1399), the central galaxy of the Fornax cluster. For FCC 213, we complemented the

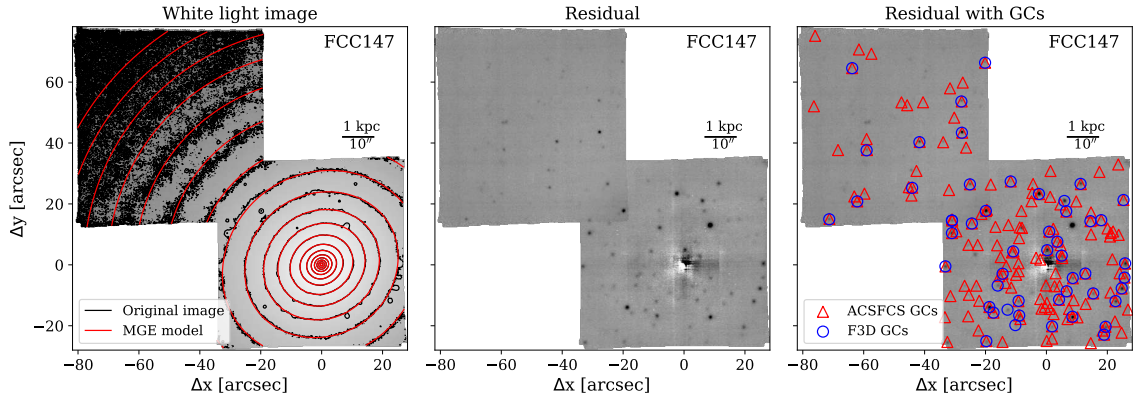

Figure 4.1.: Illustration of the MGE modelling used to create residual images in which GCs were detected. *Left*: collapsed MUSE image of FCC 147. Black and red contours illustrate isophotes of the original image and the MGE model, respectively. *Middle*: residual image after subtracting the model from the image. Otherwise hidden point sources are now visible. *Right*: Residual with GC highlighted. Red triangles show the position of GC candidates from the ACSFCS catalogue (Jordán et al. 2015). The blue circles show the position of confirmed F3D GCs in FCC 147.

F3D MUSE pointings of the middle and outer parts with archival MUSE data of the central region (Prog. ID. 094.B-0903, PI: S. Zieleniewski).

The F3D pointings cover between 2 – 3 $R_{\rm eff}$ of the host galaxies (Iodice et al. 2019a) and thus give the opportunity to spectroscopically study GC systems in the inner parts of massive galaxies. We were able to find at least one GC in every galaxy and in total, our catalogue provides a sample of LOS velocities of 722 GCs and metallicities of 238 GCs.

4.3 Methods

In the following, we briefly summarise our methods to detect the GCs in the MUSE data and to extract their spectra. We describe on how the LOS velocities and stellar population properties are determined from full spectral fitting. A more detailed description can be found in Sect. 2.3.2 and Sect. 2.4.

4.3.1 Detection of GCs in the MUSE data

At the distance of the Fornax cluster (20 Mpc, Blakeslee et al. 2009), GCs appear as unresolved point sources in the collapsed MUSE images. The majority of GCs are hidden within the high surface brightness areas of their host galaxies and thus, the underlying light distribution of the galaxy has to be removed to detect these GCs. As for FCC 47 (Chapt. 2), this was done by creating a MGE model (Bendinelli 1991; Monnet et al. 1992; Emsellem et al. 1994; Cappellari 2002) of every galaxy in our sample, which was subtracted from the image. In this way, a residual image was generated in which point sources such as GCs can be detected. To exploit the large wavelength coverage of MUSE, we did not use a single collapsed image for the MGE modelling, but instead cut the full MUSE cube into slabs of 500 wavelength slices (625 Å) that are combined to a total of seven collapsed images from

4700 to 9000 Å. The combination of several wavelength slices helps to improve the spatial S/N of the GCs and using seven instead of a single combined image further helps to reduce the contamination from emission line objects such as background star forming galaxies and planetary nebulae. In regions that have a visible dust feature, for example in the centre of FCC 167 (see Viaene et al. 2019), we did not extract GCs.

Figure 4.1 shows an example of the MGE modelling for the ETG FCC 147. In the residual image (middle panel), many point sources are clearly visible. We used DAOSTARFINDER, a Python implementation of the DAOFIND algorithm (Stetson 1987), to detect those point sources in the image and to build the initial sample of GC candidates. Because most of the F3D galaxies were also covered by the ACSFCS (Jordán et al. 2007), we used the catalogue of GC candidates from Jordán et al. (2015) for cross reference to remove the majority of background galaxies, foreground stars, and image artefacts from the GC sample (red triangles in Fig. 4.1). The remaining contamination in this sample is very low (~ 1 %), but although the ACSFCS catalogues are extensive and deeper than the MUSE data, they sometimes miss a small number of GCs. Therefore, we manually inspected the spectra of bright point sources that were not included in the ACSFCS catalogues. While redshifted background galaxies and dwarf stars are easily identified with their spectra, any additional GC candidate was checked for its LOS velocity before adding it to the catalogue. Per galaxy, there were usually only a few additional GCs found. Often, these lie in regions where the subtraction of the MGE model left a strong residual, for example in the disc of the S0 galaxy FCC 170.

FCC 113, FCC 161, FCC 176, FCC 179, FCC 263, FCC 285, FCC 290, FCC 306, FCC 308, and FCC 312 have no available ACSFCS GC catalogue and thus required that spectra of the full initial sample of point sources was checked to remove background galaxies and foreground stars. Because some of these galaxies also actively form stars (e.g. FCC 312), HII regions were also among the point source sample and were filtered out. While background galaxies, bright foreground stars, and line-emission objects such as HII regions can be found by visual inspection of the spectrum, the GC sample was finally cleaned after measuring the LOS velocity (Sect. 4.3.3) to confirm membership to the Fornax cluster ($500 < v_{\rm LOS} < 2500$ km s^{-1}). This range was based on the observed radial velocities of the F3D galaxies (Iodice et al. 2019a), but the final sample only contains GCs with $800 < v_{\rm LOS} < 2300$ km s^{-1}. The sources shown by blue circles in the right panel of Fig. 4.1 represent the final sample of confirmed GCs in FCC 147.

Because of the velocity information and the central positioning of the pointings, the association of GCs to their host was straightforward. For most galaxies, all the GCs in the FOV could be associated to the observed host, however, we found four GCs in the pointing of FCC 219 that appear to be associated to FCC 213 because of their velocities ~ 1300 km s^{-1} that are close to the systemic velocity of FCC 213, while the other GCs of FCC 219 show velocities between 1700 and 2000 km s^{-1}. These outlier GCs might classify as intra-cluster GCs, but could also be bound to FCC 213 (see, e.g. Schuberth et al. 2008). In FCC 148, we found three GCs in the pointing that are likely associated to the nearby massive galaxy FCC 147 due to their LOS velocities. In FCC 184, three GCs were found that show a velocity difference to the host systemic velocity of ~ 400 km s^{-1}, which might be possible intra-cluster GCs and one such GC was found in FCC 182.

4.3.2 Extraction of spectra

We extracted the spectrum of each GC candidate from the MUSE cubes using a PSF-weighted circular aperture assuming a Gaussian shape with FWHM of 0.8″, the mean PSF FWHM of the F3D galaxies. To determine the local galaxy background, we used an annulus aperture around each GC with an inner radius of 8 pixel and an outer radius of 13 pixel. To prevent contribution from neighbouring GCs to the background spectrum, the positions of all GCs were masked when extracting the background spectrum.

For GCs with small galactocentric distances to their host's centre, the extraction of the background spectrum is particularly challenging due to the strongly varying surface brightness profile of the galaxy. For this reason, we extracted the background spectrum of close GCs ($< 10''$) with a smaller annulus with inner and outer radii of 5 and 8 pixel, respectively. Still, the spectra of these GCs can be contaminated by galaxy light, especially in massive hosts. We found that a possible contamination mostly affects the GC metallicities that are then biased to higher values.

The spectral S/N was determined in a continuum region around 6500 Å using the ESTIMATESNR function of PYASTRONOMY (Czesla et al. 2019). For GCs with a S/N $\geq$ 3, we determined LOS velocities and for GCs with S/N $\geq$ 8, we additionally fitted for metallicities. GC candidates with S/N $<$ 3 are removed from the final sample as we cannot confirm their nature or membership to a host galaxy. Compared to Chapt. 2, we relaxed the S/N criterion for metallicity measurements from S/N $\geq$ 10 down to 8. This might lead to later metallicity uncertainties, but testing has shown that this still allows a stable recovery of the mean metallicity (similar to Appendix A).

4.3.3 Full spectral fitting

We fitted the GC spectra using full spectrum fitting with PPXF (Cappellari & Emsellem 2004; Cappellari 2017) as described in Sect. 2.4. For the GCs, we used the E-MILES models because of their broad wavelength coverage from 1680 to 50000 Å. We used the description of the line spread function from Guérou et al. (2016), but we did not attempt to measure velocity dispersions because the intrinsic velocity dispersions of GCs (usually < 20 km s^{-1}) are below the spectral resolution of MUSE (~ 80 km s^{-1}).

Figure 4.2 shows the spectra of two GCs of FCC 161 and the corresponding PPXF fits as examples. Regions with residual sky or telluric lines were masked from the fit and are shown in grey. We first fitted each GC with S/N $\geq$ 3 for the LOS velocity with

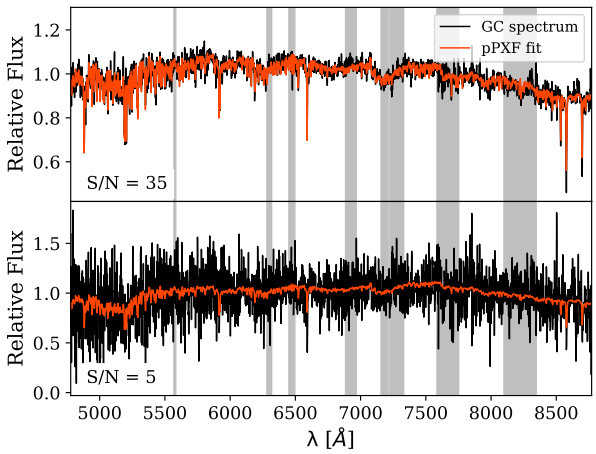

Figure 4.2.: Two exemplary GC spectra (S/N $\sim$ 35 and S/N $\sim$ 5). The original spectra are shown in black, the PPXF fit is shown in red. Regions with strong sky residual lines were masked from the fit (grey shaded areas). Both GCs were found in FCC 161.

additive polynomials of degree twelve and no multiplicative polynomials. For GCs with S/N $\geq$ 8, we fitted for the metallicity in a second step by keeping the LOS velocity fixed and using multiplicative polynomials of degree eight. To limit effects from the well known age-metallicity degeneracy, we restricted the library to ages $\geq$ 8 Gyr. As discussed in Sect. 4.4.4, this choice appears reasonable because most GCs have ages $>$ 8 Gyr with only very few exceptions.

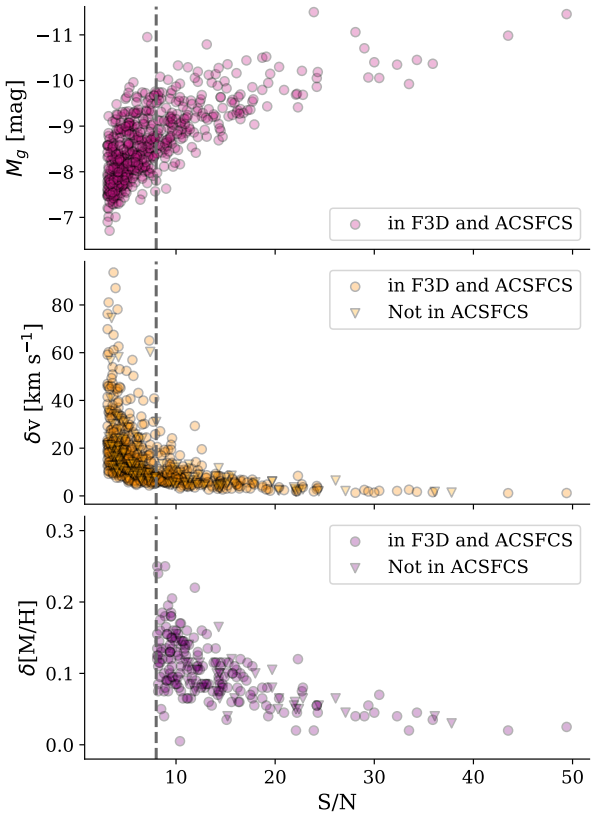

Figure 4.3.: Relation between GC S/N and absolute g-band magnitude from the ACSFCS catalogue (*top*), LOS velocity uncertainty (*middle*), and metallicity uncertainty (*bottom*) for the sample of F3D GCs. The vertical line marks S/N = 8, our limit for the metallicity measurement. In the top panel, we only show GCs with M_g from the ACSFCS, while the others show the full sample.

To estimate realistic uncertainties, we fitted each GC 100 times with the MC approach described in Sect. 2.4. The uncertainties on the velocity and metallicity depend on the S/N of the GC, as shown in Fig. 4.3. In this figure, we plot the distribution of uncertainties in dependence of S/N. The uncertainty on the velocity is typically $<$ 20 km s^{-1}, but for GCs with S/N $\sim$ 3, it can rise to values $>$ 50 km s^{-1}. Typical metallicity uncertainties are $\sim$ 0.15 dex. We also show the relation between spectral S/N and absolute g-band magnitude from the ACSFCS catalogue assuming a distance to the Fornax cluster of 20 Mpc (Blakeslee et al. 2009). In general, brighter GCs have higher S/N, but there is a large scatter in the relation. This scatter is not surprising because the GC spectra have different total exposure times depending on their location in the MUSE mosaics. Their S/N depends also on the contrast with the underlying galaxy background and the absence of strong absorption lines at low metallicities increases uncertainties for metal-poor GCs.

Table 4.1.: Overview of F3D galaxies and the number of extracted GCs. The galaxies are ordered by their FCC number. Masses are from Iodice et al. (2019a); Liu et al. (2019).

FCC	Altern. name	RA (J2000)	DEC (J2000)	$\log(M_{\rm gal})$ $\log(M_\odot)$	$R_{\rm eff}$ ($''$)	Type	$N_{\rm S/N\,>\,3}$	$N_{\rm S/N\,>\,8}$	$< R_{\rm GCs} >$ ($R_{\rm eff}$)	$<$[M/H]$_{\rm GCs}>$ (dex)
(1)	(2)	(3)	(4)	(5)	(6)	(7)	(8)	(9)	(10)	(11)
083	NGC 1351	03:30:35.1	−34:51:14	10.5	35.7	E5	57	25	0.70	-0.75 ± 0.49
090	PGC 13058	03:31:08.1	−36:17:19	8.9	12.1	E4	4	1	1.11	−1.99
113	ESO 358-015	03:33:06.8	−34:48:26	8.3	20.6	Scd	4	2	0.75	-1.58 ± 0.34
119	–	03:33:33.7	−33:34:18	9.0	17.4	S0	1	0	1.05	–
143	NGC 1373	03:34:59.1	−35:10:10	9.4	11.0	E3	20	4	1.91	-1.24 ± 0.21
147	NGC 1374	03:35:16.8	−35:13:34	10.4	24.8	E0	55	20	1.20	-0.81 ± 0.57
148	NGC 1375	03:35:16.8	−35:15:56	9.8	28.3	S0	2	2	2.10	-1.85 ± 0.14
153	IC 1963	03:35:30.9	−34:26:45	9.9	19.8	S0	14	2	1.26	-1.52 ± 0.08
161	NGC 1379	03:36:04.0	−35:26:30	10.4	28.6	E0	71	32	0.97	-0.70 ± 0.44
167	NGC 1380	03:36:27.5	−34:58:31	11.0	56.4	S0	59	17	0.68	-0.32 ± 0.56
170	NGC 1381	03:36:31.6	−35:17:43	10.4	15.9	S0	22	9	2.00	-0.74 ± 0.51
176	NGC 1369	03:36:45.0	−36:15:17	9.8	53.7	SB	11	1	0.41	−2.05
177	NGC 1380A	03:36:47.4	−34:44:17	9.9	35.9	S0	19	8	0.68	-1.23 ± 0.42
179	NGC 1386	03:36:46.3	−35:59:57	10.2	30.0	Sa	2	0	0.96	–
182	–	03:36:54.3	−35:22:23	9.2	9.9	SB0	9	3	1.74	-0.81 ± 0.28
184	NGC 1387	03:36:56.9	−35:30:24	10.7	35.5	SB0	49	18	1.25	-0.20 ± 0.47
190	NGC 1380B	03:37:08.9	−35:11:37	9.7	18.3	SB0	32	12	1.22	-1.38 ± 0.33
193	NGC 1389	03:37:11.7	−35:44:40	10.5	28.2	SB0	16	1	0.72	−1.49
213	NGC 1399	03:38:29.2	−35:27:02	11.4	308	E1	111	26	0.12	-0.50 ± 0.55
219	NGC 1404	03:38:52.1	−35:35:38	11.1	161.0	E2	22	4	0.22	-0.13 ± 0.29
249	NGC 1419	03:40:41.9	−37:30:33	9.7	9.6	E0	39	8	1.72	-0.80 ± 0.44
255	ESO 358-G50	03:41:03.4	−33:46:38	9.7	13.8	S0	19	6	1.38	-1.17 ± 0.49
263	ESO 358-051	03:41:32.2	−34:53:17	8.6	27.2	SB	1	0	0.61	–
276	NGC 1427	03:42:19.2	−35:23:36	10.3	44.7	E4	53	26	0.77	-0.54 ± 0.45
277	NGC 1428	03:42:22.6	−35:09:10	9.5	12.8	E5	8	1	1.73	−1.17
285	NGC 1437A	03:43:01.8	−36:16:11	8.3	49.9	Sd	1	0	0.68	–
290	NGC 1436	03:43:37.0	−35:51:13	9.8	48.5	Sc	2	1	0.34	−1.22
301	ESO 358-G59	03:45:03.5	−35:58:17	9.3	11.7	E4	1	0	2.05	–
306	–	03:45:45.3	−36:20:40	8.0	9.7	SB	1	1	0.38	−1.13
308	NGC 1437B	03:45:54.7	−36:21:25	8.6	37.1	Sd	7	3	1.04	-1.57 ± 0.19
310	NGC 1460	03:46:13.7	−36:41:43	9.7	35.6	SB0	13	4	0.51	-0.82 ± 0.52
312	ESO 358-063	03:46:18.9	−34:56:31	10.2	109.5	Scd	3	0	0.47	–

(1) Galaxy name from Ferguson (1989) and (2) alternative name. (3) and (4): Right ascension and declination. (5) - (7): Stellar mass, effective radius and morphological type from Iodice et al. (2019a,b) and Liu et al. (2019). (8) and (9): Number of GCs with S/N > 3 and > 8 respectively. (10) Mean projected radius and (11) mean metallicity of the F3D GCs. We found four possible intra-cluster GCs, three in FCC 184, one in FCC 182.

4.4 Results

We briefly summarise our sample of GCs in F3D in the following. Then, the kinematic modelling of the GC systems is described as well as the comparison between GC metallicities and their hosts and we and present the CZR.

4.4.1 Sample of globular clusters

In total, we determined the LOS velocities for 722 GCs in 32 galaxies and metallicities of 238 GCs. We could identify at least one GC in every F3D galaxy. Table 4.1 gives an overview of the extracted GCs per F3D galaxy. Appendix of Fahrion et al. (2020a) shows several plots for each galaxy to illustrate the GC sample[1].

From the galaxies that were also covered by the ACSFCS, we can estimate the completeness level of our GC extraction. Figure 4.4 shows the histogram of g-band magnitudes for all ACFCS GC candidates that are located within the MUSE pointings of F3D in comparison to those that are also in the final F3D GC catalogue. The lower panel shows the completeness as a function of magnitude, computed as the ratio between the number of GCs in F3D and ACSFCS, respectively. We reached a completeness of ~ 50 % at $M_g \sim -8$ mag. This is a conservative limit, because we applied no probability cut on the ACSFCS GCs. The faintest GCs in our sample have magnitudes of $M_g \approx -7$ mag ($g \approx 24.6$ mag), corresponding to $M_{\rm GC} \sim 10^5 M_\odot$. We separated the red and blue GC populations at a fixed colour of $(g-z) = 1.16$ mag (e.g. Peng et al. 2008; Liu et al. 2019). In the final sample, 60% of the GCs are blue.

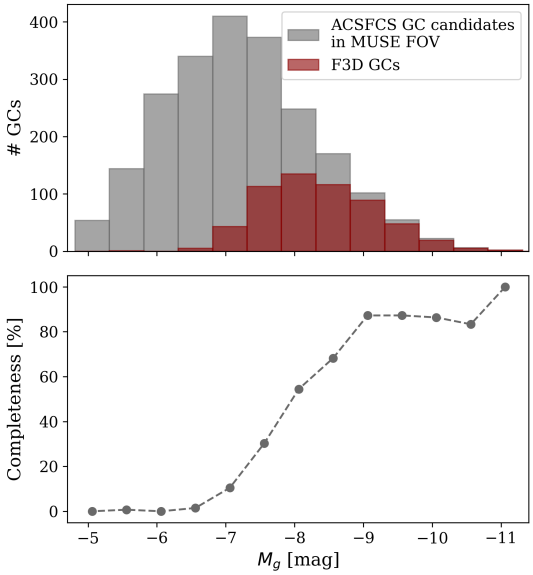

Figure 4.4.: Completeness of the F3D GC catalogue with respect to the ACSFCS catalogue (Jordán et al. 2015). *Top:* Histogram of absolute g-band magnitudes. The grey bins show all ACSFCS GC candidates located in the MUSE FOVs of F3D. Those, that are confirmed GCs and are in our F3D catalogue are shown by the red bins. *Bottom:* Completeness as ratio of number of GCs in F3D and all ACSFCS candidates as function of total g-band magnitude.

The majority of the F3D GCs are hosted by ETGs, while the number of GCs in LTGs is low. In the ETGs, we found 686 GCs in 22 galaxies, corresponding to 31 GCs per galaxy on average. We could identify 36 GCs in the 10 LTGs of F3D. FCC 176 is the only LTG in our sample for which we could identify more than 10 GCs in the FOV. The low number of detected GCs in the LTGs might have different reasons. Firstly, the LTGs have lower masses than the ETGs in the inner region of Fornax and thus the number

[1] As this thesis is focused on nuclear star clusters, I decided to not include these additional 30 pages of figures.

of expected GCs is lower because the total mass of a GC system depends on the mass of the host galaxy (Forbes et al. 2018; Liu et al. 2019) and LTGs have lower specific frequencies than ETGs in general (Georgiev et al. 2010). Secondly, most of the LTGs in our sample are actively star forming and have irregular morphologies, which made the detection of GCs in the FOV challenging because of strong residuals from MGE modelling. Thirdly, most of the LTGs were covered by a single pointing and thus we have no access to GCs at larger radii. Lastly, the LTGs were not covered by the ACSFCS and thus no catalogue of GC candidates is available that would help to identify possible GCs.

In the Scd galaxy FCC 113, we were able to detect four GCs, one of them appears to be located in the photometric centre of the galaxy and thus could classify as the nuclear star cluster of this galaxy. In addition, in FCC 290 we found a star cluster with a synthetic MUSE colour of $(g - z) \sim 0.3$ mag. For this blue star cluster, we found a stellar age of ~ 2 Gyr, significantly younger than the other GCs in our sample. This star cluster might therefore be a genuine young star cluster, maybe similar to those that are found in star forming galaxies (e.g. Larsen & Richtler 1999; Adamo et al. 2010; Fedotov et al. 2011). However, a higher S/N would be required to confirm this young age spectroscopically. Although our sample of GCs in LTGs is relatively small, these are the first spectroscopically confirmed GCs of LTGs in Fornax and might provide a basis for follow-up studies.

4.4.2 Rotation of globular cluster systems

The extracted GC LOS velocities enable us to compare them to their host galaxies using the kinematic maps that were presented in Iodice et al. (2019a). As one example, Fig. 4.5 shows the stellar LOS velocity map of FCC 083, and we overplotted the LOS velocities of the GCs with circles. Because Iodice et al. (2019a) used a slightly different setup to extract the LOS velocity, for example with a different masking of sky regions and a different wavelength range, we corrected any possible systematic offsets in velocity between the map and the GCs by separately fitting the central pixel of each galaxy with the same pPXF setup that was used for the GCs. We found no offset > 20 km s^{-1}.

The GC system of FCC 083 clearly shows rotation along the same axis as the galaxy and we found similar behaviours in other galaxies. We also found several galaxies that do not show any sign of rotation in their GC system, for example FCC 161 and FCC 213. These two galaxies also show very low rotation amplitudes in their stellar body.

Kinematic modelling

In order to quantify the rotational motion, we modelled the kinematics of the GC system (GCS) with a simple model following the description by Veljanoski & Helmi (2016). The rotation amplitude $V_{\rm GCS}$ of the GC system is described as (Côté et al. 2001):

$$v_{{\rm GC},i}(\theta) = v_0 + V_{\rm GCS} \sin(\theta_i - \theta_0), \tag{4.1}$$

where $v_{{\rm GC},i}$ is the LOS velocity of the i-th GC at position angle θ_i and $V_{\rm GCS}$ then gives the rotation amplitude of the total GCS, that reaches its maximum along position angle

Table 4.2.: Rotation amplitude $V_{\rm GCS}$ and velocity dispersion $\sigma_{\rm GCS}$ for the GC systems of the F3D galaxies.

Galaxy	$\sigma_{\rm e}$ (km s^{-1})	$N_{\rm red}$	$N_{\rm blue}$	$V_{\rm GCS}$ (km s^{-1})	$\sigma_{\rm GCS}$ (km s^{-1})	$V_{\rm red,\ GCS}$ (km s^{-1})	$\sigma_{\rm red,\ GCS}$ (km s^{-1})	$V_{\rm blue,\ GCS}$ (km s^{-1})	$\sigma_{\rm blue\ GCS}$ (km s^{-1})
(1)	(2)	(3)	(4)	(5)	(6)	(7)	(8)	(9)	(10)
FCC083	103	20	37	$82.8^{+15.6}_{-16.0}$	$97.1^{+11.0}_{-9.0}$	$110.3^{+16.9}_{-16.8}$	$64.0^{+12.7}_{-9.7}$	$61.6^{+23.6}_{-23.8}$	$113.4^{+15.4}_{-12.8}$
FCC143	62	0	20	$18.2^{+16.0}_{-11.9}$	$59.7^{+12.4}_{-9.4}$	–	–	–	–
FCC147	131	22	30	$43.4^{+26.5}_{-23.8}$	$131.1^{+14.6}_{-12.3}$	$40.3^{+39.7}_{-27.8}$	$152.6^{+28.3}_{-21.2}$	$61.6^{+32.9}_{-30.8}$	$118.6^{+17.6}_{-14.6}$
FCC153	55	1	13	$48.2^{+23.0}_{-22.4}$	$68.0^{+18.5}_{-13.2}$	–	–	$44.3^{+25.0}_{-23.0}$	$69.9^{+19.7}_{-14.1}$
FCC161	96	22	48	$22.1^{+15.6}_{-13.3}$	$90.9^{+8.4}_{-7.3}$	$26.7^{+22.1}_{-17.3}$	$67.0^{+12.4}_{-9.4}$	$23.5^{+19.1}_{-15.1}$	$101.7^{+11.2}_{-9.9}$
FCC167	143	38	21	$117.4^{+27.5}_{-26.8}$	$172.4^{+17.5}_{-15.4}$	$118.2^{+38.5}_{-39.0}$	$198.2^{+25.4}_{-21.3}$	$115.6^{+34.1}_{-34.5}$	$123.5^{+24.0}_{-18.5}$
FCC170	113	4	18	$33.3^{+29.1}_{-21.7}$	$122.9^{+23.4}_{-17.5}$	–	–	$25.6^{+30.1}_{-18.1}$	$127.5^{+27.8}_{-20.1}$
FCC176	43	1	10	$29.5^{+22.7}_{-17.6}$	$51.0^{+16.3}_{-11.4}$	–	–	$33.4^{+24.5}_{-19.9}$	$53.8^{+18.6}_{-12.6}$
FCC177	42	3	16	$40.5^{+15.7}_{-15.8}$	$51.4^{+11.4}_{-8.5}$	–	–	$49.5^{+16.5}_{-16.6}$	$49.0^{+12.0}_{-8.8}$
FCC184	143	40	9	$57.9^{+14.4}_{-14.1}$	$68.3^{+7.9}_{-6.8}$	$57.9^{+15.1}_{-14.6}$	$65.0^{+8.8}_{-7.2}$	–	–
FCC190	75	5	27	$42.7^{+31.6}_{-26.0}$	$101.6^{+14.4}_{-12.0}$	–	–	$53.3^{+37.5}_{-31.6}$	$109.1^{+17.9}_{-14.1}$
FCC193	95	7	9	$134.6^{+42.8}_{-40.6}$	$128.5^{+33.3}_{-24.8}$	–	–	–	–
FCC213	–	68	41	$51.8^{+27.2}_{-25.9}$	$228.8^{+16.3}_{-14.6}$	$30.3^{+25.6}_{-19.8}$	$192.5^{+18.2}_{-15.8}$	$102.1^{+55.9}_{-51.7}$	$282.0^{+35.0}_{-29.6}$
FCC219	154	17	7	$119.6^{+44.8}_{-43.9}$	$175.5^{+32.0}_{-25.4}$	$118.5^{+59.0}_{-55.0}$	$197.9^{+44.2}_{-33.2}$	–	–
FCC249	104	5	24	$24.7^{+22.8}_{-16.4}$	$96.0^{+15.2}_{-12.2}$	–	–	$26.4^{+26.9}_{-18.0}$	$100.4^{+18.3}_{-14.1}$
FCC255	38	1	18	$22.2^{+10.6}_{-10.3}$	$36.0^{+7.9}_{-6.0}$	–	–	$22.8^{+11.2}_{-10.8}$	$37.1^{+8.3}_{-6.3}$
FCC276	123	18	35	$29.2^{+21.3}_{-18.0}$	$140.5^{+15.5}_{-13.3}$	$34.3^{+30.3}_{-22.3}$	$123.4^{+26.2}_{-19.2}$	$34.3^{+28.5}_{-21.7}$	$153.2^{+21.2}_{-17.5}$
FCC310	48	2	11	$30.8^{+25.0}_{-19.8}$	$59.5^{+17.3}_{-12.1}$	–	–	$26.9^{+25.9}_{-17.9}$	$67.1^{+21.7}_{-14.4}$

(1) Galaxy name. (2) average LOS velocity dispersion within 1 $R_{\rm eff}$ from Iodice et al. (2019a). (3), (4): number of red and blue GCs in the F3D sample. (6) - (10): rotation amplitude and velocity dispersion. If ten or more GCs are available in the red and blue populations, we determined $V_{\rm GCS}$ and $\sigma_{\rm GCS}$ for these separately.

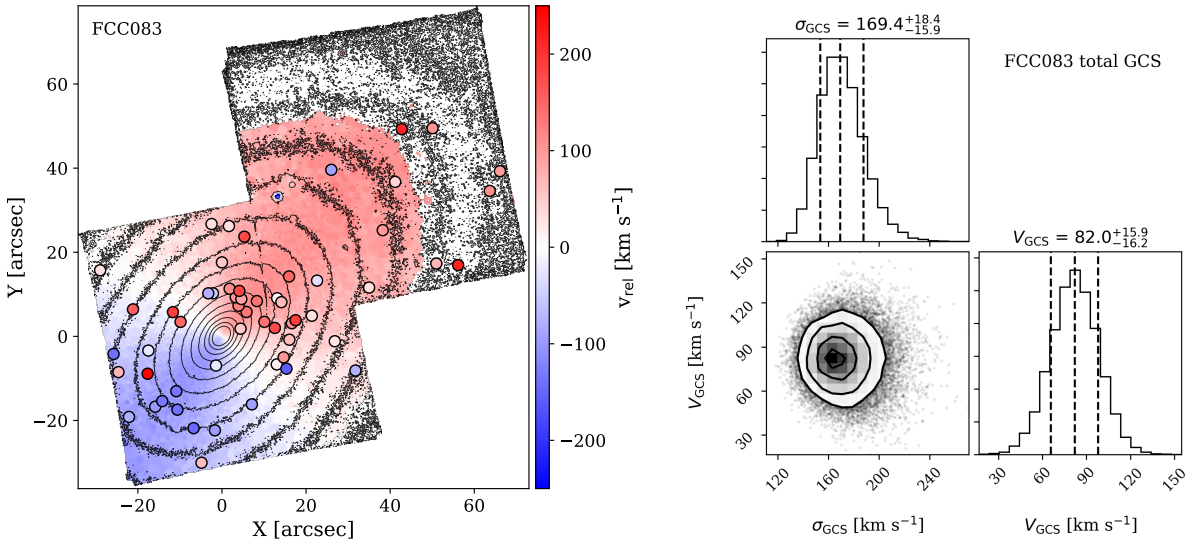

Figure 4.5.: Kinematic modelling of the GC system of FCC 083. *Left*: LOS velocity map of FCC 083 with GC velocities overplotted as circles. We used the same colourbar scaling for the stellar light bins and the GCs. The black contours are isophotes to guide the eye. *Right*: Posterior distributions for V_{GCS} and σ_{GCS} of the MCMC fit to the GCS of FCC 083 (Eq. 4.3). For θ_0, we used a Gaussian prior with $\theta_0 = 142 \pm 1°$ (Iodice et al. 2019a).

$\theta_0 + 90°$. v_0 is the mean velocity of the GCS that could in principle deviate from the systemic velocity of the host galaxy, but for the sake of simplicity we fixed this parameter to the host galaxy's systemic velocity. This model also assumes radially invariant rotation velocities and velocity dispersions, and we did not correct for inclination. The reported values are projected quantities.

Under the assumption that the velocity dispersion σ can be represented by a Gaussian, it is described as:

$$\sigma^2 = (\Delta v_{GC,\,i})^2 + \sigma^2, \tag{4.2}$$

where $\Delta v_{GC,\,i}$ is the velocity uncertainty for the i-th GC and σ denotes the LOS velocity dispersion. Combining Eq. 4.1 and 4.2, allows us to construct a model with the likelihood described by:

$$\mathcal{L} = \prod_i \frac{1}{\sqrt{2\pi\sigma^2}} \exp\left(-\frac{(v_{GC,\,i} - (v_0 + V_{GCS}\sin(\theta_i - \theta_0)))^2}{2\sigma^2}\right). \tag{4.3}$$

In this model, the radial velocities $v_{GC,\,i}$ of the GCs, their uncertainties ($\Delta v_{GC,\,i}$), and the position angles θ_i are the input data. V_{GCS}, σ_{GCS}, and θ_0 are free parameters of the model. We implemented Eq. 4.3 in EMCEE (Foreman-Mackey et al. 2013), a Python implementation of the MCMC sampler to sample the posterior probability distribution function. We used flat positive priors for V_{GCS} and σ_{GCS}, but used a Gaussian prior for the position angle θ_0 given by the host's kinematic position angle and uncertainty (Iodice et al. 2019a). This is necessary because the GC sample is geometrically limited, often along a preferred axis, due to the positioning of the MUSE pointings. In the right panel of Fig. 4.5, we show the

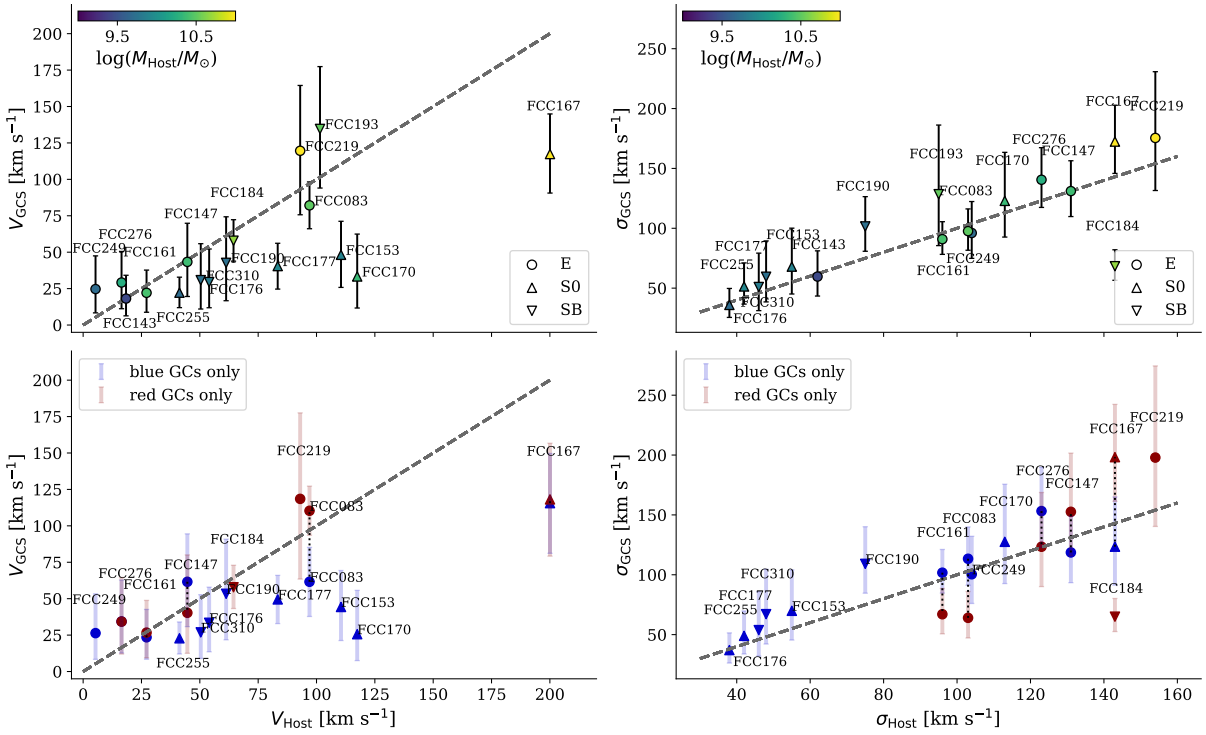

Figure 4.6.: GC rotation velocities (*left*) and velocity dispersions (*right*) compared to the stellar body of the galaxies. The stellar rotation amplitudes and velocity dispersions were extracted from the kinematic maps at 1 $R_{\rm eff}$ where possible. In the upper panels, $V_{\rm GCS}$ and $\sigma_{\rm GCS}$ for the total GCS are shown. The colour gives the stellar mass of the host galaxy and the symbols show the galaxy morphology. The bottom panel shows the values, when only the red or blue GCs were modelled. For galaxies with more than 10 GCs in either population, a dotted line connects the values. The dashed line in all panels gives the one-to-one relation. FCC 213 is not shown because no kinematic map was available.

resulting posterior distributions for FCC 083 using the described priors. FCC 083 has a strongly rotating GCS and in this case we found that also a flat prior on θ_0 results in a well constrained distribution.

We modelled all galaxies with ten or more GCs, and for galaxies that have ten or more red or blue GCs, respectively, we modelled these populations separately by only including the GCs of the respective colour. We list the resulting values for $V_{\rm GCS}$ and $\sigma_{\rm GCS}$ in Tab. 4.2. The uncertainties refer to the 16th and 84th percentile of the MCMC parameter distribution.

Comparison to host galaxy

We compare the rotation amplitude and velocity dispersion of the GCSs to the stellar bodies in Fig. 4.6. In the right panel, $\sigma_{\rm GCS}$ is plotted against σ_e, the average velocity dispersion within one effective radius from Iodice et al. (2019a). Additionally, we extracted the velocity of the host galaxy along its kinematic major axis at the effective radius, where possible. For FCC 176, FCC 310, and FCC 219, the MUSE FOV does not cover one effective radius and for those, we used the largest radius covered by the maps. In general, we found that the

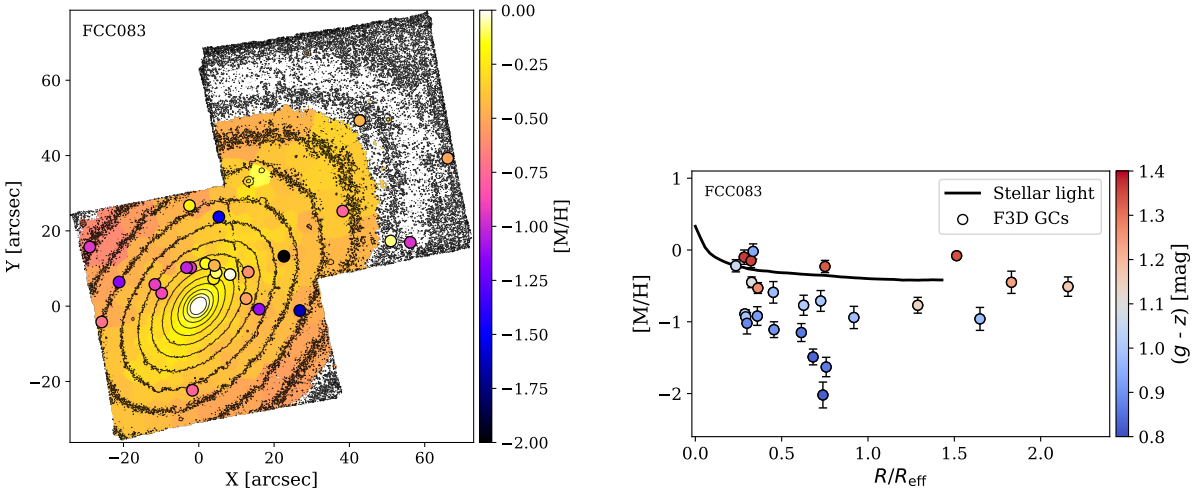

Figure 4.7.: Comparison of GC metallicities of FCC 083 to the host galaxy. *Top*: Metallicity map of FCC 083 from line-strength measurements with the GCs overplotted as circles. *Bottom*: radial profile of metallicity with GCs shown as circles, colour-coded by their $(g-z)$ colour. The black line shows the radial profile of the metallicity of the galaxy, obtained from the map shown on top.

exact choice of the extraction radius does not significantly influence this comparison.

The velocity dispersion found in the GCs is in good agreement with that of the stars and increases with stellar mass, indicating that the GCs can be used as kinematic tracers of the enclosed mass. This correlation is also seen when the red and blue GCs are modelled separately, independent of the galaxy type. However, when only using blue GCs, the relation with the stellar velocity dispersion appears tighter. FCC 184 is an outlier from this relation with a low velocity dispersion in its GCS. FCC 184 also stands out with having a large number of red, very metal-rich GCs that seem to follow the (low) rotation amplitude of the galaxy as the left panel of Fig. 4.6 shows. This could indicate that these GCs have a common origin possibly in the disc of FCC 184 and constitute a dynamically cold component in the galaxy.

The top left panel of Fig. 4.6 compares the rotation amplitudes of GCS and stars. This comparison shows that the GCs trace the rotation closely in the elliptical galaxies, similar to what was found by Pota et al. (2013) for 12 ETGs. In contrast, the three edge-on S0 galaxies (FCC 170, FCC 153, and FCC 177, Pinna et al. 2019a,b) show lower rotation amplitudes in the GCSs compared to that found in the stars. This might be caused by the strongly rotating discs that drive the high rotation amplitudes along the major axis while the GCs trace the kinematics of the spheroids of the host galaxies.

For FCC 083, FCC 161, FCC 147, FCC 167, and FCC 276, we can compare the red and blue GCs separately. Except for FCC 147, the red GCs show higher rotation amplitudes and follow the stellar rotation more closely (see also Pota et al. 2013). In general, the rotation amplitudes of the blue GCs are smaller. In FCC 161, FCC 083, and FCC 276, the red GCs further have lower velocity dispersions than the blue populations.

4.4.3 Metallicities of globular clusters

Figure 4.7 compares the radial distribution of the spectroscopic metallicities of the GCs of FCC 083 to that of the host galaxy, as an example. For this comparison, we used metallicity maps obtained from the line-strength measurements presented in Iodice et al. (2019a). Since the GC metallicities were obtained from full spectrum fitting, we adjusted possible offsets in the metallicity zero point by fitting the central pixel, but assume a similar gradient. We subtracted this offset from the metallicity maps. The plots of the other galaxies can be found in the appendix of Fahrion et al. (2020a).

These figures compare the GCs and their host galaxies, but because in some galaxies only a few spectroscopic GC metallicities are available, we combined the sample in Fig. 4.8. This figure shows a composite radial GC metallicity profile for all F3D galaxies. For better comparison, we show the metallicities relative to the metallicity of the central pixel of the host galaxies and used the projected galactocentric radii relative to the effective radius of the host (Iodice et al. 2019a,b). In this figure, the symbols are colour-coded by the stellar mass of the host (Liu et al. 2019; Iodice et al. 2019a).

As Fig. 4.8 shows, the GCs of our sample do not exceed the host's central metallicity, although there are several GCs that appear to be only slightly more metal-poor, even out to 1 $R_{\rm eff}$. While the more massive galaxies appear to have GCs spanning a large range of metallicities and some are even as metal-rich as the centres, the less massive galaxies show GCs that are more metal-poor than their host's centre. This could be connected to the different star formation histories of massive and less massive galaxies. Since massive galaxies might form on shorter time scales than less massive galaxies, they can form metal-rich GCs very early. However, the number of extracted GCs in these low-mass galaxies is quite low and better statistics are needed to address this issue.

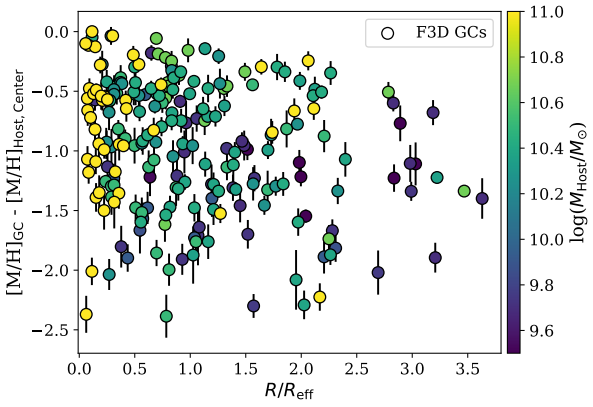

Figure 4.8.: Projected radial distribution of F3D GC metallicities from full spectral fitting. GC metallicities relative to the central pixel of the host are shown as a function of GC projected galactocentric distance relative to the host's effective radius for comparison between galaxies. The symbols are colour coded by the host's stellar mass from Iodice et al. (2019a) and Liu et al. (2019). There is one additional GC of FCC 170 with $R/R_{\rm eff} \sim 5$ that is not shown in this figure.

While the GCs with the lowest relative metallicities are found over a large range of radii, there seems to be an envelope at high GC metallicities that shows a gradient from ~ 0 to ~ -0.8 dex between the centre and 3.5 $R_{\rm eff}$ (see Fig. 4.8). This gradient might be understood as a radial gradient of GC metallicities as it is often observed in individual galaxies using colours as a proxy for metallicity (e.g. Harris et al. 2016; Caso et al. 2017). However, due to the design of the pointings, the coverage in individual F3D galaxies is not uniform. The GCs of FCC 213 dominate the inner region in Fig. 4.8 because its four MUSE pointings cover less than 0.4 $R_{\rm eff}$, whereas for example the outer pointing of the S0 galaxy

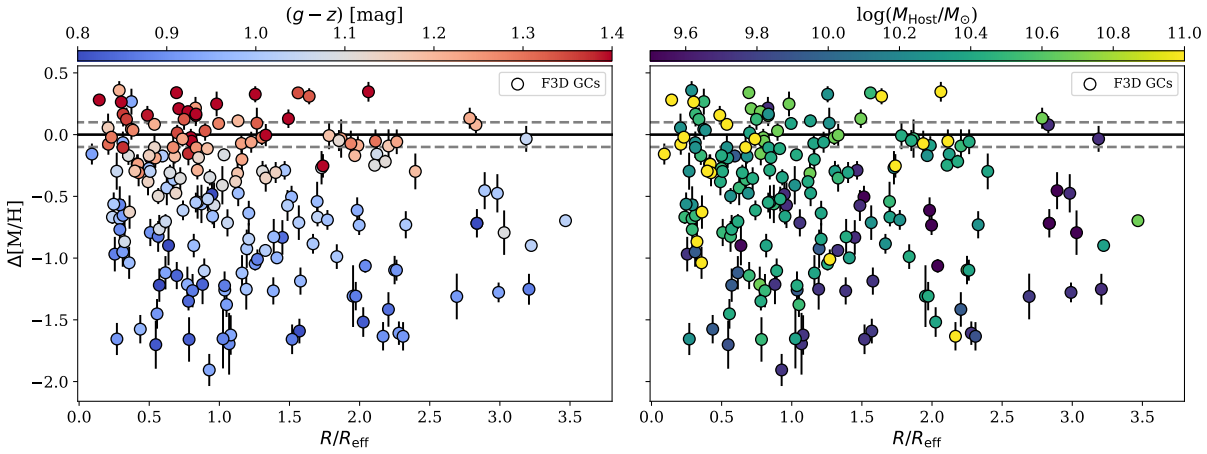

Figure 4.9.: Projected radial distribution of the metallicity of the GCs relative to the host metallicity taken from Iodice et al. (2019a), i.e. $[M/H]_{GC}$ - $[M/H]_{gal}$, colour-coded by the $(g-z)$ colour (*left*) and by the host stellar mass (*right*). The black line indicates an offset of zero dex and the dotted lines give the typical scatter found in the host metallicities of ± 0.1 dex. There are less GCs shown than in Fig. 4.8 because not all F3D galaxies have metallicity maps available.

FCC 170 reaches up to 5 $R_{\rm eff}$. The mean galactocentric distance of the GCs can be found in Table 4.1. In addition, we can only compare projected quantities and therefore, different intrinsic spatial distributions of red and blue GCs can bias the radial profile. It is typically found that the blue GCs are more extended than the red GCs (e.g. Harris et al. 2016) and thus it is possible that some of the blue GCs with small projected radii have intrinsic large galactocentric distances.

In addition to comparing the GC metallicities to their host's centre, we can compare them directly to the individual metallicity profiles of the galaxies, as seen in Fig. 4.9. Not every F3D galaxy has a metallicity map available and hence the GCs shown in Fig. 4.9 are only a sub-sample of those in Fig. 4.8. We subtracted the host metallicity at each GC position and used the $(g-z)$ colour (left panel), and the host stellar mass (right panel) to colour-code the symbols. The dotted line indicates the typical scatter of ± 0.1 dex in the metallicity profiles of the host.

Fig. 4.9 illustrates that the red GC population traces the mean stellar metallicity closely over all radii and host masses, although there is a scatter of ∼ 0.5 dex. Over most radii and stellar masses we found GCs that are more metal-rich than the underlying galaxy, but the comparison to Fig. 4.8 shows that those are not more metal-rich than the centres of their host. The blue GCs ($g-z < 1.16$ mag) show a broad range of relative metallicities and can be significantly more metal-poor than their hosts at any given radius. The spread in relative metallicities of the blue GCs appears to be independent of the host stellar mass.

4.4.4 Non-linear colour-metallicity relation

The relationship between photometric colour and spectroscopic metallicities, the CZR, needs to be understood to exploit the vast amounts of photometrically studied GC populations

and to understand their origin, as described in Sect. 1.2.2. To derive the CZR from the F3D GCs, we only included GCs with a galactocentric distance $r_{\rm gal} \geq 15''$ because testing has shown that the spectra of GCs with small galactocentric distances can still be contaminated by residual galaxy light that strongly varies in the central regions. These GCs can be biased to higher metallicities because the host galaxy tends to be more metal-rich than the GCs, especially in the centre. From the initial sample of 238 GCs with metallicity measurements, this cut in galactocentric distance leaves a sub-sample of 187 GCs in 23 galaxies, the majority in ETG hosts.

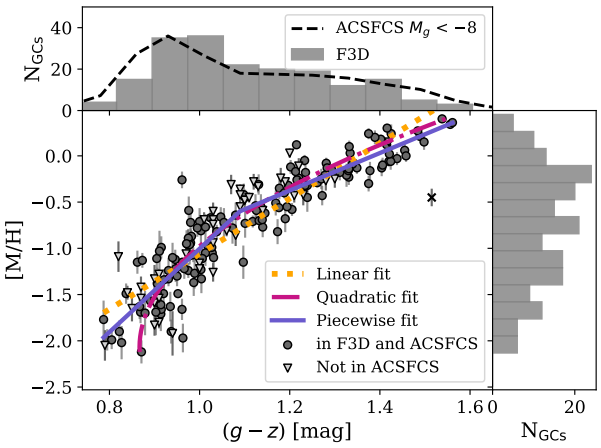

Figure 4.10.: Colour-metallicity distribution of F3D GCs. Spectroscopic GC metallicities from full spectral fitting versus $(g-z)$ colour. Filled circles and triangles refer to GCs with and without ACSFCS $(g-z)$ colours from Jordán et al. (2015), respectively. For the latter, we obtained the colour from the MUSE spectrum directly. The orange, pink and purple lines give the fit using the linear, quadratic, or piecewise function (Eqs. 4.4, 4.5, and 4.6). The corresponding residuals are found in Fig. 4.11. As described in the text, we excluded an outlier from the fit marked by a cross. Separate distributions of colour and metallicities are shown on the top and the right-hand side. In the top panel, we included the histogram from the full ACSFCS GC sample after applying a magnitude cut corresponding to our sample.

As described in Sect. 4.3.3, we fitted these GCs with the E-MILES SSP models and an age constraint of ≥ 8 Gyr. We tested the effects of GC age by fitting GCs with S/N $>$ 10 without age constraint and determined [α/Fe] abundances only for the brightest GCs with S/N $>$ 20 using the α-variable MILES models introduced in Sect. 2.4.2. The latter two approaches are to validate the results from our default approach. In Appendix B.1, we explore the choice of SSP models and also test metallicities from line-strength index measurements.

We used $(g-z)$ colours, mostly from the photometric GC catalogues of Jordán et al. (2015) that were obtained as part of the ACS Fornax Cluster Survey (ACSFCS; Jordán et al. 2007). These catalogues report the magnitudes of the GC candidates in the ACS F475W ($\sim g$ band) and F850LP ($\sim z$ band).

Not all galaxies in our sample were covered by the ACSFCS and consequently, 45 GCs in our sample have no ACS colours available. For those, we determined synthetic $(g-z)$ colours from the MUSE spectra using the F475W and F850LP transmission curves. While the F475W band is covered completely with MUSE, the F850LP bandpass extends outside the MUSE coverage. In the colour regime covered by the 45 GCs without ACS photometry, the synthetic colours agree with the ACSFCS colours within a scatter of ~ 0.05 mag.

We plot the distribution of colours and metallicities of our F3D GCs in Fig. 4.10. This figure shows the relation between the $(g-z)$ colours and spectroscopic total metallicity [M/H] as derived based on the E-MILES SSP models for the GCs with S/N ≥ 8. Although most of the GCs were covered by the ACSFCS and have HST colours, the CZR is better constrained when also including GCs with synthetic MUSE colours. There is one outlier with

a ACSFCS colour of $(g-z) \sim 1.5$ mag and a metallicity of ~ -0.5 dex that lies significantly below the relation. This is a GC found in the halo pointing of FCC 167 with a synthetic MUSE colour of $(g-z) \sim 1.2$ mag that would place it among the bulk of GCs. Usually, the synthetic colours agree within ± 0.05 mag with the ACSFCS colours, making this GC an outlier and because the origin of the large colour difference is unknown, we excluded this GC from the fit. Another visible outlier that lies above the relation at $(g-z) \sim 1.0$ is a GC found in the central pointing in FCC 276 with a small galactocentric distance of 16″. Since FCC 276 is quite massive ($\log(M_{\rm gal}/M_{\odot}) \sim 10.3$), it is possible that the spectrum of this GC is still contaminated by the bright galaxy background which could bias the measured metallicity to higher values.

The top panel of Fig. 4.10 compares the colour histogram of the F3D GCs to the full sample of ACSFCS GCs (Jordán et al. 2015), normalised to match the peak in our GC distribution. We only have metallicity estimates from GCs with spectral S/N ≥ 8. As we showed Fig. 4.3, these are GCs with $M_g \lesssim -8$ mag. Therefore, we apply the same brightness cut to the full ACSFCS sample. Our GC sample is representative of the bright GC population of the ACSFCS cluster survey, and the full colour range from 0.8 to 1.6 mag is well sampled. There is a large number of GCs with $(g-z) \sim 1$ mag, but our sample shows a deficit of GCs at very blue colours < 0.8 mag, possibly because those are expected to be very metal-poor and consequently the absence of strong absorption lines in the spectrum leads to lower S/N.

Our GC sample contains the most massive GCs of the total population and in order to apply our relation to the full GC distribution (see Sect. 4.5.4), we have to assume that the less massive GCs follow the same relation. The less massive GCs missing from our sample are expected to be even more metal-poor and thus it is unlikely that they would change the shape of the CZR. In addition, the colour span around $(g-z) \sim 1$ mag, where we observe the break in the relation, is already well sampled.

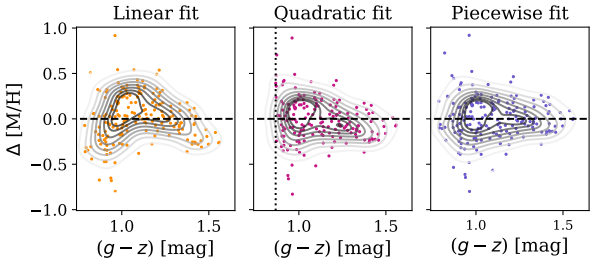

Figure 4.11.: Residuals when fitting the colour-metallicity distribution shown in Fig. 4.10 with a linear (*left*), a quadratic (*middle*) and piecewise linear function (*right*), respectively. Coloured points show the observed scatter and the contours give a kernel density estimation using an arbitrary Gaussian kernel for visualisation of the residual shape. The dotted vertical line in the middle panel shows where the quadratic model diverges.

To quantitatively describe the CZR, we fitted the distribution with different functions using a least-square algorithm. The best-fitting functions are shown as coloured lines in Fig. 4.10 and we show the respective residuals in Fig. 4.11. Using a simple linear function gives a relation of the following form:

$$[\mathrm{M/H}] = (-4.05 \pm 0.11) + (2.99 \pm 0.10)\,(g-z). \tag{4.4}$$

As Fig. 4.11 shows, the residual of this linear fit shows a bent shape. At very blue and red colours, the metallicities are overestimated and are underestimated at intermediate colours.

In order to improve the quantitative description of the CZR, we used a quadratic relation

to fit the CZR (see also Sinnott et al. 2010; Harris et al. 2017):

$$(g-z) = a\,[\mathrm{M/H}]^2 + b\,[\mathrm{M/H}] + c. \tag{4.5}$$

The least-square fit returned best-fitting parameters of $a = 1.34 \pm 0.01$, $b = 0.46 \pm 0.02$, $c = 0.11 \pm 0.01$. This best-fitting relation is shown by the pink line in Fig. 4.10. The residual shows a more symmetric shape than when using the linear fit.

In addition, we used a piecewise linear function, similar to that of Peng et al. (2006):

$$\begin{aligned} [\mathrm{M/H}] &= b_1 + m_1(g-z) \quad \text{for } (g-z) < x_0 \\ &= b_2 + m_2(g-z) \quad \text{for } (g-z) \geq x_0, \end{aligned} \tag{4.6}$$

with best-fitting parameters of $m_1 = 4.51 \pm 0.32$, $b_1 = -5.51 \pm 0.36$, $m_2 = 2.03 \pm 0.20$, $b_2 = -2.81 \pm 0.36$, and $x_0 = 1.09 \pm 0.03$ (purple line in Fig. 4.10). The residual is more symmetrical around the zero line (Fig. 4.11).

Comparing the residuals of the fitted relations shows that the linear fit is insufficient to capture the shape of the CZR accurately. The quadratic and piecewise relations return similar residuals, however, the quadratic relation shows an asymptotic behaviour for colours $(g-z) < 0.86$ mag, although our sample reaches bluer colours. To compare the models quantitatively, we derived the Bayesian information criterion (BIC) for each model. The piecewise linear relation has the lowest BIC and is preferred over the linear model by ΔBIC = 32 and over the quadratic model by ΔBIC = 35. While the residual scatter is comparable for the piecewise and the quadratic model, the asymptotic behaviour of the latter reduces the number of observables and thus increases the BIC. We conclude that the piecewise relation best represents the data.

4.4.5 Globular cluster ages

While our standard approach for fitting the GC spectra assumes an age ≥ 8 Gyr, we also fitted a sub-sample of 135 GCs with high S/N > 10 without any constraints on the age. Because of the larger SSP model grid, these fits take substantially longer, but allow us to study the effect of GC ages on the CZR due to a possible age-metallicity degeneracy.

The reddest, most metal-rich GCs in the sample have very small age and metallicity uncertainties. For them, it is likely that the small uncertainties are an effect of the limited SSP grid. Otherwise, the GC ages have typical random uncertainties of > 2 Gyr, reflecting the challenging age determination of old stellar populations (e.g. Usher et al. 2019, or Appendix A.1). The wavelength coverage of MUSE is further lacking age sensitive spectral features such as higher Balmer lines.

The top panel in Fig. 4.12 shows the age-metallicity distribution of the F3D GCs, colour-coded by the stellar mass of the host (Liu et al. 2019; Iodice et al. 2019a). This figure suggests a shallow age-metallicity correlation of the GCs in which more metal-rich GCs are also older. This trend is mainly driven by the reddest, most metal-rich GCs that show very small age and metallicity uncertainties. As mentioned, it is likely that these GCs exceed the metallicities of the SSP models, or are strong α-enhanced, as was found for several GCs of massive ETGs (e.g. Puzia et al. 2005, 2006; Woodley et al. 2010b). The other GCs show a

very mild correlation between age and metallicity that also coincides with a relation between host mass and GC age.

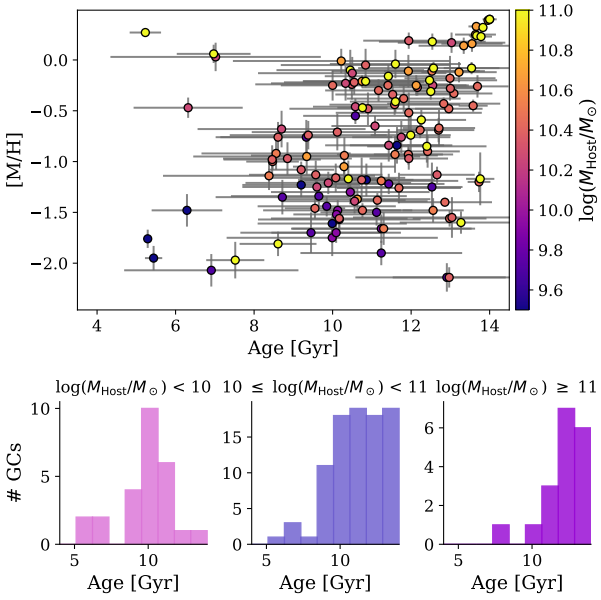

Figure 4.12.: *Top:* Best-fitting ages and metallicities of GCs, inferred from full spectral fitting with the E-MILES templates and no age constraint. The colour coding refers to the stellar mass of the host galaxy (Iodice et al. 2019a; Liu et al. 2019). *Bottom:* GC age distributions for host galaxies in three different mass bins.

To illustrate this, we binned the GC sample based on the stellar mass of the host galaxy into three mass bins and the bottom panel of Fig. 4.12 shows the GC age distribution in these mass bins. The GCs with the lowest host masses ($\log(M_{\rm Host}/M_\odot) < 10$) show a peak at 10 Gyr, whereas the intermediate and high mass bins show distributions that are dominated by very old ages. While the intermediate mass bin ($10 < \log(M_{\rm Host}/M_\odot) < 11$) shows some GCs with ages < 10 Gyr, these slightly younger GCs are apparently missing in the highest mass bin ($\log(M_{\rm Host}/M_\odot) > 11$). Although the number of GCs in each mass bin is quite low and the age uncertainties are large, we found indications that the lower mass hosts indeed have younger GC systems. Indications for such a trend were also found, for example, by Usher et al. (2019) when comparing three SLUGGS galaxies, possibly due to a top-down formation of GCs that form later in less massive galaxies. Moreover, such a behaviour is in agreement with a mass-dependent age-metallicity relation (see Leaman et al. 2013; Böcker et al. 2020 and references therein). Because low-mass galaxies also tend to have more metal-poor GCs, the observed weak age-metallicity correlation might be driven by the host mass.

4.5 Discussion

In the following, we discuss our results on GCs as tracers of kinematics and metallicities. Further, we compare our CZR with literature studies.

4.5.1 Globular cluster system rotation

We built a simple kinematic model for the GCSs in 17 F3D galaxies to derive their rotation amplitude and velocity dispersion. Due to the low numbers of GCs per galaxy, we fixed the systemic velocity of the GC system and assumed that the rotation axis of the GCs coincides with the rotation axis of the host galaxy. Using radial velocities of over 4000 GCs in 27 ETGs of the SLUGGS survey, Forbes et al. (2017) found generally a good agreement between GC mean and host systemic velocity, indicating that the GCs are at rest with respect to their

host. For the F3D galaxies with sufficient GC velocities, we also found a good agreement between mean GC and host velocity.

Pota et al. (2013) found that the kinematic position angle of the GCs can differ among red and blue GCs and when compared to the stellar light. We tested the assumption of a common rotation axis with the stars for individual galaxies such as for FCC 083 or FCC 161, where a large number of GC velocities are available, and could not find indications for a kinematic misalignment between GCS and host. However, Pota et al. (2013) found this misalignment at galactocentric distances $> 1\ R_{\rm eff}$, where we lack coverage. Nonetheless, the orientation of the MUSE pointings along an axis can bias the results. While most of the pointings where chosen along the major axis, some pointings were placed along the minor axis, for example in FCC 161 and FCC 147. With a larger MUSE coverage per galaxy, a possible misalignment between GC rotation and the stellar body could be determined, that might indicate a triaxial galaxy shape (Krajnović et al. 2011).

In our work, we obtained GC velocities only in the inner regions of galaxies. This has the advantage that we can easily compare their velocities to the underlying host, but we are insensitive to possible changes in the GC kinematics at larger radii such as twists in the kinematic position angle. For example, the halo GCs of M31 show a smaller rotation amplitude than the inner GCs (Veljanoski et al. 2014). Also Pota et al. (2013) found variations of rotation-to-dispersion ratio $(V/\sigma)_{\rm GCS}$ with radius for several of the SLUGGS galaxies. Based on simulations of dry mergers of galaxies, Bekki et al. (2005) predicted an increasing $(V/\sigma)_{\rm GCS}$ from 2 $R_{\rm eff}$ to 6 $R_{\rm eff}$, but to detect such signatures, velocity measurements of many outer GCs would be needed. With our simple model, we could only derive radial invariant values for the rotation amplitude and the velocity dispersion. Due to the limitations in this model, we refrain from discussing V/σ as any bias in the model is boosted in the ratio unnecessarily. We also investigated the specific angular momentum $\lambda_{\rm GCS}$ (e.g. Emsellem et al. 2007), but the comparison of it to the stars is complicated due to enhanced uncertainties from V/σ and the radial restriction of the GCs.

We found that the velocity dispersion of the GCs closely traces that found in the stars, similar to the findings of Pota et al. (2013) for 12 SLUGGS galaxies. This trend is seen also when differentiating between the red and blue GC population, but a separate kinematic analysis of red and blue GCs was not possible in all galaxies. For five galaxies where we could model both the red and blue population separately, we found three galaxies in which the blue GCs have a higher velocity dispersion and low rotation amplitude. This is expected as a result of their accreted origin from random infall directions.

When comparing the rotation amplitudes in the GCSs to the stellar rotation, we found differences between galaxy types. Similar to the results for the SLUGGS ETGs (Pota et al. 2013), we found that the GCs in the elliptical galaxies follow the rotation of the host. In contrast, the GCs of the S0 galaxies in our sample show much lower rotation amplitudes than the stars, especially in the three edge-on S0 galaxies. In these cases, the rotation amplitudes in the stars is maximal due to the inclination angle and is driven by the dynamically cold disc (Pinna et al. 2019a,b), whereas the GCs appear to trace the spheroid of the galaxies (e.g. Schuberth et al. 2010).

Separating into red and blue GCs, we found that the blue GCs in general show low rotation amplitudes. For the five galaxies, where both populations could be modelled, we

found higher rotation amplitudes for the red GCSs in four of them. Typically, it is expected that the red population follows the stellar light more closely because of the simultaneous formation of galaxy spheroids and metal-rich GCs. Thus, the metal-rich GCs might be the compact survivors of violent, monolithic-like collapse galaxy formation, also resulting in a higher rotation amplitude (Strader et al. 2011). However, rotation has been detected in both the red and blue GC populations, independently of the host mass or morphology (Arnold et al. 2011; Foster et al. 2011). The accreted GC population can show significant rotation if the associated host galaxies fell into the central potential from a preferred direction, as has been discussed in detail for the Local Group (Libeskind et al. 2011; Lovell et al. 2011). In simulations, the accreted GC populations are found to show rotation due to a conversion of the orbital angular momentum to intrinsic angular momentum (Bekki et al. 2005) and because the angular momentum of the stellar halo is reflected in the angular momentum of the GCs (Veljanoski & Helmi 2016).

4.5.2 Globular cluster metallicities

We determined spectroscopic metallicity measurements for 238 GCs, a sub-sample of our GC catalogue with high S/N. With this data set, a number of questions can be addressed. We studied how the metallicities of the GCs compare with their host galaxies, both relative to the host's centre and the underlying galaxy at the GC's location. In our limited sample, we found that no GC is more metal-rich than its host's centre. The central metallicity, therefore, not only constitutes the peak of the stellar metallicity, but also of the GC metallicity. Nonetheless, we found several GCs that have metallicities close to their host's central metallicity. These metal-rich GCs are generally located at small projected distances and are associated to massive hosts with $M \gtrsim 10^{10.5} M_{\odot}$. In the MW, the most metal-rich GCs are found in the bulge. They show a similar metallicity to the bulge stars (Muñoz et al. 2017, 2018), indicating an in-situ formation together with the bulge.

In our sample of F3D GC metallicities, we found GCs in the range between [M/H] ~ -2.3 dex to $\sim +0.4$ dex, fully exploiting the metallicity grid of the SSP models. We do not expect to miss GCs at lower metallicities due to the empirical metallicity floor of GCs at ~ -2.5 dex (e.g. Beasley et al. 2019). The more massive galaxies of our sample ($M \gtrsim 10^{10} M_{\odot}$) show the largest spread of GC metallicities from high metallicities comparable to the host's centre down to the very metal-poor regime, whereas the less massive F3D galaxies show a smaller spread of GC metallicities and seem to have only GCs that are more metal-poor than their host's centre. Although this difference might not be significant due to low numbers of GCs in the low-mass galaxies, this is consistent with the finding that the relative number of red GCs decreases with galaxy mass and thus low-mass galaxies only have blue GCs (Peng et al. 2006). However, the number of GCs in low-mass F3D galaxies are low, with only 1 – 3 GCs per galaxy.

Broad GC metallicity distributions have been found in many massive galaxies, for example in M31 (e.g. Barmby et al. 2000; Perrett et al. 2002; Caldwell & Romanowsky 2016), Centaurus A (Woodley et al. 2010b), Sombrero galaxy (Alves-Brito et al. 2011), and M87 (Strader et al. 2011; Villaume et al. 2019). The broad range of GC metallicities is often connected to the evolutionary history of the host galaxy with the red, most-metal rich GCs

having formed in-situ and blue GCs having been accreted from more metal-poor dwarf galaxies during the assembly of the host. From this scenario naturally follows that more massive galaxies with richer merger histories also acquire a broad GC metallicity distribution due to the accretion of satellites of different masses (e.g. Kravtsov & Gnedin 2005; Tonini 2013; Li & Gnedin 2014; Choksi et al. 2018; Kruijssen et al. 2019a,b). Conversely, low-mass galaxies that are thought to have only a limited number of mergers in their past, obtain a narrow GC metallicity distribution.

Comparing the GC metallicities to the underlying host metallicity profile has shown that there are several red GCs that are more metal-rich than their host locally. Especially FCC 184, a lenticular galaxy with a prominent bar in the centre, shows a large number of these GCs. At the same time, FCC 184 stood out as an outlier with its red GCs having a low velocity dispersion that is also lower than that of the stars. Together with the large number of very metal-rich GCs, this might indicate that these metal-rich GCs were formed in a disc that is viewed face-on. However, more rigorous modelling of the GC kinematics and stellar populations would be required to test this.

Also other galaxies have GCs that are more metal-rich than the host locally. Besides projection effects, this could be explained by different star and cluster formation conditions, if the GCs were born closer to the host centre and were ejected to larger distances (Leung et al. 2020), or as a result of violent interactions during the initial collapse and the formation from clumps (e.g. Kruijssen 2015). In addition, their existence could indicate a more metal-rich population within the galaxy that is not evident from the mean metallicity profile of the host. In a hierarchical assembly history, it is possible that such a metal-rich component including GCs formed from fast self-enrichment while the more metal-poor component was acquired during the accretion of metal-poor dwarf galaxies.

Besides an early formation in the parent halo, it has been suggested that metal-rich GCs form during major mergers of gas-rich galaxies (e.g Li & Gnedin 2014; Choksi et al. 2018), which could explained their extended radial distribution. Moreover, some of the GCs that are more metal-rich than their host locally might be UCDs rather than classical GCs. UCDs are often discussed to be the remnant NSCs of disrupted galaxies (e.g. Bekki et al. 2003; Drinkwater et al. 2003; Pfeffer & Baumgardt 2013; Strader et al. 2013), and because those can be more metal-rich than their host galaxy and the surrounding GC system (e.g. Paudel et al. 2011), finding a GC more metal-rich than the host at large separations could indicate such a remnant NSC.

Red GCs are often used as tracers of the in-situ halo metallicity. For example, Beasley et al. (2008) found a good agreement of the metallicity distribution function of the red GCs of Centaurus A with that of its halo stars, while the studied GCs appear to be more metal-poor than the inner regions of the galaxy. A similar observation was made for the brightest cluster galaxy NGC 6166, where the metal-rich GCs were found to closely follow the radial distribution, ellipticity and mean metallicity of the halo light (Harris et al. 2016). Using hydrodynamical simulations, Forbes & Remus (2018) studied the metallicity gradients of in-situ and accreted GCs, and although they appear similar to that of the metal-rich and metal-poor GCs, they found that a one-to-one connection between metal-rich and in-situ formation is not given because major mergers bring in both metal-rich and metal-poor GCs. Depending on the mass of the satellite, the accreted GCs are deposited in different regions

in the galaxy. Massive satellites can therefore deposit their metal-rich GCs in the inner regions, while the generally more metal-poor GCs of low-mass satellites end up at larger galactocentric distances.

With F3D, we have the opportunity to extend the comparison to the inner parts of galaxies ($< 1\,R_{\rm eff}$). Using the host metallicities from line-strength analysis as presented in Iodice et al. (2019a), we investigated the relative metallicity between GCs and host. The red GC population was found to trace the host metallicity closely over all studied radii and stellar host masses, indicating a co-evolution of metal-rich GCs and the host galaxy. The blue GCs, however, appeared to be more metal-poor than the hosts, even at large projected distances. Similar observations were made when comparing halo stars and halo GCs directly as described by Lamers et al. (2017), for example in the MW (Ryan & Norris 1991; An et al. 2012; Harris et al. 2016), Centaurus A (Rejkuba et al. 2005, 2014; Beasley et al. 2008; Crnojević et al. 2013), or even the Fornax dwarf spheroidal galaxy (Larsen et al. 2012). Lamers et al. (2017) argued that the metallicity contrast between GCs and halo stars is a result of galaxy assembly via mergers during which more metal-poor GCs are more likely to survive until today because of their origin in metal-poor dwarfs, where the destruction via shocks is less likely. Also, accreted GCs represent the formation conditions in their parent galaxy before the time of accretion.

4.5.3 Colour-metallicity relations in the literature

Our CZR is compared to findings from the literature in Fig. 4.13, shown by lines of different colours. We differentiated between relations based on total and iron metallicities to avoid further conversions between them. For our sample, we used used the relation obtained from the MILES stars to convert from [M/H] to [Fe/H] as the brightest GCs in our sample seem to follow the abundance trend of these stars[2].

Peng et al. (2006) studied the bimodality of GC colours in the Virgo cluster using HST ACS photometry and $(g-z)$ colours. They derived a CZR from the few spectroscopic GC metallicity measurements of the MW, M87, and M49 that were available at that time (Harris 1996; Cohen et al. 1998, 2003). Their CZR is described by a piecewise linear relation with a break at $(g-z) \approx 1.05$ mag. As Fig. 4.13 shows, their relation is close to ours, especially for the blue GCs. At redder colours their relation is shallower. As Villaume et al. (2019) discussed, the break in the Peng et al. (2006) relation might be mainly caused by the MW GCs that are significantly more metal-poor than those of M87.

Faifer et al. (2011) studied the GC systems of five massive ETGs with photometry in the g and i bands of the Gemini Multi-Object Spectrograph. Using literature metallicities (Pierce et al. 2006a,b; Norris et al. 2008), they found a linear CZR which is shown by the green line in Fig. 4.13. We converted their $(g'-i')$ colours to $(g-z)$ using the translation given in the Appendix of Usher et al. (2012). Their relation predicts higher GC metallicities at all colours, although the slope is very similar to that of Usher et al. (2012), who used literature metallicities from Kuntschner et al. (2002); Brodie et al. (2005); Cenarro et al. (2007); Chomiuk et al. (2008); Caldwell et al. (2011) and SLUGGS $(g-i)$ photometry to

[2]Details on this are found in Fahrion et al. (2020b).

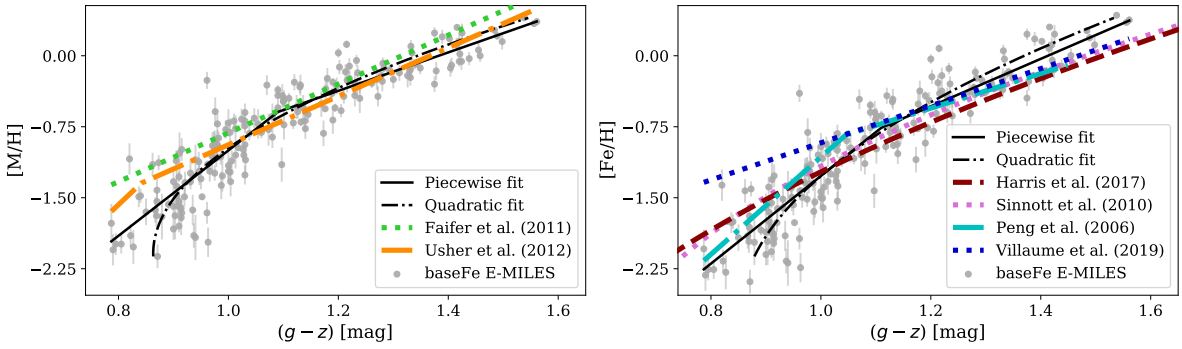

Figure 4.13.: Our CZR in comparison to literature results. We differentiate between relations based on total metallicities (*left*) and iron metallicities (*right*). The black curves give our fits. The coloured lines refer to literature CZRs as described in the text.

derive a piecewise CZR shown by the orange line in Fig. 4.13. This relation fits the red GCs of our sample quite well, but the break point is located at colour of $(g-z) \approx 0.84$ mag. The position of the break point is strongly driven by the metallicities of M31 GCs (Caldwell et al. 2011) because the other galaxies in this collection show no GC metallicities < -1.2 dex. In the sample, M31 is also the only LTG, while the others are massive ETGs.

Using metallicities from Woodley et al. (2010a) and *griz* photometry, Sinnott et al. (2010) presented a quadratic CZR for GCs of the giant elliptical Centaurus A. Harris et al. (2017) used the same metallicities, but combined the *griz* photometry of Sinnott et al. (2010) with *UBVRI* photometry available from Peng et al. (2004) to derive a very similar quadratic relation using $(g-I)$ colours. They also give the conversion to $(g-z)$ colours (see also Choksi & Gnedin 2019). Their CZR is offset to our red GCs and shallower at blue colours.

Recently, Villaume et al. (2019) presented a sample of 177 GCs of M 87 with spectroscopic metallicities and found a linear relation shown in Fig. 4.13. Their CZR follows the relation of Harris et al. (2017) at red colours and shows a deviation from our relation at the bluest GC colours. Villaume et al. (2019) discussed that their findings of more metal-rich blue GCs could indicate an environmental effect caused by the assembly history of M87 itself.

The comparison to literature CZR highlights the diversity of relations that were found using different techniques and studies of different environments. In general, it appears that studies focusing on massive ETGs generally find linear relations due to a lack of metal-poor GCs. Non-linear relations are predominantly found when incorporating measurements of metal-poor GCs, for example, from the MW or M31. This could indicate that massive ETGs indeed have a different CZR, whereas it is also possible that the lack of metal-poor GCs is due to selection effects and limited sample sizes because the most massive galaxies are dominated by more metal-rich GCs. Additionally, the radial extent of the studied GCs can bias the selection as the blue GC population usually is more extended (e.g. Harris et al. 2016) and thus concentrating on the inner regions of massive galaxies can result in a lack of blue GCs. However, because our sample uses a large variety of galaxy masses, also the metal-poor end of the CZR is well sampled.

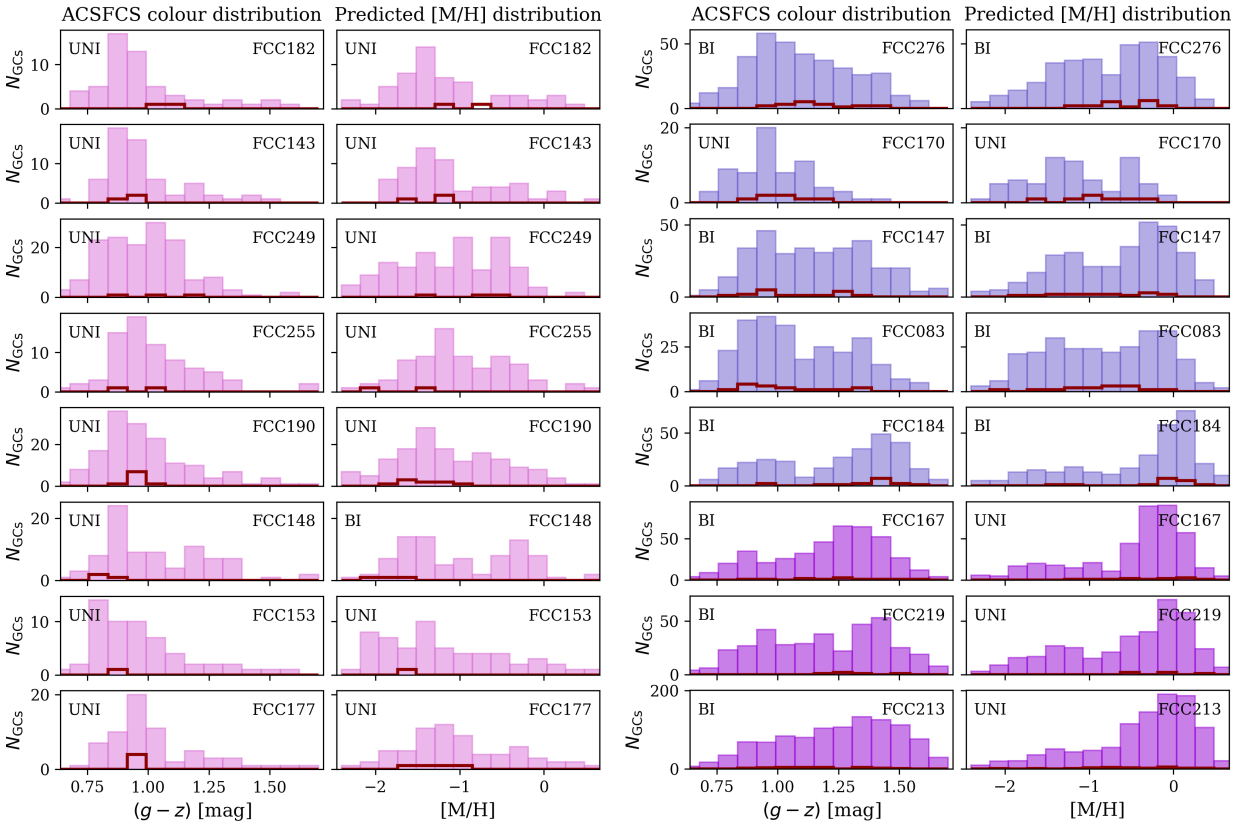

Figure 4.14.: Colour (first and third panel) and metallicity (second and forth panel) distribution for 16 F3D galaxies that have a sufficient number of GC candidates in the ACSFCS catalogue from Jordán et al. (2015) to create a well sampled distribution. MDFs were inferred from the colour distributions using Eq. 4.6 with the best-fit parameters from our default CZR. The histograms are coloured based on the stellar mass of the host using three mass bins: $\log(M_{\rm Host}/M_{\odot}) < 10$ (pink), $10 \leq \log(M_{\rm Host}/M_{\odot}) < 11$ (blue), and $\log(M_{\rm Host}/M_{\odot}) \geq 11$ (purple). The red histograms show the GCs in our sample. In the top left corner of each panel, the distributions are classified as bimodal ('BI') or unimodal ('UNI') based on the GMM test described in the text.

4.5.4 Globular cluster metallicity distributions

The non-linear CZR of the F3D GCs has consequences for the GC metallicity distribution function (MDF) of these galaxies. We can use our empirical relation to translate the extensive photometric GC catalogues from Jordán et al. (2015) to metallicity distributions and hence study the effect of this CZR in more detail. As examples, we picked 16 galaxies that are part of F3D and the ACSFCS to translate their ACSFCS GC colour distributions into metallicity distributions using Eq. 4.6 with the best-fitting parameters from our CZR. We selected all GC candidates with a probability of being a GC (pGC) greater than 50% (see Jordán et al. 2015 for details). This yields predictions for the metallicity distributions that would satisfy our CZR, shown in Fig. 4.14. The galaxies in this figure are ordered by increasing stellar mass. For comparison, we also show the confirmed GCs in our sample. We note again that our sample is deficient in the bluest GCs ($g-z < 0.8$ mag), possibly also because F3D covers the central parts of galaxies, while the relative number of blue GCs typically increases with

galactocentric radius (e.g. Faifer et al. 2011). Additionally, because the spatial coverage of the ACSFCS catalogue is limited, the ACSFCS colour distributions shown here might be deficient in blue GCs compared to the total GC distribution. However, these blue GCs are likely to be metal-poor and thus should not affect the bent shape of the CZR.

We quantified the shapes of the colour and metallicity distributions using the Gaussian mixture modelling (GMM) algorithm of Muratov & Gnedin (2010)[3]. This algorithm is a improved version of the KMM code (Ashman & Zepf 1992) and can be used to test whether a distribution is uni- or bimodal. GMM determines the best-fitting parameters of a unimodal and bimodal distribution and uses a bootstrap method to determine whether the bimodal solution is preferred. Following the suggestions of Muratov & Gnedin (2010), we consider a distribution to be bimodal if the distribution has a negative kurtosis, the relative distance between the two peaks is $D > 2$, and the bimodal solution is preferred with a probability $p > 0.9$. In Fig. 4.14, we noted the bimodal and unimodal distributions with 'BI' and 'UNI', respectively. In the GMM test, we assumed equal-width modes (homosedastic case) and this choice can influence the result (Beasley et al. 2018b).

The GMM test shows that the lower mass galaxies tend to have unimodal colour distributions with a dominant peak at ~ 0.9 mag, while the high-mass galaxies have bimodal colour distributions. The relative number of red GCs increases with galaxy mass. The MDFs, however, show a more diverse behaviour because of the non-linear shape of our CZR that smears out blue peaks to broad metal-poor distributions. At low galaxy masses, our CZR at blue colours translates the blue, unimodal colour distributions to broader unimodal MDFs with a peak at low GC metallicities. At intermediate masses (e.g. FCC 276, FCC 147 and FCC 083, $\log(M_{\rm gal}/M_\odot) \sim 10.5$), bimodal colour distributions with roughly equal numbers of red and blue GCs lead to bimodal MDFs with a broader metal-poor peak. FCC 170 is an outlier in this, and despite its high stellar mass $\log(M_{\rm gal}/M_\odot) \sim 10.4$ (Iodice et al. 2019a), shows a unimodal blue distribution with a relatively low number of GCs in total.

At the highest galaxy masses ($\log(M_{\rm gal}/M_\odot) > 11$, FCC 167, FCC 219, and FCC 213), the minor blue peak is smeared out to a tail of metal-poor GCs, resulting in unimodal MDFs with a dominant peak at high GC metallicities. This comparison shows that even with this non-linear CZR, not only unimodal MDFs are found. Instead, a diversity of MDFs is expected from our CZR and their modality appears to depend on the host galaxy.

4.5.5 Implications for galaxy assembly

Most galaxy formation theories explain GC colour and consequently metallicity bimodality by the existence of two distinct populations with different mean metallicities that are connected to different formation places. The bimodality has been linked to a two-stage formation scenario for massive galaxies (e.g. Ashman & Zepf 1992; Forbes et al. 1997; Côté et al. 1998; Beasley et al. 2002; Brodie & Strader 2006; Lee & Jang 2016; Beasley et al. 2018b) and is also expected in the hierarchical merger scheme of galaxy formation (e.g. Muratov & Gnedin 2010; Tonini 2013; Li & Gnedin 2014; Choksi et al. 2018; Kruijssen et al. 2019a). It is assumed that the red, metal-rich GCs either form in-situ in massive halos around the

[3] http://www-personal.umich.edu/~ognedin/gmm/

peak of star formation or during major mergers of gas-rich galaxies together with the bulk of in-situ stars. They share the high metallicity of the stars because both are set by the local mass-metallicity relation (e.g. Shapiro et al. 2010). In contrast, the metal-poor GCs form in smaller haloes from metal-poor gas and are accreted by the main galaxy in a series of hierarchical mergers (see also Forbes & Remus 2018).

As consequence of the steep slope of our CZR at blue colours, it predicts unimodal MDFs with a broad metal-poor component for galaxies with low-mass and a low fraction of red GCs. In contrast, truly bimodal MDFs are expected for intermediate massive galaxies that have roughly a similar number of red and blue GCs, while at the highest galaxy masses, unimodal MDFs with a peak at high ($\sim$ solar) metallicities are expected. In context of hierarchical assembly scenarios, this CZR still allows to conclude that the reddest GCs were formed in-situ and the bluest, most metal-poor GCs were formed in metal-poor dwarfs. This conclusion is also supported, for example, by the often observed different radial profiles of both components (e.g. Harris 2009a,b; Faifer et al. 2011) and different kinematics (e.g. Schuberth et al. 2010; Strader et al. 2011; Pota et al. 2013). As we showed Fig. 4.9, especially red GCs trace the metallicity of the host galaxy, as would be expected from an in-situ population, while the blue GCs show large metallicity differences.

However, for GCs of intermediate colours, their origin is less clear than a bimodal colour distribution would suggest because they fall in the region of the CZR that shows a steep slope and thus can have a large range of metallicities. This could indicate that those GCs are a mixed population of both in-situ and ex-situ GCs. For example, they could consist of a population of more metal-poor GCs that has formed in-situ very early-on from less enriched gas, or they are the relatively more metal-rich GCs accreted from more massive satellites. The unimodal MDFs of the most massive galaxies could then be an effect of a rich merger history during which the GCs of galaxies with different but mostly high masses were accreted, while the bimodal MDF of lower mass galaxies were created by a larger number of minor mergers (e.g. Xu et al. 2012; O'Leary et al. 2021). Nonetheless, the merger history of individual galaxies can be very diverse as cosmological simulations suggest and thus a model of the merger history would be required to interpret colour and metallicity distributions.

As an alternative to the two-phase scenarios, Yoon et al. (2006) showed that a strongly non-linear CZR can create a bimodal colour distribution from a unimodal MDF (see also Yoon et al. 2011a,b; Kim et al. 2013; Chung et al. 2016) without invoking the presence of two distinct populations. Instead, they proposed theoretical non-linear CZRs based on detailed stellar population modelling. Recently, Lee et al. (2019) modelled the colour distributions of a large number of galaxies in the Fornax and Virgo clusters and found that most of the GC system colour bimodality can be explained by unimodal MDFs and a non-linear CZR. They attribute the observed diversity in colour distributions to the mean metallicity of the GC system, where more massive galaxies have a more metal-rich GC system. Our non-linear CZR indeed finds unimodal, metal-poor MDFs for the least massive and unimodal, metal-rich MDFs for the most massive galaxies, in accordance to this picture. However, for intermediate mass galaxies, we still find bimodal MDFs and in the high mass galaxies, we observe a tail of more metal-poor GCs. Although it is possible that this tail consists of only GCs that were formed in-situ under different conditions, the bimodal MDFs in less massive galaxies rather supports the idea of distinct populations, although with less strict metallicity differences

than the colour distributions might suggest. This in agreement with the results from recent hydrodynamical simulations that have shown that a one-to-one relation between metallicity and in-situ or accreted population is not given (Forbes & Remus 2018).

4.6 Conclusions

In this chapter, we present a catalogue of 722 spectroscopically confirmed GCs of 32 galaxies in the Fornax cluster that was originally published in Fahrion et al. (2020a) and Fahrion et al. (2020b). We summarise our results as follows.

- By subtracting a MGE model of the galaxies from their collapsed MUSE images, we detected GCs in the inner regions of galaxies. After cross-referencing with the ACSFCS catalogue of GC candidates based on photometry and sizes (Jordán et al. 2015), we extracted the spectra of the GCs using a PSF-weighted circular aperture and subtracted the spectrum of the underlying galaxy.
- We classified the GCs based on their spectral S/N for further analysis. The S/N depends on a combination of the intrinsic brightness of the GC, the exposure time of the observation, the contrast with the underlying galaxy, and the metallicity. We determined the LOS velocities for GCs with S/N ≥ 3 and also metallicities were obtained from full spectral fitting for the GCs with S/N ≥ 8. Depending on the S/N, the resulting random uncertainties are in the range of $5 \lesssim \delta \mathrm{v} \lesssim 60$ km s^{-1} and $0.05 \lesssim \delta[\mathrm{M/H}] \lesssim 0.20$ dex, respectively.
- Using the GC LOS velocities, we modelled the rotation amplitude and velocity dispersion of the GC systems in several galaxies. Where possible, we modelled the red and blue GCs separately. We found that the GC velocity dispersion traces that of the stars. For the elliptical galaxies in our sample, especially the red GCs follow the stellar rotation while the GC rotation is lower than in the stars for the lenticular galaxies. This illustrates that the GCs follow the kinematics of the spheroid of the host galaxy rather than the disk. The blue GCs generally show low rotation amplitudes.
- We compared the GC metallicities to the centres of the respective host galaxies and found that the central metallicity not only sets an upper limit to the stellar metallicity, but also to the GC metallicity. Although no GC exceeds the metallicity of the host's centre, we found several with similar metallicities, even at distances $\sim 1\,R_{\mathrm{eff}}$. The more massive galaxies in our sample show a large spread in metallicities, from very metal-poor ($[\mathrm{M/H}] \lesssim -2.3$ dex) to super-solar values, while the less massive galaxies show a narrower distribution in GC metallicities that are on average more metal-poor.
- Comparing the GC metallicities to the metallicity of the stellar body locally showed that the red GCs trace the stellar metallicity profile closely from the inner regions out to a few R_{eff}. The blue GCs, however, are more metal-poor than the host galaxies, even in the outer regions. This was found independent of the galaxy stellar mass.
- We found a non-linear relation between GC metallicities and colours. This CZR is shallow at red colours and significantly steepens at bluer colours. The relation can be described by a quadratic function or a piecewise linear function with a breakpoint at $(g - z) \sim 1.1$ mag. A linear relation is not sufficient to describe the shape of the CZR.

- Although our default approach assumes a GC age $\geq$ 8 Gyr, we tested this assumption by also fitting the GC ages. This shows best-fitting old ages ($\geq$ 8 Gyr) with very few exceptions. We only found a weak age-metallicity relation that appears to be mostly driven by the mass of the host because the low-mass galaxies in our sample tend to have younger, more metal-poor GCs.
- Applying the non-linear CZR to photometric GC colour distributions predicts a diversity of MDFs. The shape of the CZR implies that massive galaxies with relatively small blue GC populations have a unimodal MDF with a peak at high and a tail towards lower metallicities. Galaxies with equal numbers of red and blue GCs can truly have a bimodal metallicity distribution, while low-mass galaxies show a unimodal MDF with a metal-poor peak, resulting from the lack of red GCs.
- In the context of galaxy assembly, the MDFs predicted by our CZR support different origins for GCs at the metal-poor and metal-rich end of the distribution. While the most-metal rich GCs are likely to have formed in-situ in the host galaxy, the most metal-poor GCs were possibly accreted from low-mass dwarf galaxies. However, the shape of the CZR allows a variety of metallicities for GCs with intermediate colours and this could indicate a diverse origin for these GCs. They might be a mixture of more metal-poor GCs reflecting the metal-poor end of the in-situ GC distribution and the relatively more metal-rich GCs accreted from more massive galaxies.

In accordance with other studies, we found that GCs are valuable tracers of galaxy properties as well as galaxy evolution. They serve as tracers of the enclosed mass of their host galaxy. Especially the red GCs further trace the kinematics of the galaxy spheroid and follow the galaxy metallicity from the inner parts out into the halo regions. Contrary, the blue, metal-poor GCs show larger deviations with respect to the properties of the host, independent of the host stellar mass. In this work, we could derive a non-linear CZR in the Fornax cluster, using galaxies of a variety of different masses that challenges the simplistic division of GCs into in-situ and accreted solely based on their colour. This method of extracting high quality GC spectra provides a new efficient way to assess accurate membership and chemodynamical properties of GC systems (especially in the inner regions), which will be crucial to exploit the wealth of IFU data of galaxies in the local Universe.

It's a dangerous business, Frodo, going out your door. You step onto the road, and if you don't keep your feet, there's no knowing where you might be swept off to.

J.R.R. Tolkien, The Lord of the Rings

5 | Diversity of nuclear star cluster formation mechanisms

Chapters 2 and 3 illustrated how IFS data can be used to explore NSC formation in individual galaxies. The studies of the massive ETG FCC 47 and the two nucleated dwarf galaxies showed evidence that both NSC formation channels can occur. In this chapter, I extend the analysis of nucleated galaxies to a sample of 25 nucleated galaxies, 23 in the Fornax galaxy cluster and two in the Virgo cluster, that span galaxy masses between 10^7 and $10^{10.5} M_\odot$ and NSC masses between 10^5 and $10^8 M_\odot$. I derive SFHs, ages, and metallicities of the host galaxies and their NSCs in a homogeneous fashion that enables a direct comparison of these components and allows us to observationally derive the dominant NSC formation channel as a function of galaxy properties. This chapter was originally published in Fahrion et al. (2021).

5.1 Sample galaxies

The 32 galaxies studied in this chapter are listed in Table 5.1. We chose these galaxies due to the availability of MUSE data which were previously used in stellar population and GC system studies (Sarzi et al. 2018; Pinna et al. 2019a,b; Iodice et al. 2019a; Johnston et al. 2020; Fahrion et al. 2020c,a). The galaxies comprise galaxies from the F3D survey and we concentrated on the galaxies that are defined as nucleated based on the analysis of HST data of the ACSFCS by Turner et al. (2012). For details concerning the data reduction, we refer to Sarzi et al. (2018) and Iodice et al. (2019a).

In addition to the F3D galaxies, we complemented the sample with Fornax cluster dwarf galaxies that were also in the sample analysed by Johnston et al. (2020). We included these galaxies to extend the mass range to $M_{\rm gal} < 10^9 M_\odot$. Because our study relies on an homogeneous analysis of all galaxies using the same techniques for a reliable comparison between galaxies, we included these galaxies in our analysis. Furthermore, we included two nucleated dwarf galaxies in the Virgo cluster (VCC 990 and VCC 2019) that were previously analysed by Bidaran et al. (2020) with focus on their internal kinematics. For the Virgo and Fornax dwarf galaxies, we downloaded the reduced MUSE data cubes from the ESO science archive[1] and applied the ZAP algorithm (Soto et al. 2016) to further reduce sky residuals. For FCC 202 we used the two pointings independently, because the combined mosaic provided

[1] http://archive.eso.org/scienceportal/home

by the archive showed a sub-optimal co-addition and the NSC is only covered in one. Additionally, we again included FCC 47 to ensure a homogeneous comparison to the rest of the Fornax cluster sample.

In summary, the galaxies studied here comprise ETGs and dEs with no or low levels of star formation. Where no NSC masses were available in the literature, we derived them from their $(g - z)$ colours from the ACSFCS (Turner et al. 2012) and ACSVCS and the photometric predictions of the E-MILES stellar population synthesis models (Vazdekis et al. 2016) that give M/L in the ACS g band. To determine the mass, we sample the g and z magnitudes within their uncertainties and allow ages between 5 and 14 Gyr. The age can affect the mass-to-light ratio, but the largest uncertainty stems from the uncertainties of the NSC g and z magnitudes (~ 0.2 mag).

5.2 Analysis

Understanding the formation of NSCs requires a comparison of the properties of the NSC to the host galaxy from its central regions to the outskirts. In the following, we describe how we extracted the MUSE spectra of the different spatial regions we aim to compare (see Table 5.2 for an overview). Sect. 5.2.3 then details how the spectra are fitted to extract the stellar population properties.

5.2.1 Nuclear star cluster spectra

The biggest challenge to extract the NSC properties from MUSE data is to disentangle the NSC spectra from the underlying galaxy light. The spectrum obtained from a central aperture contains significant contributions from both the NSC and the galaxy. In addition, at the distances of the Fornax and Virgo galaxy clusters (20 Mpc and 16 Mpc, respectively), NSCs are not resolved. To reduce the contribution of the galaxy, we took the following approach that aims to subtract a spectrum representing the galaxy from the central spectrum. This approach takes the method presented in Sect. 2.3.3 a step further by correcting for the surface brightness profile of the galaxy.

The NSC spectrum S_{NSC} is given by

$$S_{\mathrm{NSC}} = S_{\mathrm{central}} - S_{\mathrm{host,\ central}}, \tag{5.1}$$

where S_{central} is the central spectrum acquired directly from the data. To extract this spectrum, we used a circular aperture weighted by PSF (FWHM of $0.8''= 4$ pixel) centred on the galaxy centre, assuming an unresolved NSC. $S_{\mathrm{host,\ central}}$ is the (unknown) contribution of the host galaxy at this central position.

We estimate this galaxy contribution as

$$S_{\mathrm{host,\ central}} = \alpha\, S_{\mathrm{host,\ 2''}}, \tag{5.2}$$

where $S_{\mathrm{host,\ 2''}}$ is the spectrum of the host galaxy at $2''$ defined by an elliptical annulus aperture with 8 pixel ($1.6''= 200$ pc in Fornax and 160 pc in Virgo) inner and 13 pixel ($2.6''$)

Table 5.1.: Overview of nucleated galaxies.

Galaxy	Altern. name	$R_{\rm eff}$ (arcsec)	$R_{\rm eff}$ (kpc)	$\log(M_{\rm gal})$	$\log(M_{\rm NSC})$	Exp. time (sec)	Programme
(1)	(2)	(3)	(4)	(5)	(6)	(7)	(8)
FCC 47	NGC 1336	30.0[a]	2.9	9.97[d]	8.74[h]	3600	060.A-9192 (PI: Fahrion)
FCC 119	–	17.4[b]	1.7	9.0[d]	6.81[h]	5400	296.B-5054 (PI: Sarzi)
FCC 148	NGC 1375	28.3[b]	2.7	9.76[d]	8.37[h]	3600 + 5400	296.B-5054 (PI: Sarzi)
FCC 153	IC 1963	19.8[b]	1.9	9.88[d]	7.29[h]	3600 + 5400	296.B-5054 (PI: Sarzi)
FCC 170	NGC 1381	15.9[b]	1.5	10.35[d]	8.45[h]	3600 + 7200	296.B-5054 (PI: Sarzi)
FCC 177	NGC 1380A	35.9[b]	3.5	9.93[d]	7.83[h]	3600 + 5400	296.B-5054 (PI: Sarzi)
FCC 182	–	9.9[b]	1.0	9.18[d]	6.03[e]	5400	296.B-5054 (PI: Sarzi)
FCC 188	–	12.1[a]	1.2	8.89[e]	6.85[e]	10400	096.B-0399 (PI: Napolitano)
FCC 190	NGC 1380B	18.3[b]	1.8	9.73[d]	7.18[h]	3600 + 5400	296.B-5054 (PI: Sarzi)
FCC 193	NGC 1389	28.2[b]	2.7	10.52[d]	8.15[h]	3600 + 5400	296.B-5054 (PI: Sarzi)
FCC 202	NGC 1396	9.8[a]	1.0	9.03[e]	6.76[e]	10400 + 10400	094.B-0895 (PI: Lisker)
FCC 211	–	5.6[a]	0.5	8.52[e]	6.70[e]	10400	096.B-0399 (PI: Napolitano)
FCC 215	–	7.4[a]	0.7	6.79[e]	5.94[e]	10400	096.B-0399 (PI: Napolitano)
FCC 222	AM 0337-353	14.5[a]	1.4	8.80[e]	6.45[e]	10400	096.B-0399 (PI: Napolitano)
FCC 223	AM 0337-355	16.6[a]	1.6	8.78[e]	6.38[e]	10400	096.B-0399 (PI: Napolitano)
FCC 227	–	7.3[a]	0.7	6.73[e]	5.24[e]	10400	096.B-0399 (PI: Napolitano)
FCC 245	–	12.9[a]	1.3	8.77[e]	6.05[e]	1350	101.C-0329 (PI: Vogt)
FCC 249	NGC 1419	9.6[b]	0.9	9.70[d]	6.93[h]	3600 + 1800	296.B-5054 (PI: Sarzi)
FCC 255	ESO 358-G50	13.8[b]	1.3	9.70[d]	6.98[h]	3600 + 1800	296.B-5054 (PI: Sarzi)
FCC 277	NGC 1428	12.8[b]	1.2	9.53[d]	7.22[h]	3600 + 2160	296.B-5054 (PI: Sarzi)
FCC 301	ESO 358-G59	11.7[b]	1.1	9.30[d]	6.91[h]	3600 + 1800	296.B-5054 (PI: Sarzi)
FCC 310	NGC 1460	35.6[b]	3.5	9.73[d]	7.81[h]	3600 + 5400	296.B-5054 (PI: Sarzi)
FCCB 1241	AM 0336-323	8.4[b]	0.8	8.13[e]	5.48[e]	2160	102.B-0455 (PI: Johnston)
VCC 990	IC 3369	8.1[c]	0.6	9.10[f]	6.83[h]	3240	098.B-0619 (PI: Lisker)
VCC 2019	IC 3735	15.7[c]	1.3	9.01[g]	6.78[g]	3744	100.B-0573 (PI: Lisker)

(1, 2) galaxy name and alternative name, (3, 4) effective radius in arcsec and in kpc assuming a distance of 20 Mpc (Fornax, Blakeslee et al. 2009) and 16.5 Mpc (Virgo, Mei et al. 2007) (5) stellar mass of the host galaxy, (6) stellar mass of the NSC (7) total exposure time of the pointings covering the galaxy. (8) MUSE observing programme and PI. References: a - Ferguson (1989), b - Iodice et al. (2019a), c - Kim et al. (2014), d - Liu et al. (2019), e - Johnston et al. (2020), f - Peng et al. (2008), g - Paudel et al. (2011), h - this work.

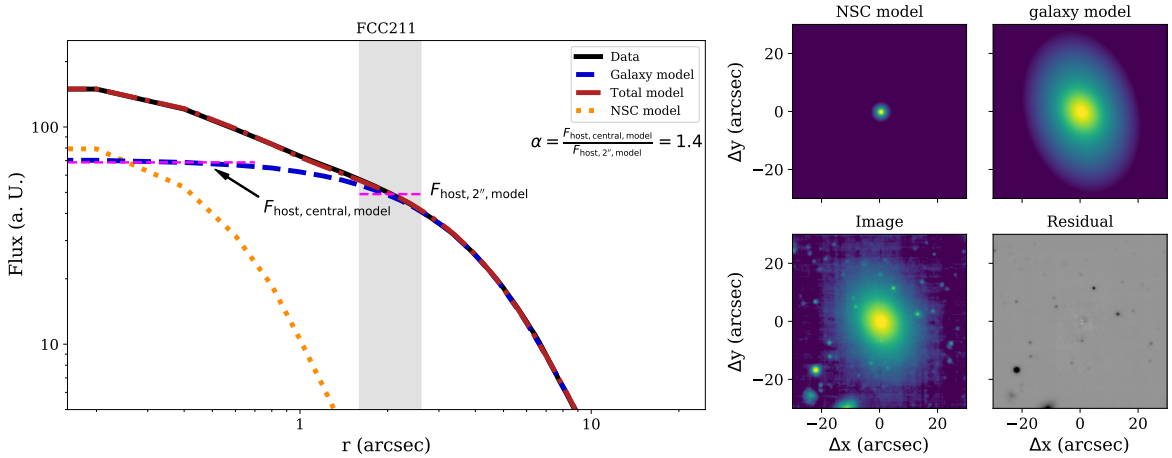

Figure 5.1.: IMFIT modelling of FCC 211 to decompose the white-light image into a galaxy and a NSC component. *Left*: radial profile of the data (solid black line), galaxy model (dashed blue line), NSC model (dotted orange line), and combined model (dash-dotted red line). The grey areas show the extraction regions. The mean fluxes in these regions are indicated by the horizontal dashed magenta lines to illustrate the scaling factor α. *Right*: 2D cutout images of the original image (*bottom left*), NSC and galaxy model (*top row*) and resulting residual image (*bottom right*). As described in the text, this decomposition is used to determine the contribution of galaxy light when extracting the NSC spectrum from the MUSE data. Each image shows a region of 60″× 60″(5.4 kpc × 5.4 kpc) centred on the NSC.

outer radius. We chose this radius to determine the spectrum of the galaxy right outside the extend of the central PSF and thus outside the influence of the NSC. The position angle and ellipticity of the elliptical aperture were derived from a MGE fit (Emsellem et al. 1994; Cappellari 2002) to the galaxy image. For the F3D galaxies, these are comparable to the ones listed in Iodice et al. (2019a). We assume that this galaxy spectrum represents the galaxy at the centre (and hence the stellar populations), but we allow for an additional scaling factor α that describes the flux level difference between the central and the annulus apertures:

$$\alpha = \frac{F_{\text{host, central}}}{F_{\text{host, 2''}}}. \tag{5.3}$$

As all fluxes are normalised by the extraction area, $\alpha = 1$ if the flux of the host galaxy is constant between 2″ and the centre.

In the dwarf galaxies, the NSC often dominates the central regions and for those, $\alpha = 1$ is a reasonable approximation. However, to optimise the NSC spectrum extraction, we used 2D surface brightness modelling with IMFIT (Erwin 2015) to determine α on model images (see Fig. 5.1 for an illustration). IMFIT is a modular 2D fitting procedure that fits images of galaxies with an user-specified set of 2D image functions (e.g. exponential, Sérsic, Gaussian). An arbitrary number of different components can be added together to model galaxy images. To fit the white-light images of our MUSE data, we modelled the unresolved NSCs with a single component described by a Moffat function. A Sérsic function yields comparable results. The galaxies, on the other hand, can consist of multiple components to capture the various physical components in the galaxy (disks, bulges etc.).

After decomposing the white-light MUSE images in this way, we obtained model images

of the NSC and the host galaxies with the same spatial scales as the original MUSE data. Using these model images, we can apply the same apertures as used on the MUSE data to estimate α:

$$\alpha = \frac{F_{\text{Host, central, model}}}{F_{\text{Host, 2}'', \text{ model}}}. \tag{5.4}$$

This approach was inspired by the technique described in Johnston et al. (2020), where the authors use similar 2D surface brightness modelling at every wavelength bin. In this way, they obtain single model spectra for every component. However, spatial stellar population gradients cannot be captured with this approach as every component is assigned a single spectrum. Dwarf galaxies, as those studied in Johnston et al. (2020), usually lack strong stellar population gradients and thus this approach is completely valid. Our sample comprises more complex galaxies with multiple structural components and strong radial gradients (see Fig. 5.2). Therefore, we adopted the approach described here that allows us to base the spectra extraction on the MUSE data directly without invoking full galaxy models. We only used the IMFIT models to infer the scaling factor α and extracted the spectra of each spatial region directly from the data.

Figure 5.1 illustrates our approach applied to FCC 211, one of the dwarf galaxies. The galaxy component is modelled in this case with two Sérsic functions, while the NSC is described by a Moffat function. For this galaxy, we found $\alpha = 1.4$, implying that the contribution of the galaxy to the NSC spectrum is roughly 40% higher than at the extraction radius of 2″. In general, we find values of α between 1.0 and 3.0. While the surface brightness distributions of dwarf galaxies in the sample can be modelled without strong residuals, some of the more massive galaxies in the sample have complex structures such as disks and X-shaped bulges which are not completely captured by the model. Nonetheless, the radial surface brightness profiles are well fitted also in these galaxies. In Appendix C.1, we present the IMFIT model for FCC 170, a massive edge-on S0 galaxy with a X-shaped bulge as well as a thin and thick stellar disk. The 2D residual of this galaxy (Fig. C.1) still shows left-over structure, despite a good fit to the radial surface brightness profile. We found $\alpha = 2.8$ for this galaxy, but as discussed in Appendix C.1, the uncertainty on α can be up to $\sim 20\%$ in these massive galaxies as it depends on the subjective choice of the number of used components.

5.2.2 Galaxy spectra

To compare the galaxies to their NSCs, we extracted averaged spectra of the galaxies at different radii. In addition to the region at 2″ that was used to estimate the galaxy stellar populations at the centre, we further extracted averaged spectra at 0.5 and 1.0 R_{eff} using elliptical annulus apertures with 20 and 40 pixel width, respectively, and the same ellipticity as before. For some of the dwarf galaxies with small R_{eff}, we decreased the width of the extraction aperture to ensure that the NSC is excluded. In addition, bright foreground stars and background galaxies are masked. For FCC 119, FCC 188, FCC 223, and FCC 227, only the spectra obtained around 0.5 R_{eff} yield a sufficient S/N for fitting due to the low surface brightness of these galaxies.

To illustrate that these averaged spectra represent the stellar populations of the galaxies, we compare them to binned spectra obtained using the Voronoi binning routine described

Table 5.2.: Overview of the different spectra.

Name	Description
Central	spectrum of the central PSF
NSC	NSC spectrum (galaxy contribution subtracted)
2″	annulus spectrum at 2″
0.5 $R_{\rm eff}$	annulus spectrum at 0.5 $R_{\rm eff}$
1.0 $R_{\rm eff}$	annulus spectrum at 1.0 $R_{\rm eff}$
Bins	Voronoi-binned spectra

in Cappellari & Copin (2003b) in Fig. 5.2. This routine bins the MUSE data to a target S/N and thus enables a continuous view of the stellar population properties. As we are interested in a comparison of the central galaxy regions to their NSCs, we chose the target S/N such that there are sufficient bins in the inner 10″ of each galaxy. In the most massive galaxies, this was reached for even very high target S/N > 300, but for some of the dwarf galaxies, target values of S/N = 30 were chosen to ensure robust fits. The data of FCC 227 and FCC 215 are too shallow for binning. We show four metallicity maps as examples in Appendix C.2 (Fig. C.2).

Table 5.2 gives a summary of the different spectra and Fig. 5.2 illustrates that the stellar population properties determined from these different annuli spectra are consistent with the properties obtained from the binned spectra. In general, we found that the stellar population results presented in the next sections are not sensitive to the choice of α. As Fig. 5.2 illustrates, the overall trends with metallicity are found even without subtracting the galaxy contribution. With this subtraction the respective trends are enhanced, illustrating that the NSC is responsible for the behaviour in the central bins. In contrast, the subtraction of the galaxy contribution has a stronger effect on the SFHs presented in Fig. 5.3, but here testing of our method has shown that similar SFHs are recovered when simply assuming $\alpha = 1$, possibly because our best-fit values for α reach moderate values between 1 and 3. Using unrealistically large values of $\alpha > 5$, however, can increase the associated uncertainties drastically and might even lead to a loss of the NSC signal.

5.2.3 Full spectral fitting

We fitted all spectra using full spectrum fitting with pPXF, as described in Sect. 2.4. We used the baseFe E-MILES SSP models with BaSTi isochrones (Pietrinferni et al. 2004, 2006). We used a MW-like double power-law IMF with a high mass slope of 1.30 (Vazdekis et al. 1996). To account for the varying instrumental resolution of MUSE, we used the description of the MUSE line spread function from Guérou et al. (2016). In FCC 119 and FCC 148, where emission lines from ionised gas are clearly visible in the spectra, we fitted them simultaneously. Telluric lines and remnant sky residual lines are masked in the fits. As recommended for example by Cappellari (2017), we first fitted for the LOS velocity distribution using additive polynomials of degree twelve. Those ensure a smooth continuum and are required to find the best-fitting LOS velocity and velocity dispersion. To then fit for the stellar population parameters (age and metallicity), we kept the LOS velocity distribution

fixed and used multiplicative polynomials of degree 8 instead of additive polynomials to preserve the line profiles.

The PPXF routine returns the weights of the models used in the fit, which allows us to determine the mean age and metallicity as the weighted means. Because the E-MILES models are normalised to 1 $M_{\odot}$, the resulting stellar population properties are mass-weighted. To extract SFHs and metallicity distributions, we applied regularisation during the fit with PPXF. Regularisation leads to a smooth distribution of mass weights of the assigned models and hence allows to reconstruct smooth distributions of ages (the SFHs) and metallicities. To derive the regularisation parameter, we followed the established approach recommended by Cappellari (2017) and McDermid et al. (2015): The regularisation parameter is given as the one that increases the χ^2 of the unregularised fit by $\sqrt{2\,N_{\rm pix}}$, where $N_{\rm pix}$ is the number of fitted spectral pixels. We calibrated this regularisation for the NSC spectrum of each galaxy.

Using the calibrated regularisation parameter in PPXF returns the smoothest SSP model weight distribution that is still compatible with the data, meaning that not every small feature in the SFHs is related with a real star formation episode. Moreover, determining the correct regularisation parameter is a non-trivial task (Cappellari 2017; Pinna et al. 2019a; Böcker et al. 2020). However, the overall trends and presence of multiple populations are reliable. We verified that the SFH distributions are robust against changes to the library of SSP models (e.g. using the scaled-solar MILES models), order of the multiplicative polynomial, chosen wavelength range (e.g. extending to 8900Å), and regularisation parameter. In our tests, the mean values of age and metallicity are recovered within their uncertainties and the general shape of the SFHs and metallicity distributions are preserved under these changes. This also holds for different choices of α.

In addition to using regularisation, we also fitted the spectra with a MC approach to derive realistic random uncertainties (see Sect. 2.4). We verified that the mean of the age and metallicity MC fits are consistent with the weighted means from the regularised fits, as shown in Appendix C.3. Table 5.3 gives the resulting mean ages and metallicities for the NSCs and their host galaxies.

5.3 Results

The following section presents the results from the stellar population analysis. First, we discuss the radial metallicity profiles and present the star formation histories and metallicity distributions. Sect. 5.3.4 then presents the mass-metallicity relation.

5.3.1 Radial metallicity profiles

Figure 5.2 shows the radial metallicity profiles obtained from the different spatial regions that we compare as well as from the Voronoi-binned data cubes. The profiles from the binned data were extracted using elliptical isophotes with same the position angle and ellipticity as used in Sect. 5.2.1. FCC 227 and FCC 215 are too faint to be binned. This figure displays that results obtained from the binned cubes are consistent with those obtained from the spectra

Table 5.3.: Mass-weighted mean ages and metallicities of NSCs and host galaxies.

Galaxy	$[M/H]_{NSC}$ (dex)	$[M/H]_{2''}$ (dex)	$[M/H]_{0.5\ R_{eff}}$ (dex)	$[M/H]_{1.0\ R_{eff}}$ (dex)	Age_{NSC} (Gyr)	$Age_{2''}$ (Gyr)	$Age_{0.5\ R_{eff}}$ (Gyr)	$Age_{1.0\ R_{eff}}$ (Gyr)
FCC 47	-0.11 ± 0.02	-0.54 ± 0.02	-0.73 ± 0.02	-0.78 ± 0.04	13.8 ± 0.1	13.4 ± 0.2	12.8 ± 0.3	12.4 ± 0.7
FCC 119	-1.02 ± 0.05	-0.52 ± 0.03	-0.55 ± 0.02	–	1.7 ± 0.5	4.5 ± 0.5	6.1 ± 0.5	–
FCC 148	0.26 ± 0.03	-0.02 ± 0.02	-0.29 ± 0.01	-0.49 ± 0.03	4.3 ± 0.7	3.7 ± 0.4	5.4 ± 0.4	7.2 ± 0.8
FCC 153	0.35 ± 0.02	0.02 ± 0.02	-0.13 ± 0.01	-0.21 ± 0.01	9.3 ± 0.6	7.6 ± 0.4	8.9 ± 0.3	9.9 ± 0.4
FCC 170	0.13 ± 0.03	-0.03 ± 0.01	-0.21 ± 0.01	-0.29 ± 0.01	13.0 ± 0.7	14.0 ± 0.0	14.0 ± 0.0	13.9 ± 0.1
FCC 177	0.40 ± 0.01	-0.05 ± 0.03	-0.36 ± 0.02	-0.40 ± 0.02	6.7 ± 0.3	4.4 ± 0.5	7.9 ± 0.4	8.2 ± 0.7
FCC 182	-0.22 ± 0.05	-0.25 ± 0.01	-0.41 ± 0.01	-0.61 ± 0.02	11.3 ± 0.9	10.8 ± 0.5	10.5 ± 0.4	10.3 ± 0.6
FCC 188	-1.07 ± 0.04	-0.76 ± 0.02	-0.81 ± 0.02	–	8.5 ± 0.8	10.3 ± 0.8	9.2 ± 0.8	–
FCC 190	0.02 ± 0.10	-0.24 ± 0.01	-0.37 ± 0.01	-0.49 ± 0.03	7.7 ± 0.9	11.5 ± 0.5	11.9 ± 0.5	13.0 ± 0.6
FCC 193	0.40 ± 0.00	0.04 ± 0.02	-0.26 ± 0.01	-0.34 ± 0.02	14.0 ± 0.0	11.0 ± 0.3	10.9 ± 0.3	11.6 ± 0.5
FCC 202	-0.95 ± 0.05	-0.39 ± 0.02	-0.47 ± 0.02	-0.57 ± 0.01	7.4 ± 1.1	7.3 ± 0.8	7.7 ± 0.7	8.0 ± 0.8
FCC 211	-1.01 ± 0.04	-1.00 ± 0.02	-1.04 ± 0.02	-1.16 ± 0.02	8.8 ± 0.8	9.5 ± 0.6	9.7 ± 0.4	9.6 ± 0.5
FCC 215	-1.64 ± 0.12	-1.05 ± 0.25	-1.59 ± 0.15	-2.16 ± 0.11	7.8 ± 2.4	5.3 ± 3.1	9.2 ± 3.2	8.3 ± 3.5
FCC 222	-1.22 ± 0.06	-0.60 ± 0.02	-0.76 ± 0.03	-0.91 ± 0.05	8.9 ± 0.8	8.1 ± 0.7	8.7 ± 1.0	9.4 ± 1.2
FCC 223	-1.89 ± 0.08	-1.13 ± 0.04	-1.18 ± 0.04	–	11.7 ± 1.1	8.7 ± 0.9	9.9 ± 1.1	–
FCC 227	-1.72 ± 0.15	-1.73 ± 0.21	-1.88 ± 0.19	–	12.4 ± 1.6	8.3 ± 3.5	11.6 ± 2.4	–
FCC 245	-0.77 ± 0.14	-0.62 ± 0.06	-0.83 ± 0.04	-1.14 ± 0.07	8.2 ± 2.1	8.4 ± 1.3	10.3 ± 1.0	12.2 ± 1.7
FCC 249	0.21 ± 0.02	-0.28 ± 0.02	-0.50 ± 0.01	-0.66 ± 0.02	13.7 ± 0.3	13.7 ± 0.1	12.7 ± 0.1	12.1 ± 0.2
FCC 255	-0.16 ± 0.04	-0.28 ± 0.02	-0.31 ± 0.02	-0.43 ± 0.02	3.7 ± 0.7	5.1 ± 0.6	5.1 ± 0.5	6.0 ± 0.6
FCC 277	0.16 ± 0.04	-0.31 ± 0.01	-0.46 ± 0.01	-0.57 ± 0.01	9.7 ± 0.8	9.7 ± 0.4	10.6 ± 0.3	11.1 ± 0.5
FCC 301	-0.23 ± 0.05	-0.24 ± 0.02	-0.53 ± 0.01	-0.74 ± 0.02	6.0 ± 1.1	6.2 ± 0.6	7.8 ± 0.6	9.2 ± 0.7
FCC 310	0.27 ± 0.04	-0.33 ± 0.02	-0.50 ± 0.04	-0.55 ± 0.08	7.5 ± 0.8	9.6 ± 0.5	10.3 ± 1.2	10.3 ± 1.8
FCCB 1241	-0.88 ± 0.13	-1.33 ± 0.05	-1.21 ± 0.05	-1.43 ± 0.07	10.6 ± 2.1	11.8 ± 1.1	12.0 ± 1.3	12.2 ± 1.3
VCC 990	-0.20 ± 0.04	-0.50 ± 0.02	-0.55 ± 0.02	-0.65 ± 0.02	4.4 ± 0.9	5.8 ± 0.6	6.0 ± 0.6	6.7 ± 0.6
VCC 2019	0.06 ± 0.05	-0.49 ± 0.02	-0.68 ± 0.02	-0.81 ± 0.03	3.2 ± 0.7	5.9 ± 0.7	7.2 ± 0.7	9.3 ± 0.9

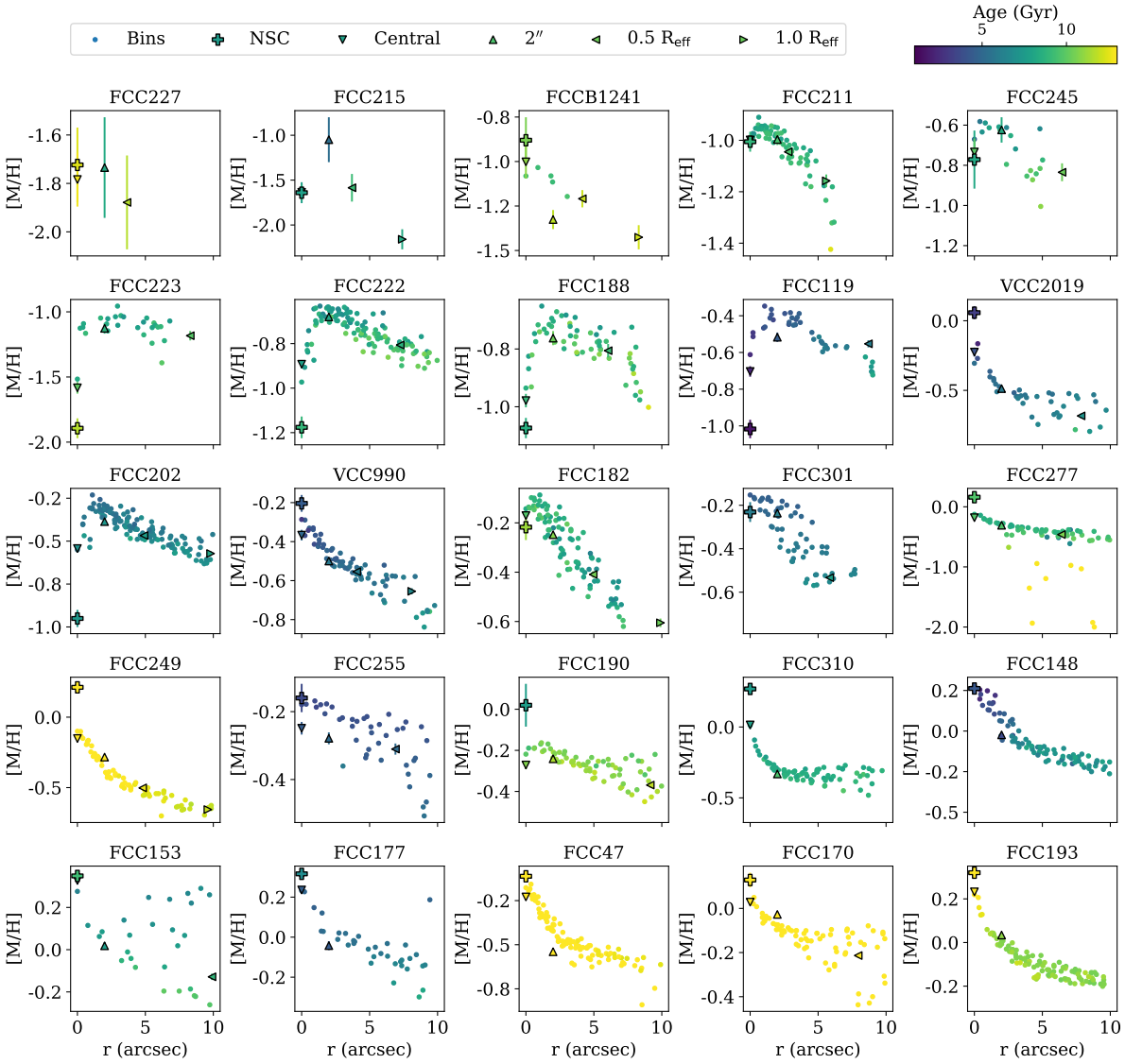

Figure 5.2.: Radial metallicity profiles for the galaxies. Small dots show individual bins from the Voronoi binned cubes, crosses refer to the NSCs, triangles to the different extraction radii as described in the legend and Table 5.2. All symbols are coloured by age. Galaxies are ordered by increasing stellar mass from top left to bottom right. FCC 227 and FCC 215 are too faint to be binned.

extracted with different aperture sizes. The metallicities and ages determined from the spectra obtained at 2″, 0.5, and 1.0 $R_{\rm eff}$ follow those from the binned data at the respective positions. In contrast, the NSC metallicities (obtained from the background-cleaned NSC spectra), follow the trends seen in the binned data, but can be more extreme – either more metal-poor or more metal-rich – than what is found in the central bins or the central spectrum. This is expected because the central binned spectra are affected by both the unresolved NSCs and the underlying galaxy, which dilutes the signal of the NSC.

The binned radial metallicity profiles generally show an increase in metallicity from the outskirts to the central region ($< 2''$), as found for most galaxies (e.g. Kuntschner et al. 2010; Martín-Navarro et al. 2018; Zhuang et al. 2019; Santucci et al. 2020). In the massive galaxies (bottom two rows), the highest metallicities are found in the central bins and their NSCs even surpass these metallicities. In contrast, many of the dwarf galaxies (top rows) show a drop in metallicity at the very centre (see also Fig. C.2). As the comparison to the NSC metallicities shows, these central decreases are caused by metal-poor NSCs that dominate the light in the central bins of the dwarf galaxies. Except for FCC 119, no central star formation is evident in these dwarf galaxies that could bias the results and for FCC 119 we find similar results when masking the emission lines and fitting the full MUSE wavelength range up to 8900 Å.

5.3.2 Star formation histories

By applying regularisation during the pPXF fit, smooth distributions of ages and metallicities that best fit the spectra are recovered. Their weights can be used to infer normalised SFHs, as shown in Fig. 5.3. Each panel shows the SFH of the NSC (top), the galaxy at 2″ from the centre (middle), and the host galaxy at 1.0 or 0.5 $R_{\rm eff}$ (bottom). The SFHs are normalised such that the peak of the distribution is at 1 for visualisation of the shape and the distributions are colour-coded to show the mean metallicity in each age bin. We only show the galaxies where the NSC and galaxy spectra have sufficient S/N to ensure a reasonable application of the regularisation approach. For this reason, FCC 215 and FCC 227 are not shown.

We find a large diversity in SFH shapes for both the NSCs and their host galaxies. Generally, the SFHs at 2″ and at 1.0 $R_{\rm eff}$ have similar shapes, while the NSCs often show a very different behaviour from the host galaxy. At lowest galaxy masses ($M_{\rm gal} < 10^9 M_\odot$, top row), the host galaxies predominantly show single peaks in the SFH with mean ages around 8 Gyr, but the SFHs of their NSCs show a greater variety, also displaying very old stellar ages and low metallicities. These could be explained by early star formation in the NSC or by the accretion of GCs which are typically old and metal-poor in such dwarf galaxies (e.g. the GCs of the Fornax dwarf spheroidal galaxy, Larsen et al. 2012). FCC 119 stands out from this with very young ages in the NSC and the presence of ionised gas indicative of star formation.

The NSCs in the most massive galaxies of our sample (bottom row) are dominated by a single peak at old ages with high metallicities, while the host galaxies exhibit similar SFHs but offset at lower metallicities. At intermediate host masses, the diversity in NSC SFHs increases. For galaxies with masses around $10^9 M_\odot$ (second and third row), we find several

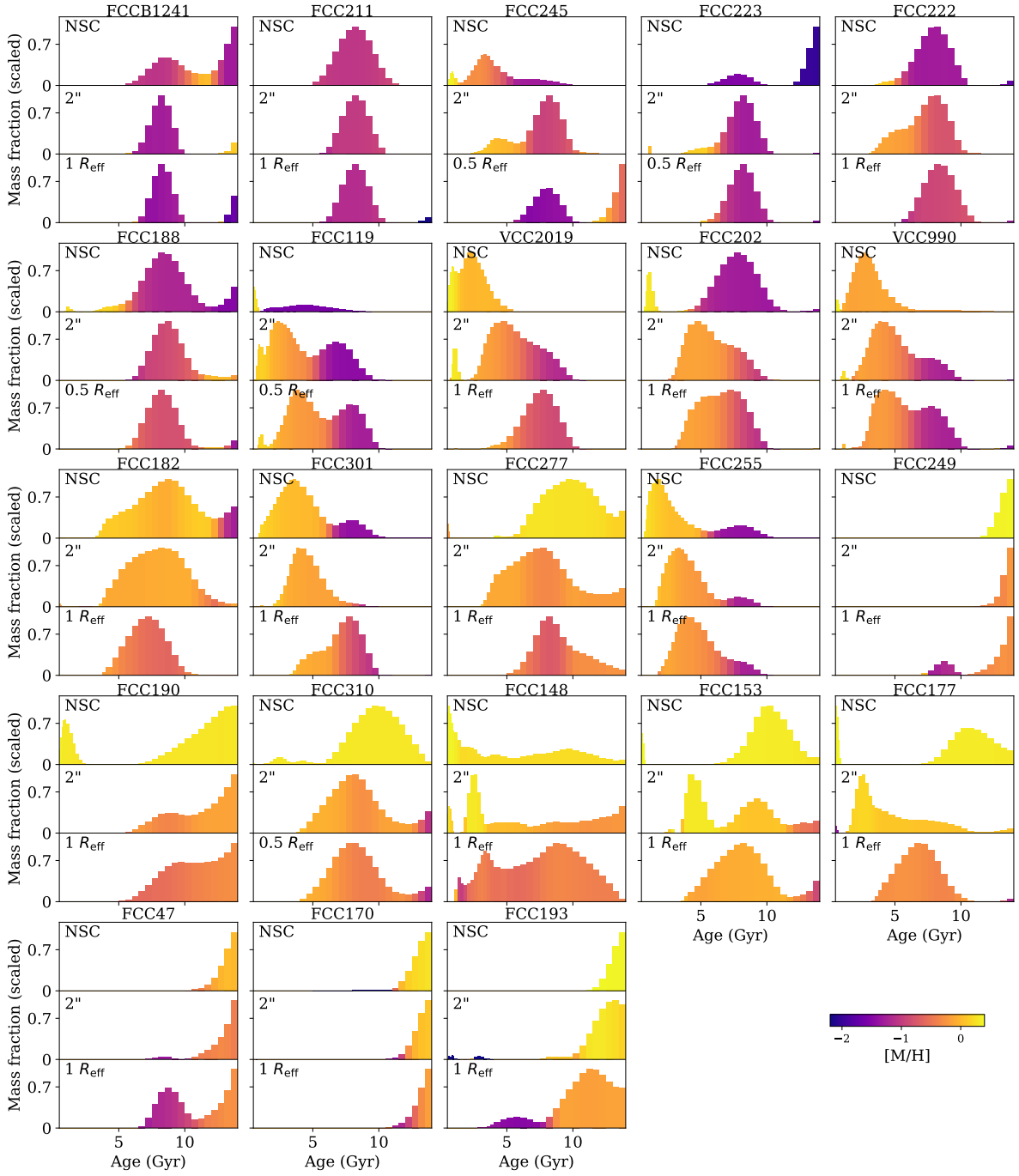

Figure 5.3.: Star formation histories of NSCs (*top*), at the 2″ extraction annulus (*middle*), and host galaxy (*bottom*), each panel corresponding to one galaxy. The mass fractions are scaled such that the peak is at 1.0 for visualisation of their shape. The galaxies are ordered by increasing stellar mass and the bins are colour-coded by their mean metallicity.

cases in which the NSC SFH is extended or shows multiple populations with different ages and metallicities, including young stellar populations.

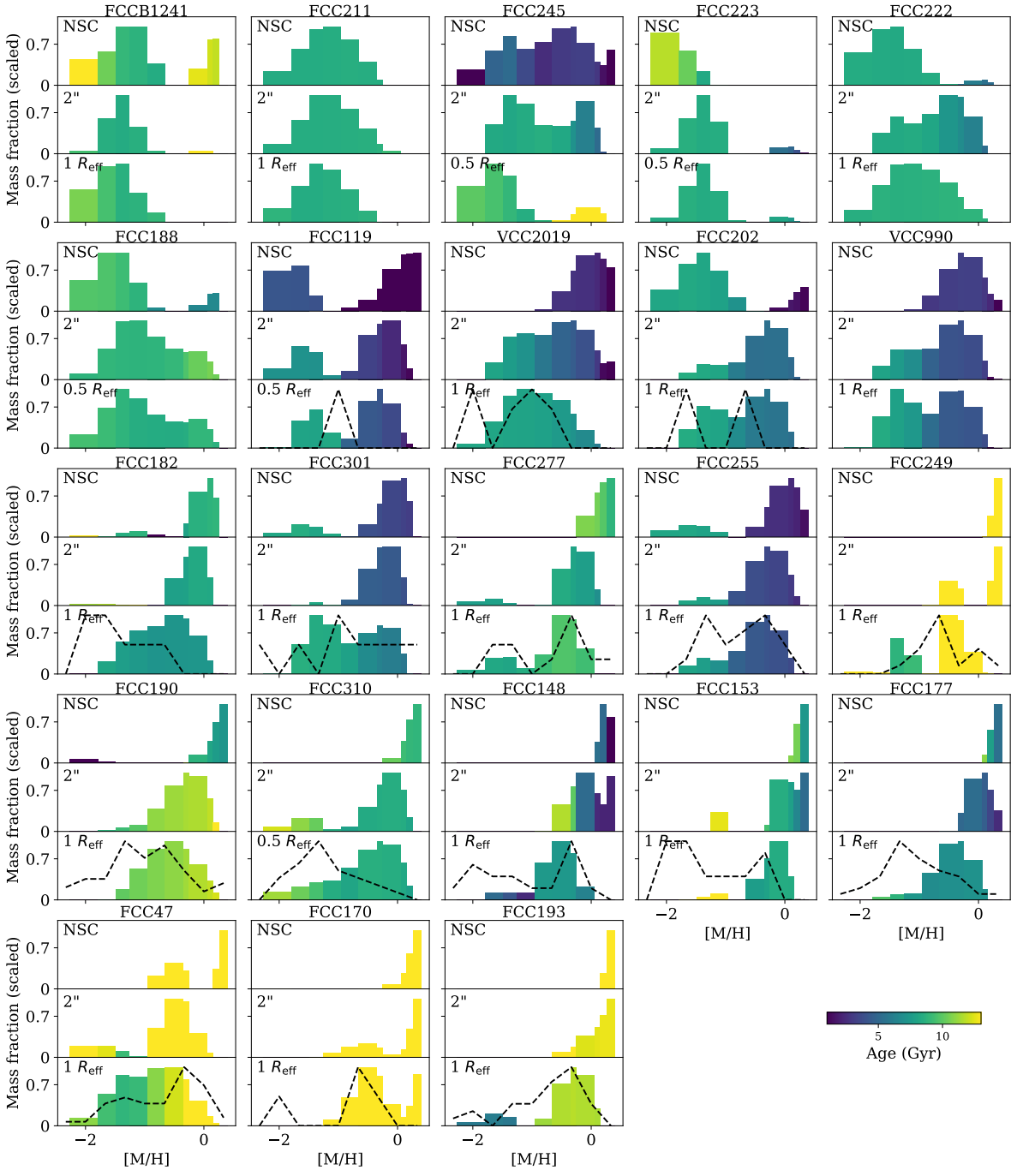

Figure 5.4.: As in Fig. 5.3 but for metallicity distributions. Dotted lines show the expected GC metallicity distributions. To obtain those, we applied the GC CZR from the F3D GCs (Sect. 4.4.4) to photometric GC catalogues from Jordán et al. (2009, 2015). For visualisation, the GC distributions are normalised to match the peak height for the galaxy mass fractions.

5.3.3 Metallicity distributions

The metallicity distributions for the NSCs and their host galaxies (at 2″ and 1 $R_{\rm eff}$ where available) are shown in Fig. 5.4, coloured by the mean age per metallicity bin. The distributions are less smooth than the SFHs in Fig. 5.3 because the E-MILES SSP models give only 12 different metallicities. In general, a trend with mass is seen in the sense that the mean metallicity increases with mass of both the host and NSC, as will be discussed in more detail in Sect. 5.3.4.

In the GC accretion scenario of NSC formation, the formed NSC should reflect the metallicity distribution of the accreted GCs. Although these GCs (or younger star clusters) might have been different from today's GC population, we also show the metallicity distributions of GCs in Fig. 5.4 for a qualitative comparison. Those are obtained for all galaxies that have photometric GC catalogues from the ACSFCS or ACSVCS available (Jordán et al. 2009, 2015). We only use GCs with projected distances to the galaxy centres $< 1.0\ R_{\rm eff}$. The catalogues provide accurate $(g-z)$ colours that we translated to metallicities using the CZR of the F3D GCs (Sect. 4.4.4). For visualisation purposes, we normalised the GC metallicity distributions to match the peak height of the galaxy metallicity mass fractions. Unfortunately, most of the dwarf galaxies have no photometric GC catalogues available.

For low-mass galaxies, we found significant mass fractions at low metallicities, while the NSCs of the high-mass galaxies are dominated by high metallicities. Comparing the GC and galaxy metallicity distributions shows a good match at high metallicities, but most galaxy metallicity distributions do not extend to low metallicities and are on average more metal-rich than the GCs. This is not surprising as most massive galaxies show two populations of GCs that differ in their metallicity with a metal-rich population that was formed in-situ in the host, and a metal-poor population stemming from accreted dwarf galaxies (e.g. Harris 1991; Peng et al. 2006; Lamers et al. 2017; Beasley 2020 or Sect. 4.5.2).

We found several cases where the NSC is significantly more metal-rich than the most metal-rich GCs observed today, for example in FCC 170, FCC 193, and FCC 249. This could indicate that these NSCs were either formed from in-situ star formation, or out of a population of massive, metal-rich star clusters that are no longer present in the central regions of these galaxies. In other cases, the GC metallicities could naturally explain the metallicities found in the NSC, for example in FCC 202 and FCC 255. In these cases, the NSCs are significantly younger (< 7 Gyr) than typical GCs (> 8 Gyr, Puzia et al. 2005), which then would require additional in-situ star formation or accretion of young massive star clusters. Unfortunately, we do not have reliable age measurements of a large sample of GCs from these galaxies. The dwarf galaxies are the most likely hosts of NSCs formed through GCs due to their low metallicities and old ages.

5.3.4 Mass-metallicity relation

We show the mass-metallicity plane of the NSCs and the host galaxies (at 1.0 $R_{\rm eff}$ where available) in Fig. 5.5. For comparison, we added the F3D GCs (Chapt. 4) which are clearly separated from the host galaxies in the mass-metallicity plane. While the galaxies follow a clear MZR (see e.g. Gallazzi et al. 2005; Kirby et al. 2013), the GCs only show a large

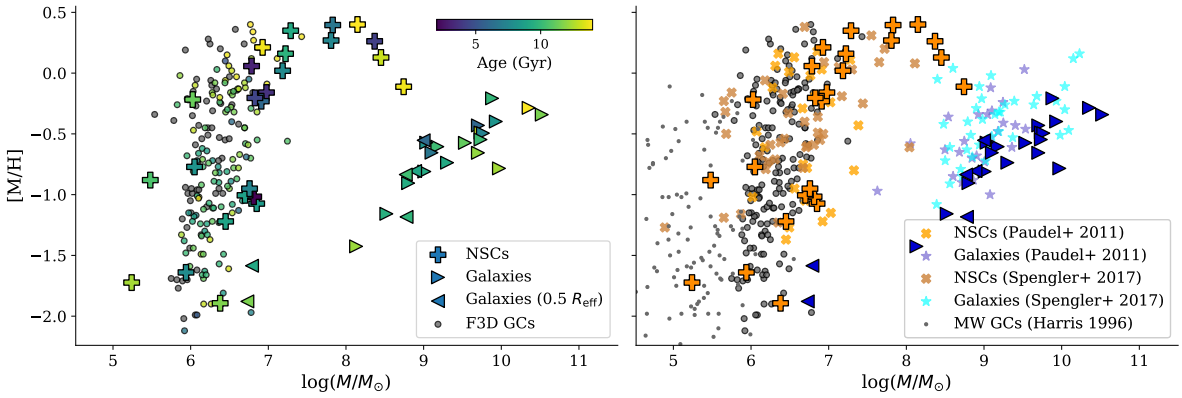

Figure 5.5.: Mass-metallicity plane. Both panels show mass and metallicity for the host galaxies of our sample at 1.0 $R_{\rm eff}$ where available (rightward triangles, otherwise leftward triangles), NSCs (plus symbols) and GCs (coloured circles, from Chapt. 4, Fahrion et al. 2020a). *Left*: Components are colour-coded by the mean age, inferred from full spectrum fitting. *Right*: We include literature NSCs (orange and brown crosses) and their hosts galaxies (bright blue and purple stars) from Paudel et al. (2011) and Spengler et al. (2017), and MW GCs (small grey dots) from Harris (1996).

scatter in both parameters (see also Zhang et al. 2018). The NSCs, however, show a different behaviour. For $M_{\rm NSC} < 10^7 M_\odot$, the NSCs lie in the same region as GCs, covering a large spread in metallicities. Higher mass NSCs ($M_{\rm NSC} > 10^7 M_\odot$) are exclusively metal-rich, and exceed the metallicity of galaxies with similar masses by 1.5 dex. Interestingly, there are a few high-mass GCs ($M_{\rm GC} \sim 10^7 M_\odot$) that also seem to follow the trend of these massive NSCs. Those could be candidates of UCDs (Hilker et al. 1999a; Drinkwater et al. 2000).

The left panel of Fig. 5.5 shows the different components colour-coded by their ages. In the massive NSCs ($M_{\rm NSC} \gtrsim 10^7 M_\odot$), we find either extremely old ($>$ 10 Gyr) or young ages ($<$ 5 Gyr), while the low-mass NSCs ($M_{\rm NSC} < 5 \times 10^6 M_\odot$) are generally old (8 - 10 Gyr), comparable to the ages of GCs. All galaxies have mean ages $>$ 5 Gyr at 1.0 $R_{\rm eff}$ as is expected since our sample consists of ETGs which have ceased star formation globally. Nonetheless, those can still show star formation in their centres (e.g. Richtler et al. 2020).

The right panel in Fig. 5.5 shows a comparison of our sample to literature values. We show NSCs and their hosts from Paudel et al. (2011) and Spengler et al. (2017), and MW GCs from (Harris 1996, catalogue version 2010). The MW GCs extend our F3D GC sample to lower masses that are not accessible with the current data due to the intrinsic brightness of these low-mass GCs at distances of the Fornax galaxy cluster. Despite the different mass ranges, they span roughly the same range in metallicity, although even metal-rich bulge GCs only reach [Fe/H] ~ -0.5 to -0.15 dex (Muñoz et al. 2017, 2018, 2020) and thus very metal-rich GCs are lacking in the MW.

The literature NSCs cover comparable ranges in masses and metallicities as our sample. They show a similar trend with increasing NSC mass: there are only a few metal-poor NSCs with masses $> 10^7 M_\odot$, while the low-mass NSCs cover the mass-metallicity space of the GCs. The literature galaxy sample spans roughly the same ranges of masses and metallicities as the galaxies studied here, but our sample extends to lower galaxy masses, which might reflect in the lack of very metal-poor NSCs in the literature sample.

5.3.5 Constraining NSC formation from stellar populations

In this section we take the results presented above together to draw conclusions for individual galaxies, grouped by similar NSC properties. We focus on the radial metallicity profiles (Fig. 5.2), the SFHs, and metallicity distributions (Figs. 5.3, 5.4). The results are summarised in Fig. 5.6. With our stellar population analysis, we can compare the ages and metallicities of the unresolved NSCs to the host galaxies and the observed GCs. While we can identify accretion signatures of old, metal-poor GCs, for young and metal-rich populations we cannot discern between in-situ star formation happening directly in the NSC or in central star clusters that were rapidly accreted into the NSC.

Most massive galaxies

The most massive galaxies in our sample ($M_{\rm gal} > 10^{10} M_{\odot}$), FCC 47, FCC 170, and FCC 193, also host the most massive NSCs ($> 10^{8} M_{\odot}$). Their NSCs are significantly more metal-rich than the hosts and any GCs, and are older than the host galaxies. This could be explained by an inside-out formation scenario, where the central regions of the galaxies assembled first and were rapidly enriched due to efficient star formation, while enrichment in the outskirts was slower and less efficient. In Chapt. 2, we argued that the old age and high metallicity of the NSC in FCC 47 indicates an efficient formation at early times. Similar arguments were made in the detailed analysis of FCC 170 by Pinna et al. (2019a) using the same F3D MUSE data which showed that FCC 170 assembled very rapidly and efficiently at early times (see also Poci et al. 2021). Their SFH of the central region of FCC 170 is similar to the one presented here. Alternatively, the high metallicity could be a result of the infall and merger of a population of young and metal-rich massive star clusters.

The high NSC masses also indicate formation from efficient central star formation rather than from ancient GCs as their high masses ($M_{\rm NSC} > 10^{8} M_{\odot}$) would require the accretion of hundreds of metal-rich star clusters with masses $\gtrsim 10^{6} M_{\odot}$ – already close to the cut-off mass typically observed for young massive star clusters in highly interacting galaxies (Adamo et al. 2020). An in-situ origin is further supported by the significant rotation in the NSCs of FCC 170 and FCC 47 found based on high angular resolution IFS with SINFONI (Lyubenova & Tsatsi 2019). Chapter 2 showed that the NSC of FCC 47 is a kinematically decoupled component, which likely indicates a major merger that has shaped the kinematic properties of this NSC. A similar merger could also explain the slightly younger, more metal-poor populations we found in the outskirts of FCC 47 and FCC 193, which could be accreted material from a lower mass galaxy.

Lower-mass edge-on S0 galaxies

FCC 153 and FCC 177 are edge-on S0 galaxies like FCC 170, but at significantly lower galaxy mass (see e.g. Pinna et al. 2019b; Poci et al. 2021 for a detailed analysis using the F3D MUSE data). Pinna et al. (2019b) and the Voronoi binned radial profiles presented in this work generally find young ages toward the galaxy centres. However, our background-subtracted NSC spectra find the NSCs to be older than their immediate surrounding although at a

similar high metallicity, but with a minor young stellar population. The NSCs are more metal-rich than any GCs found in the galaxies. The high NSC metallicity and the presence of young stars indicate a large contribution from in-situ star formation to their build-up. This star formation might have happened directly in the NSCs or in clustered star formation in the central regions of these galaxies.

Galaxies with young central populations

FCC 119 and FCC 148 are the only two sample galaxies that show the presence of ionised gas in their NSC as traced by the presence of Hα, Hβ, [NII], [SII], and [OIII] lines in the MUSE spectra (see also the emission line maps in Iodice et al. 2019a). Our analysis uncovered young stellar populations (< 3 Gyr) in both NSCs, while their host stellar bodies are older. The same was found for VCC 2019 although without the clear presence of ionised gas. This ongoing or recent star formation is a clear sign of in-situ star formation building up the NSCs. However, FCC 119 also shows an older, more metal-poor component in its NSC and is on average more metal-poor than the host galaxy. This drop in metallicity could indicate additional accretion of metal-poor GCs from the galaxy outskirts to the centre.

FCC 301 and VCC 990 have similar galaxy ($M_{\rm gal} \sim 10^9 M_\odot$) and NSC masses ($M_{\rm NSC} \sim 7 \times 10^6 M_\odot$), and their stellar population properties are also similar to that of FCC 255 which is slightly more massive. In these three galaxies, the NSCs are younger and more metal-rich than their hosts, their SFHs show a single peak at age ~ 3 Gyr. The young ages and high metallicities indicate NSC formation dominated by in-situ star formation either in recently accreted young massive star clusters or directly in the NSC.

Galaxies with old, metal-rich NSCs

FCC 190, FCC 310, FCC 277, and FCC 249 have similar stellar masses ($\sim 3 - 5 \times 10^9 M_\odot$). Their NSCs are more metal-rich than the hosts and any GCs. The NSCs and galaxies are characterised by old stellar populations (> 10 Gyr) and FCC 190 and FCC 277 show a minor young, metal-rich population in its NSC. The high metallicities of the NSCs as well as the extended SFHs in FCC 190, FCC 310, and FCC 277 are in agreement with formation from multiple episodes of in-situ star formation or the repeated accretion of young star clusters.

Based on the presence of a kinematically cold component found through Schwarzschild dynamical modelling of high spatial resolution SINFONI data of FCC 277, Lyubenova et al. (2013) came to conclusion that gas infall likely played an important role in the formation of the NSC, hence further supporting our conclusions from the stellar population properties. However, they also identified a minor population with counter-rotating orbits that indicated additional contribution from a compact object that has merged with the NSC. Consequently, this galaxy is an example where the stellar population properties indicate that the formation of the NSC was dominated by in-situ star formation, but additional GC merging (or merging of young star clusters) is required to also explain the complex kinematics of this NSC. This illustrates, that while stellar population analysis is crucial to identify the major NSC formation scenario, detailed dynamical modelling is required to fully unveil the formation history of a NSC.

Galaxies with evidence of both NSC formation scenarios

The radial metallicity profiles of FCC 188, FCC 202, FCC 222, and FCC 245 all clearly show a drop in metallicity in the galaxy centres and their NSCs are on average more metal-poor than the host galaxies. This drop in metallicity is indicating formation from the infall of metal-poor GCs, but the SFHs of these galaxies all show a secondary component with a higher metallicity and significantly younger age (also seen in FCC 119). This metal-rich, young population can be explained by additional in-situ star formation or the accretion of a young star cluster. The NSCs of these galaxies are therefore examples of NSCs were both formation channels are acting together.

FCC 182 is an especially intriguing case. The NSC has roughly the same metallicity as the galaxy at 2″, but the radial metallicity profile of FCC 182 reveals that the NSC still constitutes a dip in the metallicity profile. This suggests formation from in-spiral of one or two metal-poor GCs to the centre which could also explain the low NSC mass ($M_{\rm NSC} \sim 10^6 M_\odot$). In contrast, the GC population of FCC 182 today does not exhibit GCs that reach the metallicity of the NSC and the extended NSC SFH would rather indicate formation from prolonged in-situ star formation or the accretion of multiple star clusters of different ages. However, also the SFH shows a minor old, metal-poor component in addition to higher metallicities and younger ages. To fully explain the radial metallicity profile and the complex SFH, a likely contribution from both NSC formation channels is required.

Dwarf galaxies with old, metal-poor NSCs

FCC 215, FCC 211, and FCC 223 are dwarf galaxies in which the radial metallicity profiles reveal a drop in metallicity in the centre and the NSCs are significantly more metal-poor than their hosts. These three galaxies are prime candidates for NSC formation dominated by the accretion of old and metal-poor GCs (see also Chapt. 3).

FCCB 1241 and FCC 227 have the least massive NSCs in our sample with stellar masses $M_{\rm NSC} < 10^6 M_\odot$. We found that the NSC of FCCB 1241 is on average more metal-rich than the host galaxy, but also shows an old, metal-poor component, indicating a mixture of both NSC formation channels acting in its growth. The S/N in the NSC and galaxy spectra of FCC 227 do not allow to determine a reliable metallicity profile, but the mass, age, and metallicity of the NSCs are fully in agreement with typical GCs.

5.3.6 Trend with galaxy and nuclear star cluster masses

Figure 5.6 summarises the discussion in the previous section. It shows the NSC-galaxy mass distribution of our sample, and the different symbols indicate the identified dominant NSC formation channel. We group the galaxies into three different categories: formation from the inspiral of old, metal-poor GCs as evident from metal-poor populations in the NSC, formation as a result of central star formation as well as a mixed scenario that invokes both channels. We note that central star formation can refer to both the classical in-situ formation channel, where the star formation results from accreted gas at the NSC position, as well as to clustered star formation in the central regions of the galaxies. The two nucleated dwarf

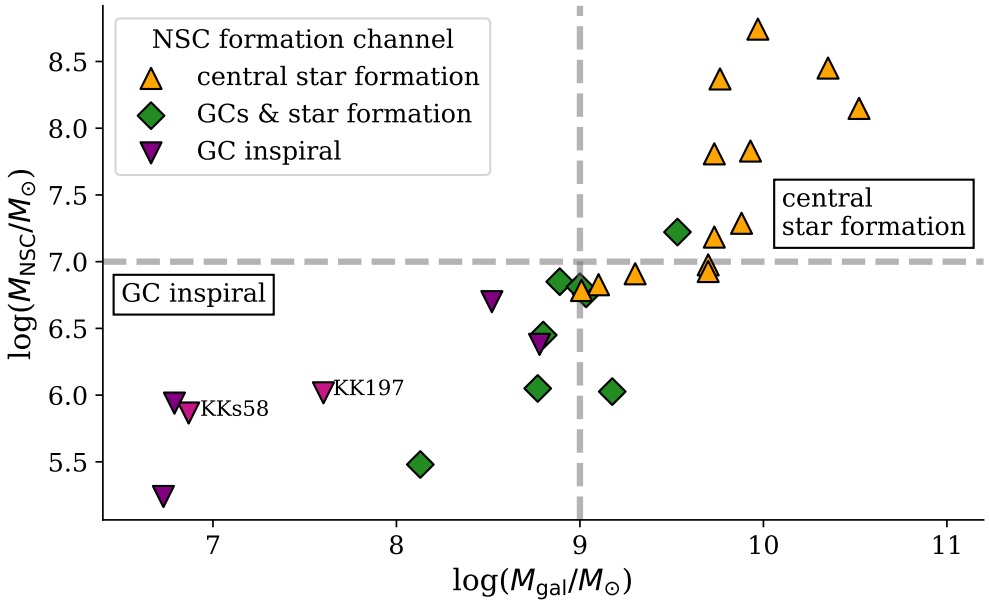

Figure 5.6.: NSC mass versus galaxy mass for our sample. The different colours and symbols refer to the identified dominant NSC formation channel. We differentiate between dominated by central in-situ star formation either directly at the NSC or in central star clusters that were rapidly accreted as determined from high metallicities or young ages (orange), formation through GC accretion as evident from central declines in metallicity (purple), and galaxies in which both channels are required to explain the NSC properties (green). We included KKs 58 and KK 197, the two nucleated dwarf galaxies with NSCs formed through GC accretion discussed in Chapt. 3 (Fahrion et al. 2020c). The dashed lines indicate the transition NSC and galaxy masses where the dominant channel changes.

galaxies KK 197 and KKs 58 that were analysed in Chapt. 3 are also included. Based on the low metallicity of their NSCs in comparison to their hosts their NSCs were likely formed via the inspiral of a few GCs to the centre.

Figure 5.6 reveals a trend in dominant NSC formation channel both with galaxy and NSC mass. At the lowest galaxy and NSC masses, we found that NSCs predominantly form via the infall of GCs, while at the highest galaxy and NSC masses NSC formation is dominated by central star formation (either in young star clusters close to the centre or in the NSC directly). At intermediate masses ($M_{gal} \sim 10^9 M_\odot$, $M_{NSC} \sim 5 \times 10^6$), we find galaxies in which either formation channel is responsible for the NSC properties observed today, as well as several cases in which both channels are acting together.

5.4 Discussion

In the following we compare our results to literature values. We further discuss the complexity we find in NSC properties and the connection to NSC formation.

5.4.1 Comparison with literature values

Iodice et al. (2019b) presented luminosity-weighted stellar population properties from line-strength measurements for the F3D galaxies. Their Table 3 lists the mean age, metallicity, and light-element abundance ratio within the central region ($R < 0.5\,R_{\rm eff}$), in a similar region as our spectra extracted at 0.5 $R_{\rm eff}$. We find generally a good match between this work and the results from Iodice et al. (2019b) despite the different spatial extraction regions and measurement methods.

The Fornax dwarf galaxies in our sample were previously analysed in Johnston et al. (2020). That work uses BUDDI (Johnston et al. 2017), a tool to decompose a MUSE datacube into different spatial components describing the NSC and the host galaxy, similar to our approach. While we used IMFIT to build a model only to estimate the contribution of the underlying galaxy light to the NSC spectrum, Johnston et al. (2020) used their modelling technique to derive model spectra of every component by considering the MUSE cubes as a series of narrow-band images. However, because each component is described by a predefined function, for example a Sérsic profile, there is only one model spectrum per component and thus internal radial stellar population gradients cannot be represented.

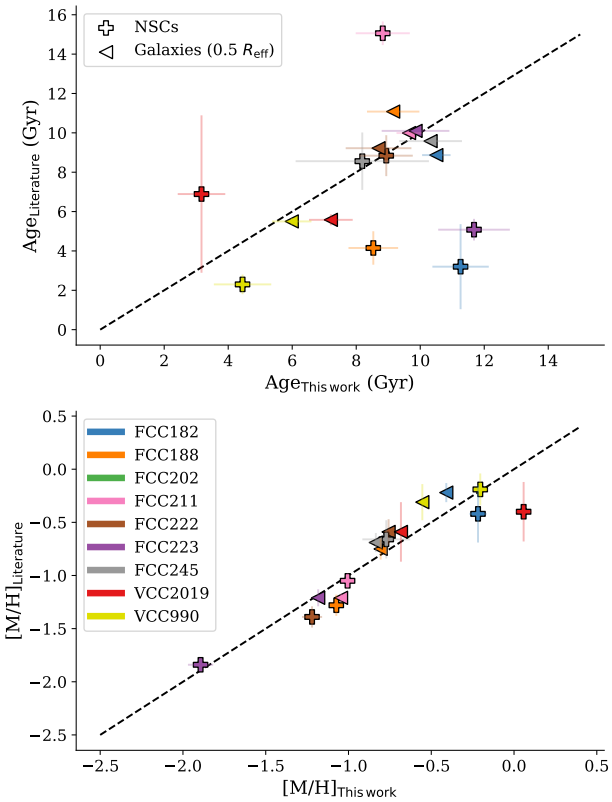

Figure 5.7.: Comparison between the NSC (crosses) and host galaxy (triangles, at 0.5 $R_{\rm eff}$) age (*top*) and metallicity (*bottom*) from the literature and this work. VCC 990 was analysed by Paudel et al. (2011), VCC 2019 by Spengler et al. (2017), and the other galaxies by Johnston et al. (2020).

In Fig. 5.7, we plot the NSC and galaxy ages and metallicities for the galaxies that were studied both here and by Johnston et al. (2020) with full spectral fitting. We also add the Virgo galaxies VCC 990, which was analysed with spectroscopy and Lick line-strength indices in Paudel et al. (2011), and VCC 2019, which was among the galaxies studied with broad-band photometry by Spengler et al. (2017). The metallicities agree well between our work and the literature. The ages show a larger scatter, but in general the overall trend (young versus old) is recovered. The only exceptions are the NSCs of FCC 182 and FCC 223, which we find to be significantly older than estimated by Johnston et al. (2020). The reason for this discrepancy is unknown, but could be caused by the different approaches to extract the stellar population properties. Johnston et al. (2020) also used PPXF with regularisation and the MILES SSP model library, but with a different grid of models based on the so-called Padova isochrones (Girardi et al. 2000). The scatter

in ages might also reflect the well-known difficulty of deriving accurate stellar ages from integrated spectroscopy (e.g. Usher et al. 2019). Further, the wavelength coverage of MUSE instrument is lacking many age-sensitive absorption features. We note that the line-strength measurements presented in Iodice et al. (2019b) also found an old age for FCC 182 of 12.6 Gyr in the central region of the galaxy.

5.4.2 Complexity in nuclear star clusters

NSCs are known to be complex stellar systems that can show a large diversity of characteristics. Some NSCs show non-spherical density distributions with flattened structures (Böker et al. 2002), and many show multiple stellar populations (Walcher et al. 2006; Lyubenova et al. 2013; Kacharov et al. 2018), often with significant contributions from young stellar populations (Rossa et al. 2006; Paudel et al. 2011). This complexity is also often seen in the internal kinematics of NSCs as some show significant rotation and distinct dynamical structures (Seth et al. 2008a, 2010; Lyubenova et al. 2013; Lyubenova & Tsatsi 2019).

In this work, we focused on the global stellar population properties of NSCs and found a large variety in ages, metallicities, SFHs, and metallicity distributions. Many of the studied NSCs show extended SFHs or multiple populations as also observed in other studies. For example, Kacharov et al. (2018) studied the NSC of six nearby galaxies ($M_{\rm gal} \sim 2{-}8{\times}10^9 M_\odot$) with high resolution spectroscopy. They found prolonged NSC SFHs which include young stars. This is in line with several other studies that have found NSCs of dEs ($M_{\rm gal} \gtrsim 10^8 M_\odot$) to be generally younger than their host galaxy (Paudel et al. 2011; Guérou et al. 2015; Paudel & Yoon 2020). In our sample, we found NSCs of dwarf galaxies both older and younger than the host galaxies, but many also share the age of their host. We note that our sample extends to lower galaxy masses than those of Paudel et al. (2011) or Spengler et al. (2017).

At the lowest galaxy and NSC masses studied here, we found that the NSCs share many similarities with GCs in their low masses, mean low metallicities, and old ages. This is a natural consequence if those NSCs were formed from GCs, but has implications for identifying remnant NSCs of disrupted satellite galaxies that might be hiding in the rich GC populations of massive galaxies (Pfeffer et al. 2014, 2016), or even in the GC population of the MW (e.g. Sakari et al. 2021; Pfeffer et al. 2021). Such an origin was proposed, for example, for ωCentauri, the most massive GC in the MW (Lee et al. 1999; Hilker & Richtler 2000; Bekki & Freeman 2003; van de Ven et al. 2006; Villanova et al. 2014) although the most compelling case has been made for M 54, which is located at the centre of the Sagittarius dwarf galaxy and shows a large spread in iron abundance as well as an extended SFH (Ibata et al. 1997; Bellazzini et al. 2008; Sills et al. 2019; Alfaro-Cuello et al. 2019).

5.4.3 Diversity in NSC formation channels

Based on the shape of the nucleation fraction function with galaxy mass which shows a peak at $M_{\rm gal} \sim 10^9 M_\odot$ and results from stellar populations, Neumayer et al. (2020) suggested a transition of the dominant NSC formation channel from GC accretion to in-situ star formation with increasing galaxy mass.

In this work, we confronted this suggestion with observations of galaxies that span a broad range in both NSC and galaxy masses and that are studied in a homogeneous fashion. We found that many of the studied NSCs exhibit complex SFHs and multiple populations of different metallicities. All NSCs residing in galaxies more massive than $10^9 M_\odot$ are significantly more metal-rich than their host galaxy, indicating formation from efficient central star formation directly at the bottom of the galactic potential well or from clustered star formation in the central regions. In contrast, at the lowest galaxy masses, the NSCs appear to be have formed through the accretion of a few metal-poor GCs. Those dwarf galaxies exhibit radial metallicity profiles with clear drops in metallicity at the galaxy centre. At intermediate galaxy and NSC masses, we found several cases of NSC SFHs showing evidence of both channels contributing to the NSC formation.

Underlying this trend with galaxy mass, we find a transition of the dominant NSC formation channel with NSC mass as evident in Fig. 5.5. For masses $M_{\rm NSC} > 10^7 M_\odot$, the NSCs clearly separate from GCs in their mass, metallicity, and age diversity. The low-mass NSCs in our sample are overall old ($\gtrsim 7$ Gyr), but span a large range in metallicity – consistent with GCs of similar mass. Conversely, more massive NSCs can also show very young stellar populations. Around NSC masses of $\sim 10^7 M_\odot$, the largest diversity in age and metallicity is found. This transition mass $\sim 10^7 M_\odot$ is probably connected to a possible mass limit of GC formation. As Norris et al. (2019) argue, there appears to be an upper mass limit of the ancient star cluster population around $\sim 5 \times 10^7 M_\odot$. As star clusters of this mass should be scarce due to their position in the high-mass tail of the GC mass function, this maximum mass would also suggest a mass limit for NSCs formed solely from GCs because more massive NSCs would require the merger of hundreds of GCs.

In summary, as Fig. 5.6 illustrates, we indeed find a transition of the dominant NSC formation channel with galaxy and NSC mass: while the short dynamical friction timescales in low-mass galaxies can form low-mass NSCs from the accretion of a few ancient metal-poor GCs, central in-situ star formation or the accretion of young and enriched star clusters is responsible for the mass build-up in the most massive NSCs. At intermediate masses, both channels can contribute.

Such a transition of dominant NSC formation channel is also likely reflected in the galaxy-NSC mass relation. While GC accretion can build the low-mass NSCs of dwarf galaxies, this process is not efficient enough to reach the high NSC masses found in more massive galaxies. In those, in-situ star formation appears to be effective in building massive NSCs, often already at early times. The large diversity in SFHs at high NSC and galaxy masses suggests that NSC formation in these systems is correlated with the evolutionary history of the galaxy, for example due to the availability of gas or the occurrence of major mergers which might prevent GC inspiral (Leung et al. 2020), but can trigger central star formation (Schödel et al. 2020).

5.5 Conclusion

In this chapter, we presented a stellar population analysis of 25 nucleated early-type and dwarf galaxies mostly in the Fornax cluster to derive the most likely NSC formation path.

We extracted the mean ages and metallicities as well as SFHs and metallicity distributions and analysed those properties with focus on the NSC formation. Our main results are:

- We found a large diversity of NSC SFHs. The NSCs of massive galaxies are metal-rich, and we found both very old NSCs and NSCs with ongoing or recent in-situ star formation. At intermediate galaxy masses ($M_{\rm gal} \sim 10^9 M_\odot$), the diversity in SFHs even increases. We found cases of single-peaked SFHs and SFHs with multiple bursts. Towards the lowest galaxy masses ($M_{\rm gal} < 10^9 M_\odot$), the NSCs tend to be as old as their host galaxies.
- Radial metallicity profiles reveal that the NSCs of massive galaxies ($M_{\rm gal} > 10^9 M_\odot$) are more metal-rich than their host galaxy. In contrast, at lower masses, several of the studied galaxies show a clear drop in metallicity at the location of the NSC.
- Putting NSCs, GCs, and galaxies on a common mass-metallicity plane, we found that the population of massive NSCs ($> 10^7 M_\odot$) is distinct from the less massive NSCs, which occupy the same region in the mass-metallicity plane as GCs. The massive NSCs, however, branch off in mass at exclusively high metallicities and can show either extremely old or young populations.
- Our results suggest different formation paths of high and low-mass NSCs to explain their different properties. The high masses and high metallicities of the massive NSCs found in massive galaxies suggest formation from in-situ star formation or the accretion of young enriched star clusters. In contrast, the low NSC metallicities found in the low-mass galaxies of our sample are likely the result of infalling metal-poor GCs forming these NSCs. Furthermore, we find several galaxies where both channels are required to explain the properties of their NSCs.
- We found clear evidence for a shift of the dominant NSC formation channel from GC accretion at low NSC and galaxy masses towards central in-situ star formation forming the most massive NSCs in our sample. The transition appears to happen for NSC masses with $M_{\rm NSC} \sim 10^7 M_\odot$ and galaxies with masses $M_{\rm gal} \sim 10^9 M_\odot$.

Our work shows that NSCs are diverse objects. Some appear as simple stellar systems that are indistinguishable from typical GCs in their mass and stellar populations, while others are complex objects with extended SFHs and metallicity distributions. This diversity in properties is most likely connected to how their mass assembled. A single formation scenario that explains the formation of all NSCs is incompatible with our results.

It's still magic even if you know how it's done.

Terry Pratchett, A Hat Full of Sky

6 | Semi-analytical modelling of nuclear star cluster formation

The previous chapters have presented how NSC formation can be constrained in individual galaxies using MUSE. These observational results have shown that there appears to be a trend in the dominant NSC formation channel with both NSC and galaxy mass. In this chapter, I aim to disentangle the relative contribution of the two NSC formation modes in individual galaxies and study their dependence on galactic properties from a more theoretical perspective. This requires models of NSC formation which can be tailored to individual host galaxies and are flexible enough to predict properties of the NSC and the galaxy's surviving star cluster population. This chapter presents a semi-analytical model of NSC formation to derive the mass fraction of individual NSCs formed via in-situ star formation ($f_{\rm in,\ NSC} = 1 - f_{\rm acc,\ NSC}$) in galaxies with stellar masses $M_{\rm gal} \sim 3 \times 10^7$ to $3 \times 10^{11} M_\odot$. This chapter is adapted from Fahrion et al. (2021, subm.).

6.1 The model

The model used in this chapter is based on the semi-analytical model of NSC formation that was presented in Leaman & van de Ven 2021 (subm., hereafter LvdV21). While other studies have attempted to model a large variety of complex physical processes involved in the mass build-up of NSCs, this model describes NSC formation solely via the accretion of GCs into the centre due to dynamical friction on a statistical basis. It uses results from $N-$body simulations to consider the orbital evolution of GCs that experience dynamical friction and simultaneously lose mass in the tidal field. Key to this model is the dependence of the host galaxy structure in modulating the efficiency of NSC formation, the mass budget of the NSCs, and surviving GCs. In the following, the main aspects of this model are presented, but we refer to LvdV21 for a detailed discussion of the derivation and the results.

6.1.1 Dynamical friction

A GC with a mass $M_{\rm GC}$ orbiting in the tidal field of a galaxy with velocity $v_{\rm GC}$ will experience dynamical friction (e.g. Chandrasekhar 1943) that leads to a change of its orbital momentum. The GC will decelerate and slowly spiral towards the centre. This can be described as:

$$\frac{dv_{\rm GC}}{dt} = \frac{-4\pi G^2 M_{\rm GC}\,\rho_b \ln(\Lambda) f(v_b < v_{\rm GC})}{v_{\rm GC}^2}, \tag{6.1}$$

where G is the gravitational constant, ρ_b is the background density, and $f(v_b < v_{\rm GC})$ is the distribution of background stars with velocity v_b less than $v_{\rm GC}$. This distribution is often assumed to follow a Maxwellian distribution:

$$f(v_b < v_{\rm GC}) = \mathrm{erf}\left(\frac{v_{\rm GC}}{\sqrt{2}\sigma_b}\right) - \frac{\sqrt{2}v_{\rm GC}}{\sqrt{\pi}\sigma_b}\exp\left(\frac{-v_{\rm GC}^2}{2\sigma_b^2}\right), \tag{6.2}$$

where erf is the error function. The expression $\ln(\Lambda)$ in Eq. 6.1 is the Coulomb logarithm that describes the ratio between minimum and maximum impact parameter $\ln(\Lambda) = \ln(b_{\rm max}/b_{\rm min})$. In the LdV20 model, this parameter is given following the description in Petts et al. (2015) that introduced radially varying impact parameters that match well with N–body simulations of dynamical friction:

$$\ln(\Lambda) = \ln\left(\frac{\min[\rho_b(R)/\Delta\rho_b(R), R]}{\max[R_{\rm GC}, GM_{\rm GC}/V_{\rm GC}^2]}\right). \tag{6.3}$$

Dynamical friction describes how the orbital distance of the GC will change over time:

$$R\frac{dR}{dt} = -\frac{GM_{\rm GC}\ln(\Lambda) f(v_b < v_{\rm GC})}{v_{\rm GC}}. \tag{6.4}$$

At the same time, the GC will experience mass loss due to tidal interactions (e.g. Spitzer 1940; Lamers et al. 2010) with a mass loss rate ξ:

$$\xi(R,t)dt = \frac{-t_{\rm rh}}{M_{\rm GC}}dM, \tag{6.5}$$

where $t_{\rm rh}$ is the relaxation time of the star cluster. The mass loss rate is time-dependent because of the internal evolution of the star cluster due stellar winds and supernovae feedback, but also has a radius dependence due to the external tidal field felt by the GC. In consequence, mass loss and dynamical friction will act simultaneously and the evolution of the GC mass and distance cannot be described analytical. For this reason, the LvdV21 model uses the fitting function given by Madrid et al. (2017) to connect both. They derive an analytical expression for the limiting mass $M_{\rm GC,\,lim}$ of a star cluster that is needed for inspiral to the centre without being disrupted in the tidal field. This limiting mass depends on the galaxy structure, but it scales roughly as $M_{\rm GC,\,lim} \propto R_{\rm gal}^2$. As described later, in application of the model we typically use observational constraints on $M_{\rm GC,\,lim}$.

6.1.2 NSC and GC system masses

From a total population of GCs, the model predicts a host galaxy-dependent limiting mass $M_{\rm GC,\,lim}$, above which GCs contribute to the NSC. An important aspect of the model is that it predicts not only the nucleation probability, but also gives limits and expectation values of the mass of the NSC and the mass of the surviving GC populations in individual galaxies.

Given an initial power-law mass function of star clusters with slope $\beta = -2$, the total mass in star clusters is (see Elmegreen 2018):

$$M_{\rm cl,\ total} = M_{\rm cl,\ max}\left[1 + \ln\left(\frac{M_{\rm cl,\ max}}{M_{\rm cl,\ min}}\right)\right], \tag{6.6}$$

where $M_{\rm cl,\ max}$ and $M_{\rm cl,\ min}$ are the most massive and least massive star cluster ever formed. This total mass in star clusters will be some fraction η of the total galaxy mass $M_{\rm gal}$:

$$M_{\rm cl,\ total} = \eta M_{\rm gal}. \tag{6.7}$$

GCs more massive than the limiting mass $M_{\rm GC,\ lim}$ will spiral to the centre to form the NSC. Therefore, using the same argument as for Eq. 6.6, the expected NSC mass from GC accretion is given as:

$$M_{\rm NSC,\ acc} = M_{\rm cl,\ max}\left[1 + \ln\left(\frac{M_{\rm cl,\ max}}{M_{\rm GC,\ lim}}\right)\right]. \tag{6.8}$$

Combining the previous equations, the NSC mass is given as:

$$M_{\rm NSC,\ acc} = \eta\, M_{\rm gal}\left[\frac{1 + \ln\left(\frac{M_{\rm cl,\ max}}{M_{\rm GC,\ lim}}\right)}{1 + \ln\left(\frac{M_{\rm cl,\ max}}{M_{\rm cl,\ min}}\right)}\right]. \tag{6.9}$$

For GCs less massive than the model threshold $M_{\rm GC,\ lim}$, a subset with masses below a dissolution mass $M_{\rm diss}$ will be destroyed in the tidal field, while the remainder will survive as the observed GCS. Therefore, the total mass of the GCS as observed today is expressed as:

$$M_{\rm GCS} = \eta\, M_{\rm gal} - M_{\rm NSC,\ acc} - M_{\rm diss}\left[1 + \ln\left(\frac{M_{\rm diss}}{M_{\rm cl,\ min}}\right)\right]. \tag{6.10}$$

We use these simultaneous predictions for the NSC and GCS masses to estimate the deficit in NSC mass predicted only from GC inspiral. For fixed host galaxy parameters, the fraction of the NSC mass assembled via in-situ formation $f_{\rm in,\ NSC}$ can therefore be estimated by scaling the predicted NSC mass ($M_{\rm NSC,\ acc}$) to the observed mass of individual NSCs:

$$M_{\rm NSC} = (1 - f_{\rm in,\ NSC})^{-1} M_{\rm NSC,\ acc}. \tag{6.11}$$

The model requires as input an estimate of the threshold mass for GC inspiral ($M_{\rm GC,\ lim}$) which can be predicted from the size and mass of the host galaxy in the LvdV21 model, or estimated based on the observed most massive surviving GC. LvdV21 showed that both methods agree within 0.26 dex, provided contaminating stripped UCDs are removed from the GC field population. The free parameters in the model are a normalisation factor for the fraction of stars forming in clusters (η), as well as estimates of the most massive, least massive, and typical dissolution mass for GCs. To estimate $f_{\rm in,\ NSC}$, the model predictions for $M_{\rm NSC}$ and $M_{\rm GCS}$ can be compared to the observed values in an individual galaxy.

We estimated the parameters for this model using EMCEE (Foreman-Mackey et al. 2013), a python implementation of the MCMC method that samples the posterior probability

distribution function. $M_{\rm NSC}$ and $M_{\rm GCS}$ are input variables that are fitted by the model and the remaining parameters are introduced as priors. For $M_{\rm gal}$ and $M_{\rm diss}$, we used Gaussian priors given by the observed stellar mass and the observed least massive, surviving GC ($M_{\rm GC,\ min}$) of an individual galaxy. The latter provides a crude observational estimate of the GC dissolution mass.

$M_{\rm GC,\ lim}$ can be derived from the LvdV21 model based on the galaxy mass and size - scaling as roughly $M_{\rm GC,\ lim} \propto R_{\rm gal}^2$. Alternatively, the most massive GC observed today ($M_{\rm GC,\ max}$), should give an observational limit to $M_{\rm GC,\ lim}$. Therefore, for galaxies with catalogues of individual GCs, we used $M_{\rm GC,\ max}$ as estimate for $M_{\rm GC,\ lim}$. For other galaxies, we used the theoretical prediction from the LvdV21 model. Possible effects relating to this choice of $M_{\rm GC,\ lim}$ are discussed in Sect. 6.4.1. For the other parameters, we adopted flat priors as listed in Table 6.1. We adopted conservative uncertainties on the stellar mass of the galaxy, NSC, and GCS of 0.3 dex (Mendel et al. 2014).

Table 6.1.: Priors used in the modelling.

Parameter	Description	Prior
$f_{\rm in,\ NSC}$	in-situ NSC mass fraction	(0.0, 1.0)
η	mass fraction in clusters	(10^{-5}, 0.5)
$M_{\rm gal}$	host stellar mass	measured
$M_{\rm cl,\ min}$	least massive GC ever	(10, 100)
$M_{\rm cl,\ max}$	most massive GC ever	($M_{\rm GC,\ max}$, $7.6 \times 10^7 M_\odot$)
$M_{\rm GC,\ lim}$	limiting mass for inspiral	$\sim M_{\rm GC,\ max}$ / LvdV21
$M_{\rm diss}$	dissolution mass limit	$\sim M_{\rm GC,\ min}$

Masses in $M_\odot$. Except for $f_{\rm in,\ NSC}$, the priors are implemented in logarithmic units.

Figure 6.1 shows an example resulting posterior distributions for FCC 47, an ETG in the Fornax cluster with a massive NSC ($M_{\rm NSC} \sim 7 \times 10^8 M_\odot$), studied in Chapt. 2. Parameters with Gaussian priors are not shown for simplicity. For FCC 47, the model finds a high $f_{\rm in,\ NSC} = 0.8$, in agreement with results from kinematic and stellar population analysis (Chapt. 2 or Fahrion et al. 2019b).

We note that our model is only applicable for galaxies with both NSCs and GCs. In nature, galaxies can be non-nucleated but still have a GCS. On the other hand, a few dwarf galaxies are known which only posses a single star cluster in their photometric centre (e.g. KKs58 from Chapt. 3 or DDO216; Leaman et al. 2020). Although there are various processes that can prohibit NSC formation or destroy NSCs, these are not included in our model and we refer to LvdV21 for a detailed discussion on how these relate to the nucleation fraction of galaxies.

6.2 Data

Our sample consists of galaxies from the Virgo and Fornax galaxy clusters, complemented by additional nucleated galaxies mainly in the Local Volume. The sample is illustrated in Fig. 6.2.

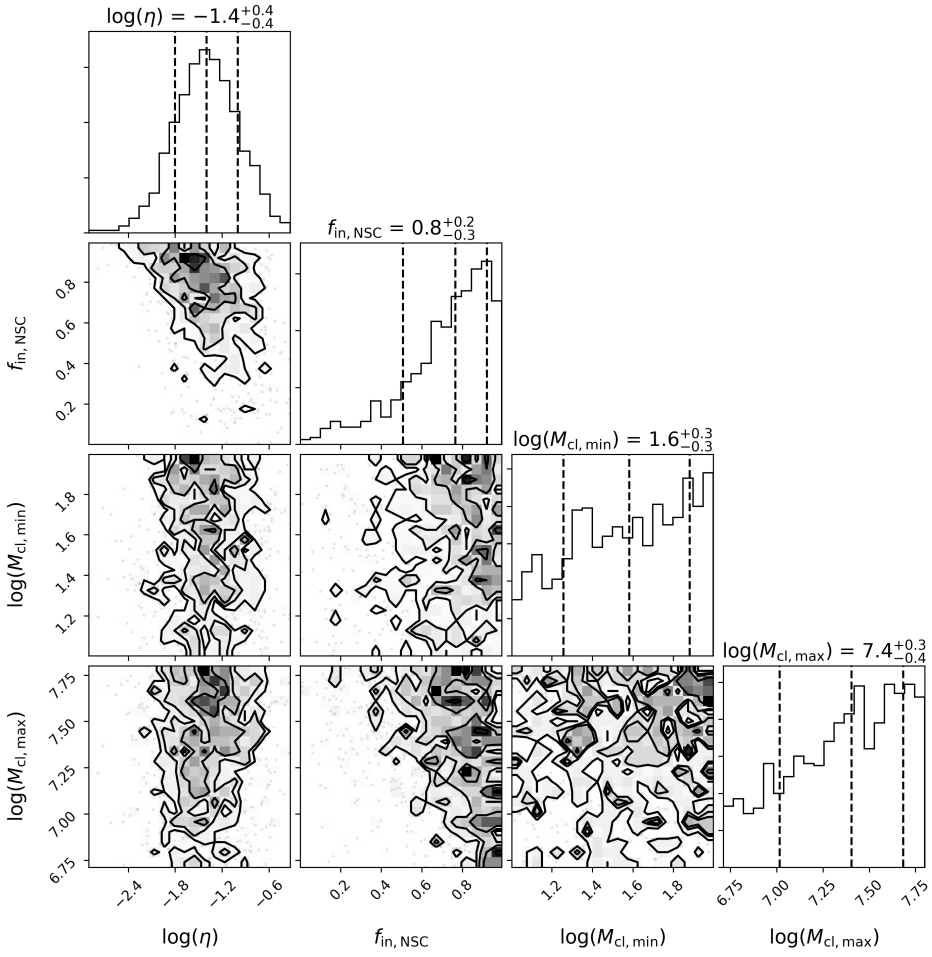

Figure 6.1.: Posterior distribution for the fit of FCC 47. We only show the parameters with flat priors. The other parameters follow Gaussian priors.

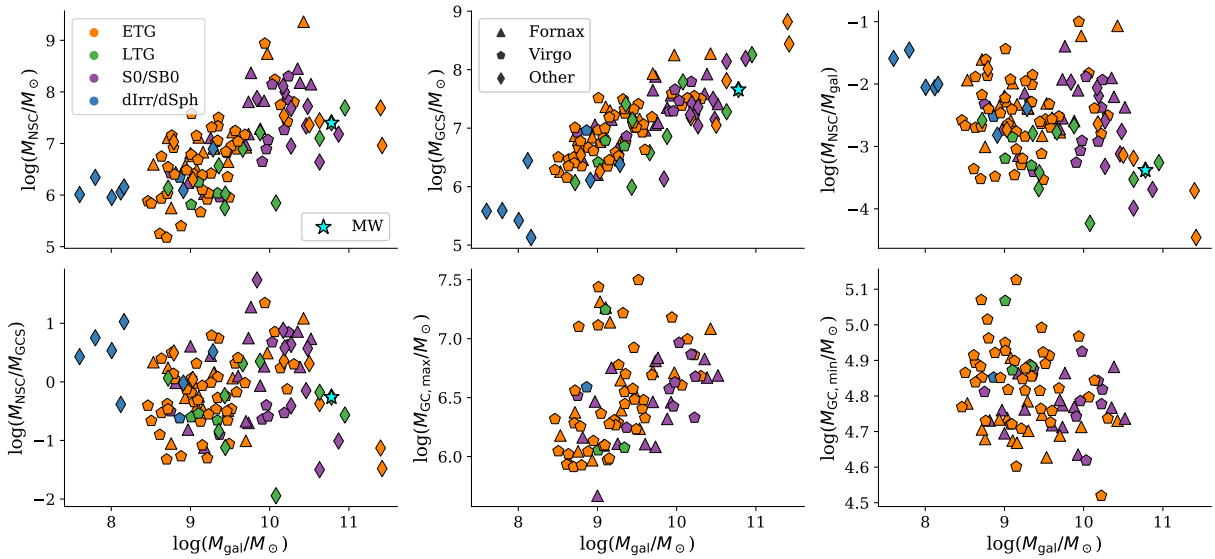

Figure 6.2.: Sample of nucleated galaxies used in this study. The symbol types differentiate between galaxies in Fornax (triangles), Virgo (hexagons), and other environments (diamonds), whereas the colours show the different galaxy types: ETGs (orange), LTGs (green), lenticular S0 and SB0 (purple), and dwarf irregulars and spheroidals (blue). The Fornax and Virgo sample only contain ETGs and lenticular galaxies. The NSC of the MW is shown in cyan. The different panels show the relation of NSC and GC system properties with the stellar mass of the host galaxy. For the Local Volume, $M_{\mathrm{GC,\,min}}$ and $M_{\mathrm{GC,\,max}}$ were not publically available.

6.2.1 ACSVCS and ACSFCS

The ACSVCS and ACSFCS (Côté et al. 2004; Jordán et al. 2007) are two surveys based on HST ACS data of galaxies with masses $> 10^8 M_\odot$ in the Virgo and Fornax galaxy cluster, respectively. The NSCs were described in Turner et al. (2012) (Fornax) and Côté et al. (2006) (Virgo) including their sizes, g and z-band magnitudes and colours. For every ACSFCS and ACSVCS galaxy, photometric GC catalogues were collected (Jordán et al. 2009, 2015). These give sizes, g and z-band magnitudes of photometric GC candidates in the ACSFCS and ACSVCS galaxies.

Photometric masses

Using the g and z-band magnitudes of the GCs, we inferred their metallicities using the CZR presented in Sect. 4.4.4 that was derived using a sample of spectroscopic GCs from the F3D project (Sarzi et al. 2018). From the metallicities and an assumed old age of 12 Gyr, we estimated the stellar masses using the photometric predictions of the E-MILES stellar population synthesis models (Vazdekis et al. 2016) that give the M/L in the ACS g-band. In this way, we derived the masses of the least massive and most massive GC ($M_{\mathrm{GC,\,min}}$ and $M_{\mathrm{GC,\,max}}$) in each galaxy directly from the catalogues. For the GCs, we limited the ACS catalogues to all candidates that have a probability of being a genuine GC $p\mathrm{GC} > 0.50$ to avoid contamination. As Fig. 6.2 shows, $M_{\mathrm{GC,\,max}}$ increases with galaxy mass, but there are a few outliers that could be UCDs. In Sect. 6.4 we discuss the choice of $M_{\mathrm{GC,\,max}}$.

NSCs often are chemically more complex than GCs and can also host young populations (Feldmeier-Krause et al. 2015), and thus might not follow the CZR. To determine their masses, we sampled the theoretical M/L based on their g and z-band magnitudes within uncertainties and allow random ages between 5 and 14 Gyr. The photometric uncertainties ($\sim$ 0.2 mag) govern the resulting mass distributions, but still allowed us to extract a mean photometric mass within $\sim$ 0.2 dex, above our default conservative limit of 0.3 dex that should also consider systematic uncertainties in stellar population synthesis models.

Total globular system mass

We determined the total mass of the GCS ($M_{\rm GCS}$) based on the GC luminosity functions given in Villegas et al. (2010). This work gives the mean and standard deviations in g and z bands of the GC luminosity distributions. Using the completeness-corrected total number of GCs $N_{\rm GCs}$ (from Peng et al. 2008; Liu et al. 2019), we created a mock GCS that is populated by drawing 1000 times $N_{\rm GCs}$ GCs from the distribution. A fraction $f_{\rm red}$ (from Peng et al. 2008; Liu et al. 2019) of them are assigned to be red GCs, the remaining ones are labeled as blue GCs. The total mass is then calculated by assigning a mean M/L to the red and blue GCs respectively, based on the CZR. We only differentiated into red and blue GCs for this mass calculation and do not consider a fraction which might be accreted from during the assembly of the host as the colour of a GC is not sufficient to determine its origin (Sect. 4.5). Alternatively, the individual GC candidates from the photometric catalogues can be summed up, but these are not completeness-corrected and can result in lower $M_{\rm GCS}$ by $\sim$ 0.2 dex. The completeness correction accounts for magnitude limits within the surveys, and spatial incompleteness of the ACS FOV.

6.2.2 Other galaxies

In addition to the ACSFCS and ACSVCS, we used a heterogeneous sample of 33 nucleated galaxies mainly in the Local Volume (D $<$ 15 Mpc), but five of those are also at larger distances. These have NSC properties presented in Georgiev et al. (2016); Pechetti et al. (2020); Neumayer et al. (2020), and the total GC system masses are from Harris et al. (2013), Forbes et al. (2018), and Spitler et al. (2008).

Fig. 6.2 illustrates that this composite sample differs from the ACSVCS and ACSFCS galaxies. At same galaxy mass, the Local Volume sample has lower NSC masses. This is caused in part by the larger number of LTGs in the local sample compared to Virgo and Fornax that are dominated by massive ETGs. LTGs galaxies are known to follow a shallower relation between NSC and host mass (Georgiev et al. 2016). However, the two most massive galaxies in the sample are classified as ETGs with NSCs that are less massive as the galaxy mass would suggest. One of those ETGs is NGC 4552 (M 89 or VCC 1632), an ETG in the Virgo cluster, in which Côté et al. (2004) did not report a stellar nucleus due to the presence of dust, but Lauer et al. (2005) reported a NSC with $M_{\rm NSC} = 9 \times 10^7 M_\odot$. NGC 4552 is known to also host a SMBH with $M_{\rm BH} = 5 \times 10^8 M_\odot$ (Gebhardt et al. 2003). The second massive ETG is IC 1459 with an even more massive SMBH of $M_{\rm BH} = 2 \times 10^9 M_\odot$ (Saglia

et al. 2016). The presence of these massive SMBHs could explain the lower NSC masses as SMBHs can inhibit NSC growth (e.g. Antonini 2013).

For this composite sample, masses of individual GCs are not available and hence we cannot use empirical estimates of the most massive and least massive observed GC for $M_{\rm GC,\,lim}$ and $M_{\rm diss}$, respectively. Therefore, we used the LvdV21 prediction for $M_{\rm GC,\,lim}$ based on the host galaxy structure. We approximated $M_{\rm diss}$ for these galaxies by fitting the $M_{\rm GC,\,min}$ - $M_{\rm gal}$ relation from the ACSFCS and ACSVCS with a log-linear function and assigning the Local Volume galaxies a randomly drawn value within this relation and its 1σ scatter. In the ACS galaxies, the mass of $M_{\rm GC,\,min}$ seems to decrease with increasing galaxy mass. This could be a sampling effect due to the larger number of GCs in the more massive galaxies causing the GC mass function to be better sampled. In general, $M_{\rm GC,\,min}$ only varies within ~ 0.4 dex from the lowest to the highest galaxy masses.

6.3 Results

We applied the model predictions described in Sect. 6.1 to measurements of $M_{\rm NSC}$ and $M_{\rm GCS}$ of 119 nucleated galaxies to infer $f_{\rm in,\,NSC}$. Figure 6.3 shows the resulting relations between $f_{\rm in,\,NSC}$ and the various input parameters. The errorbars refer to the 16th and 84th percentile of the posterior distributions (see Fig. 6.1).

6.3.1 Trend with NSC and GCS masses

As Fig. 6.3, upper left corner, illustrates, the values of $f_{\rm in,\,NSC}$ show an increase with the NSC mass $M_{\rm NSC}$. Our model predicts that low-mass NSCs are formed predominantly via the accretion of GCs ($f_{\rm in,\,NSC} \lesssim 0.50$), while the most massive NSCs (those with NSCs approximately $\sim 10\%$ of the host mass) reach $f_{\rm in,\,NSC} \gtrsim 0.90$. $f_{\rm in,\,NSC}$ shows no significant relation with $M_{\rm GCS}$ or $M_{\rm gal}$, suggesting that $f_{\rm in,\,NSC}$ is not strongly affected by potential incompleteness or contamination in the GC population. Galaxies with more massive GC systems relative to the stellar mass of the host favour low in-situ fractions as expected.

The tightest correlation is seen between $f_{\rm in,\,NSC}$ and the ratio between NSC and GCS mass, $\log(M_{\rm NSC}/M_{\rm GCS})$. Where both have comparable masses, the model predicts roughly equal contributions from both formation channels. This is likely a direct result of a single model threshold mass $M_{\rm GC,\,lim}$ sub-dividing a parent power-law distribution of GC masses. In systems where the NSC is significantly more massive than the GCS, high in-situ fractions are required to simultaneously reproduce the observed GC and NSC masses. At the same time, NSCs that only constitutes a fraction of the GCS, are found to have formed predominantly from the accretion of GCs. We show in Sect. 6.4.2, that even significant amounts of galactic scale accretion are not enough to drop the in-situ fractions for the NSCs in these systems significantly.

For convenience, we fitted the trends of $f_{\rm in,\,NSC}$ with $\log(M_{\rm NSC}/M_{\rm GCS})$ and $M_{\rm NSC}$ with a function of the form:

$$f_{\rm in,\,NSC} = \beta \tanh(x - \alpha) + (1 - \beta), \tag{6.12}$$

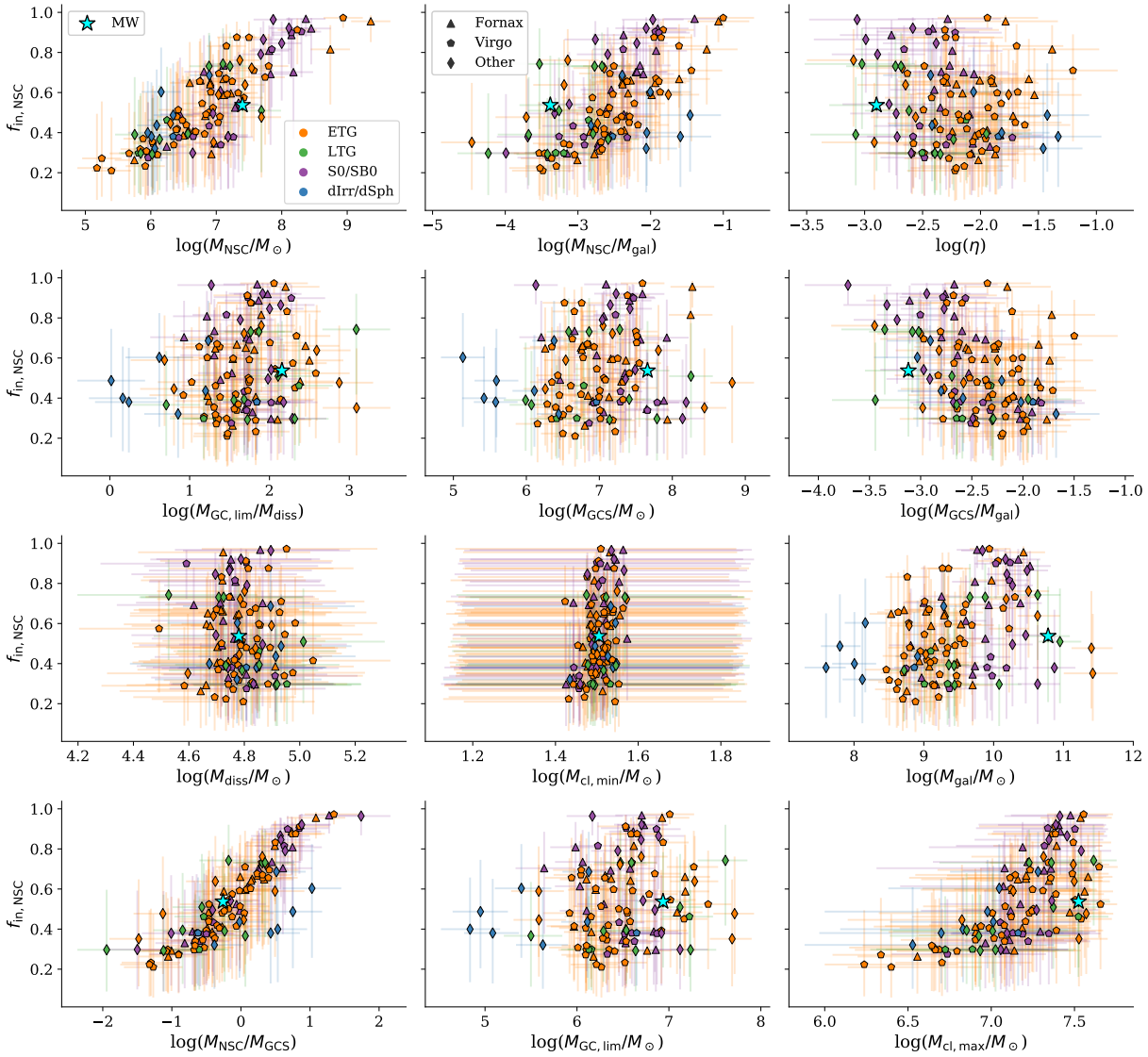

Figure 6.3.: NSC mass fraction formed from in-situ star formation ($f_{\rm in,\,NSC}$) versus model parameters. We used the same colours and symbols as in Fig. 6.2. The errorbars refer to the 16th and 84th percentile of the distribution (see Fig. 6.1).

with $x = \log(M_{\rm NSC}/M_{\rm GCS})$ or $x = \log(M_{\rm NSC}/M_{\odot})$. The parameter α describes the saddle point and β provides an offset at small x and ensures that $f_{\rm in,\,NSC} \leq 1$. The fits were performed with EMCEE using symmetrised uncertainties of $f_{\rm in,\,NSC}$, but a least-squared fit gives comparable results.

Figure 6.4 shows the fits and the residual scatter. We indicate the standard deviation of the residual considering all the data and when only including the ACSVCS and ACSFCS data. As mentioned above, the tightest relation is seen for $f_{\rm in,\,NSC}$ versus $\log(M_{\rm NSC}/M_{\rm GCS})$, but only for the ACS data. Including data from the Local Volume increases the scatter. The best-fitting values are reported in Table 6.2. These show that the switch from GC accretion-dominated to in-situ NSC formation happens at a characteristic NSC mass of $\log(M_{\rm NSC}/M_{\odot}) \sim 7.1$.

Figures 6.3 and 6.4 show that the relation between $f_{\rm in,\,NSC}$ and $\log(M_{\rm NSC}/M_{\rm GCS})$ is clearly tightest for the ACS galaxies, but some other galaxies show deviations from the relation. These are in particular the few dIrrs and dSphs in the Local Volume (Georgiev et al. 2009c,b) that are characterised by large values of $\log(M_{\rm NSC}/M_{\rm GCS})$ at low galaxy masses. As Fig. 6.2 shows, the NSC in these galaxies makes up a significant fraction of the total galaxy mass and of the total mass in star clusters. They may have had a more efficient bound cluster formation, increasing the typical spread in the ratio of $M_{\rm NSC}/M_{\rm GCS}$. In these galaxies, already the inspiral of a single GC will significantly change increase the value of $\log(M_{\rm NSC}/M_{\rm GCS})$ (but not so much $M_{\rm NSC}$) due to the low number of GCs in total. This could explain why they are outliers in the $f_{\rm in,\,NSC}$ versus $\log(M_{\rm NSC}/M_{\rm GCS})$ relation, but not in $f_{\rm in,\,NSC}$ versus $\log(M_{\rm NSC})$. At play is also the stochastic nature of how this ratio will evolve in the case of dwarf galaxies where a few cluster may form in total.

On the other hand, the two ETGs NGC 4552 and IC 1459 discussed above now stand out with having larger $f_{\rm in,\,NSC}$ values than other galaxies with $\log(M_{\rm NSC}/M_{\rm GCS})$ between -1.5 and -1.0. These two galaxies are the two most massive ones in the sample and as discussed above are known to host SMBHs. Galaxy size or cluster formation efficiency may also play a role in the location of the Local Volume sample galaxies on this diagram. However, also these two galaxies are no outliers in the $f_{\rm in,\,NSC}$ - $\log(M_{\rm NSC}/M_{\odot})$ plane.

Table 6.2.: Fitting function results, see Eq. 6.12.

x	Data	α	β	$\sigma_{\rm res}$	valid range
$\log(M_{\rm NSC}/M_{\rm GCS})$	ACS	$0.04^{+0.11}_{-0.11}$	$0.40^{+0.03}_{-0.03}$	0.05	$-1.3 < \ln(M_{\rm NSC}/M_{\rm GCS}) < 1.4$
$\log(M_{\rm NSC}/M_{\rm GCS})$	all	$-0.07^{+0.13}_{-0.13}$	$0.43^{+0.04}_{-0.04}$	0.10	$-2.0 < \ln(M_{\rm NSC}/M_{\rm GCS}) < -1.8$
$\log(M_{\rm NSC}/M_{\odot})$	ACS	$7.13^{+0.13}_{-0.12}$	$0.37^{+0.03}_{-0.03}$	0.10	$5.1 < \ln(M_{\rm NSC}/M_{\odot}) < 9.4$
$\log(M_{\rm NSC}/M_{\odot})$	all	$7.16^{+0.16}_{-0.16}$	$0.37^{+0.03}_{-0.03}$	0.11	$5.1 < \ln(M_{\rm NSC}/M_{\odot}) < 9.4$

Uncertainties from MCMC sampling, $\sigma_{\rm res}$ refers to the standard deviation of the residual scatter.

6.3.2 Trends with model parameters

Importantly, the normalization factor η, describing how much mass forms in clusters, is not correlating with the in-situ fraction. This is perhaps expected as the reproduction of the

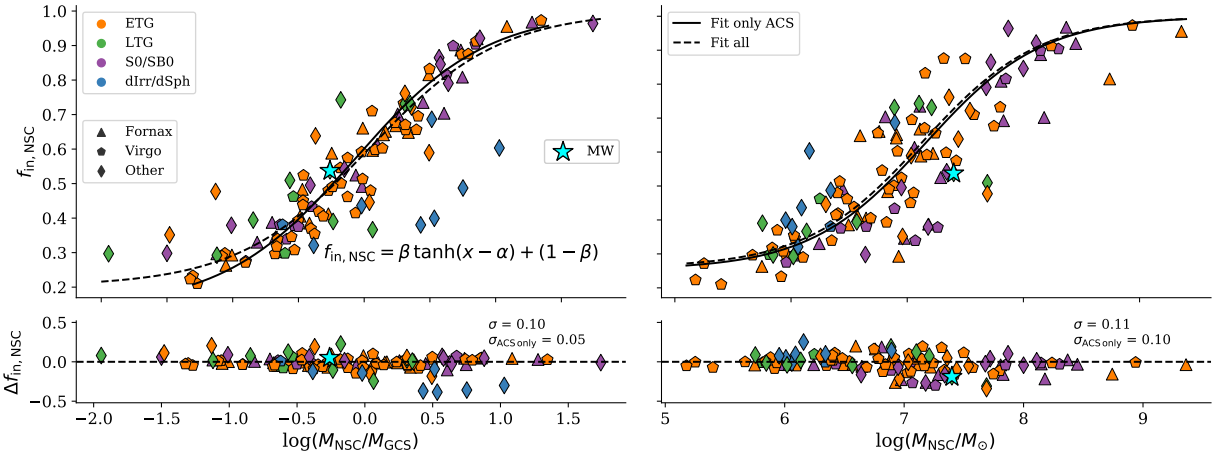

Figure 6.4.: In-situ mass fraction $f_{\mathrm{in,\,NSC}}$ versus $\log(M_{\mathrm{NSC}}/M_{\mathrm{GCS}})$ (*left*) and M_{NSC} (*right*) as seen in Fig. 6.3. The solid line shows the fit using only the ACS data (Fornax and Virgo galaxies), the dashed line when using all data. The bottom panels show the residual scatter. The standard deviations are shown in the label.

NSC and GCS masses will be influenced by the mass sub-divisions of the power-law mass function, rather than its integrated value. The most massive cluster ever formed, $M_{\mathrm{cl,\,max}}$ shows a positive correlation with $f_{\mathrm{in,\,NSC}}$ and reaches the upper limit of the prior for galaxies with high in-situ fractions. Studies of molecular cloud formation and statistical arguments on GC populations (Reina-Campos & Kruijssen 2017; Norris et al. 2019) suggest that this value is unlikely to significantly exceed the range of our default prior of $7.6 \times 10^7 M_{\odot}$ – however further discussion relaxing this is presented in Sect. 6.4.1.

We can not identify a significant environmental dependence to any of the trends of $f_{\mathrm{in,\,NSC}}$ and galactic or GC system properties shown Fig. 6.3. There may be a hint that the predominantly field galaxies of the Local Volume sample show lower values of $f_{\mathrm{in,\,NSC}}$ at fixed GC-host mass ratio ($M_{\mathrm{GCS}}/M_{\mathrm{gal}}$), however within the uncertainties it is consistent with the Fornax and Virgo samples. Further, the Local Volume sample shows larger scatter in the $f_{\mathrm{in,\,NSC}}$ - ($M_{\mathrm{NSC}}/M_{\mathrm{GCS}}$) phase space. This is likely caused by the shallower M_{NSC} - M_{gal} relation observed for the Local Volume sample (Fig. 6.2), while the M_{GCS} - M_{gal} relation agrees with the ACSFCS and ACSVCS sample.

The lack of environmental dependence for $f_{\mathrm{in,\,NSC}}$ may indicate that the processes (GC inspiral and in-situ star formation) are both occurring in the inner ($< R_{\mathrm{eff}}$) regions of the galaxy and are not significantly influenced by *minor* tidal effects affecting the outskirts. However, it also indicates that the observables which drive the model ($M_{\mathrm{NSC}}, M_{\mathrm{GCS}}, M_{\mathrm{GC,\,lim}}$) have also not been significantly altered by environmental processes at fixed galaxy density.

6.4 Discussion

By applying an analytic model for NSC formation to observations of the NSC and GC system masses in 119 galaxies, we showed in Sect. 6.3 how we estimated the relative contribution of in-situ star formation to NSC growth. The predicted $f_{\mathrm{in,\,NSC}}$ shows a strong correlation

Table 6.3.: Description of model sub-sets.

Model Run	Description
Default	Default approach described in Section 2
2nd brightest GC	Adopt the 2nd brightest GC for $M_{\rm GC,\ lim}$
Model $M_{\rm GC,\ lim}$	Adopt the LvdV21 prediction for $M_{\rm GC,\ lim}$
$M_{\rm cl,\ max} < 10^{8.8}$	Upper limit for $M_{\rm cl,\ max}$ set to $10^{8.8} M_{\odot}$
Variable accretion	Allow for a fraction $f_{\rm acc,\ gal}$ of GCs to be accreted
Adaptive priors	Allow for variable accretion, and $f_{\rm in,\ NSC}$ constrained by adaptive priors (see LvdV21)
Simulation $f_{\rm acc,\ gal}$	Adopt $f_{\rm acc}$ as a function of $M_{\rm gal}$ from the EAGLE simulations (Davison et al. 2020)

with the mass ratio of a galaxy's NSC to GC system mass, however given the simplicity of the model we wish to understand whether additional factors may bias this result.

6.4.1 Dependence on parameter setups

To explore the influence of assumptions within the model and assumed priors, we ran the model on the ACSFCS and ACSVCS data with different choices as described in Table 6.3. The resulting changes to our key variable ($f_{\rm in,\ NSC}$), and its relation to galactic star cluster system properties are shown in Fig. 6.5.

The limiting GC mass for accretion into the NSC, $M_{\rm GC,\ lim}$, is a key parameter in our model. The most massive GC observed today should give a reasonable approximation of this limiting mass, but as shown in LvdV21, a contamination from UCDs could bias it to higher masses. Therefore, we also ran the model using two alternative estimates for this parameter: 1) using the second most massive observed GC (model run '$M_{\rm GC,\ 2nd\ max}$'), and 2) deriving $M_{\rm GC,\ lim}$ from the galaxy's size and mass as in LvdV21 ('model $M_{\rm GC,\ lim}$'). While the overall relation with $M_{\rm NSC}/M_{\rm GCS}$ is robust, the highest in-situ fractions are generally found when using the default approach because both the model prediction of $M_{\rm GC,\ lim}$ and $M_{\rm GC,\ 2nd\ max}$ tend to be lower than $M_{\rm GC,\ max}$ used in the default approach. This allows for more massive GCs merging into the NSC, consequently reducing $f_{\rm in,\ NSC}$ by up to 10%.

We next tested the influence of $M_{\rm cl,\ max}$, the mass of the most massive GC ever formed. The posterior values returned by the default model for $M_{\rm cl,max}$ are well within the observed values seen in the MW and Local Volume, and even merging systems (Renaud 2018), but the upper limit to the prior of $M_{\rm cl,\ max} = 7.6 \times 10^7 M_{\odot}$ (Norris et al. 2019) is reached for some of the highest $f_{\rm in,\ NSC}$ systems. Increasing this limit by one order of magnitude to $M_{\rm cl,\ max} \sim 7 \times 10^8 M_{\odot}$ ('$M_{\rm cl,\ max} < 10^{8.8}$' model), can reduce the in-situ fractions in these galaxies by ~ 10 per cent points. While this is expected because it allows for more massive GCs being formed, but neither this nor the changes to $M_{\rm GC,\ lim}$ change the trend of $f_{\rm in,\ NSC}$ versus $\log(M_{\rm NSC}/M_{\rm GCS})$.

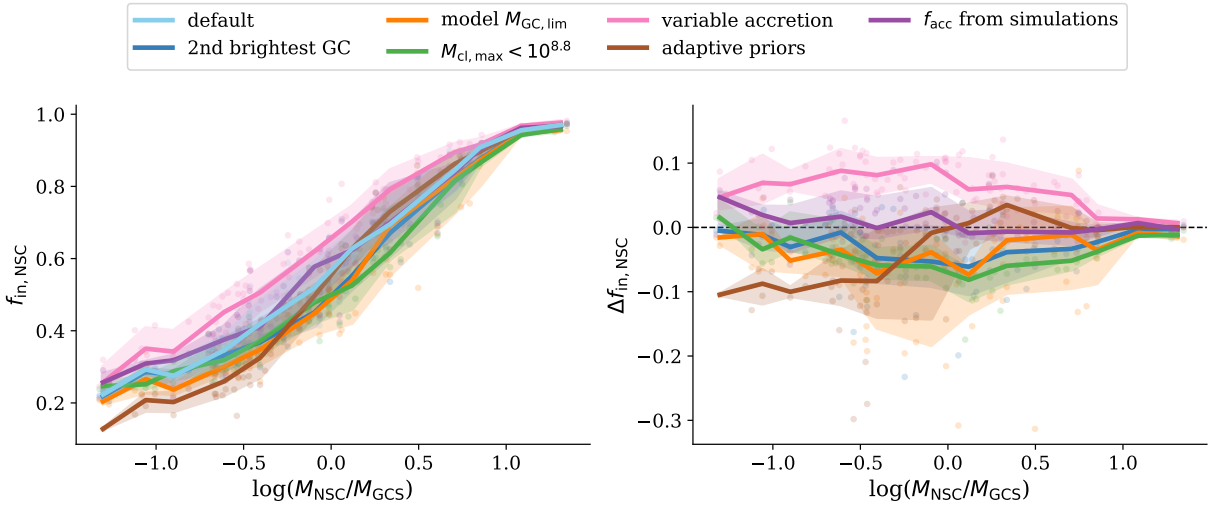

Figure 6.5.: Influence of model settings on the predicted in-situ NSC mass fractions. *Left*: $f_{\mathrm{in,\,NSC}}$ in relation with the ratio of NSC and GCS mass for the different settings. Coloured lines show median-binned data with 1σ scatter for visualisation. *Right*: differential in-situ mass fraction relative to the default model. The different settings are summarised in Table 6.3.

6.4.2 Galaxy accretion

Our model regards galaxies as isolated systems as observed today and does not consider their mass assembly via mergers and accretion of dwarf galaxies. However, these mergers alter the GCs that are available for accretion into the NSC and the dynamical friction conditions. To test the influence of galaxy accretion, we also tested a model setup where an additional parameter, f_{acc}, is introduced. This parameter describes the fraction of GCs and stellar mass accreted by a galaxy due to mergers, and scales the observed GCS mass and galaxy mass via $(1 - f_{\mathrm{acc,\,gal}})M_{\mathrm{GCS}}$ and $(1 - f_{\mathrm{acc,\,gal}})M_{\mathrm{gal}}$ (see Appendix D in LvdV21).

We implemented the galaxy accretion fraction both with a flat prior from zero to unity (model setup 'variable accretion') and with a prior that is adapted continuously via the upper and lower limits on $f_{\mathrm{in,\,NSC}}$ as given in LvdV2120 (model setup 'adaptive priors'):

$$f_{\mathrm{in,\,NSC}} \geq 1 - \left(\frac{\eta(1 - f_{\mathrm{acc,\,gal}})^2 M_{\mathrm{gal}} M_{\mathrm{GCS}}}{M_{\mathrm{NSC}} M_{\mathrm{GC,\,lim}} (1 + \ln \frac{M_{\mathrm{GC,\,lim}}}{M_{\mathrm{diss}}})} \right). \tag{6.13}$$

$$f_{\mathrm{in,\,NSC}} \leq 1 - \left(\frac{M_{\mathrm{GC,\,lim}} M_{\mathrm{GCS}}}{\eta M_{\mathrm{gal}} M_{\mathrm{NSC}}} \right). \tag{6.14}$$

Introducing $f_{\mathrm{acc,\,gal}}$ with flat priors leads to higher values of $f_{\mathrm{in,\,NSC}}$ since the same NSC mass has to be reproduced with a reduced GC system. The effect is larger in galaxies that have low in-situ fractions in the default model because those are the systems where the GCS was dominating previously. In contrast, when using the adaptive priors, the upper limit requires lower in-situ fractions for galaxies where the ratio $M_{\mathrm{NSC}}/M_{\mathrm{GCS}}$ is dominated by the GCS, further reducing $f_{\mathrm{in,\,NSC}}$.

As discussed in LvdV2120, while limits on both NSC in-situ mass fraction and galaxy accretion fraction are possibly depending on the particular stellar mass and galaxy size, we do not expect the model to uniquely infer both the NSC in-situ mass fraction $f_{\mathrm{in,\,NSC}}$ and the galaxy accretion fraction $f_{\mathrm{acc,\,gal}}$. This is reasonable as both parameters alter the mass ratio of NSC to GC system mass in degenerate ways. For this reason, we produced a model run using trends of $f_{\mathrm{acc,\,gal}}$ with host galaxy mass from the EAGLE simulations of galaxy formation (Davison et al. 2020) (model setup 'f_{acc} from simulations'). Since these theoretical predictions find low accretion fractions between ~ 0.1 and 0.5 for the galaxy mass range studied here, this results in in-situ fractions similar to the default model.

In summary, the exact setup of our model can affect the resulting $f_{\mathrm{in,\,NSC}}$ by $\sim 20\%$ except for the largest ratios of $M_{\mathrm{NSC}}/M_{\mathrm{GCS}}$, but the general trend with NSC mass remains unaltered by these systematics.

6.4.3 Expectations from stellar populations

As Neumayer et al. (2020) argue, insights from stellar population analysis of NSCs indicate that at low galaxy masses GC accretion constitutes the dominant NSC formation channel, whereas in-situ formation might become more influential for galaxies more massive than $M_* \sim 10^9 M_\odot$. This argument is mainly based on the observation that NSCs in lower mass galaxies tend to be more metal-poor than the galaxy (Neumayer et al. 2020; Fahrion et al. 2020c; Johnston et al. 2020), while NSCs in massive galaxies often show high metallicities, young subpopulations, flattened structures, and can be kinematically complex (Seth et al. 2008a; Paudel et al. 2011; Spengler et al. 2017; Lyubenova et al. 2013; Lyubenova & Tsatsi 2019; Fahrion et al. 2019b).

In Chapt. 5 we could confirm such a trend with the analysis of 25 ETGs and dEs. The stellar population analysis showed that the dominant NSC formation channel transitions from GC accretion to in-situ star formation with increasing galaxy and NSC mass (see Fig. 5.6). In our stellar population analysis, we found that the transition happens at masses at $M_{\mathrm{gal}} \sim 10^9 M_\odot$ and $M_{\mathrm{NSC}} \sim 10^7 M_\odot$, respectively.

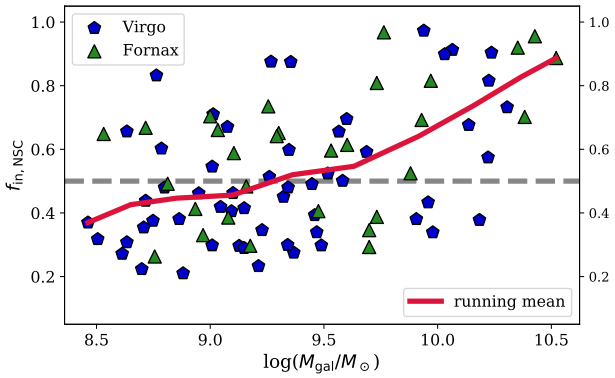

Figure 6.6.: In-situ mass fraction $f_{\mathrm{in,\,NSC}}$ versus galaxy mass for galaxies in Virgo and Fornax. The red line is the moving average (not considering the uncertainties in $f_{\mathrm{in,\,NSC}}$) that crosses $f_{\mathrm{in,\,NSC}} = 50\%$ for galaxy masses $M_{\mathrm{gal}} \sim 1.5 \times 10^9 M_\odot$.

Using the semi-analytical model presented in this chapter, we quantified the fraction of the NSC mass assembled via in-situ star formation, $f_{\mathrm{in,\,NSC}}$, and we showed that it is strongly correlated with the total NSC mass (see Fig. 6.4). The model can reproduce the transition at NSC masses $M_{\mathrm{NSC}} \sim 10^7 M_\odot$, but the correlation with galaxy mass is weaker as Fig. 6.6 shows. This figure again shows the in-situ NSC fraction versus galaxy mass, but now only focusing on the homogeneous ACS sample of ETGs in Virgo and Fornax. The moving average reaches $f_{\mathrm{in,\,NSC}} = 50\%$ for galaxy

masses $M_{\rm gal} \sim 1.5 \times 10^9 M_\odot$, but the scatter is significant. A trend with host mass in the model is a secondary effect as more massive galaxies tend to have more massive NSCs (see Fig. 6.2 or Ordenes-Briceño et al. 2018; Sánchez-Janssen et al. 2019), but at the same time have a large scatter in the ratio of NSC-to-GC system mass (Fig. 6.2), the most sensitive parameter in our model. As the detailed stellar population analysis is limited to 25 galaxies (plus the two dwarf galaxies KKs 58 and KK197, Chapt. 3), it is yet unclear how large the scatter in the dominant NSC formation channel is found from observations.

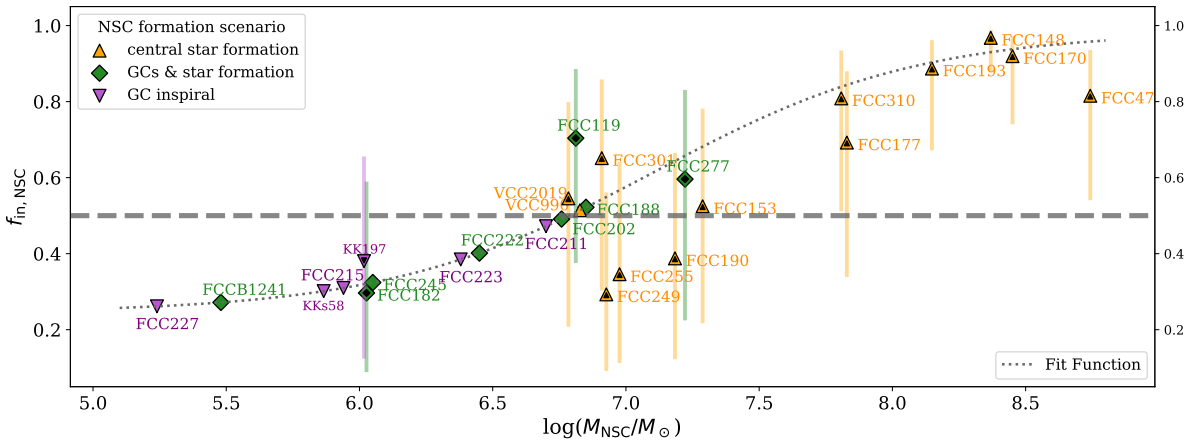

Figure 6.7.: NSC mass versus in-situ NSC mass fraction for the 25 galaxies studied in Chapt. 5 as well as the two dwarf galaxies KK 197 and KKs 58 (Chapt. 3). The colours and symbols give the dominant NSC formation channel as identified in Sect. 5.3.5, see also Fig. 5.6. Galaxies that were modelled in this chapter are highlighted with a small black symbol and show the inferred uncertainties on $f_{\rm in,\,NSC}$. For the other galaxies, the fitting function for the ACS galaxies as in Tab. 6.2 was used (dotted line). The grey dashed line shows $f_{\rm in,\,NSC} = 50\%$.

We compare the results from our semi-analytical model to the stellar population analysis of the 25 ETGs presented in Chapt. 5 and the two dwarfs KK 197 and KKs 58 (Chapt. 3) in Fig. 6.7. This figure shows the inferred in-situ mass fraction either from the model directly or from the fitting function of NSC mass versus $f_{\rm in,\,NSC}$ (Table 6.2) for those galaxies that do not have information on their GC system available. This figure illustrates that the semi-analytical model and the stellar population analysis agree in their determination of the NSC formation channel for the least massive and most massive NSCs. For the highest NSC masses ($\log(M_{\rm NSC}) > 7.5$), the model reports high values of $f_{\rm in,\,NSC}$, in agreement with the result from the stellar population analysis that identified the in-situ channel as the dominant NSC formation pathway in these galaxies. In addition, for the low-mass NSCs ($\log(M_{\rm NSC}) < 6.5$) the model predicts low in-situ fractions, in agreement with the stellar population analysis that identified those NSCs to form at least part of their mass from accreted GCs.

However, at intermediate NSC masses around ($\log(M_{\rm NSC}) \sim 7$), the model shows scatter in the inferred in-situ NSC fraction and found low values of $f_{\rm in,\,NSC} < 0.4$ for three galaxies (FCC 249, FCC 255, and FCC 190) in which the stellar population analysis identified in-situ star formation to be the dominant NSC formation channel. It is likely that the model

prefers low values of $f_{\mathrm{in,\,NSC}} < 0.4$ for these galaxies because they have rather low NSC masses for their galaxy mass ($M_{\mathrm{gal}} \sim 5 \times 10^9 M_{\odot}$), but high NSC-to-GC system mass ratios. This mismatch between the likely robust stellar population result and the model prediction indicates the limitations of the model as it is only based on dynamical arguments. While the overall trends are reproduced in the model, the behaviour of systems with intermediate NSC and galaxy masses can deviate from the model predictions. In a future development of the purely mass-based model presented here, we plan to include predictions for stellar population parameters to better explore the evolutionary history of individual NSC-galaxy systems.

6.5 Concluding remarks

This chapter presents a semi-analytic model of NSC formation (Leaman & van de Ven 2021, subm.) to determine the dominant NSC-formation channel (either in-situ star formation or accretion of GCs) in a sample of 119 nearby galaxies in the Local Volume, the Fornax and the Virgo clusters, with galaxy masses from 3×10^7 to $3 \times 10^{11} M_{\odot}$, whose NSC and GC system masses have been previously determined. We quantified the fraction of the NSC mass assembled via in-situ formation, $f_{\mathrm{in,\,NSC}}$, in each NSC and explored its dependence with various properties of the host galaxy and its GC system.

Our analysis revealed that $f_{\mathrm{in,\,NSC}}$ strongly correlates with the NSC mass, such that low-mass NSCs have low in-situ mass fractions, meaning that they were formed predominantly via the merging of GCs. Higher-mass NSCs have high $f_{\mathrm{in,\,NSC}}$ indicating that they assembled mostly through in-situ star formation. The transition between the relative importance of the GC accretion and in-situ star formation happens for NSC masses $\sim 10^7 M_{\odot}$. In galaxies that host the most massive NSCs (those that encompass $\sim 10\%$ of the host galaxy mass) we find that the in-situ channel is the dominant one, responsible for the build-up of more than $\sim 90\%$ of the NSC mass. As more massive NSCs are found in more massive galaxies, this further indicates a shift from GC accretion dominated to in-situ dominated formation with galaxy mass, as suggested by recent studies relying on stellar population properties (Neumayer et al. 2020; Johnston et al. 2020 or Chapt. 5).

We further found a strong correlation between $f_{\mathrm{in,\,NSC}}$ and the ratio of the NSC-to-host GCS mass. The GC accretion channel is dominant in galaxies in which the GC system is more massive than the NSCs. Both NSC formation channels contribute equally in galaxies with comparable masses of the NSC and the GCS.

Comparing with stellar population results (Chapt. 5), we found that the model predictions for $f_{\mathrm{in,\,NSC}}$ match the observationally inferred dominant NSC channel for the lowest and highest NSC masses, but exhibits a larger scatter at intermediate NSC masses around the transition mass ($M_{\mathrm{NSC}} \sim 10^7 M_{\odot}$). In the model, a trend with galaxy mass is less clear and likely reflects the underlying NSC-to-galaxy mass relation. The semi-analytic model presented in this work relies solely on dynamical arguments and only exploits structural properties of the host galaxy, NSC, and GCS. In future work, we will incorporate stellar population predictions to enable a more detailed comparison to spectroscopic observations.

Look forward, not back. Correct your course and go on. You cannot undo yesterday's journey.

Robin Hobb, Mad Ship

7 | Summary, Discussion & Outlook

Nuclear star clusters are the densest stellar systems in the Universe and are found in a majority of galaxies, from low-mass dwarf galaxies to massive spirals and ellipticals. This thesis explores the ways through which NSCs form and grow by investigating the properties of NSCs in comparison to their host galaxies and other star clusters such as GCs. In this chapter, I summarise the main results of this thesis and put them in context of open questions regarding NSC formation and galaxy evolution. Additionally, I discuss future applications of the techniques presented here and provide an outlook how further observations and future telescopes might help to understand the evolution of galaxies using dense star clusters as tracers of galaxy evolution.

7.1 How do nuclear star clusters form?

Located at the centres of galaxies, NSCs experience a large variety of different physical processes that can influence their properties and shape their evolution. As described in the introduction, there are two main NSC formation pathways that are discussed: through the merger of star clusters, in particular ancient GCs, or through in-situ star formation directly at the galaxy centre. These different formation channels imply different expectations on the kinematics and stellar population properties of NSCs in comparison to their host galaxy and the GC population. The GC inspiral scenario can explain the presence of old, metal-poor populations – reflecting the stellar populations of ancient GCs. In contrast, metal-rich populations and extended SFHs with possible signatures of young stars are expected in the in-situ formation channel through efficient star formation from pre-enriched gas. In order to differentiate between these scenarios, this thesis presents a comprehensive analysis of all involved components using IFS with the MUSE instrument of individual galaxies.

To analyse NSCs and GCs from MUSE data, I developed techniques to extract background-cleaned MUSE spectra of individual star clusters, and applied these methods to both NSCs and GCs. Using the established full spectrum fitting code pPXF, I extracted kinematics and stellar population properties of star clusters and their host galaxies. While binned maps give a continuous view of the kinematic and stellar population properties of the host galaxies, the star clusters are mostly unresolved and act as bright point-source tracers. The NSCs dominate the light in the galaxy centres and consequently high S/N spectra can be extracted that allow us to derive mean ages and metallicities as well as SFHs (see Chapt. 2 and 5). In contrast, GCs usually have a low spectral S/N and consequently only the LOS velocities – and for the brighter ones mean metallicities – can be recovered with these

techniques. Chapter 4 presents a catalogue of 722 spectroscopically confirmed GCs in the 32 F3D galaxies that is used to establish the value of GCs as bright point-source tracers of the underlying galaxy kinematics and stellar populations. This sample is further used to compare stellar populations between NSCs and GCs.

Chapter 2 presents the analysis of the ETG FCC 47 ($M_{\rm gal} \sim 10^{10} M_{\odot}$) in the Fornax cluster (distance $\sim$ 20 Mpc, Blakeslee et al. 2009) which is particularly interesting for NSC studies because of its large NSC that is resolved in the MUSE data. Based on its kinematically decoupled nature, its high mass ($M_{\rm NSC} \sim 7 \times 10^{8} M_{\odot}$), and high metallicity, the main result of this analysis is that the NSC of FCC 47 is most likely the product of early, efficient in-situ star formation. However, the kinematic decoupling between NSC and host galaxy likely indicates a past merger event that has shaped FCC 47. In contrast, focusing on the two nucleated dwarf galaxies KK 197 and KKs 58 near Centaurus A (Chapt. 3), presents a different picture. These two dwarf galaxies are less massive than the NSC in FCC 47 and their NSCs resemble typical GCs with their low masses ($M_{\rm NSC} \lesssim 10^{6} M_{\odot}$) and metal-poor populations. We found that both NSCs are significantly more metal-poor than their hosts and consequently concluded that they were likely formed from the inspiral of a few metal-poor GCs.

The case studies of FCC 47 and the two dwarf galaxies already illustrate that NSCs do not form through a single unified channel, but that both proposed scenarios can occur. To further explore the dependence of the dominant channel on galaxy properties, Chapt. 5 presents an analysis of the NSC stellar populations and SFHs in comparison to the underlying host galaxy in 25 nucleated galaxies, again including FCC 47. Based on the metallicity contrast between host and NSC and features in the SFHs, the dominant formation channel for individual galaxies was established. This chapter provides solid observational evidence for a transition of the dominant NSC formation channel with both galaxy and NSC mass and adds detail to the case studies presented in Chapt. 2 and 3: low-mass NSCs found predominantly in low-mass galaxies are formed through the merger of a few GCs, whereas high-mass NSCs assemble their mass mainly through efficient central star formation – either directly in-situ in the NSC or through the accretion of young enriched star clusters that formed close to the galaxy's centre. It has to be noted that we compare integrated stellar population properties and hence cannot differentiate between the traditionally discussed in-situ star formation happening directly in the NSC and the accretion of young enriched star clusters because both channels result in similar total stellar population properties. To disentangle them, a detailed chemo-dynamical model of the internal kinematics and stellar population distributions is required, as accreted star clusters result in a different orbital configuration in the NSC than pure dissipitative processes (see e.g. Lyubenova et al. 2013).

The semi-analytical model presented in Chapt. 6 allows us to understand underlying trends with galaxy and NSC mass from a theoretical viewpoint. The model presented here considers the evolution of GCs under dynamical friction and mass loss in the tidal field of a galaxy. While the least massive GCs will be destroyed, the most massive ones spiral into the centre and build a NSC. By matching the expected NSC mass from GC inspiral to observations, the NSC mass fraction formed through additional in-situ star formation is estimated. Using this consideration of the mass budget in star clusters, the model finds that infalling GCs can form the low-mass NSCs of low-mass galaxies, but significant in-situ

star formation is required to grow massive NSCs ($M_{\rm NSC} > 10^7 M_\odot$). In the model, a trend with galaxy mass is only seen as a secondary effect stemming from the galaxy-to-NSC mass and galaxy-to-GC system relations. The model does not cover the full range of physical processes that can affect individual NSCs and their host galaxies such as galaxy mergers and interactions. Nonetheless, the predictions from this simple model match the results from the stellar population analysis well.

In conclusion, NSC formation can be understood as a consequence of clustered star formation occurring in the high density regions of galaxies. In low-mass galaxies, star clusters might not form initially in the centre but as GCs in dense clumps at high redshift. If these galaxies are undisturbed, the short dynamical timescales in dwarf galaxies will result in the inspiraling of the GCs to the centre to form metal-poor NSCs with very similar properties as GCs. This process might also happen in more massive galaxies, in which inspiraling GCs might form the initial NSC seeds. However, over the course of the evolution of massive host galaxies, the NSCs can grow in mass together with their host, either through in-situ formation directly at the centre or through the subsequent accretion of enriched young star clusters that formed in the central regions.

7.2 Comparison to the literature

As described in Chapt. 1, the idea that the dominant NSC formation channel depends on the galaxy mass has been proposed before. Based on the increasingly large dynamical friction timescales for GC inspiral, Turner et al. (2012) argued that GC accretion is only a reasonable formation channel for low-mass galaxies. In addition, they noted that the NSCs of more massive galaxies are redder, which they interpreted as an increase in metallicity from dissipative processes that efficiently enrich the NSCs. For this reason, they proposed a shift from GC inspiral forming NSCs in low-mass galaxies to in-situ formation at higher galaxy masses.

In a similar spirit, Antonini (2013) modelled the formation of NSCs from inspiraling GCs and while they could reproduce properties of observed NSCs, they also found that the dynamical friction timescales exceed the age of the Universe in massive galaxies. Additional, they argued that SMBHs with $M_{\rm BH} > 10^8 M_\odot$ cause tidal disruptions of inspiraling GCs and hence make this formation channel inefficient in building NSCs in massive galaxies ($M_{\rm gal} \gtrsim 10^{11} M_\odot$). Building on this work, Antonini et al. (2015) presented a semi-analytical model of galaxy evolution that follows the evolution of galaxies through merger trees and included prescription for both the GC accretion and the in-situ NSC formation channel. In their model, they found that the in-situ channel contributes between $\sim 20 - 50\%$ of the NSC mass in both ETGs and LTGs, but this fraction rises to $> 60\%$ for ETGs with $M_{\rm gal} > 10^{11} M_\odot$, likely because inspiraling GCs at these high galaxy masses get tidally disrupted by pre-existing SMBHs. However, the observed nucleation fraction of galaxies at these galaxy masses is very low ($< 10\%$, Sánchez-Janssen et al. 2019), much lower than the prediction by Antonini et al. (2015).

In their recent review, Neumayer et al. (2020) proposed a transition of NSC formation via GC accretion to in-situ formation at galaxy masses of $M_{\rm gal} \sim 10^9 M_\odot$ based on several

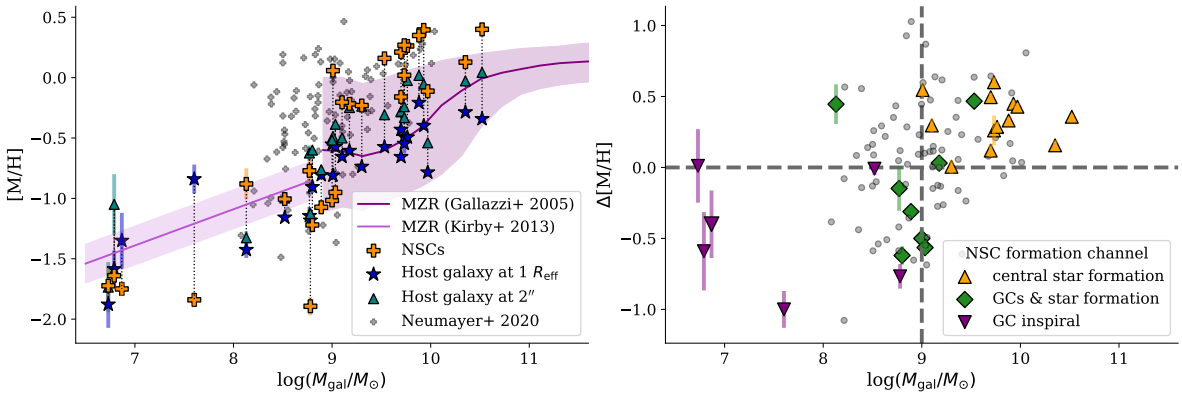

Figure 7.1.: Metallicity contrast between NSCs and host galaxies. *Left*: NSC (coloured plus symbols) and host galaxy (stars and triangles) metallicities for the galaxies presented in this thesis (Chapt. 2, 3, and 5) as a function of galaxy mass. The components from each galaxy are connected by a dotted line and we show the metallicities in the NSC, at a central radius of 2″, and at 1 $R_{\rm eff}$ where available (see Sect. 5.2.2). The small grey symbols are the ones shown in Neumayer et al. (2020) from literature compilations and without a reliable measurement of the host metallicity. The solid lines and shaded regions are the MZRs from Gallazzi et al. (2005) and Kirby et al. (2013) with their uncertainties, respectively. *Right*: Relative metallicity (central host metallicity subtracted from NSC metallicity) as a function of galaxy mass. Coloured symbols refer to the galaxies studied in this work, the grey ones are from Neumayer et al. (2020) and refer to the difference between NSC metallicity and host as expected from the MZR. The colour-coding and the symbols show the dominant NSC formation channel inferred for the individual galaxies as described in Sect. 5.3.5, see also Fig. 5.3.5.

arguments such as the shape of NSC mass - galaxy mass relation. Including dwarf galaxies, Ordenes-Briceño et al. (2018) and Sánchez-Janssen et al. (2019) suggested that this relation is steeper for galaxies with $M_{\rm gal} \gtrsim 5\times10^9 M_\odot$. This change in slope coincides roughly with the transition mass proposed by Neumayer et al. (2020), but at the moment theoretical models of this transition are lacking. As Neumayer et al. (2020) and Sánchez-Janssen et al. (2019) noted, numerical simulations from the GC infall scenario produce NSC-to-host mass relations that match the observed one only at low galaxy masses (Gnedin et al. 2014; Antonini et al. 2015), whereas the upturn in the NSC-to-galaxy mass ratio for massive galaxies is not found in the models (Ordenes-Briceño et al. 2018; Sánchez-Janssen et al. 2019). In addition, most studies of NSC formation typically consider massive galaxies and hence detailed predictions for the formation of NSCs in low-mass dwarf galaxies ($M_{\rm gal} < 10^8 M_\odot$) are missing.

Neumayer et al. (2020) collected a diverse sample of NSC metallicities from the literatue and compared them to the expected host metallicity as predicted from the MZR. Based on the observation that NSCs in low-mass galaxies can be more metal-poor than the expected metallicity of their host galaxy, they argued that those might have been formed from the inspiral of metal-poor GCs. This interpretation hinges on the MZR and does not consider scatter in this relation or the effect of a radial metallicity gradient. With the work in this thesis (Chapt. 2, 3, and 5) we can now repeat this comparison, but with accurate metallicity measurements of the involved components. This is shown in Fig. 7.1, which reproduces Fig. 9 of Neumayer et al. (2020) but with the results of this work added as coloured symbols. The host galaxy metallicities show significant scatter around the MZR and once again

illustrate the need for accurate measurements. Our sample also covers a larger range in host metallicities including low-mass dwarf galaxies ($M_{\rm gal} < 10^8 M_\odot$). Nonetheless, the trend suggested by Neumayer et al. (2020) is confirmed. All NSCs in galaxies more massive than $10^9 M_\odot$ of our sample are more metal-rich than the host and these are the ones where the dominant NSC channel was identified as the in-situ formation channel. NSCs in less massive galaxies often are significantly more metal-poor and were formed through mergers of GCs or a combined scenario. Our extensive analysis presented in Chapt. 5 certainly gives a more detailed picture, but the metallicity contrast between NSC and host appears to be a valuable parameter to differentiate between NSC formation from GC accretion and in-situ or central star formation.

7.3 Nuclear star clusters in late-type galaxies

In this thesis, I presented an analysis of 27 galaxies. These galaxies are mainly massive ETGs and low-mass systems without strong star formation such as dEs and dSphs. The lack of star formation enables a straightforward analysis of their stellar populations from stellar absorption spectra, but consequently, the findings of a relation between NSC formation mechanisms and galaxy properties presented in this thesis might only hold for ETGs.

In general, all evidence for a shift of the dominant NSC formation channel with galaxy mass discussed in the literature comes from ETGs, as also described by Neumayer et al. (2020). The NSC mass - galaxy mass relation is best explored for ETGs because the respective studies focused on the central regions of galaxy clusters where LTGs are scarce. Therefore, the low-mass end of this relation constitutes mostly dEs. (Ordenes-Briceño et al. 2018; Sánchez-Janssen et al. 2019; Zanatta et al. 2021). In contrast, the abundance of NSCs in low-mass LTGs is yet unexplored. To date, the largest sample of 228 NSCs in LTGs was presented in Georgiev & Böker (2014) based on HST observations of LTGs within 40 Mpc. As Fig. 7.2 shows this sample mostly contains massive galaxies with $M_{\rm gal} > 10^9 M_\odot$. In addition, Georgiev et al. (2009c) presented a search for star clusters in archival HST data of 68 dIrrs in nearby groups ($D < 12$ Mpc) and they identified 10 NSCs (Georgiev et al. 2009a), but overall the population of nucleated low-mass LTGs remains largely unconstrained.

Ongoing deep photometric surveys like the MATLAS Survey (Mass Assembly of early-Type GaLAxies with their fine Structures, Duc et al. 2015) that targets massive galaxies and their satellite systems will be able to constrain the abundance of NSCs in dwarf galaxies, at least in those associated with massive galaxies. Additionally, upcoming wide field surveys like the Euclid space mission or the Legacy Survey of Space and Time (LSST) at the Vera C. Rubin Observatory (Ivezić et al. 2019) that cover a significant portion of the sky will be able to further constrain the nucleation fraction of isolated dwarf galaxies in the Local Volume.

Currently, most of the stellar population studies were done for ETGs or dEs (Paudel et al. 2011; Spengler et al. 2017; Johnston et al. 2020). The sample of LTGs in which their NSCs were analysed is restricted to massive bulge-less galaxies ($> 10^9 M_\odot$) and studies with long-slit spectroscopy (Walcher et al. 2006; Seth et al. 2006; Rossa et al. 2006; Kacharov et al. 2018), as highlighted in Fig. 7.2. Those have shown that LTG NSCs usually have

complex star formation histories, a significant fraction of young stars, and can be rotationally flattened, which is expected from in-situ formation. However, these studies do not have the sensitivity to compare the NSCs to the host galaxy and hence it is unclear how they compare to the galaxies studied in this thesis. In addition, spectroscopic investigations at lower galaxy masses are lacking completely. Consequently, the question arises how NSCs in dwarf LTGs are assembled: are their NSCs seeded by inspiraling GCs as we found for dEs? Or did they form directly at the centres of their galaxies out of infalling gas like their massive counterparts?

To address these questions, future studies like the ones presented in this thesis targeting LTGs are required. In particular, a comparison between NSCs and their hosts is missing for LTGs, but is crucial to understand the complex interplay in the NSC-galaxy system. The techniques presented in this thesis could be further developed to be also applicable to star forming galaxies in order to facilitate a detailed study of NSC formation in LTGs. Although emission lines can complicate analysis of stellar absorption features, they also hold information about the kinematics and metallicity of the ionised gas. Exploring these properties could be used to study how gas is funnelled to the NSC and to identify outflows from strong star formation in the NSC as well as possible signature of BH accretion. Figure 7.2 highlights twelve known nucleated low-mass LTGs which are suitable for such a study if observed with MUSE. Two of those already have archival MUSE data available and the other ten are targets of an submitted ESO proposal for period P108. If accepted and scheduled, this data will be used to present the first stellar population analysis of NSCs in dwarf LTGs.

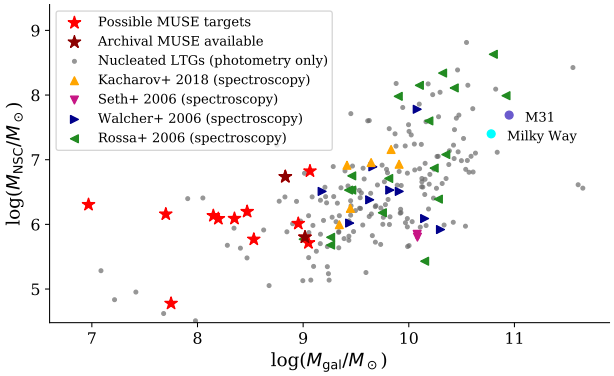

Figure 7.2.: NSC mass versus galaxy mass for LTGs. Grey circles show the largest photometric sample to date (Georgiev & Böker 2014; Georgiev et al. 2016). Galaxies with long-slit spectroscopy of their NSCs as coloured triangles (Walcher et al. 2006; Seth et al. 2006; Rossa et al. 2006; Kacharov et al. 2018). Those are exclusively galaxies more massive than $10^9 M_\odot$. Dark red stars show two low-mass LTGs with archival MUSE data that could be analysed with similar methods as presented in this thesis. Bright red stars show additional possible MUSE targets that might be considered for future observations.

Analysing LTGs will not only help to understand the processes that form and grow NSCs, but also to constrain the formation sites of GCs. Their old ages between ∼10 - 13 Gyr imply that GCs were formed in the early Universe at high redshifts $z \gtrsim 2$, but current observational limitations do not allow the direct observation of their formation processes. In simulations, GC formation is also difficult to study in a cosmological context due to the required mass resolution (Ma et al. 2020). Young massive clusters that were found in galaxies with high levels of star formation overlap in masses and sizes with the GC population and are regarded as young analogues of the ancient GC progenitors. Their chemical properties, masses, sizes, and their spatial distribution could reveal the conditions of GC formation. At the moment, most studies of such young massive clusters are based on high resolution photometry (e.g.

Adamo et al. 2020), but including IFS would allow us to better understand their stellar populations and kinematics.

Analysing star cluster formation in local galaxies is also relevant for upcoming telescopes like JWST or ESO's ELT. With coverage from 0.6 to 27 μm, JWST will fundamentally change observations of star (cluster) formation at high redshift, because it will allow us to study the rest-frame visible wavelengths of galaxies with redshifts $> 2 - 6$, finally accessing the formation redshifts of GCs (Vanzella et al. 2017). Using similar techniques as used today for local (star forming) clusters, the rest-frame optical continuum that bears stellar absorption lines in addition to emission lines can be accessed. In addition, the unprecedented spatial resolution provided by the ELT and its AO-supported IFS instrument HARMONI or the spectrograph MICADO will resolve individual high redshift star forming clumps in gravitationally lensed galaxies and hence will give the opportunity to observe GC formation directly (Renzini 2020).

7.4 Nuclear star clusters and galaxy evolution

In most cases, NSC formation is regarded as an internal process of a galaxy, but there are several ways how galaxy mergers and interactions can affect NSCs. The analysis of FCC 47 (Chapt. 2) has shown that the kinematically decoupled nature of its NSC is likely the result of a merger that has shaped the dynamic structure of this galaxy. Because of the old ages, we cannot say whether the NSC was formed in this merger or if it was already located in the galaxy beforehand, but it was clearly fundamentally affected by FCC 47's assembly history. A different example might be found in the MW NSC, as the recently discovered metal-poor population could have been accreted from a disrupted dwarf galaxy (Arca Sedda et al. 2020). In addition, mergers and accretion of galaxies are often considered as mechanisms to supply gas to the galaxy centre, where it can fuel in-situ NSC formation (e.g. Hopkins & Quataert 2010). Even the first theoretical study of this NSC formation channel by Mihos & Hernquist (1994) considered the in-situ formation channel as a result of gas-rich mergers that funnel gas to the galaxy centre.

Galaxy interactions might also prohibit NSC formation. One example of this might be found in the Fornax dSph which has five massive GCs, but no NSC. Under the assumption of a cuspy[1] Navarro-Frenk-White (NFW) dark matter halo (Navarro et al. 1996), the GCs are expected to sink towards the centre within 5 Gyr due to dynamical friction. The fact that the Fornax dSph is non-nucleated constitutes the so-called timing problem (Goerdt et al. 2006; Angus & Diaferio 2009), which is still unresolved (Meadows et al. 2020). The proposed solutions to this problem range from tidal interactions with the MW (Oh et al. 2000) or cored dark matter profiles (Goerdt et al. 2006; Meadows et al. 2020) to alternative flavours of dark matter (Bar et al. 2021). A more straightforward solution might be the assumption that the GCs have started from much larger galactocentric radii than where they are currently (Boldrini et al. 2019), and Leung et al. (2020) proposed that a recent dwarf galaxy merger could have ejected the clusters to the outskirts of the galaxy.

[1]Cuspy DM haloes rise steeply towards the centre, while cored haloes show a flattening.

In addition, when two massive galaxies merge, it is expected that their central SMBHs form a BH binary at the centre of the merger remnant (e.g. Menou et al. 2001; Chapon et al. 2013; Rantala et al. 2019). Dynamical interactions between stars of a preexisting NSC and such a BH binary can transfer energy to the stars and hence destroy the NSC (e.g. Quinlan & Hernquist 1997; Milosavljević & Merritt 2001; Arca Sedda et al. 2019).

These examples illustrate the importance of considering the effects of galaxy evolution on NSCs in individual systems, and it is also an open question of how the environment shapes NSC formation. Comparing the nucleation fraction of low-mass galaxies ($M_{\rm gal} < 10^9 M_\odot$) in different environments, Sánchez-Janssen et al. (2019) reported higher NSC occupation fractions in denser environments. In contrast, Baldassare et al. (2014) found no dependence on the environment in their comparison between massive field ETGs and galaxies in Virgo. It is unclear whether the discrepancy between these two studies stems from the different mass ranges that are considered or from the restricted sample sizes in the latter study (Neumayer et al. 2020). Moreover, there are indications that the fraction of nucleated ETGs increases towards the dense centres of galaxy clusters (Ferguson & Sandage 1989; Lisker et al. 2007; Lim et al. 2018), but again all these studies come from ETGs. Additionally, most studies of the nucleation fraction of galaxies were done in dense environments like the Virgo, Fornax, or Coma galaxy clusters (den Brok et al. 2014; Sánchez-Janssen et al. 2019; Zanatta et al. 2021). In contrast, the nucleation fraction in less dense environments – for example in the Local Group or around massive galaxies like the Centaurus group – is largely unconstrained due to lacking observations at low galaxy masses. Upcoming wide field photometric surveys with Euclid or the LSST might help to constrain the nucleation fraction in these environments. Nevertheless, besides establishing the abundance of NSCs, further studies of the properties of these NSCs will be required to test how galaxy nucleation is affected by the environment.

7.5 Nuclear star clusters as hosts of black holes

NSCs are known to co-exist with massive BHs and the ratio between BH and NSC mass seems to increase with increasing galaxy mass (Sect. 1.4.2), indicating that BHs start to dominate the mass in a galaxy's centre for galaxies with $M_{\rm gal} > 10^{10} M_\odot$. As described above, interactions between stars and a SMBH might destroy NSCs and the existence of SMBHs might prohibit NSC growth (e.g. Antonini 2013; Antonini et al. 2015), but NSCs could also be fundamental in the formation and growth of SMBHs.

In general, the formation sites and mechanisms of SMBHs are not well constrained and different formation channels were proposed (see recent reviews by Greene et al. 2020 and Inayoshi et al. 2020). One channel directly involves dense star clusters such as GCs or NSCs and describes the formation of a massive BH through repeated BH mergers or runaway collisions of stars (e.g. Begelman & Rees 1978; Miller & Hamilton 2002; Freitag et al. 2006b,a; Fragione & Silk 2020; Das et al. 2021). As merging BHs can experience a recoil in the dynamical interaction (Holley-Bockelmann et al. 2008), the BH merger process is particularly efficient in dense star clusters where the escape velocity is high enough to prevent ejection of BHs from the star cluster (Antonini et al. 2019). As a consequence, BHs

produced by BH mergers can be retained and grow to larger masses with repeated mergers. At the moment, such a BH merger scenario is only theoretical, but makes NSCs to key targets of future multi-messenger astronomy with gravitational wave facilities such as the Laser Interferometer Space Antenna (LISA).

NSCs might also provide the sites in which massive BH seeds can grow. For example, NSCs provide the stellar densities to enable SMBH growth via tidal disruption and capture of stars (Strubbe & Quataert 2009). Tidal disruption events occur when stars pass sufficiently close to a massive BH and get tidally perturbed. As part of the stellar mass falls back to the BH, this process causes a bright transient event that might be used to find low-mass BHs in dwarf galaxies (Greene et al. 2020). The expected rates of these events are 100 times higher in NSCs than in non-nucleated galaxies (Pfister et al. 2020) and thus this capture of stars in NSCs might provide a way for BH growth. Currently, the number of observed tidal disruption events is very low, but future observations with LSST or eROSITA in the X-ray can test the predicted rates and hence constrain SMBH growth in massive star clusters. However, also the discussed NSC formation scenarios entail pathways for the growth of SMBHs. On the one hand, funneling of gas to a galaxy centre that leads to NSC growth via in-situ star formation can also feed an existing SMBH (Hopkins & Quataert 2010) and some NSCs show indeed signatures of gas accretion onto a BH (Seth et al. 2008a). On the other hand, inspiraling GCs can bring in their own central BHs which then might merge in the NSC in a gravitational wave event (Liu & Lai 2020), but it is still debated whether GCs can host massive BHs or if any BH merger remnant is likly to escape the GC due to the lower escape velocities (Antonini et al. 2019).

In addition, NSCs might prove fundamental in the search for the illusive intermediate mass black holes (IMBHs). Those BHs with masses $M_{\rm BH} \sim 100 - 10^5 M_\odot$ are expected to bridge between the stellar mass BHs that are the end products of massive stars and SMBHs (e.g. Greene et al. 2020). Detections of IMBHs have been claimed for several massive MW GCs such as ωCen, 47 Tuc, or M 54 (see the compilation by Greene et al. 2020) using dynamical modelling, and X-ray spectra have been used to identify accretion signatures of possible IMBHs in dwarf galaxies (Straub et al. 2014; Pasham et al. 2014). Since massive NSCs are known to host SMBHs, it has been suggested that lower-mass NSCs, in particular in low-mass galaxies, might host IMBHs. NSCs might provide the high stellar densities required to detect a dynamical imprint of a IMBH, but so far searches for IMBHs in NSCs and GCs remain inconclusive (e.g. Baumgardt et al. 2019; Greene et al. 2020). In the coming decades, next-generation extremely large telescopes such as ESO's ELT are expected to bring the spatial resolution and sensitivity to unambiguously detect non-active BHs with $M_{\rm BH} < 10^5 M_\odot$ in massive star clusters, if they exist (Casares & Jonker 2014; Fiorentino et al. 2020; Greene et al. 2020).

7.6 Constraining the assembly of galaxies with star clusters

According to the standard cosmological model, galaxies form hierarchically. After an initial phase of gas accretion and in-situ star formation in the early Universe, they grow through

mergers and the accretion of dwarf galaxies. As these mergers and interactions alter the galaxy structure, disentangling the mass assembly history of galaxies is challenging – but fundamentally important to study galaxy evolution. Thanks to Gaia, the assembly history of the MW can be decomposed into individual merger events (Helmi et al. 2018), but similar studies are unfortunately not possible beyond the Local Group with current telescopes. However, it is possible to study the evolution of distant galaxies using dense star clusters such as NSCs and GCs that preserve their stellar populations even after mergers, and thus are excellent tracers of the assembly history of their host galaxy.

In the context of galaxy evolution, GCs are often regarded as fossil records that contain the information of their birth place encapsulated in their stellar populations which makes them valuable tracers of galaxy evolution. The analysis of GCs using MUSE data presented in Chapt. 4 indicates that GCs hold up to this promise. Their kinematics trace the rotation of the galaxy spheroid and the metallicities of the red, metal-rich GCs follow the mean galaxy metallicity from the central regions out to several effective radii. In addition, the metallicity distribution of GCs holds information of accreted dwarf galaxies that have brought in more metal-poor GCs and the age-metallicity distribution of MW GCs has been recently used to reconstruct the assembly history of the MW (Kruijssen et al. 2019a,b, 2020).

In addition to genuine GCs, stripped NSCs of disrupted galaxies are powerful probes of galaxy assembly as they directly signify a merger or accretion event. In the MW, some GCs (or rather stripped NSCs) can be traced back to their host galaxy (Massari et al. 2019; Pfeffer et al. 2020). The most prominent example here is M 54 which is traditionally classified as a MW GC, but still sits in the centre of the Sagittarius dSph (Ibata et al. 1997; Alfaro-Cuello et al. 2019). In addition, ωCen might be the stripped NSC of the progenitor of the Gaia-Enceladus or maybe the Sequoia accretion event (Myeong et al. 2019; Pfeffer et al. 2020). These conclusions are based on the complex internal abundances and their orbital properties within the MW, but there are several more candidates of stripped NSCs in the MW (Neumayer et al. 2020; Pfeffer et al. 2020). Because of the underlying relations connecting galaxies and their NSCs, identifying a stripped NSC allows an estimate of the host galaxy properties such as its mass and chemical abundance (Alfaro-Cuello et al. 2019). However, NSCs that are still located in the centres of their hosts might also be equally valuable records of galaxy assembly.

NSCs provide a unique window into the various physical processes that shape the central regions of galaxies, for example central bursts of star formation or mergers of BHs, but unlike BHs they retain their evolutionary history imprinted in their stellar populations and internal kinematics. The metallicity distribution and the star formation history of a NSC reflect the stellar populations of inspiraled GCs with an additional contribution from central in-situ star formation. Disentangling these two processes with stellar population analysis as presented in this thesis therefore allows us to get a handle on both the initial GC population and the conditions of central star formation throughout the galaxy's assembly. For this reason, NSCs are potentially powerful tracers of the central evolution of a galaxy, but are rarely used as such.

Unveiling the details of the complex interplay of galaxies and their star clusters is crucial not only to understand star cluster formation, but also to disentangle the assembly histories of galaxies using star clusters as fossil tracers. Together, dense star clusters such as NSCs

and GCs probe the properties of a galaxy from the centre to the halo regions, and from the early in-situ star formation to the accretion of low-mass dwarf galaxies. Detailed studies of star cluster abundances and properties in various galaxy environments as well as flexible models that incorporate all relevant relations between host galaxies and their star clusters will be essential to unlock their potential as tracers of galaxy evolution.

A | Appendix of Chapter 2

A.1 S/N requirements

In order to verify that we can extract stellar kinematic and population properties from the low S/N spectra (e.g. GCs), we set up several tests that use the E-MILES SSP model templates as test spectra with known LOSVD parameters, metallicity, and age. We cut the spectra to the MUSE wavelength range, artificially redshifted, and broadened it to a certain radial velocity and velocity dispersion. Then, random noise was added to reach a specific S/N before fitting the spectrum with pPXF. Figure A.1 illustrates how well velocity, age, and metallicity are recovered by pPXF as a function of the spectral S/N. This is shown with four different SSP templates as input and at each S/N value, the fit is repeated five times to estimate the mean and standard deviation.

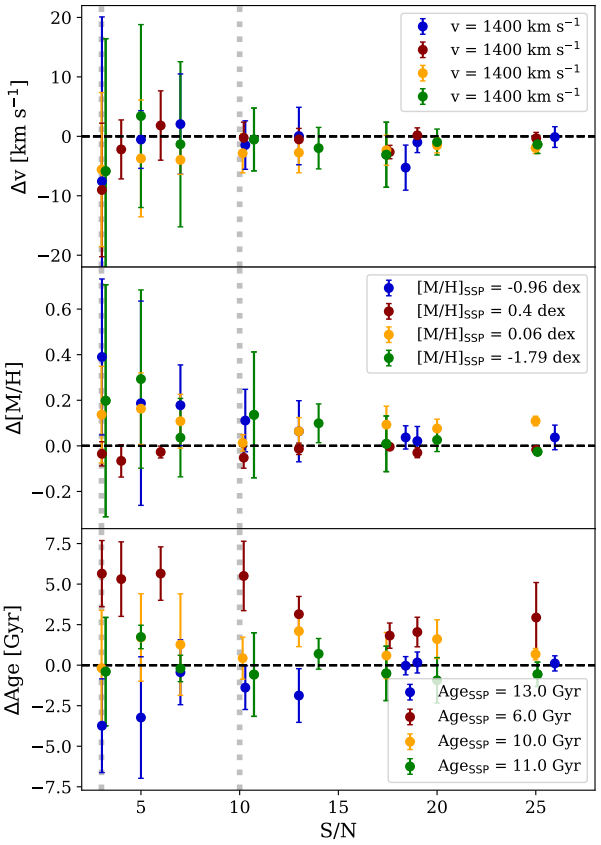

Figure A.1.: Recovery of SSP input parameters with pPXF versus S/N of the spectrum. We use four different SSP templates (as indicated by different colours). The vertical lines indicate the threshold S/N values of ten and three that we chose for reliable measurements of metallicities and velocities, respectively.

We found that a S/N $\geqslant$ 5 is needed to get a radial velocity estimate within 10 km s^{-1} accuracy. A S/N $\geqslant$ 3 is required to get radial velocities within $\sim$ 20 km s^{-1} accuracy. This should be sufficient to determine the velocity dispersion of a large sample of GCs or identifying rotating substructure. Testing with different metallicities, we find that the uncertainties of the radial velocities increase for more metal-poor spectra. This is most likely caused by the lack of strong lines, which makes fitting for the velocity with pPXF's cross-correlation method more difficult.

We found a S/N $\geqslant$ 10 is required to determine the metallicity within 0.2 dex. The age is

less well recovered at these low S/N, in particular young ages. For Chapt. 4, the metallicity S/N threshold was lowered to S/N $\geqslant$ 10.

B | Appendix of Chapter 4

B.1 Different metallicity measurements

Our default approach to measure GC metallicities used the E-MILES SSP models with an age constraint $\geq$ 8 Gyr. In the following, we present the CZR using different approaches to fit metallicities based on a smaller sub-sample of 135 GCs with S/N > 10. Besides E-MILES models with and without age constraint, we also used the scaled solar MILES and the α-enhanced MILES models. They have smaller wavelength range and have [α/Fe] = 0 dex (scaled solar) and 0.4 dex (α-enhanced) at all metallicities, respectively.

In addition to full spectral fitting, we determined metallicities of 135 GCs with S/N > 10 from our sample using line-strength indices following the method described in Iodice et al. (2019a) and Sarzi et al. (2018). To avoid contamination from sky residuals, a restricted wavelength region between 4800 and 5500 Å was used. The line-strengths of Hβ, Fe5015, Mgb, Fe5720, and Fe5335 were determined in the LIS system (Vazdekis et al. 2010, 2015) and were compared to the predictions from the MILES models (Vazdekis et al. 2012). The best-fitting values were determined using a MCMC algorithm (Martín-Navarro et al. 2018).

Table B.1 lists the different approaches and we show the resulting CZRs in Fig. B.1 for both total and iron metallicities using [M/H] = [Fe/H] + 0.75 [α/Fe] as a conversion for the MILES models and the line-strength metallicities. The default values derived with the E-MILES models (method A) are shown as the grey dots. In each case, we fitted the relation both with a quadratic equation (Eq. 4.5) and a piecewise linear curve (Eq. 4.6). The best-fitting parameters from least-square fits to the respective CZRs are reported in Table B.2.

Irrespective of the chosen SSP models, we always found a steep slope of the colour-

Table B.1.: Overview of different approaches to determine metallicities from the GCs. Method A is the default approach, as also used in paper I.

	Method name	Description
A	E-MILES	baseFe, age $\geq$ 8 Gyr
B	scaled solar MILES	[α/Fe] = 0 dex, age $\geq$ 8 Gyr
C	α-enhanced MILES	[α/Fe] = 0.4 dex, age $\geq$ 8 Gyr
D	full E-MILES	baseFe, no age constraint
E	Line-strength indices	age > 10 Gyr

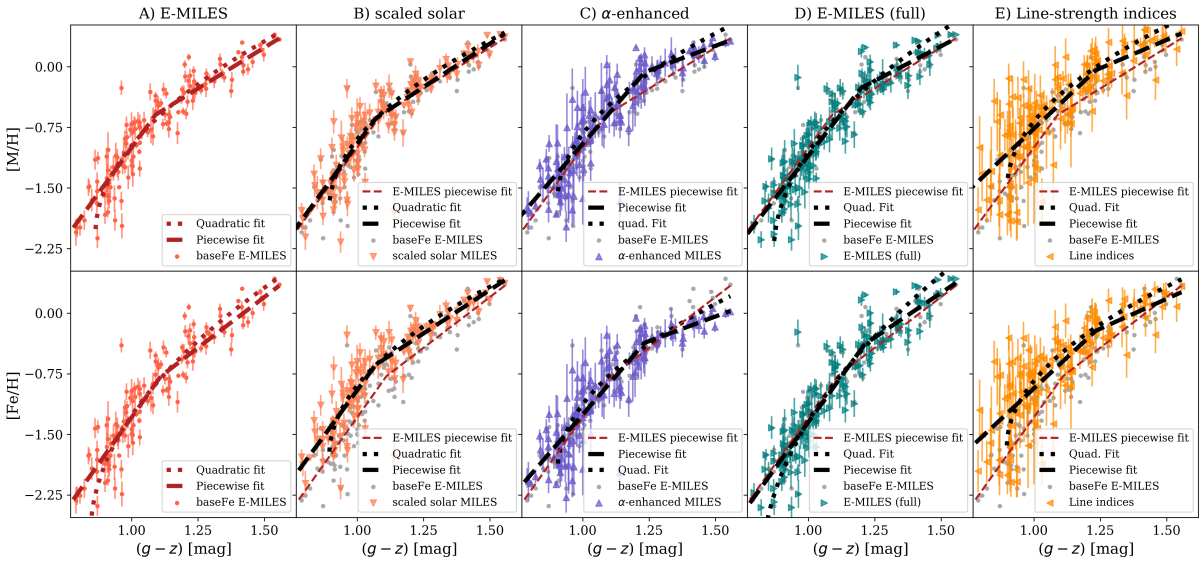

Figure B.1.: CZR for different metallicity measurement approaches (listed in Table B.1) based on total metallicities (*top*) and iron metallicities (*bottom*). From left to right: CZR using the E-MILES library with age constraint ≥ 8 Gyr (method A), scaled-solar MILES models (method B), α-enhanced MILES models (method C), E-MILES models without age constraint (method D), and line-strength indices (method E). The grey symbols show the points from method A as reference, and the lines show the respective fits. The best-fitting parameters are found in Table B.2.

metallicity relation at low metallicities when using full spectral fitting with PPXF. Using line-strength indices (method E) to measure metallicities results in a significantly larger scatter and larger errorbars, possibly due to the limited wavelength range that is used, but we observed the same non-linear trend in the CZR.

C | Appendix of Chapter 5

C.1 Modelling of more complex galaxies

In Sect. 5.2.1, we describe our approach to disentangle the NSC and galaxy contribution to the central PSF spectrum based on IMFIT modelling. Fig. 5.1 shows this approach for one of the dwarf galaxies to illustrate the method, but especially the more massive galaxies are structurally more complex and their models still show some residuals in the 2D maps. To illustrate this, we show the decomposition of FCC 170 in Fig. C.1.

FCC 170 is an edge-on S0 galaxy with multiple structural components including a thin disk, thick disk, and a X-shaped bulge component (see e.g. Pinna et al. 2019a; Poci et al.

Table B.2.: Colour-metallicity relation fit parameters when using total metallicities [M/H] or iron metallicities [Fe/H].

Method	a	b	c	m_1	b_1	m_2	b_2	x_0
[M/H]								
A)	1.34 ± 0.01	0.46 ± 0.02	0.11 ± 0.01	4.51 ± 0.32	−5.51 ± 0.36	2.03 ± 0.20	−2.81 ± 0.36	1.09 ± 0.03
B)	1.33 ± 0.01	0.49 ± 0.03	0.14 ± 0.01	4.51 ± 0.49	−5.47 ± 0.54	2.15 ± 0.26	−2.94 ± 0.54	1.07 ± 0.04
C)	1.32 ± 0.01	0.48 ± 0.03	0.13 ± 0.01	4.58 ± 0.49	-5.53 ± 0.55	2.16 ± 0.26	−2.94 ± 0.54	1.07 ± 0.04
D)	1.31 ± 0.01	0.39 ± 0.02	0.08 ± 0.01	4.21 ± 0.27	−5.31 ± 0.35	1.72 ± 0.39	−2.32 ± 0.35	1.20 ± 0.04
E)	1.24 ± 0.01	0.45 ± 0.03	0.15 ± 0.02	3.11 ± 0.29	−3.88 ± 0.45	1.41 ± 0.71	−1.77 ± 0.44	1.23 ± 0.08
[Fe/H]								
A)	1.37 ± 0.01	0.38 ± 0.02	0.07 ± 0.01	4.63 ± 0.31	−5.90 ± 0.38	2.51 ± 0.24	−3.55 ± 0.37	1.11 ± 0.03
B)	1.33 ± 0.01	0.49 ± 0.03	0.14 ± 0.01	4.51 ± 0.49	−5.47 ± 0.54	2.15 ± 0.26	−2.94 ± 0.54	1.07 ± 0.04
C)	1.47 ± 0.02	0.55 ± 0.03	0.13 ± 0.01	3.69 ± 0.26	−5.00 ± 0.36	1.64 ± 0.47	−2.51 ± 0.35	1.21 ± 0.05
D)	1.34 ± 0.01	0.32 ± 0.02	0.05 ± 0.01	4.55 ± 0.27	−5.90 ± 0.38	2.21 ± 0.47	−3.06 ± 0.37	1.21 ± 0.04
E)	1.32 ± 0.01	0.51 ± 0.03	0.15 ± 0.02	3.07 ± 0.29	−4.00 ± 0.46	1.48 ± 0.71	−2.04 ± 0.45	1.23 ± 0.09

The parameters a, b, and c refer to least-square fits with a quadratic equation (Eq. 4.5), the m_1, b_1, m_2, b_2, and x_0 to the piecewise linear fit (Eq. 4.6). The different methods are described in Table B.1.

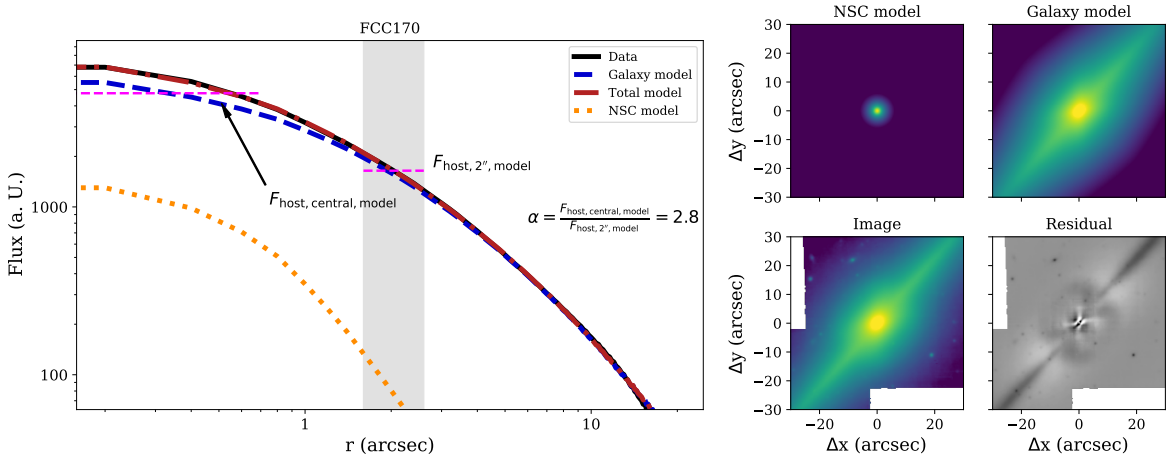

Figure C.1.: IMFIT modelling of FCC 170 to decompose the white-light image into a galaxy and a NSC component, similar to Fig. 5.1. *Left*: radial profile of the data (solid black line), galaxy model (dashed blue line), NSC model (dotted orange line), and combined model (dashed-dotted red line). The grey areas show the extraction regions. The mean fluxes in these regions are indicated by the horizontal dashed magenta lines to illustrate the scaling factor α. *Right*: 2D cutout images of the original image (bottom left), NSC and galaxy model (top row) and resulting residual image (bottom right). In this case, the galaxy model consists of a Sérsic, a edge-on disk model and a generalised exponential function to describe the numerous components in this galaxy. The NSC model is a Moffat function. Even with this multi-component model, there are still residuals left.

2021). Modelling this galaxy with IMFIT is challenging. Our best-fit model includes a Sérsic component, a 2D edge-on disk model, and generalised elliptical function to describe the X-shaped bulge in addition to the point-source Moffat function of the NSC[1]. While the radial profile exhibits a close fit of this model to the data, the 2D residual still shows structure in the centre. In this best-fit model, we find $\alpha = 2.8$, but this value is subject to uncertainties of up to $\sim 20\%$ arising from the modelling choice. For example, including further galaxy components in the centre can decrease the flux from the model NSC and thus enhance α. For this reason, we attempted to base our set of IMFIT models on physical components in the galaxy (e.g. disks, bulge, NSC), instead of choosing an arbitrary number of components. Nonetheless, as discussed in Sect. 5.2.2, our stellar population results are robust against changes in α.

C.2 Exemplary binned metallicity maps

We present the radial metallicity profiles from Voronoi binned maps in Fig. 5.2 and compare them to the different extraction radii. To illustrate how these one-dimensional profiles relate to the binned maps, we show cut-outs of the metallicity maps of four galaxies as examples in Fig. C.2. Two of those (FCC 188 and FCC 202) show drops in the radial metallicity profile corresponding to central bins with lower metallicity, while the other two (VCC 990 and FCC 310) show higher metallicity in their centres than in the surroundings.

[1]See https://www.mpe.mpg.de/~erwin/code/imfit/ for a detailed description of these components.

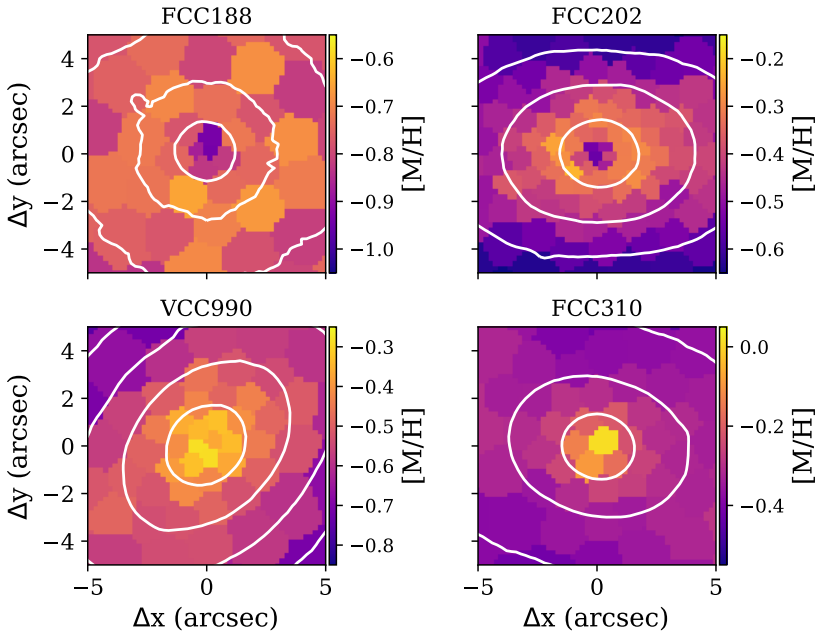

Figure C.2.: Voronoi-binned metallicity map of the central 5 × 5″ of FCC 188, FCC 202, VCC 990, and FCC 310 to illustrate the central metallicity behaviour in two dimensions rather than the radial profiles presented in Fig. 5.2. FCC 188 and FCC 202 are two galaxies that show drops in metallicity at the NSC position, while VCC 990 and FCC 310 show increasing metallicity towards the centre. Arbitrary surface brightness levels shown in white to guide the eye. The different panels have different metallicity scaling.

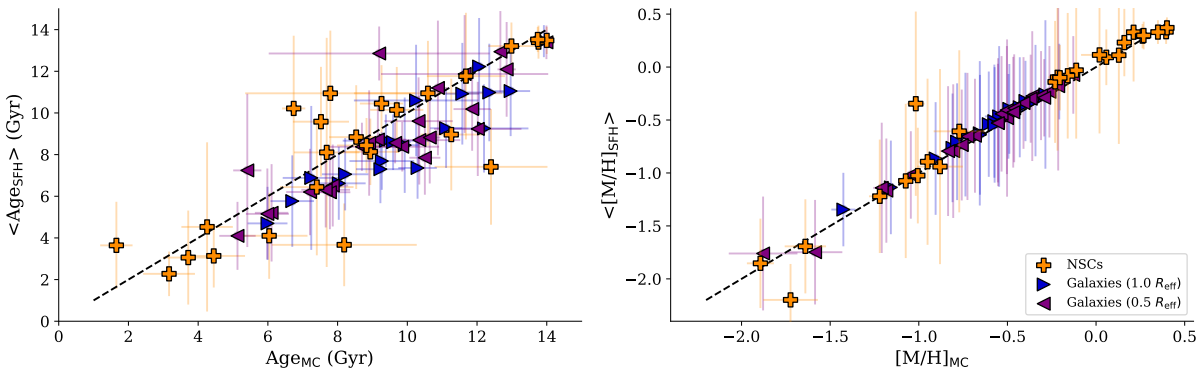

Figure C.3.: Comparison of mean ages (*top*) and metallicities (*bottom*) as inferred from the MC approach (x-axis) and regularisation approach (y-axis). For the regularisation approach, errorbars refer to the weighted uncertainties that also reflect the width of the age and metallicity distributions.

C.3 Ages and metallicities from different approaches

Figure C.3 shows a comparison of the extracted ages and metallicities of the different components using either the weighted mean from the regularised fit or the MC approach as described in Sect. 2.4. Both methods agree within the uncertainties. The metallicities obtained from both methods agree very well, except for the NSC of FCC 119, for which the MC approach gives a lower metallicity than the regularisation approach, although both methods agree within uncertainties. This difference is most likely caused by the presence of strong emission lines in the NSC spectrum that affect the line profiles.

References

Abazajian, K., Adelman-McCarthy, J. K., Agüeros, M. A., et al. 2003, AJ, 126, 2081

Adamo, A., Hollyhead, K., Messa, M., et al. 2020, MNRAS, 499, 3267

Adamo, A., Östlin, G., Zackrisson, E., et al. 2010, MNRAS, 407, 870

Afanasiev, A. V., Chilingarian, I. V., Mieske, S., et al. 2018, MNRAS, 477, 4856

Agarwal, M. & Milosavljević, M. 2011, ApJ, 729, 35

Ahn, C. P., Seth, A. C., Cappellari, M., et al. 2018, ApJ, 858, 102

Ahn, C. P., Seth, A. C., den Brok, M., et al. 2017, ApJ, 839, 72

Alfaro-Cuello, M., Kacharov, N., Neumayer, N., et al. 2019, ApJ, 886, 57

Alves-Brito, A., Hau, G. K. T., Forbes, D. A., et al. 2011, MNRAS, 417, 1823

An, D., Beers, T. C., Johnson, J. A., et al. 2012, Astronomical Society of the Pacific Conference Series, Vol. 458, Metallicity Distribution of the Galactic Halo from SDSS Photometry, ed. W. Aoki, M. Ishigaki, T. Suda, T. Tsujimoto, & N. Arimoto, 179

Anderson, J. & King, I. R. 2000, PASP, 112, 1360

Angus, G. W. & Diaferio, A. 2009, MNRAS, 396, 887

Antonini, F. 2013, ApJ, 763, 62

Antonini, F., Barausse, E., & Silk, J. 2015, ApJ, 812, 72

Antonini, F., Capuzzo-Dolcetta, R., Mastrobuono- Battisti, A., & Merritt, D. 2012, ApJ, 750, 111

Antonini, F., Gieles, M., & Gualandris, A. 2019, MNRAS, 486, 5008

Arca Sedda, M., Berczik, P., Capuzzo-Dolcetta, R., et al. 2019, MNRAS, 484, 520

Arca-Sedda, M. & Capuzzo-Dolcetta, R. 2014, ApJ, 785, 51

Arca-Sedda, M. & Capuzzo-Dolcetta, R. 2016, arXiv e-prints, arXiv:1601.04861

Arca-Sedda, M., Capuzzo-Dolcetta, R., & Spera, M. 2016, MNRAS, 456, 2457

Arca Sedda, M., Gualandris, A., Do, T., et al. 2020, ApJ, 901, L29

Arnold, J. A., Romanowsky, A. J., Brodie, J. P., et al. 2011, ApJ, 736, L26

Asa'd, R. & Goudfrooij, P. 2020, MNRAS, 498, 2814

Asa'd, R., Goudfrooij, P., As'ad, A. M., et al. 2021, arXiv e-prints, arXiv:2104.11873

Ashman, K. M. & Zepf, S. E. 1992, ApJ, 384, 50

Bacon, R., Accardo, M., Adjali, L., et al. 2010, in Proc. SPIE, Vol. 7735, Ground-based and Airborne Instrumentation for Astronomy III, 773508

Bacon, R., Copin, Y., Monnet, G., et al. 2001, MNRAS, 326, 23

Balcells, M., Graham, A. W., Domínguez-Palmero, L., & Peletier, R. F. 2003, ApJ, 582, L79

Balcells, M. & Quinn, P. J. 1990, ApJ, 361, 381

Baldassare, V. F., Gallo, E., Miller, B. P., et al. 2014, ApJ, 791, 133

Bar, N., Blas, D., Blum, K., & Kim, H. 2021, arXiv e-prints, arXiv:2102.11522

Barmby, P., Huchra, J. P., Brodie, J. P., et al. 2000, AJ, 119, 727

Barnes, J. E. & Hernquist, L. 1992, Annual Review of Astronomy and Astrophysics, 30, 705

Bastian, N., Covey, K. R., & Meyer, M. R. 2010, ARA&A, 48, 339

Bastian, N. & Lardo, C. 2018, ARA&A, 56, 83

Baumgardt, H., He, C., Sweet, S. M., et al. 2019, MNRAS, 488, 5340

Baumgardt, H. & Hilker, M. 2018, MNRAS, 478, 1520

Beasley, M., Bridges, T., Peng, E., et al. 2008, MNRAS, 386, 1443

Beasley, M. A. 2020, Globular Cluster Systems and Galaxy Formation, 245–277

Beasley, M. A., Baugh, C. M., Forbes, D. A., Sharples, R. M., & Frenk, C. S. 2002, MNRAS, 333, 383

Beasley, M. A., Leaman, R., Gallart, C., et al. 2019, MNRAS, 487, 1986

Beasley, M. A., Trujillo, I., Leaman, R., & Montes, M. 2018a, Nature, 555, 483

Beasley, M. A., Trujillo, I., Leaman, R., & Montes, M. 2018b, Nature, 555, 483

Begelman, M. C. & Rees, M. J. 1978, MNRAS, 185, 847

Bekki, K. 2007, Publications of the Astronomical Society of Australia, 24, 77

Bekki, K., Beasley, M. A., Brodie, J. P., & Forbes, D. A. 2005, MNRAS, 363, 1211

Bekki, K., Couch, W. J., Drinkwater, M. J., & Shioya, Y. 2003, MNRAS, 344, 399

Bekki, K., Couch, W. J., & Shioya, Y. 2006, ApJ, 642, L133

Bekki, K. & Freeman, K. C. 2003, MNRAS, 346, L11

Bellazzini, M., Ferraro, F. R., & Ibata, R. 2003, AJ, 125, 188

Bellazzini, M., Ibata, R. A., Chapman, S. C., et al. 2008, AJ, 136, 1147

Bellstedt, S., Robotham, A. S. G., Driver, S. P., et al. 2021, MNRAS, 503, 3309

Belokurov, V., Zucker, D. B., Evans, N. W., et al. 2007, ApJ, 654, 897

Bendinelli, O. 1991, ApJ, 366, 599

Bidaran, B., Pasquali, A., Lisker, T., et al. 2020, MNRAS, 497, 1904

Binney, J. 1978, MNRAS, 183, 501

Bittner, A., Falcón-Barroso, J., Nedelchev, B., et al. 2019, A&A, 628, A117

Blakeslee, J. P., Jordán, A., Mei, S., et al. 2009, ApJ, 694, 556

Bland-Hawthorn, J. & Gerhard, O. 2016, ARA&A, 54, 529

Blum, R. D., Ramírez, S. V., Sellgren, K., & Olsen, K. 2003, ApJ, 597, 323

Blumenthal, G. R., Faber, S. M., Primack, J. R., & Rees, M. J. 1984, Nature, 311, 517

Böcker, A., Leaman, R., van de Ven, G., et al. 2020, MNRAS, 491, 823

Bois, M., Emsellem, E., Bournaud, F., et al. 2011, MNRAS, 416, 1654

Böker, T. 2010, in Star Clusters: Basic Galactic Building Blocks Throughout Time and Space, ed. R. de Grijs & J. R. D. Lépine, Vol. 266, 58–63

Böker, T., Laine, S., van der Marel, R. P., et al. 2002, AJ, 123, 1389

Böker, T., Sarzi, M., McLaughlin, D. E., et al. 2004, AJ, 127, 105

Boldrini, P., Mohayaee, R., & Silk, J. 2019, MNRAS, 485, 2546

Bradley, L., Sipocz, B., Robitaille, T., et al. 2019, astropy/photutils: v0.7.1

Bressan, A., Marigo, P., Girardi, L., et al. 2012, MNRAS, 427, 127

Brodie, J. P., Romanowsky, A. J., Strader, J., & Forbes, D. A. 2011, AJ, 142, 199

Brodie, J. P., Romanowsky, A. J., Strader, J., et al. 2014, ApJ, 796, 52

Brodie, J. P. & Strader, J. 2006, ARA&A, 44, 193

Brodie, J. P., Strader, J., Denicoló, G., et al. 2005, AJ, 129, 2643

Brown, G., Gnedin, O. Y., & Li, H. 2018, ApJ, 864, 94

Brüns, R. C., Kroupa, P., Fellhauer, M., Metz, M., & Assmann, P. 2011, A&A, 529, A138

Burbidge, E. M., Burbidge, G. R., & Prendergast, K. H. 1959, ApJ, 130, 739

Caldwell, N. & Romanowsky, A. J. 2016, ApJ, 824, 42

Caldwell, N., Schiavon, R., Morrison, H., Rose, J. A., & Harding, P. 2011, AJ, 141, 61

Cantiello, M., Venhola, A., Grado, A., et al. 2020, A&A, 639, A136

Cappellari, M. 2002, MNRAS, 333, 400

Cappellari, M. 2016, ARA&A, 54, 597

Cappellari, M. 2017, MNRAS, 466, 798

Cappellari, M. & Copin, Y. 2003a, MNRAS, 342, 345

Cappellari, M. & Copin, Y. 2003b, MNRAS, 342, 345

Cappellari, M. & Emsellem, E. 2004, PASP, 116, 138

Cappellari, M., Emsellem, E., Krajnović, D., et al. 2011, MNRAS, 413, 813

Capuzzo-Dolcetta, R. & Mastrobuono-Battisti, A. 2009, A&A, 507, 183

Capuzzo-Dolcetta, R. & Miocchi, P. 2008a, ApJ, 681, 1136

Capuzzo-Dolcetta, R. & Miocchi, P. 2008b, MNRAS, 388, L69

Capuzzo-Dolcetta, R. & Tesseri, A. 1999, MNRAS, 308, 961

Capuzzo-Dolcetta, R. & Tosta e Melo, I. 2017, MNRAS, 472, 4013

Carollo, C. M., Danziger, I. J., Rich, R. M., & Chen, X. 1997, ApJ, 491, 545

Carson, D. J., Barth, A. J., Seth, A. C., et al. 2015, AJ, 149, 170

Casares, J. & Jonker, P. G. 2014, Space Sci. Rev., 183, 223

Caso, J. P., Bassino, L. P., & Gómez, M. 2017, MNRAS, 470, 3227

Cenarro, A. J., Beasley, M. A., Strader, J., Brodie, J. P., & Forbes, D. A. 2007, AJ, 134, 391

Chandrasekhar, S. 1943, ApJ, 97, 255

Chapon, D., Mayer, L., & Teyssier, R. 2013, MNRAS, 429, 3114

Chies-Santos, A. L., Larsen, S. S., Wehner, E. M., et al. 2011, A&A, 525, A19

Choksi, N. & Gnedin, O. Y. 2019, MNRAS, 488, 5409

Choksi, N., Gnedin, O. Y., & Li, H. 2018, MNRAS, 480, 2343

Chomiuk, L., Strader, J., & Brodie, J. P. 2008, AJ, 136, 234

Chung, C., Yoon, S.-J., Lee, S.-Y., & Lee, Y.-W. 2016, ApJ, 818, 201

Cohen, J. G., Blakeslee, J. P., & Côté, P. 2003, ApJ, 592, 866

Cohen, J. G., Blakeslee, J. P., & Ryzhov, A. 1998, ApJ, 496, 808

Colless, M., Peterson, B. A., Jackson, C., et al. 2003, arXiv e-prints, astro

Conroy, C. 2013, ARA&A, 51, 393

Conroy, C., Graves, G. J., & van Dokkum, P. G. 2014, ApJ, 780, 33

Conselice, C. J. 2014, ARA&A, 52, 291

Corsini, E. M. 2014, in Astronomical Society of the Pacific Conference Series, Vol. 486, Multi-Spin Galaxies, ed. E. Iodice & E. M. Corsini, 51

Côté, P. 1999, AJ, 118, 406

Côté, P., Blakeslee, J. P., Ferrarese, L., et al. 2004, ApJS, 153, 223

Côté, P., Marzke, R. O., & West, M. J. 1998, ApJ, 501, 554

Côté, P., McLaughlin, D. E., Hanes, D. A., et al. 2001, ApJ, 559, 828

Côté, P., Piatek, S., Ferrarese, L., et al. 2006, ApJS, 165, 57

Cresci, G., Mannucci, F., Maiolino, R., et al. 2010, Nature, 467, 811

Crnojević, D., Ferguson, A. M. N., Irwin, M. J., et al. 2013, MNRAS, 432, 832

Crnojević, D., Grebel, E. K., & Koch, A. 2010, A&A, 516, A85

Crnojević, D., Sand, D. J., Bennet, P., et al. 2019, ApJ, 872, 80

Crnojević, D., Sand, D. J., Caldwell, N., et al. 2014, ApJ, 795, L35

Crnojević, D., Sand, D. J., Spekkens, K., et al. 2016, ApJ, 823, 19

Czesla, S., Schröter, S., Schneider, C. P., et al. 2019, PyA: Python astronomy-related packages

Da Rocha, C., Mieske, S., Georgiev, I. Y., et al. 2011, A&A, 525, A86

Dabringhausen, J., Hilker, M., & Kroupa, P. 2008, MNRAS, 386, 864

Dabringhausen, J., Kroupa, P., & Baumgardt, H. 2009, MNRAS, 394, 1529

Das, A., Schleicher, D. R. G., Leigh, N. W. C., & Boekholt, T. C. N. 2021, MNRAS, 503, 1051

Davies, R. L. & Illingworth, G. 1983, ApJ, 266, 516

Davison, T. A., Norris, M. A., Pfeffer, J. L., Davies, J. J., & Crain, R. A. 2020, MNRAS, 497, 81

de Vaucouleurs, G. 1948, Annales d'Astrophysique, 11, 247

de Zeeuw, P. T., Bureau, M., Emsellem, E., et al. 2002, MNRAS, 329, 513

Dekker, H., D'Odorico, S., Kaufer, A., Delabre, B., & Kotzlowski, H. 2000, Society of Photo-Optical Instrumentation Engineers (SPIE) Conference Series, Vol. 4008, Design, construction, and performance of UVES, the echelle spectrograph for the UT2 Kueyen Telescope at the ESO Paranal Observatory, ed. M. Iye & A. F. Moorwood, 534–545

den Brok, M., Peletier, R. F., Seth, A., et al. 2014, MNRAS, 445, 2385

Do, T., Kerzendorf, W., Konopacky, Q., et al. 2018, ApJ, 855, L5

Dopita, M., Rhee, J., Farage, C., et al. 2010, Ap&SS, 327, 245

Dotter, A., Sarajedini, A., Anderson, J., et al. 2010, ApJ, 708, 698

Drinkwater, M. J., Gregg, M. D., & Colless, M. 2001, ApJ, 548, L139

Drinkwater, M. J., Gregg, M. D., Hilker, M., et al. 2003, Nature, 423, 519

Drinkwater, M. J., Jones, J. B., Gregg, M. D., & Phillipps, S. 2000, PASA, 17, 227

Duc, P.-A., Cuillandre, J.-C., Karabal, E., et al. 2015, MNRAS, 446, 120

Efstathiou, G., Ellis, R. S., & Carter, D. 1982, MNRAS, 201, 975

Eigenthaler, P., Puzia, T. H., Taylor, M. A., et al. 2018, ApJ, 855, 142

Eisenhauer, F., Abuter, R., Bickert, K., et al. 2003, in Society of Photo-Optical Instrumentation Engineers (SPIE) Conference Series, Vol. 4841, Instrument Design and Performance for Optical/Infrared Ground-based Telescopes, ed. M. Iye & A. F. M. Moorwood, 1548–1561

Elmegreen, B. G. 2010, ApJ, 712, L184

Elmegreen, B. G. 2018, ApJ, 869, 119

Emsellem, E., Cappellari, M., Krajnović, D., et al. 2007, MNRAS, 379, 401

Emsellem, E., Monnet, G., & Bacon, R. 1994, A&A, 285, 723

Emsellem, E., Renaud, F., Bournaud, F., et al. 2015, MNRAS, 446, 2468

Emsellem, E. & van de Ven, G. 2008, ApJ, 674, 653

Emsellem, E., van der Burg, R. F. J., Fensch, J., et al. 2019, A&A, 625, A76

Erwin, P. 2015, ApJ, 799, 226

Erwin, P. & Gadotti, D. A. 2012, Advances in Astronomy, 2012, 946368

Event Horizon Telescope Collaboration, Akiyama, K., Alberdi, A., et al. 2019, ApJ, 875, L1

Evstigneeva, E. A., Gregg, M. D., Drinkwater, M. J., & Hilker, M. 2007, AJ, 133, 1722

Fahrion, K., Georgiev, I., Hilker, M., et al. 2019a, A&A, 625, A50

Fahrion, K., Leaman, R., Lyubenova, M., & van de Ven, G. 2021, subm., submitted to A&A.

Fahrion, K., Lyubenova, M., Hilker, M., et al. 2020a, A&A, 637, A26

Fahrion, K., Lyubenova, M., Hilker, M., et al. 2020b, A&A, 637, A27

Fahrion, K., Lyubenova, M., van de Ven, G., et al. 2021, A&A, 650, A137

Fahrion, K., Lyubenova, M., van de Ven, G., et al. 2019b, A&A, 628, A92

Fahrion, K., Müller, O., Rejkuba, M., et al. 2020c, A&A, 634, A53

Faifer, F. R., Forte, J. C., Norris, M. A., et al. 2011, MNRAS, 416, 155

Falcón-Barroso, J., Sánchez-Blázquez, P., Vazdekis, A., et al. 2011, A&A, 532, A95

Fedotov, K., Gallagher, S. C., Konstantopoulos, I. S., et al. 2011, AJ, 142, 42

Feldmeier, A., Neumayer, N., Seth, A., et al. 2014, A&A, 570, A2

Feldmeier-Krause, A., Kerzendorf, W., Do, T., et al. 2020, MNRAS, 494, 396

Feldmeier-Krause, A., Kerzendorf, W., Neumayer, N., et al. 2017a, MNRAS, 464, 194

Feldmeier-Krause, A., Neumayer, N., Schödel, R., et al. 2015, A&A, 584, A2

Feldmeier-Krause, A., Zhu, L., Neumayer, N., et al. 2017b, MNRAS, 466, 4040

Fellhauer, M. & Kroupa, P. 2002, MNRAS, 330, 642

Fellhauer, M. & Kroupa, P. 2005, MNRAS, 359, 223

Ferguson, H. C. 1989, AJ, 98, 367

Ferguson, H. C. & Sandage, A. 1989, ApJ, 346, L53

Ferrarese, L., Côté, P., Cuilland re, J.-C., et al. 2012, ApJS, 200, 4

Ferrarese, L., Côté, P., Dalla Bontà, E., et al. 2006, ApJ, 644, L21

Ferrarese, L. & Merritt, D. 2000, The Astrophysical Journal, Volume 539, Issue 1, pp. L9-L12., 539, L9

Filippenko, A. V. & Ho, L. C. 2003, ApJ, 588, L13

Fiorentino, G., Bellazzini, M., Spera, M., et al. 2020, MNRAS, 494, 4413

Fitzpatrick, M. J. 1993, in Astronomical Society of the Pacific Conference Series, Vol. 52, Astronomical Data Analysis Software and Systems II, ed. R. J. Hanisch, R. J. V. Brissenden, & J. Barnes, 472

Forbes, D., Spitler, L., Strader, J., et al. 2011, MNRAS, 413, 2943

Forbes, D. A., Alabi, A., Brodie, J. P., et al. 2017, AJ, 153, 114

Forbes, D. A., Bastian, N., Gieles, M., et al. 2018, Proceedings of the Royal Society of London Series A, 474, 20170616

Forbes, D. A. & Bridges, T. 2010, MNRAS, 404, 1203

Forbes, D. A., Brodie, J. P., & Grillmair, C. J. 1997, AJ, 113, 1652

Forbes, D. A., Read, J. I., Gieles, M., & Collins, M. L. M. 2018, MNRAS, 481, 5592

Forbes, D. A. & Remus, R.-S. 2018, MNRAS, 479, 4760

Foreman-Mackey, D., Hogg, D. W., Lang, D., & Goodman, J. 2013, PASP, 125, 306

Foster, C., Pastorello, N., Roediger, J., et al. 2016, MNRAS, 457, 147

Foster, C., Spitler, L. R., Romanowsky, A. J., et al. 2011, MNRAS, 415, 3393

Fouqué, P., Solanes, J. M., Sanchis, T., & Balkowski, C. 2001, A&A, 375, 770

Fragione, G. & Silk, J. 2020, MNRAS, 498, 4591

Fragkoudi, F., Di Matteo, P., Haywood, M., et al. 2017, A&A, 607, L4

Franx, M., Illingworth, G., & Heckman, T. 1989, AJ, 98, 538

Franx, M. & Illingworth, G. D. 1988, ApJ, 327, L55

Freeman, K. C. 1970, ApJ, 160, 811

Freitag, M., Gürkan, M. A., & Rasio, F. A. 2006a, MNRAS, 368, 141

Freitag, M., Rasio, F. A., & Baumgardt, H. 2006b, MNRAS, 368, 121

Freudling, W., Romaniello, M., Bramich, D. M., et al. 2013, A&A, 559, A96

Gaia Collaboration, Prusti, T., de Bruijne, J. H. J., et al. 2016, A&A, 595, A1

Gallazzi, A., Charlot, S., Brinchmann, J., White, S. D. M., & Tremonti, C. A. 2005, MNRAS, 362, 41

Galleti, S., Bellazzini, M., Buzzoni, A., Federici, L., & Fusi Pecci, F. 2009, A&A, 508, 1285

Gao, H. & Ho, L. C. 2017, ApJ, 845, 114

Gebhardt, K., Richstone, D., Tremaine, S., et al. 2003, ApJ, 583, 92

Genzel, R., Eisenhauer, F., & Gillessen, S. 2010, Reviews of Modern Physics, 82, 3121

Georgiev, I. Y. & Böker, T. 2014, MNRAS, 441, 3570

Georgiev, I. Y., Böker, T., Leigh, N., Lützgendorf, N., & Neumayer, N. 2016, MNRAS, 457, 2122

Georgiev, I. Y., Goudfrooij, P., & Puzia, T. H. 2012, MNRAS, 420, 1317

Georgiev, I. Y., Goudfrooij, P., Puzia, T. H., & Hilker, M. 2008, AJ, 135, 1858

Georgiev, I. Y., Hilker, M., Puzia, T. H., Goudfrooij, P., & Baumgardt, H. 2009a, MNRAS, 396, 1075

Georgiev, I. Y., Hilker, M., Puzia, T. H., Goudfrooij, P., & Baumgardt, H. 2009b, MNRAS, 396, 1075

Georgiev, I. Y., Puzia, T. H., Goudfrooij, P., & Hilker, M. 2010, MNRAS, 406, 1967

Georgiev, I. Y., Puzia, T. H., Hilker, M., & Goudfrooij, P. 2009c, MNRAS, 392, 879

Gerhard, O. E. 1993, MNRAS, 265, 213

Giavalisco, M., Ferguson, H. C., Koekemoer, A. M., et al. 2004, ApJ, 600, L93

Girardi, L., Bressan, A., Bertelli, G., & Chiosi, C. 2000, A&AS, 141, 371

Glover, S. 2005, Space Sci. Rev., 117, 445

Gnedin, O. Y., Ostriker, J. P., & Tremaine, S. 2014, The Astrophysical Journal, 785, 71

Goerdt, T., Moore, B., Read, J. I., Stadel, J., & Zemp, M. 2006, MNRAS, 368, 1073

Graham, A. W. & Guzmán, R. 2003, AJ, 125, 2936

Graham, A. W. & Spitler, L. R. 2009, MNRAS, 397, 2148

Gravity Collaboration, Abuter, R., Amorim, A., et al. 2018, A&A, 618, L10

Grebel, E. K. 2001, Astrophysics and Space Science Supplement, 277, 231

Greene, J. E., Strader, J., & Ho, L. C. 2020, ARA&A, 58, 257

Greif, T. H. 2015, Computational Astrophysics and Cosmology, 2, 3

Guérou, A., Emsellem, E., Krajnović, D., et al. 2016, A&A, 591, A143

Guérou, A., Emsellem, E., McDermid, R. M., et al. 2015, ApJ, 804, 70

Guillard, N., Emsellem, E., & Renaud, F. 2016, MNRAS, 461, 3620

Haşegan, M., Jordán, A., Côté, P., et al. 2005, ApJ, 627, 203

Hanuschik, R., Data Processing, & Quality Control Group. 2017, in ESO Calibration Workshop: The Second Generation VLT Instruments and Friends, 15

Harris, W. E. 1991, ARA&A, 29, 543

Harris, W. E. 1996, AJ, 112, 1487

Harris, W. E. 2009a, ApJ, 699, 254

Harris, W. E. 2009b, ApJ, 703, 939

Harris, W. E., Blakeslee, J. P., Whitmore, B. C., et al. 2016, The Astrophysical Journal, 817, 58

Harris, W. E., Blakeslee, J. P., Whitmore, B. C., et al. 2016, ApJ, 817, 58

Harris, W. E. & Canterna, R. 1979, ApJ, 231, L19

Harris, W. E., Ciccone, S. M., Eadie, G. M., et al. 2017, ApJ, 835, 101

Harris, W. E., Harris, G. L. H., & Alessi, M. 2013, ApJ, 772, 82

Hartmann, M., Debattista, V. P., Seth, A., Cappellari, M., & Quinn, T. R. 2011, MNRAS, 418, 2697

Helmi, A., Babusiaux, C., Koppelman, H. H., et al. 2018, Nature, 563, 85

Herrmann, K. A., Ciardullo, R., Feldmeier, J. J., & Vinciguerra, M. 2008, ApJ, 683, 630

Hilker, M., Baumgardt, H., Infante, L., et al. 2007, A&A, 463, 119

Hilker, M., Infante, L., & Richtler, T. 1999a, Astronomy and Astrophysics Supplement Series, 138, 55

Hilker, M., Infante, L., Vieira, G., Kissler-Patig, M., & Richtler, T. 1999b, A&AS, 134, 75

Hilker, M. & Richtler, T. 2000, A&A, 362, 895

Holley-Bockelmann, K., Gültekin, K., Shoemaker, D., & Yunes, N. 2008, ApJ, 686, 829

Hopkins, P. F. & Quataert, E. 2010, MNRAS, 407, 1529

Hubble, E. P. 1926, ApJ, 64, 321

Huchra, J., Davis, M., Latham, D., & Tonry, J. 1983, ApJS, 52, 89

Hunt, L. K., Combes, F., García-Burillo, S., et al. 2008, A&A, 482, 133

Husemann, B., Jahnke, K., Sánchez, S. F., et al. 2013, A&A, 549, A87

Ibata, R. A., Bellazzini, M., Malhan, K., Martin, N., & Bianchini, P. 2019, Nature Astronomy, 3, 667

Ibata, R. A., Wyse, R. F. G., Gilmore, G., Irwin, M. J., & Suntzeff, N. B. 1997, AJ, 113, 634

Inayoshi, K., Visbal, E., & Haiman, Z. 2020, ARA&A, 58, 27

Iodice, E., Capaccioli, M., Grado, A., et al. 2016, ApJ, 820, 42

Iodice, E., Sarzi, M., Bittner, A., et al. 2019a, A&A, 627, A136

Iodice, E., Spavone, M., Capaccioli, M., et al. 2019b, A&A, 623, A1

Ivezić, Ž., Kahn, S. M., Tyson, J. A., et al. 2019, ApJ, 873, 111

Ivkovich, N. & McCall, M. L. 2019, MNRAS, 486, 1964

Janz, J., Norris, M. A., Forbes, D. A., et al. 2016, MNRAS, 456, 617

Jerjen, H., Binggeli, B., & Freeman, K. C. 2000a, AJ, 119, 593

Jerjen, H., Freeman, K. C., & Binggeli, B. 2000b, AJ, 119, 166

Jesseit, R., Naab, T., Peletier, R. F., & Burkert, A. 2007, MNRAS, 376, 997

Johnson, C. I., Rich, R. M., Pilachowski, C. A., et al. 2015, AJ, 150, 63

Johnston, E. J., Häußler, B., Aragón-Salamanca, A., et al. 2017, MNRAS, 465, 2317

Johnston, E. J., Puzia, T. H., D'Ago, G., et al. 2020, MNRAS, 495, 2247

Jordán, A., Blakeslee, J. P., Côté, P., et al. 2007, ApJS, 169, 213

Jordán, A., Peng, E. W., Blakeslee, J. P., et al. 2015, ApJS, 221, 13

Jordán, A., Peng, E. W., Blakeslee, J. P., et al. 2009, ApJS, 180, 54

Kacharov, N., Neumayer, N., Seth, A. C., et al. 2018, MNRAS, 480, 1973

Karachentsev, I. D. & Kashibadze, O. G. 2006, Astrophysics, 49, 3

Karachentsev, I. D., Tully, R. B., Dolphin, A., et al. 2007, AJ, 133, 504

Katz, H. & Ricotti, M. 2014, MNRAS, 444, 2377

Kim, H.-S., Yoon, S.-J., Sohn, S. T., et al. 2013, ApJ, 763, 40

Kim, S., Rey, S.-C., Jerjen, H., et al. 2014, ApJS, 215, 22

Kim, W.-T. & Elmegreen, B. G. 2017, ApJ, 841, L4

King, I. 1962, AJ, 67, 471

King, I. R., Bedin, L. R., Cassisi, S., et al. 2012, AJ, 144, 5

Kirby, E. N., Cohen, J. G., Guhathakurta, P., et al. 2013, ApJ, 779, 102

Kissler-Patig, M. & Gebhardt, K. 1998, AJ, 116, 2237

Kissler-Patig, M., Jordán, A., & Bastian, N. 2006, A&A, 448, 1031

Koleva, M., Prugniel, P., De Rijcke, S., & Zeilinger, W. W. 2011, MNRAS, 417, 1643

Kormendy, J. 1977, ApJ, 218, 333

Kormendy, J., Fisher, D. B., Cornell, M. E., & Bender, R. 2009, ApJS, 182, 216

Kormendy, J. & Ho, L. C. 2013, Annual Review of Astronomy and Astrophysics, 51, 511

Kormendy, J. & Illingworth, G. 1982, ApJ, 256, 460

Kornei, K. A. & McCrady, N. 2009, ApJ, 697, 1180

Kovalev, M., Brinkmann, S., Bergemann, M., & MPIA IT-department. 2018, NLTE MPIA web server, [Online]. Available: http://nlte.mpia.de Max Planck Institute for Astronomy, Heidelberg.

Krajnović, D., Emsellem, E., Cappellari, M., et al. 2011, MNRAS, 414, 2923

Krajnović, D., Karick, A. M., Davies, R. L., et al. 2013, MNRAS, 433, 2812

Krajnović, D., Weilbacher, P. M., Urrutia, T., et al. 2015, MNRAS, 452, 2

Kravtsov, A. V. & Gnedin, O. Y. 2005, ApJ, 623, 650

Kruijssen, J. M. D. 2015, MNRAS, 454, 1658

Kruijssen, J. M. D., Pfeffer, J. L., Chevance, M., et al. 2020, MNRAS, 498, 2472

Kruijssen, J. M. D., Pfeffer, J. L., Crain, R. A., & Bastian, N. 2019a, MNRAS, 486, 3134

Kruijssen, J. M. D., Pfeffer, J. L., Reina-Campos, M., Crain, R. A., & Bastian, N. 2019b, MNRAS, 486, 3180

Kubo, J. M., Stebbins, A., Annis, J., et al. 2007, ApJ, 671, 1466

Kundu, A. & Whitmore, B. C. 2001, AJ, 121, 2950

Kuntschner, H., Emsellem, E., Bacon, R., et al. 2010, MNRAS, 408, 97

Kuntschner, H., Ziegler, B. L., Sharples, R. M., Worthey, G., & Fricke, K. J. 2002, A&A, 395, 761

Lamers, H. J. G. L. M., Baumgardt, H., & Gieles, M. 2010, MNRAS, 409, 305

Lamers, H. J. G. L. M., Kruijssen, J. M. D., Bastian, N., et al. 2017, A&A, 606, A85

Larsen, S. S., Brodie, J. P., Huchra, J. P., Forbes, D. A., & Grillmair, C. J. 2001, AJ, 121, 2974

Larsen, S. S., Brodie, J. P., & Strader, J. 2012, A&A, 546, A53

Larsen, S. S. & Richtler, T. 1999, A&A, 345, 59

Lauer, T. R., Faber, S. M., Gebhardt, K., et al. 2005, AJ, 129, 2138

Law, D. R. & Majewski, S. R. 2010, ApJ, 714, 229

Leaman, R., Ruiz-Lara, T., Cole, A. A., et al. 2020, MNRAS, 492, 5102

Leaman, R., VandenBerg, D. A., & Mendel, J. T. 2013, MNRAS, 436, 122

Lee, J. C., Whitmore, B. C., Thilker, D. A., et al. 2021, arXiv e-prints, arXiv:2101.02855

Lee, M. G. & Jang, I. S. 2016, ApJ, 822, 70

Lee, M. G., Park, H. S., Kim, E., et al. 2008, ApJ, 682, 135

Lee, S.-Y., Chung, C., & Yoon, S.-J. 2019, ApJS, 240, 2

Lee, Y.-W., Gim, H. B., & Casetti-Dinescu, D. I. 2007, ApJ, 661, L49

Lee, Y. W., Joo, J. M., Sohn, Y. J., et al. 1999, Nature, 402, 55

Lelli, F., Fraternali, F., & Verheijen, M. 2014, A&A, 563, A27

Leśniewska, A. & Michałowski, M. J. 2019, A&A, 624, L13

Leung, G. Y. C., Leaman, R., van de Ven, G., & Battaglia, G. 2020, MNRAS, 493, 320

Li, H. & Gnedin, O. Y. 2014, ApJ, 796, 10

Li, H. & Gnedin, O. Y. 2019, MNRAS, 486, 4030

Libeskind, N. I., Knebe, A., Hoffman, Y., et al. 2011, MNRAS, 411, 1525

Lieder, S., Lisker, T., Hilker, M., Misgeld, I., & Durrell, P. 2012, A&A, 538, A69

Lim, S., Peng, E. W., Côté, P., et al. 2018, ApJ, 862, 82

Lindner, U., Einasto, J., Einasto, M., et al. 1995, A&A, 301, 329

Lisker, T., Grebel, E. K., Binggeli, B., & Glatt, K. 2007, ApJ, 660, 1186

Liu, B. & Lai, D. 2020, Phys. Rev. D, 102, 023020

Liu, C., Peng, E. W., Côté, P., et al. 2015, ApJ, 812, 34

Liu, Y., Peng, E. W., Jordán, A., et al. 2019, ApJ, 875, 156

Longmore, S. & Kruijssen, J. M. D. 2018, Galaxies, 6, 55

Lotz, J. M., Miller, B. W., & Ferguson, H. C. 2004, ApJ, 613, 262

Lovell, M. R., Eke, V. R., Frenk, C. S., & Jenkins, A. 2011, MNRAS, 413, 3013

Lu, J. R., Do, T., Ghez, A. M., et al. 2013, ApJ, 764, 155

Lynden-Bell, D. & Rees, M. J. 1971, MNRAS, 152, 461

Lyubenova, M. & Tsatsi, A. 2019, A&A, 629, A44

Lyubenova, M., van den Bosch, R. C. E., Côté, P., et al. 2013, MNRAS, 431, 3364

Ma, X., Grudić, M. Y., Quataert, E., et al. 2020, MNRAS, 493, 4315

Ma, X., Quataert, E., Wetzel, A., Faucher-Giguére, C.-A., & Boylan-Kolchin, M. 2021, MNRAS[arXiv:2006.10065]

Madau, P. & Dickinson, M. 2014, ARA&A, 52, 415

Madrid, J. P., Leigh, N. W. C., Hurley, J. R., & Giersz, M. 2017, MNRAS, 470, 1729

Mahani, H., Zonoozi, A. H., Haghi, H., et al. 2021, MNRAS, 502, 5185

Majewski, S. R., Patterson, R. J., Dinescu, D. I., et al. 2000, in Liege International Astrophysical Colloquia, Vol. 35, Liege International Astrophysical Colloquia, ed. A. Noels, P. Magain, D. Caro, E. Jehin, G. Parmentier, & A. A. Thoul, 619

Malin, D. F. & Carter, D. 1983, ApJ, 274, 534

Mapelli, M. & Bressan, A. 2013, MNRAS, 430, 3120

Maraston, C., Bastian, N., Saglia, R. P., et al. 2004, A&A, 416, 467

Marín-Franch, A., Aparicio, A., Piotto, G., et al. 2009, ApJ, 694, 1498

Marino, A. F., Milone, A. P., Karakas, A. I., et al. 2015, MNRAS, 450, 815

Martín-Navarro, I., Vazdekis, A., Falcón-Barroso, J., et al. 2018, MNRAS, 475, 3700

Massari, D., Koppelman, H. H., & Helmi, A. 2019, A&A, 630, L4

Massari, D., Mucciarelli, A., Dalessandro, E., et al. 2017, MNRAS, 468, 1249

Masters, K. L., Jordán, A., Côté, P., et al. 2010, ApJ, 715, 1419

Matthews, L. D. & Gallagher, John S., I. 1997, AJ, 114, 1899

Matthews, L. D., Gallagher, John S., I., Krist, J. E., et al. 1999, AJ, 118, 208

McConnachie, A. W. 2012, AJ, 144, 4

McConnell, N. J. & Ma, C.-P. 2013, ApJ, 764, 184

McDermid, R. M., Alatalo, K., Blitz, L., et al. 2015, MNRAS, 448, 3484

McDermid, R. M., Emsellem, E., Shapiro, K. L., et al. 2006, MNRAS, 373, 906

McDermid, R. M., Emsellem, E., Shapiro, K. L., et al. 2007, in IAU Symposium, Vol. 241, Stellar Populations as Building Blocks of Galaxies, ed. A. Vazdekis & R. Peletier, 399–403

McLaughlin, D. E. 1995, AJ, 109, 2034

McQuinn, K. B. W., Skillman, E. D., Cannon, J. M., et al. 2010, ApJ, 721, 297

Meadows, N., Navarro, J. F., Santos-Santos, I., Benítez-Llambay, A., & Frenk, C. 2020, MNRAS, 491, 3336

Mei, S., Blakeslee, J. P., Côté, P., et al. 2007, ApJ, 655, 144

Mendel, J. T., Simard, L., Palmer, M., Ellison, S. L., & Patton, D. R. 2014, ApJS, 210, 3

Menou, K., Haiman, Z., & Narayanan, V. K. 2001, ApJ, 558, 535

Mieske, S., Frank, M. J., Baumgardt, H., et al. 2013, A&A, 558, A14

Mieske, S., Hilker, M., & Infante, L. 2002, A&A, 383, 823

Mieske, S., Hilker, M., & Infante, L. 2004, A&A, 418, 445

Mieske, S., Hilker, M., Infante, L., & Jordán, A. 2006, AJ, 131, 2442

Mieske, S., Hilker, M., Jordán, A., et al. 2008, A&A, 487, 921

Mieske, S., Hilker, M., & Misgeld, I. 2012, A&A, 537, A3

Mieske, S. & Kroupa, P. 2008, ApJ, 677, 276

Mihos, J. C. & Hernquist, L. 1994, ApJ, 437, L47

Miller, B. P., Gallo, E., Greene, J. E., et al. 2015, ApJ, 799, 98

Miller, M. C. & Hamilton, D. P. 2002, MNRAS, 330, 232

Milosavljević, M. 2004, ApJ, 605, L13

Milosavljević, M. & Merritt, D. 2001, ApJ, 563, 34

Minniti, D., Kissler-Patig, M., Goudfrooij, P., & Meylan, G. 1998, AJ, 115, 121

Minniti, D., Ripepi, V., Fernández-Trincado, J. G., et al. 2021, A&A, 647, L4

Misgeld, I. & Hilker, M. 2011, MNRAS, 414, 3699

Monnet, G., Bacon, R., & Emsellem, E. 1992, A&A, 253, 366

Muñoz, C., Geisler, D., Villanova, S., et al. 2018, A&A, 620, A96

Muñoz, C., Villanova, S., Geisler, D., et al. 2020, MNRAS, 492, 3742

Muñoz, C., Villanova, S., Geisler, D., et al. 2017, A&A, 605, A12

Muñoz, R. P., Eigenthaler, P., Puzia, T. H., et al. 2015, ApJ, 813, L15

Müller, O., Fahrion, K., Rejkuba, M., et al. 2021a, A&A, 645, A92

Müller, O., Jerjen, H., & Binggeli, B. 2015, A&A, 583, A79

Müller, O., Jerjen, H., & Binggeli, B. 2017, A&A, 597, A7

Müller, O., Jerjen, H., & Binggeli, B. 2018a, A&A, 615, A105

Müller, O., Jerjen, H., Pawlowski, M. S., & Binggeli, B. 2016, A&A, 595, A119

Müller, O., Pawlowski, M. S., Jerjen, H., & Lelli, F. 2018b, Science, 359, 534

Müller, O., Pawlowski, M. S., Lelli, F., et al. 2021b, A&A, 645, L5

Müller, O., Rejkuba, M., & Jerjen, H. 2018c, A&A, 615, A96

Müller, O., Rejkuba, M., Pawlowski, M. S., et al. 2019, A&A, 629, A18

Muratov, A. L. & Gnedin, O. Y. 2010, ApJ, 718, 1266

Murray, N. 2009, ApJ, 691, 946

Myeong, G. C., Vasiliev, E., Iorio, G., Evans, N. W., & Belokurov, V. 2019, MNRAS, 488, 1235

Nasonova, O. G., de Freitas Pacheco, J. A., & Karachentsev, I. D. 2011, A&A, 532, A104

Navarro, J. F., Frenk, C. S., & White, S. D. M. 1996, ApJ, 462, 563

Neumayer, N., Seth, A., & Böker, T. 2020, A&A Rev., 28, 4

Neumayer, N. & Walcher, C. J. 2012, Advances in Astronomy, 2012, 709038

Nguyen, D. D., Seth, A. C., den Brok, M., et al. 2017, ApJ, 836, 237

Nguyen, D. D., Seth, A. C., Neumayer, N., et al. 2019, ApJ, 872, 104

Nguyen, D. D., Seth, A. C., Neumayer, N., et al. 2018, ApJ, 858, 118

Nguyen, D. D., Seth, A. C., Reines, A. E., et al. 2014, ApJ, 794, 34

Norris, M. A., Escudero, C. G., Faifer, F. R., et al. 2015, MNRAS, 451, 3615

Norris, M. A. & Kannappan, S. J. 2011, MNRAS, 414, 739

Norris, M. A., Kannappan, S. J., Forbes, D. A., et al. 2014, MNRAS, 443, 1151

Norris, M. A., Sharples, R. M., Bridges, T., et al. 2008, MNRAS, 385, 40

Norris, M. A., van de Ven, G., Kannappan, S. J., Schinnerer, E., & Leaman, R. 2019, MNRAS, 488, 5400

Ocvirk, P. 2010, ApJ, 709, 88

Oh, K. S., Lin, D. N. C., & Richer, H. B. 2000, ApJ, 531, 727

O'Leary, J. A., Moster, B. P., Naab, T., & Somerville, R. S. 2021, MNRAS, 501, 3215

Ordenes-Briceño, Y., Puzia, T. H., Eigenthaler, P., et al. 2018, ApJ, 860, 4

Oser, L., Ostriker, J. P., Naab, T., Johansson, P. H., & Burkert, A. 2010, ApJ, 725, 2312

Parikh, T., Thomas, D., Maraston, C., et al. 2021, arXiv e-prints, arXiv:2102.06703

Pasham, D. R., Strohmayer, T. E., & Mushotzky, R. F. 2014, Nature, 513, 74

Paudel, S., Lisker, T., & Kuntschner, H. 2011, MNRAS, 413, 1764

Paudel, S. & Yoon, S.-J. 2020, ApJ, 898, L47

Peñarrubia, J., Ma, Y.-Z., Walker, M. G., & McConnachie, A. 2014, MNRAS, 443, 2204

Pechetti, R., Seth, A., Neumayer, N., et al. 2020, ApJ, 900, 32

Peletier, R. F., Davies, R. L., Illingworth, G. D., Davis, L. E., & Cawson, M. 1990, AJ, 100, 1091

Peng, C. Y., Ho, L. C., Impey, C. D., & Rix, H.-W. 2002, AJ, 124, 266

Peng, C. Y., Ho, L. C., Impey, C. D., & Rix, H.-W. 2010, AJ, 139, 2097

Peng, E. W., Ford, H. C., & Freeman, K. C. 2004, ApJ, 602, 705

Peng, E. W., Jordán, A., Côté, P., et al. 2006, ApJ, 639, 95

Peng, E. W., Jordán, A., Côté, P., et al. 2008, ApJ, 681, 197

Perets, H. B. & Mastrobuono-Battisti, A. 2014, ApJ, 784, L44

Perina, S., Galleti, S., Fusi Pecci, F., et al. 2011, A&A, 531, A155

Perrett, K. M., Bridges, T. J., Hanes, D. A., et al. 2002, AJ, 123, 2490

Petts, J. A., Gualandris, A., & Read, J. I. 2015, MNRAS, 454, 3778

Pfeffer, J. & Baumgardt, H. 2013, MNRAS, 433, 1997

Pfeffer, J., Griffen, B. F., Baumgardt, H., & Hilker, M. 2014, MNRAS, 444, 3670

Pfeffer, J., Hilker, M., Baumgardt, H., & Griffen, B. F. 2016, MNRAS, 458, 2492

Pfeffer, J., Kruijssen, J. M. D., Crain, R. A., & Bastian, N. 2018, MNRAS, 475, 4309

Pfeffer, J., Lardo, C., Bastian, N., Saracino, S., & Kamann, S. 2021, MNRAS, 500, 2514

Pfeffer, J. L., Trujillo-Gomez, S., Kruijssen, J. M. D., et al. 2020, MNRAS, 499, 4863

Pfister, H., Volonteri, M., Dai, J. L., & Colpi, M. 2020, MNRAS, 497, 2276

Phillipps, S., Drinkwater, M. J., Gregg, M. D., & Jones, J. B. 2001, ApJ, 560, 201

Phillips, A. C., Illingworth, G. D., MacKenty, J. W., & Franx, M. 1996, AJ, 111, 1566

Pierce, M., Beasley, M. A., Forbes, D. A., et al. 2006a, MNRAS, 366, 1253

Pierce, M., Bridges, T., Forbes, D. A., et al. 2006b, MNRAS, 368, 325

Pietrinferni, A., Cassisi, S., Salaris, M., & Castelli, F. 2004, ApJ, 612, 168

Pietrinferni, A., Cassisi, S., Salaris, M., & Castelli, F. 2006, ApJ, 642, 797

Pillepich, A., Nelson, D., Hernquist, L., et al. 2018, MNRAS, 475, 648

Pillepich, A., Vogelsberger, M., Deason, A., et al. 2014, MNRAS, 444, 237

Pinna, F., Falcón-Barroso, J., Martig, M., et al. 2019a, A&A, 625, A95

Pinna, F., Falcón-Barroso, J., Martig, M., et al. 2019b, A&A, 623, A19

Planck Collaboration, Ade, P. A. R., Aghanim, N., et al. 2014, A&A, 571, A16

Poci, A., McDermid, R. M., Lyubenova, M., et al. 2021, A&A, 647, A145

Pota, V., Forbes, D. A., Romanowsky, A. J., et al. 2013, MNRAS, 428, 389

Pota, V., Napolitano, N. R., Hilker, M., et al. 2018, MNRAS, 481, 1744

Puzia, T. H., Kissler-Patig, M., & Goudfrooij, P. 2006, ApJ, 648, 383

Puzia, T. H., Kissler-Patig, M., Thomas, D., et al. 2005, A&A, 439, 997

Quinlan, G. D. & Hernquist, L. 1997, New A, 2, 533

Radburn-Smith, D. J., de Jong, R. S., Seth, A. C., et al. 2011, ApJS, 195, 18

Ramachandran, V., Hamann, W. R., Oskinova, L. M., et al. 2019, A&A, 625, A104

Rantala, A., Johansson, P. H., Naab, T., Thomas, J., & Frigo, M. 2019, ApJ, 872, L17

Recio-Blanco, A., Aparicio, A., Piotto, G., de Angeli, F., & Djorgovski, S. G. 2006, A&A, 452, 875

Reina-Campos, M. & Kruijssen, J. M. D. 2017, MNRAS, 469, 1282

Rejkuba, M. 2004, A&A, 413, 903

Rejkuba, M., Dubath, P., Minniti, D., & Meylan, G. 2007, A&A, 469, 147

Rejkuba, M., Greggio, L., Harris, W. E., Harris, G. L. H., & Peng, E. W. 2005, ApJ, 631, 262

Rejkuba, M., Harris, W. E., Greggio, L., et al. 2014, ApJ, 791, L2

Renaud, F. 2018, New A Rev., 81, 1

Renaud, F., Agertz, O., & Gieles, M. 2017, MNRAS, 465, 3622

Renzini, A. 2020, in Uncovering Early Galaxy Evolution in the ALMA and JWST Era, ed. E. da Cunha, J. Hodge, J. Afonso, L. Pentericci, & D. Sobral, Vol. 352, 33–37

Richtler, T. 2006, Bulletin of the Astronomical Society of India, 34, 83

Richtler, T., Hilker, M., Arnaboldi, M., & Barbosa, C. E. 2020, A&A, 643, A119

Rossa, J., van der Marel, R. P., Böker, T., et al. 2006, AJ, 132, 1074

Rubin, V. C. & Ford, Jr., W. K. 1970, ApJ, 159, 379

Rubin, V. C., Ford, Jr., W. K., & Thonnard, N. 1980, ApJ, 238, 471

Ryan, S. G. & Norris, J. E. 1991, AJ, 101, 1865

Saglia, R. P., Opitsch, M., Erwin, P., et al. 2016, ApJ, 818, 47

Sakari, C. M., Shetrone, M. D., McWilliam, A., & Wallerstein, G. 2021, MNRAS, 502, 5745

Salpeter, E. E. 1964, ApJ, 140, 796

Sánchez-Blázquez, P., Rosales-Ortega, F. F., Méndez-Abreu, J., et al. 2014, Astronomy & Astrophysics, 570, A6

Sánchez-Janssen, R., Côté, P., Ferrarese, L., et al. 2019, ApJ, 878, 18

Sandage, A. & Binggeli, B. 1984, AJ, 89, 919

Santucci, G., Brough, S., Scott, N., et al. 2020, ApJ, 896, 75

Sarzi, M., Iodice, E., Coccato, L., et al. 2018, A&A, 616, A121

Saulder, C., van Kampen, E., Chilingarian, I. V., Mieske, S., & Zeilinger, W. W. 2016, A&A, 596, A14

Schauer, A. T. P., Glover, S. C. O., Klessen, R. S., & Clark, P. 2020, arXiv e-prints, arXiv:2008.05663

Schiavi, R., Capuzzo-Dolcetta, R., Georgiev, I. Y., Arca-Sedda, M., & Mastrobuono-Battisti, A. 2021, MNRAS, 503, 594

Schiavon, R. P., Rose, J. A., Courteau, S., & MacArthur, L. A. 2004, ApJ, 608, L33

Schinnerer, E., Böker, T., Emsellem, E., & Downes, D. 2007, A&A, 462, L27

Schinnerer, E., Böker, T., Emsellem, E., & Lisenfeld, U. 2006, ApJ, 649, 181

Schlafly, E. F. & Finkbeiner, D. P. 2011, ApJ, 737, 103

Schödel, R., Feldmeier, A., Kunneriath, D., et al. 2014, A&A, 566, A47

Schödel, R., Nogueras-Lara, F., Gallego-Cano, E., et al. 2020, A&A, 641, A102

Schreiber, C., Pannella, M., Elbaz, D., et al. 2015, A&A, 575, A74

Schuberth, Y., Richtler, T., Bassino, L., & Hilker, M. 2008, A&A, 477, L9

Schuberth, Y., Richtler, T., Hilker, M., et al. 2010, A&A, 513, A52

Scott, N., Davies, R. L., Houghton, R. C. W., et al. 2014, MNRAS, 441, 274

Scott, N. & Graham, A. W. 2013, ApJ, 763, 76

Segers, M. C., Schaye, J., Bower, R. G., et al. 2016, MNRAS, 461, L102

Sérsic, J. L. 1968, Atlas de Galaxias Australes

Seth, A., Agüeros, M., Lee, D., & Basu-Zych, A. 2008a, ApJ, 678, 116

Seth, A. C., Blum, R. D., Bastian, N., Caldwell, N., & Debattista, V. P. 2008b, ApJ, 687, 997

Seth, A. C., Cappellari, M., Neumayer, N., et al. 2010, ApJ, 714, 713

Seth, A. C., Dalcanton, J. J., Hodge, P. W., & Debattista, V. P. 2006, The Astronomical Journal, 132, 2539

Seth, A. C., van den Bosch, R., Mieske, S., et al. 2014, Nature, 513, 398

Shapiro, K. L., Genzel, R., & Förster Schreiber, N. M. 2010, MNRAS, 403, L36

Shapley, H. 1938, Nature, 142, 715

Shappee, B. J. & Stanek, K. Z. 2011, ApJ, 733, 124

Sharina, M. E., Karachentsev, I. D., Dolphin, A. E., et al. 2008, MNRAS, 384, 1544

Shlosman, I., Begelman, M. C., & Frank, J. 1990, Nature, 345, 679

Shlosman, I., Frank, J., & Begelman, M. C. 1989, Nature, 338, 45

Sikkema, G., Carter, D., Peletier, R. F., et al. 2007, A&A, 467, 1011

Sills, A., Dalessandro, E., Cadelano, M., Alfaro-Cuello, M., & Kruijssen, J. M. D. 2019, MNRAS, 490, L67

Simon, J. D. 2019, ARA&A, 57, 375

Sinnott, B., Hou, A., Anderson, R., Harris, W. E., & Woodley, K. A. 2010, AJ, 140, 2101

Sormani, M. C., Sobacchi, E., Fragkoudi, F., et al. 2018, MNRAS, 481, 2

Soto, K. T., Lilly, S. J., Bacon, R., Richard, J., & Conseil, S. 2016, MNRAS, 458, 3210

Spengler, C., Côté, P., Roediger, J., et al. 2017, ApJ, 849, 55

Spitler, L. R., Forbes, D. A., & Beasley, M. A. 2008, MNRAS, 389, 1150

Spitzer, Lyman, J. 1940, MNRAS, 100, 396

Springel, V., White, S. D. M., Jenkins, A., et al. 2005, Nature, 435, 629

Stetson, P. B. 1987, PASP, 99, 191

Strader, J., Brodie, J. P., Cenarro, A. J., Beasley, M. A., & Forbes, D. A. 2005, AJ, 130, 1315

Strader, J., Brodie, J. P., Spitler, L., & Beasley, M. A. 2006, AJ, 132, 2333

Strader, J., Caldwell, N., & Seth, A. C. 2011, AJ, 142, 8

Strader, J., Seth, A. C., Forbes, D. A., et al. 2013, ApJ, 775, L6

Straub, O., Godet, O., Webb, N., Servillat, M., & Barret, D. 2014, A&A, 569, A116

Strubbe, L. E. & Quataert, E. 2009, MNRAS, 400, 2070

Tailo, M., Di Criscienzo, M., D'Antona, F., Caloi, V., & Ventura, P. 2016, MNRAS, 457, 4525

Taylor, M. A., Eigenthaler, P., Puzia, T. H., et al. 2018, ApJ, 867, L15

Taylor, M. A., Muñoz, R. P., Puzia, T. H., et al. 2016, arxiv:1608.07285

Taylor, M. A., Puzia, T. H., Harris, G. L., et al. 2010, ApJ, 712, 1191

Thomas, D., Maraston, C., Bender, R., & Mendes de Oliveira, C. 2005, ApJ, 621, 673

Thornley, M. D., Förster Schreiber, N. M., Lutz, D., et al. 2000, ApJ, 539, 641

Tonini, C. 2013, ApJ, 762, 39

Tonry, J. & Davis, M. 1979, AJ, 84, 1511

Tremaine, S. D., Ostriker, J. P., & Spitzer, Jr., L. 1975, ApJ, 196, 407

Tsatsi, A., Macciò, A. V., van de Ven, G., & Moster, B. P. 2015, ApJ, 802, L3

Tsatsi, A., Mastrobuono-Battisti, A., van de Ven, G., et al. 2017, MNRAS, 464, 3720

Tully, R. B. 2015, AJ, 149, 171

Tully, R. B., Libeskind, N. I., Karachentsev, I. D., et al. 2015, ApJ, 802, L25

Turner, M. L., Côté, P., Ferrarese, L., et al. 2012, ApJS, 203, 5

Usher, C., Brodie, J. P., Forbes, D. A., et al. 2019, MNRAS, 490, 491

Usher, C., Forbes, D. A., Brodie, J. P., et al. 2012, MNRAS, 426, 1475

Usher, C., Forbes, D. A., Brodie, J. P., et al. 2015, MNRAS, 446, 369

Valenti, E., Zoccali, M., Mucciarelli, A., et al. 2018, A&A, 616, A83

van de Ven, G., de Zeeuw, P. T., & van den Bosch, R. C. E. 2008, MNRAS, 385, 614

van de Ven, G., van den Bosch, R. C. E., Verolme, E. K., & de Zeeuw, P. T. 2006, A&A, 445, 513

van den Bosch, R. C. E., van de Ven, G., Verolme, E. K., Cappellari, M., & de Zeeuw, P. T. 2008, MNRAS, 385, 647

van der Marel, R. P. & Franx, M. 1993, ApJ, 407, 525

van Dokkum, P., Danieli, S., Cohen, Y., et al. 2018, Nature, 555, 629

van Dokkum, P., Wasserman, A., Danieli, S., et al. 2019, ApJ, 880, 91

van Dokkum, P. G., Abraham, R., Merritt, A., et al. 2015, ApJ, 798, L45

VandenBerg, D. A., Brogaard, K., Leaman, R., & Casagrande, L. 2013, ApJ, 775, 134

Vanzella, E., Calura, F., Meneghetti, M., et al. 2017, MNRAS, 467, 4304

Vazdekis, A., Casuso, E., Peletier, R. F., & Beckman, J. E. 1996, ApJS, 106, 307

Vazdekis, A., Coelho, P., Cassisi, S., et al. 2015, MNRAS, 449, 1177

Vazdekis, A., Koleva, M., Ricciardelli, E., Röck, B., & Falcón-Barroso, J. 2016, MNRAS, 463, 3409

Vazdekis, A., Ricciardelli, E., Cenarro, A. J., et al. 2012, MNRAS, 424, 157

Vazdekis, A., Sánchez-Blázquez, P., Falcón-Barroso, J., et al. 2010, MNRAS, 404, 1639

Veljanoski, J. & Helmi, A. 2016, A&A, 592, A55

Veljanoski, J., Mackey, A. D., Ferguson, A. M. N., et al. 2014, MNRAS, 442, 2929

Venhola, A., Peletier, R., Laurikainen, E., et al. 2020, A&A, 633, C2

Viaene, S., Sarzi, M., Zabel, N., et al. 2019, A&A, 622, A89

Villanova, S., Geisler, D., Gratton, R. G., & Cassisi, S. 2014, ApJ, 791, 107

Villaume, A., Romanowsky, A. J., Brodie, J., & Strader, J. 2019, The Astrophysical Journal, 879, 45

Villegas, D., Jordán, A., Peng, E. W., et al. 2010, ApJ, 717, 603

Vogelsberger, M., Genel, S., Springel, V., et al. 2014, MNRAS, 444, 1518

Voggel, K., Hilker, M., & Richtler, T. 2016, A&A, 586, A102

Voggel, K. T., Seth, A. C., Neumayer, N., et al. 2018, ApJ, 858, 20

Walcher, C. J., Böker, T., Charlot, S., et al. 2006, ApJ, 649, 692

Walcher, C. J., van der Marel, R. P., McLaughlin, D., et al. 2005, ApJ, 618, 237

Watkins, L. L., van der Marel, R. P., Sohn, S. T., & Evans, N. W. 2019, ApJ, 873, 118

Wehner, E. H. & Harris, W. E. 2006, ApJ, 644, L17

Weilbacher, P. M., Streicher, O., & Palsa, R. 2016, MUSE-DRP: MUSE Data Reduction Pipeline, Astrophysics Source Code Library

Weilbacher, P. M., Streicher, O., Urrutia, T., et al. 2012, in Proc. SPIE, Vol. 8451, Software and Cyberinfrastructure for Astronomy II, 84510B

Weilbacher, P. M., Streicher, O., Urrutia, T., et al. 2014, in Astronomical Society of the Pacific Conference Series, Vol. 485, Astronomical Data Analysis Software and Systems XXIII, ed. N. Manset & P. Forshay, 451

White, S. D. M. & Rees, M. J. 1978, MNRAS, 183, 341

Wise, J. H. 2019, arXiv e-prints, arXiv:1907.06653

Wolfe, A. M. & Burbidge, G. R. 1970, ApJ, 161, 419

Woodley, K. A. 2006, AJ, 132, 2424

Woodley, K. A., Gómez, M., Harris, W. E., Geisler, D., & Harris, G. L. H. 2010a, AJ, 139, 1871

Woodley, K. A., Harris, W. E., Beasley, M. A., et al. 2007, AJ, 134, 494

Woodley, K. A., Harris, W. E., Puzia, T. H., et al. 2010b, ApJ, 708, 1335

Worthey, G. 1994, ApJS, 95, 107

Xu, C. K., Zhao, Y., Scoville, N., et al. 2012, ApJ, 747, 85

Yoon, S.-J., Lee, S.-Y., Blakeslee, J. P., et al. 2011a, ApJ, 743, 150

Yoon, S.-J., Sohn, S. T., Lee, S.-Y., et al. 2011b, ApJ, 743, 149

Yoon, S.-J., Yi, S. K., & Lee, Y.-W. 2006, Science, 311, 1129

Zanatta, E. J. B., Sánchez-Janssen, R., Chies-Santos, A. L., de Souza, R. S., & Blakeslee, J. P. 2021, arXiv e-prints, arXiv:2103.02123

Zepf, S. E., Ashman, K. M., English, J., Freeman, K. C., & Sharples, R. M. 1999, AJ, 118, 752

Zhang, H.-X., Puzia, T. H., Peng, E. W., et al. 2018, The Astrophysical Journal, 858, 37

Zhu, L., van de Ven, G., Méndez-Abreu, J., & Obreja, A. 2018a, MNRAS, 479, 945

Zhu, L., van den Bosch, R., van de Ven, G., et al. 2018b, MNRAS, 473, 3000

Zhuang, Y., Leaman, R., van de Ven, G., et al. 2019, MNRAS, 483, 1862

Zinn, R. 1985, ApJ, 293, 424

> While it is always best to believe in oneself, a little help from others can be a great blessing.
>
> Iroh, Avatar: The Last Airbender

Acknowledgements

This thesis is the result of three years of work, but it could not have been possible without the collaboration, help, encouragement, and emotional support from a large number of people. First of all, I want to thank those that helped in the completion of this document by reading parts over and over in the hope to eradicate the last typo (likely in vain): my awesome sister Jana Fahrion, my travel buddy Georg Laage, my best flatmate Mattis Magg, my Beer Friday co-conspirator Adrian Bittner, my office mate Thomas Davison, and the greatest partner anyone could ever have - Dominik Dold.

Secondly, my greatest gratitude to my advisors. My greatest thanks to Mariya Lyubenova for your support and encouragement. You are always inspiring me to go further and always provided me with valuable advice – not only from the science side, but also on everything else: how to do talks, write papers and job applications, overcome imposter syndrome, and many other things that helped me to mature as a researcher on all levels. Similarly, I want to thank Michael Hilker for always answering my questions, scientific and otherwise, and being interested in collaborating on new exciting ideas. I am also grateful to Glenn van de Ven for continuous support on all my projects and for always helping with comments and ideas. I consider myself extremely lucky to have Mariya, Michael, and Glenn as advisors that treated me as a researcher from the beginning.

I am also grateful to all the collaborators I met and worked with during my PhD: Ryan Leaman, Oliver Müller, Marina Rejkuba, Ignacio Martín-Navarro, Jesús Falcón-Barroso, and the Fornax3D team. Thank you for being supportive of my ideas and projects. My gratitude also to the members of my PhD thesis committee for volunteering their time for me.

Huge thanks also to Nelma Silva for her continuous support at ESO, from arranging travel to emotional support by sharing cat pictures. Further, I am grateful to the many people that helped me experience three unforgettable weeks at the APEX telescope and at Paranal in Chile.

Finally, I would like to thank my parents and my friends for always supporting me throughout all stages of my PhD and my life in general. Lastly, my deepest gratitude to Dominik who did so much more than reading my thesis, but also accompanied me through fun and stressful times alike. I am extremely grateful for your never-failing support and encouragement.